

Linking climatic changes and North Atlantic volcanism across the
Paleocene-Eocene Thermal Maximum at Fur, Denmark

Ella Wulfsberg Stokke



Thesis submitted for the degree of Philosophiae Doctor

*The Centre for Earth Evolution and Dynamics
Department of Geosciences
Faculty of Mathematics and Natural Sciences
University of Oslo, Norway*

October, 2020

© Ella Wulfsberg Stokke, 2020

*Series of dissertations submitted to the
Faculty of Mathematics and Natural Sciences, University of Oslo
No. 2350*

ISSN 1501-7710

All rights reserved. No part of this publication may be
reproduced or transmitted, in any form or by any means, without permission.

Cover: Hanne Baadsgaard Utigard.
Print production: Reprosentralen, University of Oslo.

Preface

This doctoral thesis titled “Linking climatic changes and North Atlantic volcanism across the Paleocene-Eocene Thermal Maximum at Fur, Denmark” has been submitted to the Department of Geoscience at the University of Oslo in accordance with the requirements for the degree of Philosophiae Doctor (PhD). The work was conducted under the supervision of **main supervisor Morgan T. Jones** and **co-supervisor Henrik H. Svensen**.

The work presented in this thesis is part of project ASHLANTIC, supported by the Research Council of Norway’s funding schemes “Unge Forskертallenter” project number 263000 (project Ashlantic) and “Centres of Excellence” project number 223272. The sample material used in the thesis was collected during a two week field campaign at the island of Fur in northwest Denmark in August 2017. I have been based at the Centre for Earth Evolution and Dynamics and the Department of Geoscience during the whole period, starting the 1st of July 2017. However, much of the analytical work has been conducted during several visits at the Department of Earth Science at the University of Bergen and the Department of Earth Sciences at the University of Cambridge. An additional two month research stay at the National Oceanographic Centre in Southampton was funded by the Norwegian Research School DEEP, project number 249040/F60.

Summary

This thesis focuses on a sedimentary sequence on the island of Fur in northwest Denmark that covers a period between about 56–54 million years ago including the Paleocene-Eocene transition. This was a period of greenhouse conditions, with temperatures on average up to 10 °C warmer than today. On top of this already warm climate, there were several periods of increased global warming. The most extreme of these is called the Paleocene-Eocene Thermal Maximum (PETM). This event was associated with a large perturbation to the carbon cycle caused by voluminous emissions of isotopically light carbon into the ocean-atmosphere system. Today, we are emitting carbon into the atmosphere at an even higher rate, and it is therefore crucial to get a better understanding of the potential consequences.

During the Paleocene and Eocene, Denmark was submerged under water in the eastern North Sea. The first chapter of this thesis reconstructs how the temperatures in the North Sea surface waters changed as a consequence of the carbon emissions. To do this, we use an organic thermometer called TEX₈₆, which record how algae cell membranes change in response to variations in ocean temperature. We find that temperatures increased at least 10 °C across the PETM onset, which is dramatic considering the onset is supposed to have taken only a few thousand years. More surprisingly, we find that temperatures actually decreased just before the onset, and cooled much more drastically afterwards than previously thought. The North Sea is in close proximity to the North Atlantic Igneous Province (NAIP). This is a vast complex of extrusive and intrusive igneous rocks surrounding the margins of the present day North Atlantic, which were emplaced before, during and after the PETM global warming. Throughout geological time, there is a temporal, and potentially causal, relationship between such large igneous provinces and periods of environmental crisis. We find that the cool periods recorded in the sediments corresponds to periods of increased volcanic activity and ash deposition, and propose that the NAIP activity may have had a regional cooling effect.

The second chapter of this thesis looks closer at the hundreds of thick basaltic volcanic ash layers from the NAIP that are found throughout the North Sea area and are particularly well preserved in Denmark. They represent the largest and most explosive basaltic eruptions known, yet the eruptive processes causing them are not fully understood. We measure the sulfur content of the volcanic glass and find that the ashes are not fully degassed, which

indicates that they erupted under high pressure such as during submarine eruptions. The shape and texture of the glass also suggests that the erupting lava cooled very rapidly, most likely in contact with water. We therefore conclude that the basaltic ashes represent extremely explosive hydromagmatic eruptions (magma-water interaction), most likely erupting in shallow water (<200 m deep) during the opening of the northeast Atlantic Ocean. We also estimate that each of these explosive eruptions may have emitted 0.72 ± 0.18 to 7.2 ± 1.8 Gt SO₂. Large emissions of SO₂ have caused long periods of volcanic cooling in the past, and may have been responsible for the cool ocean temperatures recorded in the North Sea after the PETM.

The last chapter of this thesis looks at the environmental changes in and around the North Sea area during the PETM. We analysed the mineralogy and chemistry of the clays to look at changes in sediment input and in the oxygen concentration of the ocean. The data reveal a large amount of the volcanically derived minerals smectite and zeolites, suggesting that the NAIP was the most important source area during this period. An influx of the mineral kaolinite just after the PETM onset show that the climate became more humid. This led to increased weathering and erosion on land, with a subsequent rise in sediment transport into the ocean. Basaltic volcanic material is easily weathered, and the enormous amount of flood basalts and ash emplaced by the NAIP would also contribute significantly to boost the global silicate weathering. Enhanced freshwater input led to stratification of the water column, which combined with ocean warming decreased the bottom water oxygen content leading to an anoxic-sulfidic environment. Increased sediment input combined with ash falls brought a lot of nutrients to the surface ocean, which enhanced the primary productivity. A rise in the organic matter burial in the ocean together with increased silicate weathering on land contributed to draw CO₂ out of the atmosphere. This show the importance of marginal shelf areas such as the Danish North Sea area in tracking, and contributing to, the PETM recovery.

Acknowledgement

First and foremost, I wish to thank my supervisors Morgan and Henrik. Writing a PhD has been the most demanding and rewarding challenge of my life, and the last three and a half years have changed me more than I ever thought it could. I will forever be grateful that you gave me this opportunity! Morgan, you have been incredibly supportive throughout this project, both in science and in life. You have given me freedom and room to explore and figure things out for myself, but have always been available to guide me and answer all my questions. Thank you for always having my back and being both a supervisor and a friend when things have been a bit rough. When I was 19 and wondered what I should do with my life I went to see Henrik give a talk about geology and natural disasters and decided that I wanted to be a geologist. It feels pretty amazing that you ended up supervising my PhD, you have always inspired me so much!

Furthermore, I would like to thank Emma Liu for making me feel so welcome in Cambridge and for being so incredibly supportive and inspiring. You have been a huge part of this project supervising me in all the work for the second chapter; and making it just so much fun! You and Morgan dancing salsa in the lab at 2AM will be a forever memory.

There are so many amazing people that have helped, supported, and inspired me on the way. I particularly want to thank my master supervisor Deta Gasser, who taught me just how exciting and fun geology and research can be and encouraged me to continue in academia. A special thanks goes to collaborators and colleagues during this project. Haflidi Haflidason for all the help and for trusting me in the lab in Bergen even though I almost broke the XRF core scanner. Ivar Midtkandal for helping and believing in me not just now, but since my master. Jessica Whiteside for welcoming me in Southampton. I would also like to thank Thanusha Naidoo and Mufak Naoroz for teaching and helping me out in their labs in Oslo, and Sarge Bray in Southampton for teaching me all about organic geochemistry. I would like to thank all of my amazing colleagues at CEED and the department for making the last years so enjoyable. Particularly thank you to the Earth Crisis team, and to Thea, Chloe, Eirik, Hans Jørgen, Joost, Manon, Bjørgunn, Nils and many more for good company and interesting discussions through the years.

Life is believe it or not about more than geology, and having a life outside work is important, so I would very much like to thank my friends and family for reminding me of that. Although a special thanks to Bergliot and Ingjerd for letting me combine friendship with the love of rocks, and to Alma for just being you. A big thanks also goes to Foss jentene for many years of friendship and emotional support. I would also like to thank my very wise mother for always supporting me and my choices and giving me such good advice on the way.

Finally and most importantly I want to thank my Gauti. No one have supported me more. The last year has been so hard, but coming home to homemade food, clean clothes, and tonnes of laughter has got me through it. You keep me together, thank you!

Scientific output

First author papers

Stokke, E. W., Jones, M. T., Tierney, J. E., Svensen, H. H., & Whiteside, J. H. (2020). Temperature changes across the Paleocene-Eocene Thermal Maximum—a new high-resolution TEX₈₆ temperature record from the Eastern North Sea Basin. *Earth and Planetary Science Letters*, 544, 116388.

Stokke, E. W., Liu, E. J., & Jones, M. T. (2020). Evidence of explosive hydromagmatic eruptions during the emplacement of the North Atlantic Igneous Province. *Volcanica*

Stokke, E. W., Jones, M. T., Riber, L., Haflidason, H., Midtkandal, I., Schultz, B.P., & Svensen, H. H. (*In review*). Rapid and sustained environmental response to global warming: The Paleocene-Eocene Thermal Maximum in Denmark. *Climate of the Past Discussions*, 1-38

Co-authorships

Jones, M. T., Percival, L. M., Stokke, E. W., Frieling, J., Mather, T. A., Riber, L., ... & Svensen, H. H. (2019). Mercury anomalies across the Palaeocene–Eocene thermal maximum. *Climate of the Past*, 15(1).

Longman, J., Gernon, T. M., Palmer, M. R., Jones, M. T., Stokke, E. W. & Svensen, H. H. (*In review*). Marine diagenesis of tephra accelerated the Paleocene-Eocene Thermal Maximum termination. *Nature Geoscience*

Pogge von Strandmann, P. A. E., Jones, M. T., Murphy, M. J., Stokke, E. W., Tarbuck, G., Wilson, D. J., Pearce, C. R., Schmidt, D. N. (*In review*). Lithium isotope evidence for enhanced weathering and erosion during the Palaeocene-Eocene Thermal Maximum. *Nature Communications*

First author conference proceedings

Stokke, E.W., Jones, M.T., Hammer, Ø. & Svensen, H. Geochemical variations during the PETM and later Eocene hyperthermals: investigating a new drill core from Fur, Denmark. Nordic Geological Winter Meeting, Copenhagen, 10/1/2018 – 12/1/2018

Stokke, E.W., Whiteside, J.H., Svensen, H.H., Hammer, Ø. & Jones, M.T. Linking warming, environmental changes, and volcanic ash falls from onset to recovery of the PETM: investigations from Fur, Denmark. European Geosciences Union General Assembly, Vienna, 8/4/2018 – 13/4/2018

Stokke, E.W., Whiteside, J.H., Riber, L., Haflidason, H., Tierney, J.E, Svensen, H.H. & Jones, M.T. Linking warming, environmental changes, and volcanic ash falls from onset to recovery of the PETM: a multi-proxy study from Fur, Denmark. Goldschmidt, Barcelona, 19/8/2019 – 23/8/2019

Stokke, E.W., Jones, M.T., Tierney, J.E., Riber, L., Svensen, H.H. & Whiteside, J.H. Volcanic cooling followed by a warm and wet Paleocene-Eocene Thermal Maximum in Denmark. Nordic Geological Winter Meeting, Oslo, 8/1/2020 – 10/1/2020

Stokke, E.W., Liu, E.J. & Jones, M.T. Eruption mechanism and volatile budget of the early Eocene Danish ash series, and implications for the emplacement of the North Atlantic Igneous Province. Virtual Goldschmidt, 22/6/2020 – 26/6/2020

Table of content

1. Motivation and approach	1
2. Scientific background	3
2.1 <i>The Paleocene-Eocene Period</i>	
2.2 <i>The Paleocene-Eocene Thermal Maximum</i>	
2.3 <i>The North Atlantic Igneous Province</i>	
2.3.1 Potential climatic impact of the NAIP	
2.4 <i>Denmark and the North Sea Basin</i>	
2.4.1 The PETM in the North Sea	
2.4.2 The island of Fur	
3. Summary of papers	15
4. Outlook	17
5. References	18
Paper I	29
<i>Temperature changes across the Paleocene-Eocene Thermal Maximum—a new high-resolution TEX86 temperature record from the Eastern North Sea Basin.</i>	
Paper II	53
<i>Evidence of explosive hydromagmatic eruptions during the emplacement of the North Atlantic Igneous Province</i>	
Paper III	95
<i>Rapid and sustained environmental response to global warming: The Paleocene-Eocene Thermal Maximum in Denmark</i>	

1. Motivation and approach

Constraining the processes that shape Earth's climate is key to understanding not just our past, but also our future. Anthropogenic carbon emissions are only increasing, leading us into a period of global warming with all the associated implications. The storms will be more extreme, as will the droughts, and ocean warming and acidification will devastate marine ecosystems. Scientists have run thousands of climate models trying to predict and perhaps mitigate against these future changes. However, to fully understand the consequences of current carbon emissions, we also need to look back. Periods of severe environmental stress and climatic changes have occurred repeatedly throughout Earth's history. By investigating these events, we gain knowledge of what might occur in the future, and we may test the accuracy of our models against these observations. One of the most recent and best suited analogues for future global warming is the Paleocene-Eocene Thermal Maximum (PETM; ~55.9 Ma; Alley, 2016; Foster et al., 2018; Westerhold et al., 2018; Svensen et al., 2019), which was associated with large carbon emissions and extreme global warming. Although there will never be a perfect analogue, studying events such as the PETM gives us crucial information on how the environment may respond to large changes in the carbon cycle.

This thesis focuses on an exceptional locality covering the PETM interval; the island of Fur in northwest Denmark (Fig. 1). Although there are not many places in the world where this transition period is found onshore, and few are so complete and well-preserved, there are surprisingly few studies focusing on this locality. This area is also unique due to the preservation and abundance of volcanic ash layers. These ashes are all sourced from the North Atlantic Igneous Province (NAIP; ~62–54 Ma; Fig. 1; Wilkinson et al., 2017), and represent a scale of explosive basaltic eruptions unheard of in both historical and geological records. A hydromagmatic origin has been suggested for these ashes due to their unusual explosivity (e.g. Morton and Knox et al., 1990), yet no studies thus far have done any quantitative attempts to test the eruptive mechanisms creating them. Through geological time, there is a temporal link between Large Igneous Provinces (LIPs) and periods of climate crisis, suggesting a causal relationship (Wignall, 2005). This is also the case for the NAIP, which correlates in time with the PETM and is therefore

considered one of the primary contenders for instigating this prolonged warming, either through direct forcing or as a catalyst for positive climate feedbacks (Svensen et al., 2004; Storey et al., 2007a; Frieling et al., 2016; Gutjahr et al., 2017). Tracking NAIP activity during the PETM is therefore of vital scientific interest. Using the exceptionally well-preserved sediments and ash layers in Denmark, this thesis aims to investigate: 1) the environmental changes during the PETM, 2) the nature of NAIP explosive volcanism, and 3) the potential link between the NAIP and climatic and environmental changes recorded in the sediments in Denmark.

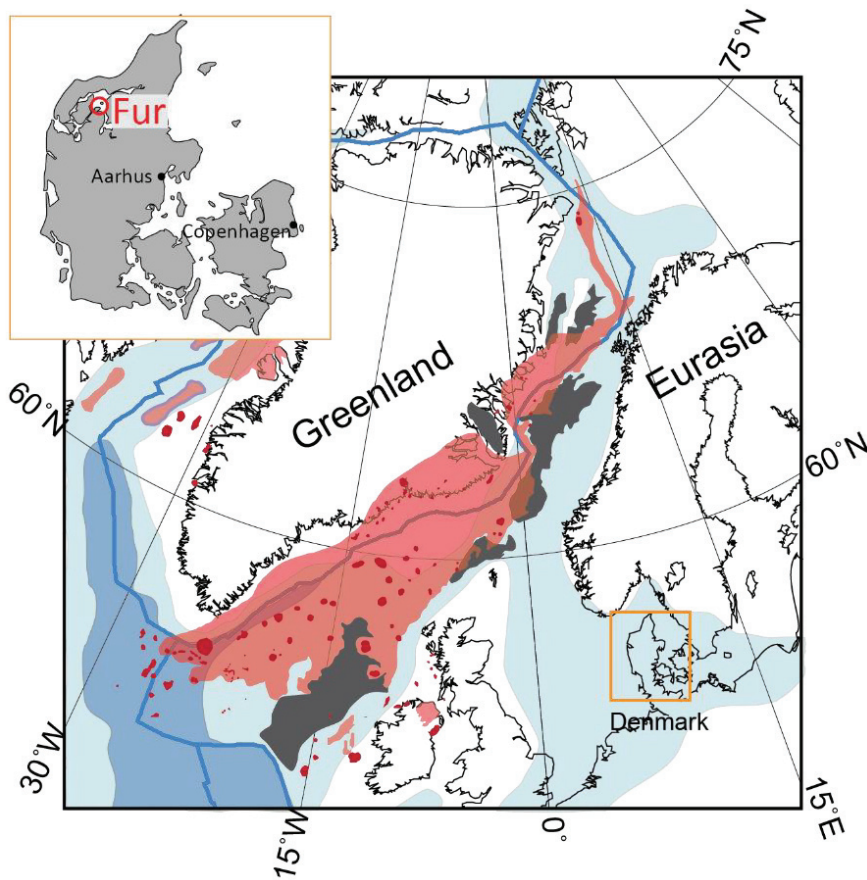


Figure 1: Palaeogeographic reconstruction at 56 Ma showing the known extent of the North Atlantic Igneous Province (NAIP). Dark red: volcanic centres. Red areas: the known extent of subaerial and submarine extrusive NAIP volcanism. Dark grey areas: known extent of NAIP sill intrusions (note that the extent of intrusions under the extrusive areas is unknown due to poor seismic retrieval data). Blue lines: plate boundaries. Black lines: present-day coastlines. Light blue: shelf areas. Dark blue: ocean basins.

Figure modified from Abdelmalak et al. (2016); Horni et al. (2017); Jones et al. (2019) and references therein. The small map shows the location of Fur within Denmark.

This thesis consequently stretches its aim wide, covering a range of scientific disciplines. It aims to understand all the aspects of this particular stratigraphic interval, and the myriad ways that the NAIP emplacement affected the environment during this critical period. To achieve this aim it is necessary to be interdisciplinary, implementing novel and cutting-edge methods from a range of backgrounds. Paper 1 uses organic geochemistry to identify biomarkers and to reconstruct sea surface temperatures with the palaeotemperature proxy TEX₈₆. Paper 2 uses volcanic ash grain morphology and chemistry to constrain the type of eruption that produced widespread explosive basaltic tephra layers, and to estimate the extent of volatile degassing. Paper 3 focuses on the sedimentary inorganic geochemistry and mineralogy in order to investigate changes in terrestrial runoff, seawater redox conditions, and volcanic influences.

2. Scientific background

2.1 The Paleocene-Eocene period

The Cenozoic is characterised by a gradually changing climate state from greenhouse to icehouse conditions (Fig. 2; Zachos et al., 2008; Westerhold et al., 2020). The Early Cenozoic (the Palaeogene) greenhouse climates are characterised by high atmospheric carbon dioxide concentrations ($p\text{CO}_2$; Pearson and Palmer, 2000; Anagnostou et al., 2016) and sea surface temperatures (SSTs; Bijl et al., 2009; Hollis et al., 2012), and no permanent polar ice caps (e.g. Zachos et al., 2008). In the aftermath of the Cretaceous-Palaeogene mass extinction at 66 Ma, the Paleocene and Eocene climate was characterised by increasing greenhouse conditions, driven by high CO_2 concentrations (Anagnostou et al., 2016). The warming culminated in the Early Eocene Climate Optimum (EECO; ~53–50 Ma; Fig. 2). This represents the warmest global temperatures in the last 66 million years; at least 10 °C warmer than present day (Zachos et al., 2008; Cramwinckel et al., 2018; Westerhold et al., 2020). Superimposed on this gradual warming trend are a series of short-lived transient hyperthermal events associated with rapid warming and significant changes in the carbon cycle (Thomas and Zachos, 2000; Lourens et al., 2005; Lunt et al., 2011). These transient events are associated with negative Carbon Isotope Excursions

(CIEs) in the sedimentary record that correspond to maxima in Earth's orbital eccentricity on both 100 and 400 kyr timescales (Cramer et al., 2003; Littler et al., 2014). The eccentricity regulates the distance to the sun and variations in insolation, and orbital forcing could subsequently explain most of these transient events (Cramer et al., 2003; Zachos et al., 2010). The EECO is followed by substantial cooling during the Eocene towards establishment of the Antarctic icecap in the earliest Oligocene (~35 Ma; Zachos et al., 2008; Inglis et al., 2015; Westerhold et al., 2020).

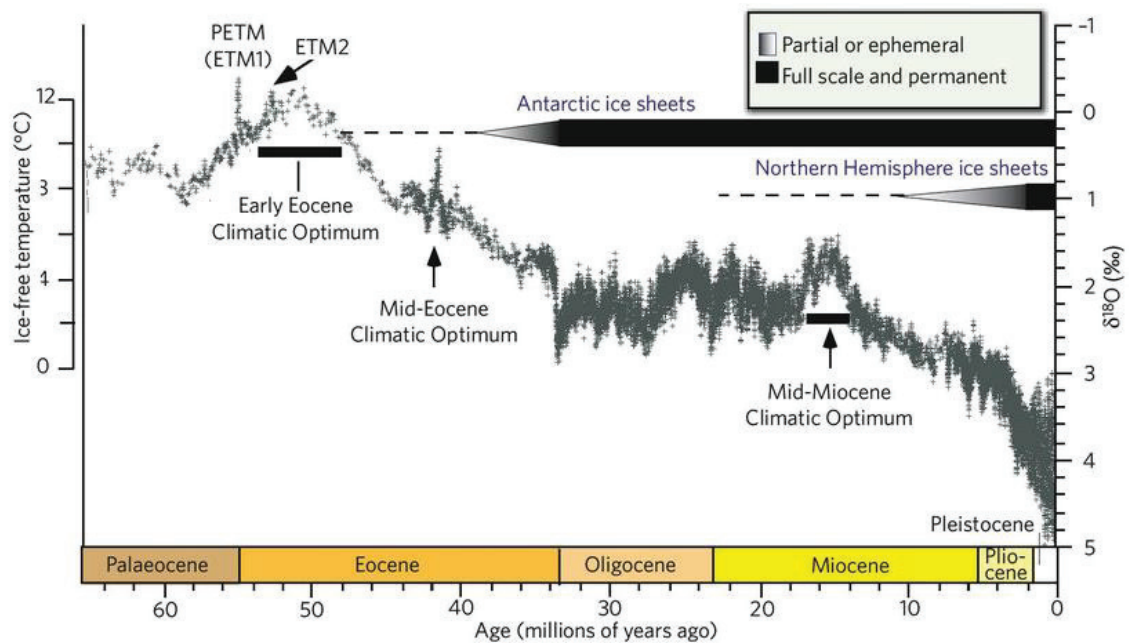


Figure 2: The climate of the Cenozoic – the last 65 Myr. Figure from Zachos et al. (2008). PETM = Paleocene-Eocene thermal Maximum; ETM2 = Eocene Thermal Maximum 2

2.2 The Paleocene-Eocene Thermal Maximum

The most prominent Palaeogene hyperthermal was the PETM (Fig. 1; Zachos et al., 2008; Westerhold et al., 2020). It is associated with a rapid and sustained global ocean surface warming of 4–5 °C (Dunkley Jones et al., 2013; Frieling et al., 2017), and a carbon cycle perturbation causing a prominent negative CIE of 2–7 ‰ in marine and terrestrial sediments (McInerney and Wing, 2011). The timing of the PETM onset is still disputed (Zeebe and Lourens, 2019), but was most likely close to 55.93 Ma (Charles et al., 2011; Westerhold et al., 2018). The CIE lasted for 120–200 kyr (Röhl et al., 2007; Murphy et al., 2010; Westerhold et al., 2018), and is commonly

composed of a rapid onset (~1–5 kyr; Kirtland-Turner et al., 2017), a stable body of sustained warming (~100 kyr; van der Meulen et al., 2020), and a gradual recovery to pre-PETM $p\text{CO}_2$ values and temperatures (McInerney and Wing, 2011). Most hyperthermal events during the Palaeogene were astronomically paced (Littler et al., 2014). However, the PETM is considered out of phase and amplified in both magnitude and duration, suggesting that some other source or amplifying effect was responsible for the large magnitude (Cramer et al., 2003; Zachos et al., 2010; Komar and Zeebe, 2017). Several sources have been suggested, including the dissolution of methane hydrates (Dickens et al., 1995), a bolide impact activating terrestrial reservoirs (Kent et al., 2003), and/or mantle- and sediment-derived degassing from the NAIP (Svensen et al., 2004; Storey et al., 2007a). Consequently, the exact trigger for the PETM remains controversial, and perhaps the PETM was the result of a combination of triggers and positive feedback mechanisms (Bowen, 2013; Frieling et al., 2016; Komar and Zeebe, 2017; Frieling et al., 2019).

The extensive carbon release led to deep-ocean acidification, causing substantial deep-sea carbonate dissolution and shoaling of the calcite compensation depth (Zachos et al., 2005; Babila et al., 2018). Temperature increases and ocean acidification were accompanied by transient ocean circulation changes, increased halocline stratification, and deep-sea anoxia (Kennet and Stott, 1991; Kender et al., 2012), leading to the extinction of 30–50 % of all benthic foraminifera species (Thomas and Shackleton, 1996; Alegret et al., 2009). On land, the biological response to the CIE includes a burst of mammalian first appearances and biogeographic reorganisation, and a reduction in mammal body size (Koch et al., 1992; Gingerich et al., 2003; McInerney and Wing, 2011). There is also extensive evidence for an intensified hydrological cycle during the PETM (Carmichael et al., 2017), and an overall increase in extreme weather events (Carmichael et al., 2018). Proxy evidence indicates an overall wet-wetter, dry-dryer climatic response, due to increased meridional transport of water vapour from low to high latitudes (Carmichael et al., 2017). This resulted in a more humid climate with increased erosion rates and sediment transport especially in higher latitudes and marginal marine areas (Robert and Kennett, 1994; Harding et al., 2011; John et al., 2012; Khozyem et al., 2013). Increased silicate weathering is one of the most important mechanisms in carbon drawdown (Gislason and Oelkers, 2011), and was likely one of the main drivers of the PETM recovery (Kelly et al., 2005; Penman, 2016). However, a key PETM

feature is the unusually rapid recovery, suggesting that additional mechanisms such as increased export productivity and organic carbon burial contributed to the carbon drawdown (Bowen and Zachos, 2010; Komar and Zeebe, 2017; Bridgestock et al., 2019). Yet more work is needed to understand the processes driving this rapid recovery.

2.3 The North Atlantic Igneous Province

Large Igneous Provinces (LIPs) are the remnants of volcanic episodes with particularly large magma production erupted over a geologically short time (in pulses <5 Myr) and spread over wide areas (Coffin & Eldholm, 1991; Bryan & Ernst, 2008; Ernst and Youbi, 2017). When emplaced in continental settings, they commonly form continental flood basalts with associated large sub-volcanic and intrusive complexes, and are often linked to volcanic passive margins (Planke et al., 2005) and continental break-up (Coutillot et al., 1999; Buiter and Torsvik, 2014). The NAIP is one of the most recent LIPs in Earth history emplaced between ~ 62 – 54 Ma (Wilkinson et al., 2017). This encompasses both the long term Early Palaeogene warming and the PETM interval (Storey et al., 2007b; Larsen and Tegner, 2006). It is composed of massive continental flood basalts, widespread sill intrusions, and large volcanic centres that surround the margins of the present-day northeast Atlantic and Labrador Sea (Figs. 1, 3; Saunders et al., 1997; Storey et al., 2007b; Abdelmalak et al., 2016; Horni et al., 2017). The deposits cover an area up to 1.3×10^6 km² with an estimated total volume of 5 – 10×10^6 km³ (Eldholm and Grue, 1994; Horni et al., 2017).

The NAIP emplacement can broadly be divided into two phases; 1) an initial pre-breakup phase of continental flood basalt volcanism with associated subvolcanic intrusions and plutonism starting at about 62 Ma, and 2) a second and by far most voluminous phase between 56–54 Ma of thick lava flows, large sill intrusions, and plutonic complexes associated with the break-up of the Northeast Atlantic Ocean (Larsen et al., 2016; Saunders et al., 1997; Storey et al., 2007b; Wilkinson et al., 2017). Although mainly composed of tholeiitic basaltic magmas, calc-alkaline magmas do occur, particularly within the early stages (Saunders et al., 1997). By the time of continental break-up and seafloor spreading new oceanic crust formed and the extruding magmas were dominantly tholeiitic (Saunders et al., 1997). Eruption rates decreased rapidly towards 50 Ma, but persisted on a smaller scale in a narrow area at the western end of the

Greenland-Iceland ridge surrounding today's Icelandic hotspot (Storey et al., 2007a; Upton, 1988).

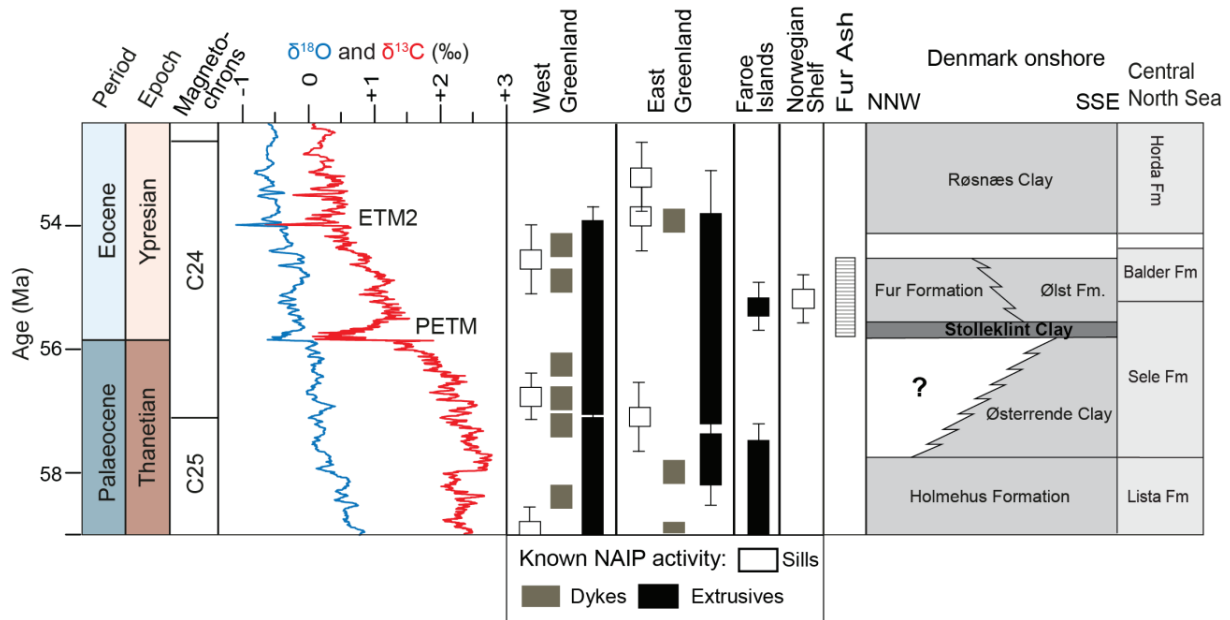


Figure 3: Composite figure of the late Paleocene and early Eocene interval plotted on the GTS2012 timescale (Ogg, 2012). Both the Danish stratigraphy and the correlative offshore North Sea stratigraphy are indicated, based on Schiøler et al. (2007) and King (2016). Carbon and oxygen isotope data from Cramer et al. (2009) and Littler et al. (2014). The $\delta^{13}\text{C}$ and $\delta^{18}\text{O}$ curves indicate the stratigraphic position of two periods of carbon perturbation; the Paleocene-Eocene Thermal Maximum (PETM) and the Eocene Thermal Maximum 2 (ETM2). The overview of NAIP intrusive and extrusive activity is based on age data filtered to only include robust $^{40}\text{Ar}/^{39}\text{Ar}$ mineral ages (recalibrated to Kuiper et al., 2008) and U-Pb zircon ID-TIMS ages: Storey et al. (1998); (2007b); Jolley et al. (2002); Svensen et al. (2010); Larsen et al. (2016).

Explosive volcanism played an integral part of NAIP activity. This activity is recorded in the abundant tephra layers preserved in sedimentary sequences along the North Atlantic margins, in the North Sea, and throughout Northern Europe (Egger et al., 2005; Haaland et al., 2000; Morton and Knox, 1990; Larsen et al., 2003). While an early phase of tephra erupted in the Late Paleocene, corresponding to the earlier phases of NAIP emplacement, these are sparse and overall poorly preserved (Knox and Morton, 1988). A second and much more voluminous phase erupted during the early Eocene and the Northeast Atlantic seafloor spreading, comprising

several hundred well-preserved tephra layers mostly post-dating the PETM (Knox and Morton, 1988; Larsen et al., 2003). These are suggested to have formed by explosive magma-water interactions during the opening of the northeast Atlantic Ocean (Haaland et al., 2000; Morton and Knox et al., 1990; Larsen et al., 2003). However, the exact mode of eruption is still uncertain, and needs to be rigorously investigated.

2.3.1 Potential climatic impact of the NAIP

The majority of significant environmental crises since the Permian correlate temporarily with LIP emplacements (Wignall, 2005). Although the mechanisms are still not completely understood, the temporal correlation strongly suggests that major volcanic activity can have a potentially devastating environmental effect (Rampino and Stothers, 1988; Wignall, 2005; Jones et al., 2016). There are two main mechanisms of major greenhouse gas emissions from LIPs; 1) through direct magmatic degassing (Self et al., 2005; Saunders, 2016; Gutjahr et al., 2017), or 2) through thermogenic degassing generated by contact metamorphism around sills in sedimentary basins (Svensen et al., 2004; Aarnes et al., 2010). The PETM coincides with a roughly 0.4 to 1 Myr interval of massive flood basalt volcanism (Larsen and Tegner, 2006; Storey et al., 2007b; Wotzlaw et al., 2012; Jones et al., 2019) and the emplacement of magmatic sills (Svensen et al., 2010; Frieling et al., 2016), indicating that the NAIP may have played a vital role in triggering the PETM hyperthermal conditions (Svensen et al., 2004; Storey et al., 2007a; Frieling et al., 2016; Gutjahr et al., 2017).

Direct degassing from flood basalts are dominated by H₂O (50–90 %), but also substantial amounts of CO₂ (1–40 %) and SO₂ (2–35 %), with minor quantities of halogens such as HCl and HF (Self et al., 2014). Volcanically-derived sulfate aerosols is well-known to instigate periods of cooling in the historical record (Robock, 2000), such as the 2–3 year cooling following the 1783–84 eruption of Laki in Iceland (Thordarson and Self, 2003). Subsequently, several studies have suggested the possibility that the massive amounts of erupted material during LIP emplacements may have had a similar cooling effect (Self et al., 2005; Bond and Wignall, 2014; Ernst and Youbi, 2017). Particularly as LIPs that correlate with large environmental impacts appear to be particularly sulfur-rich (Callegaro et al., 2014), and as modelling studies have found that

continuous sulfur degassing from long-lasting (~10 year) flood basalt eruptions may lead to cooling lasting several decades (Schmidt et al., 2016). However, few volcanic cooling events are identified in the geological record due to the short atmospheric residence time of sulfur (Robock, 2000). A major task is therefore to both identify possible cooling events in the stratigraphic record, and to constrain the rate and magnitude of sulfur emissions from LIP volcanism.

CO₂ has a longer residence time than sulfur in the ocean-atmosphere-biosphere system, and could have a severe climatic effect lasting for much longer periods if large-scale degassing occurs in a short period of time (Jones et al., 2016). Recent studies suggest that mantle degassing may be enough to trigger the PETM warming (Gutjahr et al., 2017), and Self et al. (2006) found that ~100 km³ of flood basalts could yield up to ~14 Gt CO₂. Still, the actual annual flux of mantle derived CO₂ would be minor compared to the atmospheric and oceanic carbon reservoirs, and are most likely not sufficient to significantly change atmospheric concentrations on their own (Self et al., 2006; Self et al., 2014). Contact metamorphism between igneous sills and organic-rich shales or hydrocarbons in the host rocks causes thermogenic degassing of large amount of isotopically light carbon (Svensen et al., 2015). While the isotopic composition of mantle derived carbon is about -5 ‰ (Pineau & Javoy, 1983; Gales et al., 2020), thermogenic carbon degassing (CO₂ and CH₄) is much lower, between -27 to -44 ‰ (Jones et al., 2016), and would require less degassing to account for the observed PETM CIE magnitude (McInerney and Wing, 2011). In addition to flood basalts, the NAIP comprises large complexes of sills and dykes, emplaced into the organic-rich sediments on the continental shelves surrounding the North Atlantic (Planke et al., 2005). Large vent complexes at the edges of these volcanic sills are evidence of explosive degassing generated during their emplacement, indicating that the NAIP may have had a potentially big climatic impact (Svensen et al., 2004). While the current geochronological constraints are not precise enough to correlate this activity with the PETM onset, there is compelling evidence to suggest that explosive vent complexes were active during the PETM body and may have had an amplifying effect on the unusually large magnitude and duration (Frieling et al., 2016).

2.4 Denmark and the North Sea Basin

During the Paleocene and Eocene the Danish mainland was part of the Norwegian-Danish Basin, an extension of the modern day North Sea. This basin formed a NW-SE striking depression bounded by the Fennoscandian Shield and the Sorgenfrei-Tornquist Zone to the NE and basement blocks in the Ringkøbing-Fyn High to the SW (Fig. 4; Schiøler et al., 2007). The North Sea Basin is characterised by major rift systems that developed in the Mesozoic, forming the large Central Basin and Viking Graben (Fig. 4; Petersen et al., 2008). The Norwegian-Danish Basin is a marginal basin to the larger North Sea Basin system, and formed by subsidence during margin hyperextension rather than through rifting (Rasmussen et al., 2008). This has resulted in a relatively undisturbed, westward-thickening sedimentary sequence stretching from the Permian throughout the Cenozoic (Petersen et al., 2008).

2.4.1 The PETM in the North Sea

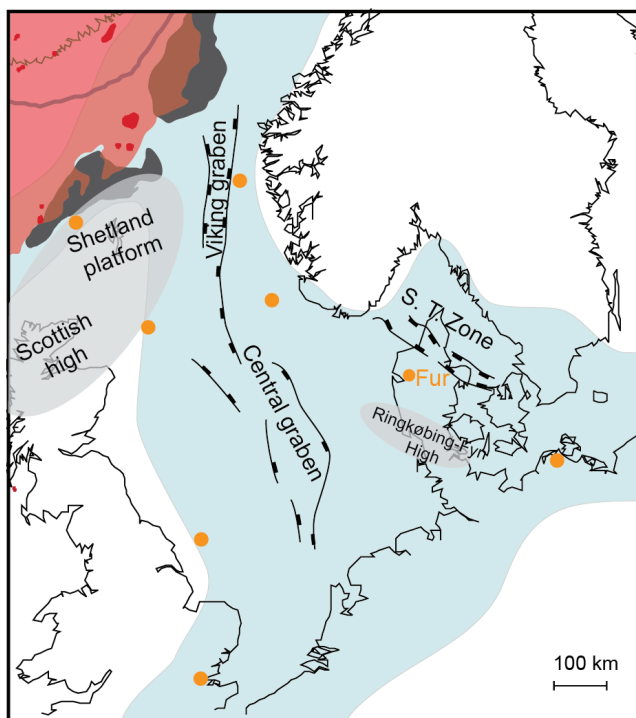


Figure 4: Map of the North Sea area indicating the main basins and structural elements. “S. T. Zone” = Sorgenfrei-Tornquist Zone. The figure is a zoom-in on Figure 1, with modifications based on Schiøler et al.

(2007). Yellow points indicate selected known localities comprising NAIP tephra layers (Morton and Knox, 1990; Haaland et al., 2000; Jolley and Widdowson, 2005).

During the Paleocene-Eocene the North Sea was characterised by a high sedimentary input, particularly from the Faroe-Shetland platform. This resulted in an expanded, almost uninterrupted sedimentary sequence across the Paleocene-Eocene transition and the PETM. The proximity to the NAIP also makes the North Sea an ideal area to track NAIP activity. However, despite these advantages as key localities, only a few PETM studies have focused on the North Sea. During the PETM, palynological records from the central North Sea indicate significant surface water freshening, likely due to an increased hydrological cycle (Kender et al., 2012). A similar increase in fresh water discharge into the North Sea was indicated close to the Paleocene-Eocene transition by shark tooth apatite $\delta^{18}\text{O}$ records from Denmark and England (Zacke et al., 2009). The PETM climatic changes, combined with NAIP thermal uplift in the latest Paleocene, led to basin-wide development of stratification and anoxia in the North Sea (Kender et al., 2012). These changes were also recorded in Denmark, where Schoon et al. (2015) found indications of anoxia and photic zone euxinia following the PETM onset. Only one previous study has attempted to reconstruct sea surface and continental mean annual air temperatures across the PETM in the North Sea. They focused on two sedimentary sections in Denmark including the island of Fur, and found that temperatures decreased immediately below the PETM and increased about 7 °C across the CIE onset, before decreasing during the PETM recovery (Schoon et al., 2015). However, this was based on a limited dataset that only covered the PETM onset and recovery. A high-resolution reconstruction of temperatures across the PETM was therefore still lacking from the North Sea before this thesis, as was a detailed investigation into the environmental changes in Denmark during the PETM.

2.4.2 The island of Fur

This thesis is centred on the island of Fur, a small island (22 km²) within Limfjorden in northwest Denmark (Fig. 1). This is a unique and well suited locality for several reasons. Firstly, the entire latest Paleocene and earliest Eocene stratigraphy is exposed on land, easily accessible in coastal cliffs (e.g. Stolleklint, Fig. 5) and quarries. The area was at the edge of the last Scandinavian Ice

Sheet, and the effects of glaciotectonism and regional uplift has led to the current exposure of Palaeogene sediments around Limfjorden. Secondly, although the effects of glaciotectonism have resulted in both small- and large-scale folding, the sediments have never been deeply buried and are therefore still thermally immature, unlithified, and easy to sample. We can therefore apply organic geochemical methods that are typically restricted to modern sediments. The ashes are also exceptionally well-preserved, possibly aided by a silica-saturated depositional environment dominated by diatomites. Volcanic glass grains are normally very easily weathered and devitrified. The abundance of pristine volcanic glass in the Danish ashes is therefore extremely rare for sediments of this age, and also enables us to apply geochemical methods commonly used in modern environments.



Figure 5: The beach at Stolleklint on the northern shore of the island of Fur, where most of data compiled in this thesis is collected. Photo taken from the sea by a drone. The dark lower clay is the Stolleklint Clay, and the light upper part the Fur Formation diatomites. Darker layers within the diatomite are volcanic ash layers.

The Paleocene-Eocene transition at Fur is marked by a shift in sedimentary facies from the hemipelagic and bioturbated clays in the Holmehus/Østerrende Formation, into an expanded section of dark, laminated clays termed the Stolleklint Clay (Figs. 3, 6; Heilmann-Clausen, 1995; Heilmann-Clausen et al., 1985). The Stolleklint Clay is an unofficial stratigraphic member correlating to the lowermost Ølst Formation southward in Denmark, and the Sele Formation offshore in the North Sea (Fig. 3). The boundary is followed by an almost complete removal of benthic fauna and preferential dissolution of remaining calcareous organisms (e.g. Heilmann-Clausen, 1995). At Fur, the PETM is identified at the base of the Stolleklint Clay by a 4–8 ‰ CIE

and appearance of the diagnostic dinoflagellate *Apectodyinium augustum* (Schmitz et al., 2004; Schoon et al., 2013; Jones et al., 2019).

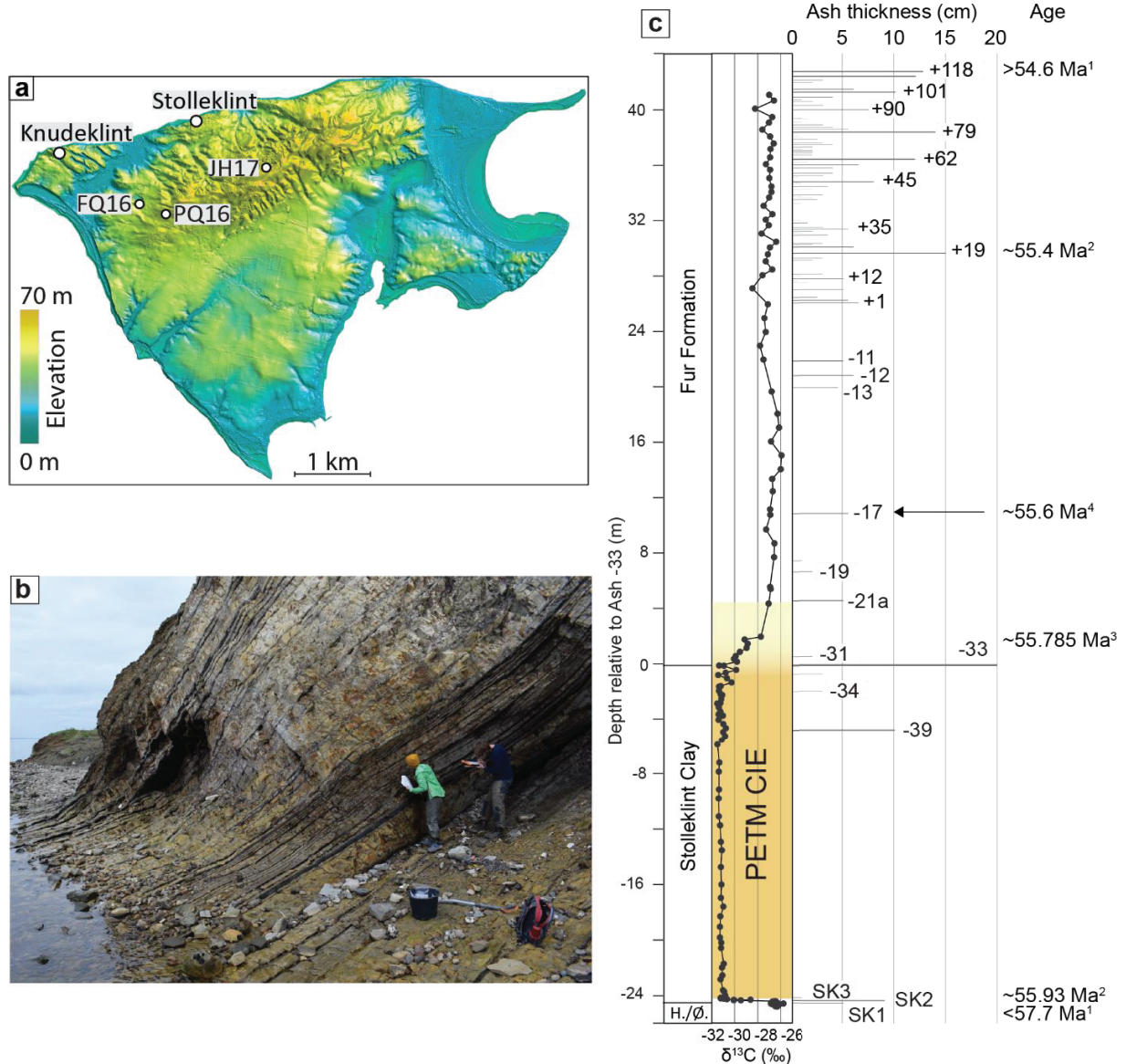


Figure 6: **a)** Topographic map of the island of Fur, Denmark. This thesis focus primarily on Stolleklint, with additional samples from three quarries termed FQ16, JH17, and PQ17 in this study. Ash samples are mainly from Knudeklint. The high topography in the north marks a partially overturned anticline of Fur Formation and upper Stolleklint Clay strata. Map courtesy of Egon Nørmark. **b)** Photo showing the cliff side at Knudeklint looking east, showing positive series black ash layers in light coloured diatomite of the Fur Formation **c)** Overview of the local stratigraphy that is the focus of this thesis. Depth is measured upwards and downwards from the main marker bed Ash -33. The yellow column indicates the PETM CIE

duration, based on the $\delta^{13}\text{C}$ curve from Jones et al. (2019). Ages are indicated based on ¹King (2016); ²Westerhold et al. (2009); ³Charles et al. (2011), assuming the timings of the Svalbard and Fur CIEs are coeval; ⁴Storey et al. (2007a) recalibrated to Kuiper et al. (2008).

The NAIP thermal uplift led to a relative sea-level fall in the latest Paleocene (Rasmussen et al., 2008; Anell et al., 2012). This was superimposed on the marine transgression that characterises the Paleocene-Eocene transition globally, likely due to thermal expansion of seawater (Sluijs et al., 2008). Following the initial sea-level fall, most of the Stolleklint Clay is deposited during a gradual sea-level rise (Heilmann-Clausen, 1995). Towards the end of the PETM, the Stolleklint Clay grades upward into a ~60 m thick Fur Formation diatomitic succession (Figs. 5, 6). This is part of a narrow belt of diatomite deposition stretching westward from NW-Denmark into the nearby North Sea (Knox et al., 2010; Schiøler et al., 2007). Localised upwelling has been suggested as the main cause of these diatomite blooms, controlled either by wind (Bonde, 1979), and/or by increased runoff and the build-up of monsoon-like pressure systems causing sporadic basin eutrophication (Mitlehner, 1996). Increased nutrient supply from volcanic ash dispersal would also contribute to sporadic eutrophication (Jones & Gislason, 2008; Mitlehner, 1996).

More than 180 ash layers are identified on land in Denmark, recorded as the positive and negative ash series by Bøggild (1918) based on their outcrop appearance and chemistry (Fig. 6). The negative series (Ashes -1 to -39) correlate with tephras within the Sele Formation offshore (phase 2a of Knox and Morton, 1988), and comprise a heterogeneous mix of ash compositions (Larsen et al., 2003). These were likely sourced from different volcanic centres on the British Isles, East Greenland, and around the northeast Atlantic margin (Larsen et al., 2003). At least three heavily altered tholeiitic basaltic tephra layers have since been recognized below Ash -39 (e.g. Schmitz et al., 2004), termed SK1 to SK3 by Jones et al. (2019). Most of the ashes (>140) are found within the positive ash series, which correlate temporally and chemically with the Balder Formation tephras offshore (phases 2b and 2c of Knox and Morton, 1988). These are, with the exception of the rhyolitic ashes +13 and +19, composed of tholeiitic basalts (Larsen et al., 2003). The entire positive ash series post-dates the PETM, and likely originated from the main rift zone during the Northeast Atlantic Ocean opening (Larsen et al., 2003; Morton and Knox, 1990).

3. Summary of papers

3.1 Paper I

The first paper is published in *Earth and Planetary Science Letters* in 2020 and is titled **“Temperature changes across the Paleocene-Eocene Thermal Maximum – a new high-resolution TEX₈₆ temperature record from the Eastern North Sea Basin”**. This paper focuses on reconstructing the sea surface temperature evolution in the Danish sediments using the organic palaeothermometer TEX₈₆. The new temperature record covers the top of the Holmehus/Østerrende Formation in the latest Paleocene, the PETM onset, body and recovery, and the earliest Eocene post-PETM section before the next hyperthermal event the Eocene Thermal Maximum 2. We find that temperatures increased rapidly by ~10 °C across the PETM onset, before decreasing gradually throughout the PETM body and recovery. Although at the upper end of previous studies, this is in line with other PETM sea surface temperature reconstructions. We also show that temperatures were depressed both pre-and post-PETM in Denmark. While some analytical uncertainty is likely to be partially responsible, parts of the cooling are expected to be a real feature. A cooling pre-PETM is contrary to the global signal, but post-PETM there are indications also elsewhere in the North Sea that temperatures were unusually cool. We conclude that if the cooling is genuine, it must be linked to regional conditions. This cooling corresponds to the most voluminous event of ash deposition from the NAIP, and we speculate whether this volcanism led to regional cooling after the PETM, and perhaps to some degree before.

3.2 Paper II

The second paper is published in *Volcanica* in 2020 and is titled **“Evidence of explosive hydromagmatic eruptions during the emplacement of the North Atlantic Igneous Province”**. This paper focuses on the abundant volcanic ash layers and aims to test whether the ashes were caused by hydromagmatic activity. Volcanic glass quenches rapidly in contact with water, leading to brittle fragmentation. Increased overlying pressure, such as eruptions under water, suppresses the volatile degassing leading to elevated residual volatile content in the glass. The exceptional preservation of the Danish ashes enables us examine the volcanic glass morphology and textural

distribution, and analyse their residual sulfur content. We find that the high degree of brittle fragmented glass, low vesicularity, and overall elevated residual sulfur content all indicate that the ashes were produced in hydromagmatic eruptions. By modelling the theoretical sulfur content at sulfur saturation, we estimate the likely sulfur concentrations of the melts prior to each eruption, which enables us to assess that the glasses were only partly degassed in sulfur (55–80 % degassed). This allows us to estimate that the total amount of degassed sulfur from the Danish ashes was between 0.72 ± 0.18 to 7.2 ± 1.8 Gt SO₂, which could have had a substantial climatic effect. This demonstrates that this large-magnitude explosive volcanism may have contributed to the unusually cool post-PETM temperatures observed in paper 1. We further speculate that the ashes were produced during shallow-marine subaqueous eruptions, occurring along the main rift during the northeast Atlantic Ocean opening.

3.3 Paper III

The third manuscript is currently unpublished and is titled **“Rapid and sustained environmental response to global warming: The Paleocene-Eocene Thermal Maximum in Denmark”**. This manuscript explores the environmental response to the temperature changes reported in paper 1, focusing on the PETM interval and the Stolleklint Clay marine clays. We use a combination of sedimentological, geochemical, and mineralogical proxies to reconstruct changes in sediment supply, weathering, productivity, and basin redox conditions. Chemical indices indicate the presence of volcanic ash earlier than previously thought, both during the pre-PETM cooling and within the PETM body. An influx of kaolinite and an increase in the chemical index of alteration indicates a rise in the influx of terrestrial material to the basin, both in the lower part of the PETM body shortly after the CIE onset and during the PETM recovery. Combined with a large increase in sedimentation accumulation rate across the PETM onset, it suggests an enhanced hydrological cycle leading to a rise in continental weathering and runoff. While the environment may have already been partly suboxic pre-PETM, multiple lines of evidence suggest that the environment becomes fully anoxic after the PETM onset, shortly following the CIE and temperature increase. Despite some variations in the degree of oxygenation, the bottom water environment remains anoxic during the PETM, possibly reaching euxinic conditions in the upper half of the PETM body.

Outlook

In the uppermost interval, chemical indices and an abundance of buried organic matter suggest a strong increase in export productivity prior to the PETM recovery. Combined, this indicates a relatively rapid environmental response to changes in the carbon cycle and temperatures. It also shows that negative feedback mechanisms such as silicate weathering and burial of organic matter were active throughout the PETM. This study highlights the important role of marginal marine areas as carbon sinks driving the PETM recovery.

4. Outlook

The PETM poses major research challenges, and there are still many unresolved questions and uncertainties regarding the causes and consequences of the carbon cycle perturbations. Most importantly, there is a need to identify the sources and rates of the rise in atmospheric carbon, and constrain the timing and magnitude of carbon release. Feedback mechanisms likely played an important role in prolonging the PETM duration, and in driving the unusually rapid recovery. High resolution shallow marine records such as in Denmark could hold vital clues to resolve some of the uncertainties regarding the Earth system response. While we have covered a wide variety of processes in this project, there are still so many aspects that could receive further attention. Most important is the need for additional high-resolution sites to constrain the regional variability, but for now we will focus on a few unresolved issues that could be approached using the Danish sedimentary record.

1) Identify sedimentary tracers of volcanic activity

One highly important aspect is to constrain the distribution of volcanic proxies across the PETM. A record of sedimentary mercury have already been published by Jones et al. (2019). Future work therefore needs to include osmium isotopes, which is an ideal tracer for the weathering of basaltic terrains and has already been used to identify NAIP activity in Svalbard (Wieczorek et al., 2013) and in the Arctic and Tethys Oceans (Dickson et al., 2015). The third manuscript indicates that additional trace metal analyses may be useful as additional volcanic tracers, and a more detailed analysis could therefore be warranted. The third manuscript also reveals the potential presence of cryptotephra, which are ash layers that are not visible to the naked eye (e.g. Cassidy

et al., 2014). An important further step is therefore detailed petrographic studies of the sediments in order to identify possible volcanic glass grains.

2) Improve the estimates of volatile degassing

A major limitation in Paper 2 is the lack of residual CO₂ and H₂O estimates in the volcanic glass, which has so far prevented us to make a quantitative estimate of the variations in eruption depth. While sulfur measurements can be conducted easily using an electron microprobe, both CO₂ and H₂O needs to be analysed using Fourier-Transform Infrared Spectroscopy. This is more expensive, less easily available, and requires more complex preparation and microanalysis, and was therefore not included at this stage. Sulfur is soluble in silicate melts until low pressures, and can indicate the relative changes in eruption depth. However, a quantitative assessment of the eruption depth relies on thermodynamic modelling using the volatile saturation pressures combined with an appropriate pressure gradient. Although some attempts have been made to develop this for sulfur, it is so far not well suited to basaltic systems (Witham et al., 2012). We are therefore dependent on knowing the CO₂ and H₂O contents, for which pressure- and temperature-dependent solubilities are well-constrained (Newman and Lowernstern, 2002). If this can be done, it would be a significant step towards understanding evolution of NAIP explosive hydromagmatic activity.

5. References

- Aarnes, I., Svensen, H., Connolly, J.A.D., & Podladchikov, Y.Y., (2010). How contact metamorphism can trigger global climate changes: Modeling gas generation around igneous sills in sedimentary basins. *Geochimica et Cosmochimica Acta* 74, 7179-7195.
- Abdelmalak, M. M., Planke, S., Faleide, J. I., Jerram, D. A., Zastrozhnov, D., Eide, S., & Myklebust, R. (2016). The development of volcanic sequences at rifted margins: New insights from the structure and morphology of the Vøring Escarpment, mid-Norwegian Margin. *Journal of Geophysical Research: Solid Earth*, 121(7), 5212-5236.
- Alegret, L., Ortiz, S., & Molina, E. (2009). Extinction and recovery of benthic foraminifera across the Paleocene–Eocene Thermal Maximum at the Alamedilla section (Southern Spain). *Palaeogeography, Palaeoclimatology, Palaeoecology*, 279(3-4), 186-200.

References

- Alley, R. B. (2016). A heated mirror for future climate. *Science*, 352(6282), 151-152.
- Anagnostou, E., John, E. H., Edgar, K. M., Foster, G. L., Ridgwell, A., Inglis, G. N., ... & Pearson, P. N. (2016). Changing atmospheric CO₂ concentration was the primary driver of early Cenozoic climate. *Nature*, 533(7603), 380-384.
- Anell, I., Thybo, H., & Rasmussen, E. (2012). A synthesis of Cenozoic sedimentation in the North Sea. *Basin Research*, 24(2), 154-179.
- Babila, T. L., Penman, D. E., Hönisch, B., Kelly, D. C., Bralower, T. J., Rosenthal, Y., & Zachos, J. C. (2018). Capturing the global signature of surface ocean acidification during the Palaeocene–Eocene Thermal Maximum. *Philosophical Transactions of the Royal Society A: Mathematical, Physical and Engineering Sciences*, 376(2130), 20170072.
- Bijl, P. K., Schouten, S., Sluijs, A., Reichert, G. J., Zachos, J. C., & Brinkhuis, H. (2009). Early Palaeogene temperature evolution of the southwest Pacific Ocean. *Nature*, 461(7265), 776-779.
- Bond, D. P., & Wignall, P. B. (2014). Large igneous provinces and mass extinctions: an update. *Volcanism, impacts, and mass extinctions: causes and effects*, 505, 29-55.
- Bonde, N. (1979). Palaeoenvironment in the 'North Sea' as indicated by the fish bearing Mo-clay deposit (Paleocene/Eocene), Denmark. *Mededelingen van de Werkgroep voor Tertiaire en Kwartaire Geologie*, 16(1), 3-16.
- Bowen, G. J. (2013). Up in smoke: A role for organic carbon feedbacks in Paleogene hyperthermals. *Global and Planetary Change*, 109, 18-29.
- Bowen, G. J., & Zachos, J. C. (2010). Rapid carbon sequestration at the termination of the Palaeocene–Eocene Thermal Maximum. *Nature Geoscience*, 3(12), 866-869.
- Bridgestock, L., Hsieh, Y. T., Porcelli, D., & Henderson, G. M. (2019). Increased export production during recovery from the Paleocene–Eocene thermal maximum constrained by sedimentary Ba isotopes. *Earth and Planetary Science Letters*, 510, 53-63.
- Bryan, S.E. & Ernst, R.E. (2008). Revised definition of large igneous provinces (LIPs). *Earth-Science Reviews*, 86(1): 175-202.
- Buiter, S.J. & Torsvik, T.H. (2014). A review of Wilson Cycle plate margins: A role for mantle plumes in continental break-up along sutures? *Gondwana Research*, 26(2): 627-653.
- Bøggild, O.B. (1918). Den vulkanske Aske i Moleret samt en Oversigt over Danmarks ældre Tertiærbjergarter. *Bulletin of the Geological Society of Denmark*, 33, 1-159.

References

- Callegaro, S., Baker, D. R., De Min, A., Marzoli, A., Geraki, K., Bertrand, H., ... & Nestola, F. (2014). Microanalyses link sulfur from large igneous provinces and Mesozoic mass extinctions. *Geology*, 42(10), 895-898.
- Carmichael, M. J., Inglis, G. N., Badger, M. P., Naafs, B. D. A., Behrooz, L., Remmelzwaal, S., ... & Dickson, A. J. (2017). Hydrological and associated biogeochemical consequences of rapid global warming during the Paleocene-Eocene Thermal Maximum. *Global and Planetary Change*, 157, 114-138.
- Carmichael, M. J., Pancost, R. D., & Lunt, D. J. (2018). Changes in the occurrence of extreme precipitation events at the Paleocene–Eocene thermal maximum. *Earth and Planetary Science Letters*, 501, 24-36.
- Cassidy, M., Watt, S. F., Palmer, M. R., Trofimovs, J., Symons, W., Maclachlan, S. E., & Stinton, A. J. (2014). Construction of volcanic records from marine sediment cores: A review and case study (Montserrat, West Indies). *Earth-Science Reviews*, 138, 137-155.
- Charles, A. J., Condon, D. J., Harding, I. C., Pälike, H., Marshall, J. E., Cui, Y., ... & Croudace, I. W. (2011). Constraints on the numerical age of the Paleocene-Eocene boundary. *Geochemistry, Geophysics, Geosystems*, 12(6).
- Coffin, M. & Eldholm, O. (1991). Large igneous provinces: JOI/USSAC workshop report.
- Courtillot, V., Jaupart, C., Manighetti, I., Tapponnier, P. & Besse, J. (1999). On causal links between flood basalts and continental breakup. *Earth and Planetary Science Letters*, 166(3): 177-195.
- Cramer, B. S., Wright, J. D., Kent, D. V., & Aubry, M. P. (2003). Orbital climate forcing of $\delta^{13}\text{C}$ excursions in the late Paleocene–early Eocene (chrons C24n–C25n). *Paleoceanography*, 18(4).
- Cramer, B. S., Toggweiler, J. R., Wright, J. D., Katz, M. E., & Miller, K. G. (2009). Ocean overturning since the Late Cretaceous: Inferences from a new benthic foraminiferal isotope compilation. *Paleoceanography*, 24(4).
- Cramwinckel, M. J., Huber, M., Kocken, I. J., Agnini, C., Bijl, P. K., Bohaty, S. M., ... & Peterse, F. (2018). Synchronous tropical and polar temperature evolution in the Eocene. *Nature*, 559(7714), 382-386.
- Dickens, G. R., O'Neil, J. R., Rea, D. K., & Owen, R. M. (1995). Dissociation of oceanic methane hydrate as a cause of the carbon isotope excursion at the end of the Paleocene. *Paleoceanography and Paleoclimatology*, 10(6), 965-971.
- Dickson, A. J., Cohen, A. S., Coe, A. L., Davies, M., Shcherbinina, E. A., & Gavrillov, Y. O. (2015). Evidence for weathering and volcanism during the PETM from Arctic Ocean and Peri-Tethys osmium isotope records. *Palaeogeography, Palaeoclimatology, Palaeoecology*, 438, 300-307.

References

- Dunkley Jones, T., Lunt, D. J., Schmidt, D. N., Ridgwell, A., Sluijs, A., Valdes, P. J., & Maslin, M. (2013). Climate model and proxy data constraints on ocean warming across the Paleocene–Eocene Thermal Maximum. *Earth-Science Reviews*, 125, 123-145.
- Egger, H., Homayoun, M., Huber, H., Rögl, F., & Schmitz, B. (2005). Early Eocene climatic, volcanic, and biotic events in the northwestern Tethyan Untersberg section, Austria. *Palaeogeography, Palaeoclimatology, Palaeoecology*, 217(3-4), 243-264.
- Eldholm, O., & Grue, K. (1994). North Atlantic volcanic margins: dimensions and production rates. *Journal of Geophysical Research: Solid Earth*, 99(B2), 2955-2968.
- Ernst, R. E., & Youbi, N. (2017). How Large Igneous Provinces affect global climate, sometimes cause mass extinctions, and represent natural markers in the geological record. *Palaeogeography, palaeoclimatology, palaeoecology*, 478, 30-52.
- Foster, G. L., Hull, P., Lunt, D.J., & Zachos J.C. (2018). Placing our current 'hyperthermal' in the context of rapid climate change in our geological past. *Philosophical Transactions of the Royal Society*. 376: 20170086
- Frieling, J., Svensen, H. H., Planke, S., Cramwinckel, M. J., Selnes, H., & Sluijs, A. (2016). Thermogenic methane release as a cause for the long duration of the PETM. *Proceedings of the National Academy of Sciences*, 113(43), 12059-12064.
- Frieling, J., Gebhardt, H., Huber, M., Adekeye, O. A., Akande, S. O., Reichart, G. J., ... & Sluijs, A. (2017). Extreme warmth and heat-stressed plankton in the tropics during the Paleocene-Eocene Thermal Maximum. *Science Advances*, 3(3), e1600891.
- Frieling, J., Peterse, F., Lunt, D. J., Bohaty, S. M., Sinninghe Damsté, J. S., Reichart, G. J., & Sluijs, A. (2019). Widespread warming before and elevated barium burial during the Paleocene-Eocene Thermal Maximum: Evidence for methane hydrate release?. *Paleoceanography and Paleoclimatology*, 34(4), 546-566.
- Gales, E., Black, B., & Elkins-Tanton, L. T. (2020). Carbonatites as a record of the carbon isotope composition of large igneous province outgassing. *Earth and Planetary Science Letters*, 535, 116076.
- Gingerich, P.D. (2003). "Mammalian responses to climate change at the Paleocene-Eocene boundary: Polecat Bench record in the northern Bighorn Basin, Wyoming" (PDF). In Wing, Scott L. (ed.). *Causes and Consequences of Globally Warm Climates in the Early Paleogene*. 369. Geological Society of America. pp. 463–78. doi:10.1130/0-8137-2369-8.463
- Gislason, S. R., & Oelkers, E. H. (2011). Silicate rock weathering and the global carbon cycle. *Frontiers in Geochemistry: Contribution of Geochemistry to the Study of the Earth*, 84-103.

References

- Gutjahr, M., Ridgwell, A., Sexton, P. F., Anagnostou, E., Pearson, P. N., Pälike, H., ... & Foster, G. L. (2017). Very large release of mostly volcanic carbon during the Palaeocene–Eocene Thermal Maximum. *Nature*, 548(7669), 573-577.
- Haaland, H.J., Furnes, H., & Martinsen, O.J. (2000). Paleogene tuffaceous intervals, Grane Field (Block 25/11), Norwegian North Sea: their depositional, petrographical, geochemical character and regional implications. *Marine and Petroleum Geology*, 17(1), 101-118.
- Harding, I. C., Charles, A. J., Marshall, J. E., Pälike, H., Roberts, A. P., Wilson, P. A., ... & Pearce, R. B. (2011). Sea-level and salinity fluctuations during the Paleocene–Eocene thermal maximum in Arctic Spitsbergen. *Earth and Planetary Science Letters*, 303(1-2), 97-107.
- Heilmann-Clausen, C. (1995). Palæogene aflejringer over Danskekalken. In: Nielsen, O.B. (Ed.), *Aarhus Geokompender No. 1, Danmarks geologi fra Kridt til i dag*, pp. 69-114.
- Heilmann-Clausen, C., Nielsen, O. B., & Gersner, F. (1985). Lithostratigraphy and depositional environments in the Upper Paleocene and Eocene of Denmark. *Bulletin of the Geological Society of Denmark*, 33, 287-323.
- Hollis, C. J., Taylor, K. W., Handley, L., Pancost, R. D., Huber, M., Creech, J. B., ... & Gibbs, S. (2012). Early Paleogene temperature history of the Southwest Pacific Ocean: Reconciling proxies and models. *Earth and Planetary Science Letters*, 349-350, 53-66.
- Horni, J.A., Hopper, J.R., Blischke, A., Geisler, W.H., Stewart, M., McDermott, K., Judge, M., Elerlendsson, O., & Arting, U.E. (2017). Regional distribution of volcanism within the North Atlantic Igneous Province. In: Peron-Pinvidic, G., Hopper, J.R., Stoker, M.S., Gaina, C., Doornenbal, J.C., Funck, T., & Arting, U.E. (Eds.), *A Reappraisal of Crustal Structure, Tectonostratigraphy and Magmatic Evolution*. Geological Society, London, special publications.
- Inglis, G. N., Farnsworth, A., Lunt, D., Foster, G. L., Hollis, C. J., Pagani, M., ... & Raynham, L. (2015). Descent toward the Icehouse: Eocene sea surface cooling inferred from GDGT distributions. *Paleoceanography*, 30(7), 1000-1020.
- John, C. M., Banerjee, N. R., Longstaffe, F. J., Sica, C., Law, K. R., & Zachos, J. C. (2012). Clay assemblage and oxygen isotopic constraints on the weathering response to the Paleocene-Eocene thermal maximum, east coast of North America. *Geology*, 40(7), 591-594.
- Jolley, D.W. & Widdowson, M. (2005). Did Paleogene North Atlantic rift-related eruptions drive early Eocene climate cooling? *Lithos*, 79, 355-366.
- Jolley, D.W., Clarke, B., & Kelley, S. (2002). Paleogene time scale miscalibration: Evidence from the dating of the North Atlantic igneous province. *Geology*, 30, 7-10.

References

- Jones, M. T., & Gislason, S. R. (2008). Rapid releases of metal salts and nutrients following the deposition of volcanic ash into aqueous environments. *Geochimica et Cosmochimica Acta*, 72(15), 3661-3680.
- Jones, M.T., Jerram, D.A., Svensen, H.H. & Grove, C. (2016). The effects of large igneous provinces on the global carbon and sulphur cycles. *Palaeogeography, Palaeoclimatology, Palaeoecology*, 441, 4-21.
- Jones, M. T., Percival, L. M., Stokke, E. W., Frieling, J., Mather, T. A., Riber, L., ... & Svensen, H. H. (2019). Mercury anomalies across the Palaeocene–Eocene thermal maximum. *Climate of the Past*, 15(1).
- Kelly, D. C., Zachos, J. C., Bralower, T. J., & Schellenberg, S. A. (2005). Enhanced terrestrial weathering/runoff and surface ocean carbonate production during the recovery stages of the Paleocene–Eocene thermal maximum. *Paleoceanography*, 20(4).
- Kender, S., Stephenson, M. H., Riding, J. B., Leng, M. J., Knox, R. W. B., Peck, V. L., ... & Jamieson, R. (2012). Marine and terrestrial environmental changes in NW Europe preceding carbon release at the Paleocene–Eocene transition. *Earth and Planetary Science Letters*, 353, 108-120.
- Kennett, J. P., & Stott, L. D. (1991). Abrupt deep-sea warming, palaeoceanographic changes and benthic extinctions at the end of the Palaeocene. *Nature*, 353(6341), 225-229.
- Kent, D. V., Cramer, B. S., Lanci, L., Wang, D., Wright, J. D., & Van der Voo, R. (2003). A case for a comet impact trigger for the Paleocene/Eocene thermal maximum and carbon isotope excursion. *Earth and Planetary Science Letters*, 211(1-2), 13-26.
- Khozyem, H., Adatte, T., Spangenberg, J. E., Tantawy, A. A., & Keller, G. (2013). Palaeoenvironmental and climatic changes during the Palaeocene–Eocene Thermal Maximum (PETM) at the Wadi Nukhul Section, Sinai, Egypt. *Journal of the Geological Society*, 170(2), 341-352.
- King C. (2016). *A Revised Correlation of Tertiary Rocks in the British Isles and Adjacent Areas of NW Europe* (Gale, A.S. & Barry, T.L., editors). Special reports, 27. The Geological Society, London.
- Kirtland Turner, S., Hull, P. M., Kump, L. R., & Ridgwell, A. (2017). A probabilistic assessment of the rapidity of PETM onset. *Nature communications*, 8(1), 1-10.
- Knox, R.O.B. & Morton, A.C. (1988). The record of early Tertiary N Atlantic volcanism in sediments of the North Sea Basin. *Geological Society, London, Special Publications*, 39(1), 407-419.
- Knox, R.W.O'B., Bosch, J.H.A., Rasmussen, E.S., Heilmann-Clausen, C., Hiss, M., De Lugt, I.R., Kasinski, J., King, C., Köthe, A., Slodkowska, B., Standke, G., Vandenberghe, N. (2010). Cenozoic. In: Dornenbaal, H., Stevenson, A. (Eds.), *Petroleum Geological Atlas of the Southern Permian Basin Area*. EAGE Publications b.v, Houten, pp. 211–223.

References

- Koch, P.L., Zachos, J.C. & Gingerich, P.D. (1992). Correlation between isotope records in marine and continental carbon reservoirs near the Palaeocene/Eocene boundary. *Nature*, 358(6384): 319-322.
- Komar, N., & Zeebe, R. E. (2017). Redox-controlled carbon and phosphorus burial: A mechanism for enhanced organic carbon sequestration during the PETM. *Earth and Planetary Science Letters*, 479, 71-82.
- Kuiper, K. F., Deino, A., Hilgen, F. J., Krijgsman, W., Renne, P. R., & Wijbrans, A. J. (2008). Synchronizing rock clocks of Earth history. *Science*, 320(5875), 500-504.
- Larsen, L. M., Fitton, J. G., & Pedersen, A. K. (2003). Paleogene volcanic ash layers in the Danish Basin: compositions and source areas in the North Atlantic Igneous Province. *Lithos*, 71(1), 47-80.
- Larsen, L.M., Pedersen, A.K., Tegner, C., & Duncan, R.A. (2016). Age of Tertiary volcanic rocks on the West Greenland continental margin: volcanic evolution and event correlation to other parts of the North Atlantic Igneous Province. *Geological Magazine*, 153, 487-511.
- Larsen, R. B. & Tegner, C. (2006). Pressure conditions for the solidification of the Skaergaard intrusion: Eruption of East Greenland flood basalts in less than 300,000 years. *Lithos* 92, 181-197, doi:10.1016/j.lithos.2006.03.032
- Littler, K., Röhl, U., Westerhold, T., & Zachos, J. C. (2014). A high-resolution benthic stable-isotope record for the South Atlantic: Implications for orbital-scale changes in Late Paleocene–Early Eocene climate and carbon cycling. *Earth and Planetary Science Letters*, 401, 18-30.
- Lourens, L. J., Sluijs, A., Kroon, D., Zachos, J. C., Thomas, E., Röhl, U., ... & Raffi, I. (2005). Astronomical pacing of late Palaeocene to early Eocene global warming events. *Nature*, 435(7045), 1083-1087.
- Lunt, D. J., Ridgwell, A., Sluijs, A., Zachos, J., Hunter, S., & Haywood, A. (2011). A model for orbital pacing of methane hydrate destabilization during the Palaeogene. *Nature Geoscience*, 4(11), 775-778.
- McInerney, F. A., & Wing, S. L. (2011). The Paleocene-Eocene Thermal Maximum: A perturbation of carbon cycle, climate, and biosphere with implications for the future. *Annual Review of Earth and Planetary Sciences*, 39, 489-516.
- van der Meulen, B., Gingerich, P. D., Lourens, L. J., Meijer, N., van Broekhuizen, S., van Ginneken, S., & Abels, H. A. (2020). Carbon isotope and mammal recovery from extreme greenhouse warming at the Paleocene–Eocene boundary in astronomically-calibrated fluvial strata, Bighorn Basin, Wyoming, USA. *Earth and Planetary Science Letters*, 534, 116044.
- Mitlehner, A. G. (1996). Palaeoenvironments in the North Sea Basin around the Paleocene-Eocene boundary: evidence from diatoms and other siliceous microfossils. *Geological Society, London, Special Publications*, 101(1), 255-273.

References

- Morton, A.C. & Knox, R.W.O'B. (1990). Geochemistry of late Palaeocene and early Eocene tephras from the North Sea Basin. *Journal of the Geological Society*, 147, 425-437.
- Murphy, B. H., Farley, K. A., & Zachos, J. C. (2010). An extraterrestrial ^3He -based timescale for the Paleocene–Eocene thermal maximum (PETM) from Walvis Ridge, IODP Site 1266. *Geochimica et Cosmochimica Acta*, 74(17), 5098-5108.
- Newman, S., & Lowenstern, J. B. (2002). VolatileCalc: a silicate melt–H₂O–CO₂ solution model written in Visual Basic for excel. *Computers & Geosciences*, 28(5), 597-604. years. *Nature*, 406(6797), 695-699.
- Ogg, J., (2012). Geomagnetic Polarity Time Scale, in: Gradstein, F., Ogg, J., Schmitz, M., Ogg, G. (Eds.), *The Geologic Time Scale 2012*. Elsevier, pp. 85-113.
- Pearson, P. N., & Palmer, M. R. (2000). Atmospheric carbon dioxide concentrations over the past 60 million years. *Nature*, 406(6797), 695-699.
- Penman, D. E. (2016). Silicate weathering and North Atlantic silica burial during the Paleocene-Eocene thermal maximum. *Geology*, 44(9), 731-734.
- Petersen, H. I., Nielsen, L. H., Bojesen-Koefoed, J. A., Mathiesen, A., Kristensen, L., & Dalhoff, F. (2008). Evaluation of the quality, thermal maturity and distribution of potential source rocks in the Danish part of the Norwegian–Danish Basin. *Geological Survey of Denmark and Greenland Bulletin*, 16, 1-27.
- Pineau, F., & Javoy, M. (1983). Carbon isotopes and concentrations in mid-oceanic ridge basalts. *Earth and Planetary Science Letters*, 62(2), 239-257.
- Planke, S., Rasmussen, T., Rey, S. S., & Myklebust, R. (2005). Seismic characteristics and distribution of volcanic intrusions and hydrothermal vent complexes in the Vøring and Møre basins. In *Geological Society, London, Petroleum Geology Conference series* (Vol. 6, No. 1, pp. 833-844). Geological Society of London.
- Rampino, M. R., & Stothers, R. B. (1988). Flood basalt volcanism during the past 250 million years. *Science*, 241(4866), 663-668.
- Rasmussen, E. S., Heilmann-Clausen, C., Waagstein, R., & Eidvin, T. (2008). The tertiary of Norden. *Episodes*, 31(1), 66.
- Robert, C., & Kennett, J. P. (1994). Antarctic subtropical humid episode at the Paleocene-Eocene boundary: Clay-mineral evidence. *Geology*, 22(3), 211-214.
- Robock, A., (2000). Volcanic eruptions and climate. *Reviews of Geophysics*, 38, 191-219.
- Röhl, U., Westerhold, T., Bralower, T.J., & Zachos, J.C. (2007). On the duration of the Paleocene-Eocene thermal maximum (PETM). *Geochemistry, Geophysics, Geosystems*, 8(12).

References

- Saunders, A.D. (2016). Two LIPs and two Earth-system crises: the impact of the North Atlantic Igneous Province and the Siberian Traps on the Earth-surface carbon cycle. *Geological Magazine*, 153, 201-222,
- Saunders, A.D., Fitton, J., Kerr, A., Norry, M., & Kent, R. (1997). The north Atlantic igneous province. In: Mahoney, J.J. & Coffin, M.F. (eds.) *Large igneous provinces: Continental, oceanic, and planetary flood volcanism*, American Geophysical Union, 100, 45-93.
- Schiøler, P., Andsbjerg, J., Clausen, O. R., Dam, G., Dybkjær, K., Hamberg, L., ... & Rasmussen, J. A. (2007). Lithostratigraphy of the Palaeogene, Lower Neogene Succession of the Danish North Sea (Vol. 12). *Geological Survey of Denmark and Greenland*.
- Schmidt, A., Skeffington, R.A., Thordarson, T., Self, S., Forster, P.M., Rap, A., Ridgwell, A., Fowler, D., Wilson, M., Mann, G.W., Wignall, Paul B., & Carslaw, K.S. (2016). Selective environmental stress from sulphur emitted by continental flood basalt eruptions. *Nature Geoscience*, 9, 77-82.
- Schmitz, B., Peucker-Ehrenbrink, B., Heilmann-Clausen, C., Åberg, G., Asaro, F., & Lee, C. T. A. (2004). Basaltic explosive volcanism, but no comet impact, at the Paleocene–Eocene boundary: high-resolution chemical and isotopic records from Egypt, Spain and Denmark. *Earth and Planetary Science Letters*, 225(1-2), 1-17.
- Schoon, P. L., Heilmann-Clausen, C., Schultz, B. P., Sluijs, A., Damsté, J. S. S., & Schouten, S. (2013). Recognition of Early Eocene global carbon isotope excursions using lipids of marine Thaumarchaeota. *Earth and Planetary Science Letters*, 373, 160-168.
- Schoon, P. L., Heilmann-Clausen, C., Schultz, B. P., Damsté, J. S. S., & Schouten, S. (2015). Warming and environmental changes in the eastern North Sea Basin during the Palaeocene–Eocene Thermal Maximum as revealed by biomarker lipids. *Organic Geochemistry*, 78, 79-88.
- Self, S., Thordarson, T., & Widdowson, M. (2005). Gas fluxes from flood basalt eruptions. *Elements*, 1(5), 283-287.
- Self, S., Widdowson, M., Thordarson, T. & Jay, A. E. (2006). Volatile fluxes during flood basalt eruptions and potential effects on the global environment: A Deccan perspective. *Earth and Planetary Science Letters*, 248(1), 518-532.
- Self, S., Schmidt, A., & Mather, T. A. (2014). Emplacement characteristics, time scales, and volcanic gas release rates of continental flood basalt eruptions on Earth. *Geological Society of America Special Papers*, 505, 505-16.
- Sluijs, A., Brinkhuis, H., Crouch, E. M., John, C. M., Handley, L., Munsterman, D., ... & Pancost, R. D. (2008). Eustatic variations during the Paleocene-Eocene greenhouse world. *Paleoceanography*, 23(4).

References

- Storey, M., Duncan, R., Pedersen, A., Larsen, L., & Larsen, H. (1998). $^{40}\text{Ar}/^{39}\text{Ar}$ geochronology of the West Greenland Tertiary volcanic province. *Earth and Planetary Science Letters*, 160, 569-586.
- Storey, M., Duncan, R.A., & Swisher, C.C. (2007a). Paleocene-Eocene thermal maximum and the opening of the northeast Atlantic. *Science*, 316 (5824), 587-589
- Storey, M., Duncan, R.A., & Tegner, C. (2007b). Timing and duration of volcanism in the North Atlantic Igneous Province: Implications for geodynamics and links to the Iceland hotspot. *Chemical Geology*, 241(3), 264-281.
- Svensen, H., Planke, S., Møllegaard-Sørensen, A. & Jamveit, B. (2004). Release of methane from a volcanic basin as a mechanism for initial Eocene global warming. *Nature*, 429(6991): 542.
- Svensen, H., Planke, S., & Corfu, F. (2010). Zircon dating ties NE Atlantic sill emplacement to initial Eocene global warming. *Journal of the Geological Society*, 167(3), 433-436.
- Svensen, H., Fristad, K., Polozov, A. & Planke, S. (2015). Volatile generation and release from continental large igneous provinces. In: Schmidt, A., Fristad, K. E. & Elkins-Tanton, L. T. (Eds.). *Volcanism and global environmental change*. Cambridge University Press, Cambridge, pp. 177-192
- Svensen, H. H., Bjærke, M. R., & Kverndokk, K. (2019). The Past as a Mirror: Deep Time Climate Change Exemplarity in the Anthropocene. *Culture Unbound*, 11(3-4), 330-352.
- Thomas, E., & Shackleton, N. J. (1996). The Paleocene-Eocene benthic foraminiferal extinction and stable isotope anomalies. *Geological Society, London, Special Publications*, 101(1), 401-441.
- Thomas, E., & Zachos, J. C. (2000). Was the late Paleocene thermal maximum a unique event?. *Gff*, 122(1), 169-170.
- Thordarson, T., & Self, S. (2003). Atmospheric and environmental effects of the 1783–1784 Laki eruption: A review and reassessment. *Journal of Geophysical Research: Atmospheres*, 108(D1), AAC-7.
- Upton, B., (1988). History of Tertiary igneous activity in the N Atlantic borderlands. *Geological Society of London Special Publications*, 39(1): 429-453.
- Westerhold, T., Röhl, U., McCarren, H. K., & Zachos, J. C. (2009). Latest on the absolute age of the Paleocene–Eocene Thermal Maximum (PETM): new insights from exact stratigraphic position of key ash layers+ 19 and– 17. *Earth and Planetary Science Letters*, 287(3-4), 412-419.
- Westerhold, T., Röhl, U., Wilkens, R. H., Gingerich, P. D., Clyde, W. C., Wing, S. L., Bowen, G. J., and Kraus, M. J. (2018). Synchronizing early Eocene deep-sea and continental records – cyclostratigraphic age models for the Bighorn Basin Coring Project drill cores, *Climate of the Past*, 14, 303-319.

References

- Westerhold, T., Marwan, N., Drury, A. J., Liebrand, D., Agnini, C., Anagnostou, E., ... & Frederichs, T. (2020). An astronomically dated record of Earth's climate and its predictability over the last 66 million years. *Science*, 369(6509), 1383-1387.
- Wieczorek, R., Fantle, M. S., Kump, L. R., & Ravizza, G. (2013). Geochemical evidence for volcanic activity prior to and enhanced terrestrial weathering during the Paleocene Eocene Thermal Maximum. *Geochimica et Cosmochimica Acta*, 119, 391-410.
- Wignall, P. (2005). The link between large igneous province eruptions and mass extinctions. *Elements*, 1(5), 293-297.
- Wilkinson, C. M., Ganerød, M., Hendriks, B. W., & Eide, E. A. (2017). Compilation and appraisal of geochronological data from the North Atlantic Igneous Province (NAIP). *Geological Society, London, Special Publications*, 447(1), 69-103,
- Witham, F., Blundy, J., Kohn, S. C., Lesne, P., Dixon, J., Churakov, S. V., & Botcharnikov, R. (2012). SolEx: a model for mixed COHSL-volatile solubilities and exsolved gas compositions in basalt. *Computers & Geosciences*, 45, 87-97.
- Wotzlaw, J., Bindeman, I., Schaltegger, U., Brooks, C. & Naslund, H. (2012). High-resolution insights into episodes of crystallization, hydrothermal alteration and remelting in the Skaergaard intrusive complex. *Earth and Planetary Science Letters*, 355, 199-212.
- Zachos, J. C., Röhl, U., Schellenberg, S. A., Sluijs, A., Hodell, D. A., Kelly, D. C., ... & McCarren, H. (2005). Rapid acidification of the ocean during the Paleocene-Eocene thermal maximum. *Science*, 308(5728), 1611-1615.
- Zachos, J. C., Dickens, G. R., & Zeebe, R. E. (2008). An early Cenozoic perspective on greenhouse warming and carbon-cycle dynamics. *Nature*, 451(7176), 279-283.
- Zachos, J. C., McCarren, H., Murphy, B., Röhl, U., & Westerhold, T. (2010). Tempo and scale of late Paleocene and early Eocene carbon isotope cycles: Implications for the origin of hyperthermals. *Earth and Planetary Science Letters*, 299(1-2), 242-249.
- Zacke, A., Voigt, S., Joachimski, M. M., Gale, A. S., Ward, D. J., & Tütken, T. (2009). Surface-water freshening and high-latitude river discharge in the Eocene North Sea. *Journal of the Geological Society*, 166(5), 969-980.
- Zeebe, R. E., & Lourens, L. J. (2019). Solar System chaos and the Paleocene–Eocene boundary age constrained by geology and astronomy. *Science*, 365(6456), 926-929.

Temperature changes across the Paleocene-Eocene Thermal Maximum – a new high-resolution TEX86 temperature record from the Eastern North Sea Basin

Ella W. Stokke, Morgan T. Jones, Jessica E. Tierney, Henrik H. Svensen, and Jessica H. Whiteside

Earth and Planetary Science Letters 544 (2020), 116388

1



Temperature changes across the Paleocene-Eocene Thermal Maximum – a new high-resolution TEX₈₆ temperature record from the Eastern North Sea Basin

Ella W. Stokke^{a,*}, Morgan T. Jones^a, Jessica E. Tierney^b, Henrik H. Svensen^a, Jessica H. Whiteside^c

^a Centre for Earth Evolution and Dynamics (CEED), University of Oslo, PO Box 1028 Blindern, 0315, Oslo, Norway

^b The University of Arizona, Department of Geosciences, 1040 E 4th St, Tucson, AZ 85721, USA

^c School of Ocean and Earth Science, National Oceanography Centre Southampton, University of Southampton, Southampton SO14 3ZH, United Kingdom

ARTICLE INFO

Article history:

Received 23 September 2019

Received in revised form 27 May 2020

Accepted 2 June 2020

Available online xxxx

Editor: L. Robinson

Keywords:

PETM

North Atlantic Igneous Province

palaeotemperatures

TEX₈₆

ABSTRACT

The Paleocene-Eocene Thermal Maximum (PETM; ~55.9 Ma) was a hyperthermal event associated with large carbon cycle perturbations, sustained global warming, and marine and terrestrial environmental changes. One possible trigger and/or source of the carbon release that initiated the PETM is the emplacement of the North Atlantic Igneous Province (NAIP). This study focuses on an expanded section of marine clays and diatomite on Fur Island in northern Denmark, where the entire PETM sequence has been identified by a negative ~4.5‰ $\delta^{13}\text{C}_{\text{TOC}}$ excursion. This remarkably well-preserved section also contains >180 interbedded ash layers sourced from the NAIP, making it an ideal site for investigating the correlations between large-scale volcanism and environmental changes. This study provides a new and complete high-resolution TEX₈₆-derived sea-surface temperature (SST) reconstruction over the entire PETM and the post-PETM section (up to about 54.6 Ma). The palaeothermometry record indicates an apparent short-lived cooling episode in the late Paleocene, followed by a pronounced temperature response to the PETM carbon cycle perturbations with a ~10°C SST increase during the PETM onset (up to ~33°C). Extreme SSTs fall shortly after the PETM onset, and continue to decrease during the PETM body and recovery, down to anomalously cool SSTs post-PETM (~11–23°C). Both phases of potential cooling coincide with proxies of active NAIP volcanism, suggesting a causal connection, although several overprinting non-thermal factors complicate interpretations of the TEX₈₆ values. Indices of effusive and explosive NAIP volcanism are largely absent from the Danish stratigraphy during the PETM body, though a re-emergence toward the end of the PETM suggest NAIP volcanism might have played a role in the PETM termination in the North Sea. This new SST record completes the previous fragmented view of climate changes at this globally important PETM site, and indicates large temperature variations in the North Sea during the earliest Eocene that are possibly linked to NAIP volcanism.

© 2020 The Author(s). Published by Elsevier B.V. This is an open access article under the CC BY license (<http://creativecommons.org/licenses/by/4.0/>).

1. Introduction

The Paleocene-Eocene Thermal Maximum (PETM) was an extreme hyperthermal event that punctuated the already greenhouse climate of the early Cenozoic (Zachos et al., 2010). The onset of the PETM was between 56.0 and 55.9 Ma (Charles et al., 2011; Westerhold et al., 2018; Zeebe and Lourens, 2019). It was associated with a global negative carbon isotopic excursion (CIE) of 3–5‰, attributed to the voluminous input of isotopically light car-

bon to the ocean and atmosphere (e.g. Zachos et al., 2010). This led to global ocean acidification, increased halocline stratification, and deep-sea anoxia (Babila et al., 2018; Kender et al., 2012; Schoon et al., 2015). On land, temperature changes were accompanied by hydrological changes and mammalian biogeographic reorganisation (e.g. McInerney and Wing, 2011). There are several hyperthermal events in the Palaeogene, but the PETM is unique in terms of both the magnitude and duration of warming (Zachos et al., 2010). Several sources of ¹²C-rich carbon sources have been proposed for the PETM, including methane hydrates (Dickens et al., 1995), a bolide impact activating terrestrial carbon reservoirs (Schaller et al., 2016), and volcanic and thermogenic degassing from the North

* Corresponding author.

E-mail address: e.w.stokke@geo.uio.no (E.W. Stokke).

Atlantic Igneous Province (NAIP; Storey et al., 2007a; Svensen et al., 2004).

Existing PETM reconstructions of bottom-water temperature (BWT) and sea surface temperature (SST) show large variations in temperature increase, depending on depth, latitude, seawater chemistry, and the choice of proxy and calibration (Dunkley Jones et al., 2013; Frieling et al., 2017; Hollis et al., 2019). The severe ocean acidification and substantial deep-sea sediment dissolution during the PETM (Babila et al., 2018) puts severe limitations on applying carbonate-based temperature proxies such as Mg/Ca ratios and $\delta^{18}\text{O}$ compositions (e.g. Dunkley Jones et al., 2013). In contrast, the organic SST proxy TEX_{86} is based on the relative distribution of glycerol dialkyl glycerol tetraethers (GDGT) membrane lipids of marine *Thaumarchaeota* (Schouten et al., 2002), and is therefore unaffected by carbonate dissolution. Unlike Mg/Ca and $\delta^{18}\text{O}$, TEX_{86} is also insensitive to salinity and pH, and does not need to be corrected for ocean chemistry changes (Frieling et al., 2017; Hollis et al., 2019). This makes TEX_{86} ideal for investigating PETM temperatures, and has been applied to a number of PETM sections worldwide (Frieling et al., 2017; Schoon et al., 2015; Sluijs et al., 2006, 2011; Zachos et al., 2006).

The NAIP consists of extrusive and intrusive rocks around the modern Northeast Atlantic margins (Fig. 2). It was emplaced between 63–52 Ma, with the most voluminous activity occurring between 56–54 Ma during the opening of the North Atlantic (Storey et al., 2007b). Both the volcanic activity and contact metamorphism of organic-rich sediments are potentially major sources of carbon and other volatiles around the time of the PETM (Storey et al., 2007a; Svensen et al., 2004). The close proximity of the North Sea Basin to the NAIP makes this an ideal area to study climatic and volcanic proxies in the same section. NAIP-sourced tephra are numerous and widespread across the North Sea and in Denmark (e.g. King, 2016). A recent study also documented elevated Hg/TOC ratios in five continental shelf settings around the North Atlantic, interpreted as an indicator of elevated NAIP volcanic activity (Jones et al., 2019). An exceptionally well preserved and complete PETM section crops out on the island of Fur in north-west Denmark. It includes an expanded section of marine clays and interbedded ash layers, providing a unique opportunity to investigate a direct link between NAIP volcanism and PETM climatic changes.

Despite the clear advantages of studying the North Sea area, only one previous study has applied TEX_{86} in this region, presenting records from two localities in Denmark (Fur Island and Store Bælt; Schoon et al., 2015; Figs. 1, 2). They documented a SST increase of 7–12 °C at the PETM onset, followed by an overall decrease back to pre-PETM values by the end of the CIE recovery. They also suggested a pre-PETM cooling in the Danish strata (Schoon et al., 2015), which is at odds with the pre-PETM warming identified in most PETM sites globally (Frieling et al., 2019). However, the existing record from Fur is sparse, with only 10 samples from the onset and recovery of the CIE. This preliminary study lacks high-resolution in key intervals and does not include data from the CIE body and post-PETM strata. Here, we present a new high-resolution record from Fur covering the entire PETM from the latest Paleocene, including post-PETM sediments that have not been analysed before (Fig. 2). Constraining palaeotemperatures across significant climatic perturbations such as the PETM is crucial for understanding climate sensitivity and environmental change in the past, present, and future. By combining a detailed record of $\delta^{13}\text{C}_{\text{TOC}}$ and TEX_{86} SST estimates in conjunction with volcanic proxies, we aim to evaluate the link between the palaeotemperature record and NAIP volcanism in the North Sea basin and expand the global temperature dataset during the PETM.

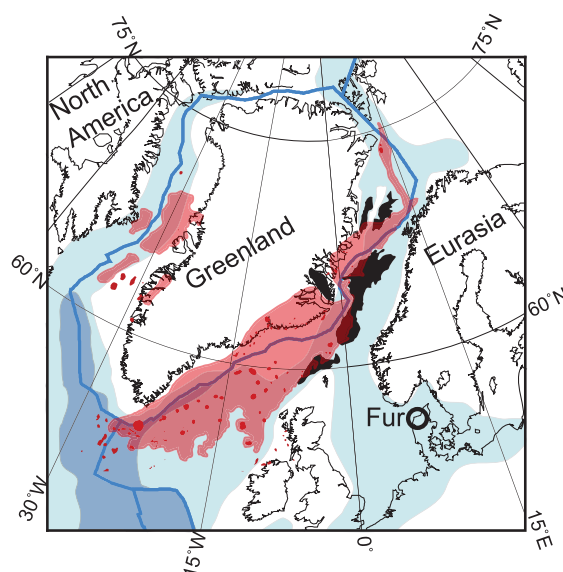


Fig. 1. Location of the island of Fur in a plate reconstruction at 56 Ma with the known extent of the NAIP indicated. Blue lines: plate boundaries. Black lines: present day coastlines. Light and dark blue areas: shelf and deep marine areas respectively. Light red areas: Known extent of subaerial and submarine volcanism from the NAIP. Dark red: individual volcanic centres. Black areas: extent of known NAIP sill intrusions in sedimentary basins. Figure modified from Jones et al. (2019). (For interpretation of the colours in the figure(s), the reader is referred to the web version of this article.)

2. Materials and methods

2.1. Stratigraphy and sampling

2.1.1. Stratigraphy

Fur is a small island (22 km²) in Limfjorden, Denmark (Fig. 2). During the latest Paleocene and earliest Eocene, thermal uplift around the NAIP led to the almost complete isolation of the North Sea Basin (Knox et al., 2010). Water depths around the study area were outer neritic, probably between 100–200 m (Knox et al., 2010; Schoon et al., 2015). The Paleocene-Eocene transition is marked at Fur by a shift in sedimentary facies from a condensed section of bioturbated Holmehus/Østerrende Fm. clay, into the dark, laminated clays of the Stolleklint Clay (Figs. 3, 4; Heilmann-Clausen et al., 1985; Schoon et al., 2015). A thin glauconitic silt unit (−24.61 to −24.55 m in Figs. 4, 5) marks the boundary, indicating a period of very slow sedimentation (Heilmann-Clausen et al., 1985). Although the boundary is poorly exposed at Fur, the glauconitic silt is likely underlain by an unconformity (~−24.6 m in Fig. 5; King, 2016; Schmitz et al., 2004). The PETM is identified just above the base of the Stolleklint Clay by a 4–8‰ negative CIE and appearance of the diagnostic dinoflagellate *Apectodinium augustum* (Jones et al., 2019; Schmitz et al., 2004; Schoon et al., 2015). The Stolleklint Clay grades upward into the ~60 m thick diatomite-rich Fur Fm. (Figs. 2b, 3, 4). More than 180 ash layers up to 20 cm thick are interbedded in the stratigraphy, with the majority (~140) found within the Fur Fm. (Figs. 3, 4). The volcanic ashes are grouped into a negative and positive ash series (Larsen et al., 2003), with additional ash layers (termed SK1, SK2, and SK3) within the base of the Stolleklint Clay (Figs. 4, 5). All of the ashes are sourced from NAIP explosive volcanism (Larsen et al., 2003), and distributed throughout the North Sea and Northern Europe (Larsen et al., 2003).

2.1.2. Sampling

This study focuses on the Stolleklint beach locality (Fig. 2a). Here, the PETM was identified just above the base of the Stollek-

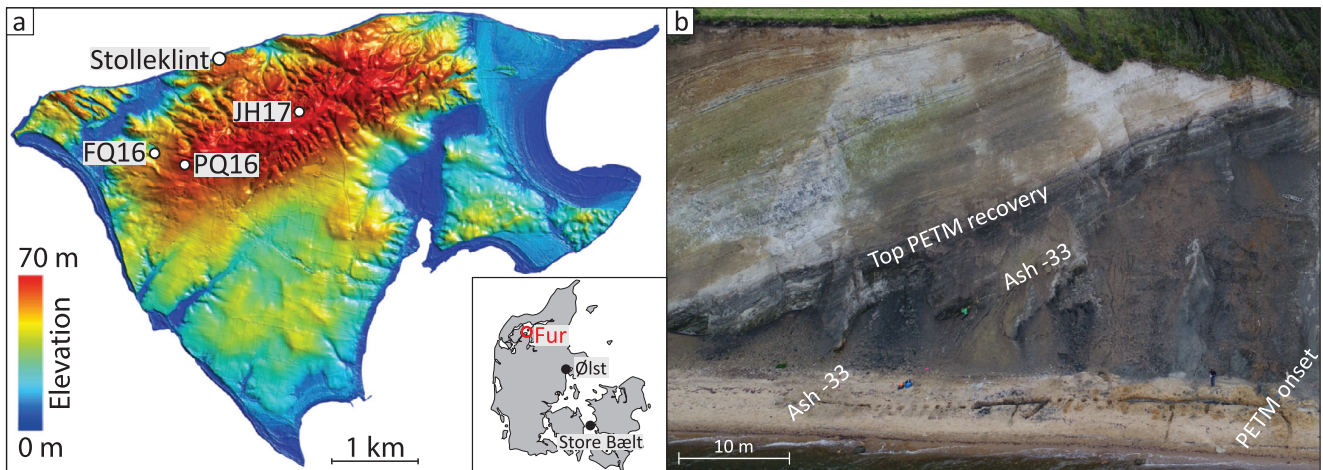


Fig. 2. a) Topographic map of the island of Fur. Samples are from four marked localities: the main locality Stolleklint (56°50'29"N, 8°59'33"E), the quarries near Fur Camping (FQ16 at 56°49'51"N, 8°58'45"E and PQ16 at 56°49'48"N 8°59'07"E), and Jenshøy (JH17; 56°50'05"N 9°00'31"E). The high topography in the north of the island is a partially overturned anticline of Fur Fm. and upper Stolleklint Clay strata. Map courtesy of Egon Nørmark. b) Photo of the Stolleklint beach from the sea, with the PETM indicated. The boundary between the Stolleklint Clay and Fur Fm. is at Ash -33, followed by a gradual transition from clay to diatomite. The inclined bedding is due to the glaciectonic folding. Note the 43 m long trench along the beach.

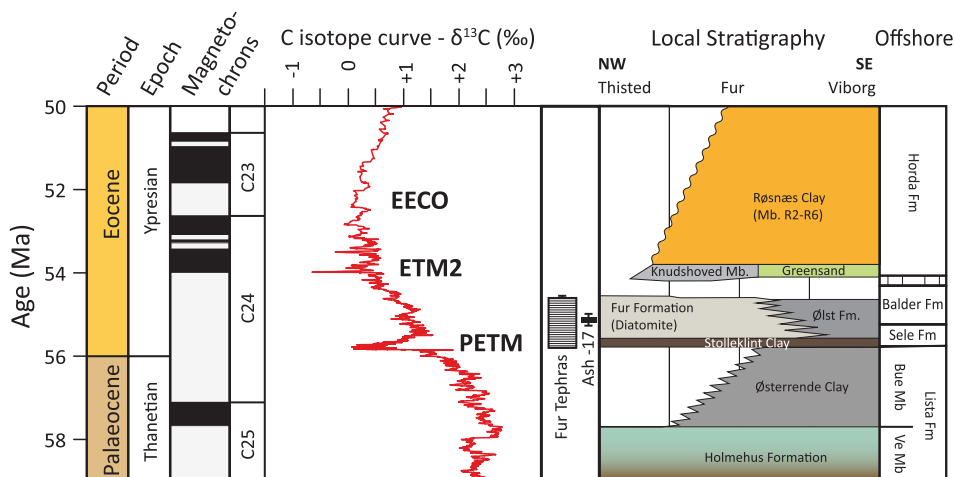


Fig. 3. Composite figure of the Paleocene-Eocene interval, indicating both the local Danish stratigraphy and the correlative offshore North Sea stratigraphy in relation to the PETM and other intervals of environmental change during the Palaeogene. Local stratigraphic section courtesy of Claus Heilmann-Clausen, offshore correlation adapted from King (2016). Carbon isotope data from Cramer et al. (2009) and Littler et al. (2014) and plotted on the GTS2012 timescale (Ogg, 2012). PETM = Paleocene-Eocene Thermal Maximum; ETM2 = Eocene Thermal Maximum 2; EECO = Early Eocene Climatic Optimum.

lint Clay, while Ash -33 marks the end of the CIE body, and Ash -21 the final end of recovery (Jones et al., 2019). The sediments at Fur have experienced very little consolidation and lithification, leaving them soft and easy to sample. Recent glaciectonic activity has created abundant small-scale folding and thrusting, although only one fault has been identified at Stolleklint, causing a doubling of Ash -33 (Fig. 4). High-resolution sampling was conducted throughout the section by combining samples from three different localities. The main locality is the Stolleklint beach (56°50'29"N, 8°59'33"E; Fig. 2a). Here, a 43 m long and 0.5 m deep trench was excavated (Fig. 2b) in order to reach the base of the Stolleklint Clay and the uppermost Holmehus/Østerrende Fm., which is otherwise poorly exposed. Jones et al. (2019) used careful trigonometry to estimate a local Stolleklint Clay thickness of 24.4 ± 2 m (24.2 m excluding ash layers) from the base of Ash SK1 to the base of Ash -33. The lowermost part of the trench was sampled every cm from ~25 cm below to ~90 cm above Ash SK1, recovering the entirety of the CIE onset. The remainder of the trench

up to Ash -33 was sampled every 0.5 m (0.2–0.3 m estimated local thickness). Samples from the CIE recovery and lower post-PETM stratigraphy were collected from the cliff face at Stolleklint (Fig. 2b) and from quarries near Fur Camping (FQ16 at 6°49'51"N, 8°58'45"E and PQ16 at 56°49'48"N 8°59'07"E; Fig. 2a). Samples from Ash +1 upwards were collected from the quarry at Jenshøy (JH17; 56°50'05"N 9°00'31"E; Fig. 2a).

2.2. Analytical methods

2.2.1. Carbon isotopes

Analyses of total organic carbon (TOC) and stable carbon isotopes of bulk samples ($\delta^{13}\text{C}_{\text{TOC}}$) from Ash -11 and up were conducted at the Jahren Lab at the University of Oslo. Powdered samples were decalcified using 1M HCl, then oven-dried at 50 °C and re-homogenised. About 8 mg of decalcified sample was sealed in tin capsules and loaded into a Costech Analytical Zero-Blank Autosampler. Organic $\delta^{13}\text{C}_{\text{TOC}}$ measurements and TOC concentrations

were analysed using a Thermo Fisher Scientific Flash Elemental Analyzer, coupled with a Thermo Fisher Scientific DeltaV Isotope Ratio Mass Spectrometer. Reproducibility of TOC and $\delta^{13}\text{C}_{\text{TOC}}$ was better than 0.01 wt% and 0.06‰, respectively. Previously published $\delta^{13}\text{C}_{\text{TOC}}$ and TOC analyses from the base of the section up to Ash -13 from Jones et al. (2019) are included.

2.2.2. Molecular extraction and fractionation

Crushed samples (1 g) were extracted using a Thermo 350 Accelerated Solvent Extractor with the following program: pre-heat = 5 min; heat = 5 min; static = 5 min; pressure = 10.34 MPa; flush = 70%, purge = 300 s.; cycles = 3; solvent = 9:1 dichloromethane:methanol. Solvent extracts were reduced to dry with a Genevac EZ-2 vacuum centrifuge. Total lipid extracts were quantified gravimetrically before column fractionation. Aliquots of the total lipid extracts were loaded onto small silica gel columns and fractions were eluted with hexane, hexane:dichloromethane (4:1), and dichloromethane:methanol (1:1) yielding the nonpolar, aromatic, and polar fractions, respectively.

2.2.3. GC- and LC-MS analysis

Aliphatic and aromatic fractions were desulphurised using copper beads, before being analysed for biomarker identification using a Thermo Trace 1310 gas chromatograph coupled to a Thermo TSQ8000 mass spectrometer at the National Oceanographic Centre, Southampton. The gas chromatograph used DB-5 column (30 m \times 0.25 mm i.d., 0.25- μm film thickness). The oven program was started at 40°C (held for 2 min), increased at a rate of 6°C/min to 310°C, and then held for 20 min. GC-MS analyses of the aliphatic and aromatic fractions generally yield low concentrations of biomarkers, with the *n*-alkanes and related compounds of *m/z* = 57 being the most abundant throughout. Compound identification of *n*-alkanes and pristane/phytane was made using mass spectra, library matches, and comparisons to known standards.

The polar fraction containing GDGTs was re-dissolved in hexane:isopropanol (99:1) and filtered with a 0.45 micron PTFE filter. The GDGTs were analysed on an Agilent 1260 Infinity HPLC coupled to an Agilent 6120 single quadrupole mass spectrometer at the University of Arizona, using two BEH HILIC silica columns (2.1 \times 150 mm, 1.7 μm ; Waters) and the improved chromatographic methodology of Hopmans et al. (2016). We calculated peak areas using the MATLAB package software ORIGAmI (Fleming and Tierney, 2016).

2.2.4. TEX_{86} values and calibration

TEX_{86} values were calculated from isoprenoid GDGT (isoGDGT) peak areas according to Schouten et al. (2002), yielding values that are all within the calibration range in modern oceans (0.3 to 0.8; Fig. 4), suggesting that no extrapolation is required (Hollis et al., 2019). Several calibrations for estimating SSTs from TEX_{86} values have been developed, based on extensive modern global core-top datasets. The earliest calibration by Schouten et al. (2002) used a linear relationship, which has since been shown to correlate poorly in temperatures $<5^\circ\text{C}$ and in some extreme settings such as the Red Sea (e.g. Kim et al., 2010). Other calibrations have been developed to circumvent this, such as the exponential calibration $\text{TEX}_{86}^{\text{H}}$ (Kim et al., 2010), which excludes Red Sea data and temperatures below 10°C . However, recent studies show that $\text{TEX}_{86}^{\text{H}}$ has a statistical bias (regression dilution) that results in systematic underestimation of temperatures at high TEX_{86} values (Tierney and Tingley, 2014). Based on the recommendations of the DeepMIP model comparison project (Hollis et al., 2019), the use of $\text{TEX}_{86}^{\text{H}}$ is no longer recommended for SST determinations in warm greenhouse climates. We refer readers to Hollis et al. (2019) for a full discussion of the limitations of $\text{TEX}_{86}^{\text{H}}$ and recommendations for temperature estimates in the PETM and early Eocene intervals.

Following DeepMIP recommendations, we apply the Bayesian regression model BAYSPAR (Tierney and Tingley, 2014) to convert TEX_{86} values to SSTs. The linear BAYSPAR calibration varies its regression terms spatially, taking into account the regional differences in the relationship between SST and TEX_{86} that are observed today (Tierney and Tingley, 2014). BAYSPAR also includes modern Red Sea data, which is likely a strength as Red Sea-type distributions are commonly observed in PETM and early Eocene sites (Hollis et al., 2019). However, for deep-time applications, BAYSPAR is run in analogue mode, which does not use regionally specific calibration parameters. Rather, analogue mode uses all regression parameters associated with TEX_{86} values within a specified threshold of the data, regardless of location. We applied BAYSPAR to infer SST with the following settings: prior mean = 20, prior standard deviation = 10, TEX_{86} tolerance = 0.15, number of iterations = 2500. As $\text{TEX}_{86}^{\text{H}}$ has been applied to other PETM sites, the $\text{TEX}_{86}^{\text{H}}$ calibration can be found in the Supplementary data for comparative use.

2.2.5. Other biomarker indices

There are several caveats and overprinting factors that can potentially bias TEX_{86} values, particularly through the addition of isoGDGTs that are not produced by Thaumarchaeota in the upper water column. Several methods are applied to assess the potential bias of TEX_{86} values. The Branched and Isoprenoid Tetraether (BIT) index measures the relative input of terrestrially derived branched GDGTs (brGDGT) and the marine-derived crenarchaeol. BIT was calculated following Hopmans et al. (2004). BIT values above 0.4 may indicate that TEX_{86} temperatures are compromised by terrestrially derived isoGDGTs (Weijers et al., 2006). However, there is no universal cut-off for BIT values as BIT does not straightforwardly relate to terrestrial organic matter (OM) fluxes and brGDGTs can also be produced *in situ* in marine environments (e.g. Peterse et al., 2009).

The Methane Index (MI) assess the potential influence of methanotrophic and methanogenic GDGT producers, which can bias TEX_{86} values (Zhang et al., 2011). MI values >0.5 characterise sedimentary conditions with a substantial methanogenic influence, typically in anoxic basins or near methane seeps (Zhang et al., 2011). Methanogenic archaea can also synthesise GDGT-0 (Blaga et al., 2009). The ratio GDGT-0/Crenarchaeol has been suggested as an indicator of methanogenesis on the isoGDGT population, with a substantial contribution indicated by values >2 (Blaga et al., 2009). The delta-ring index (ΔRI ; Zhang et al., 2016) detects whether the isoGDGT distributions differ from the surface calibration dataset. It can indicate if factors other than temperature are controlling the GDGT distribution, often detecting anything that would otherwise be flagged by BIT and MI. ΔRI is calculated by comparing the temperature dependent Ring Index (RI) and TEX_{86} to the modern global TEX_{86} -RI relationship, with an upper limit of |0.3| (95% confidence interval of the modern regression). TEX_{86} derived SSTs where BIT values are >0.4 are shown as open circles (Figs. 4, 5). All samples where ΔRI exceeds |0.3| also have BIT >0.4 , and have been marked red in Figs. 3 and 4. All marked samples should be interpreted with some care.

Additional environmental constraints are indicated by biomarker proxies from the aliphatic fraction analysed with GC-MS. The Terrigenous Aquatic Ratio (TAR; Peters et al., 2005) is a proxy of potential terrigenous input relative to marine. It is defined as the ratio of the primarily land-plant derived long-chain *n*-alkanes $n\text{C}_{27}$, $n\text{C}_{29}$ and $n\text{C}_{31}$, over the short-chain *n*-alkanes $n\text{C}_{15}$, $n\text{C}_{17}$ and $n\text{C}_{19}$ mainly derived from marine algae. Pristane and phytane are derived from the phytol side-chains of chlorophyll in algae and bacteria. These can be used as a proxy for both source region and redox conditions. Reducing conditions promote the reduction of phytol to phytane, while oxic conditions leads to oxidation of phytol to pristane (Peters et al., 2005).

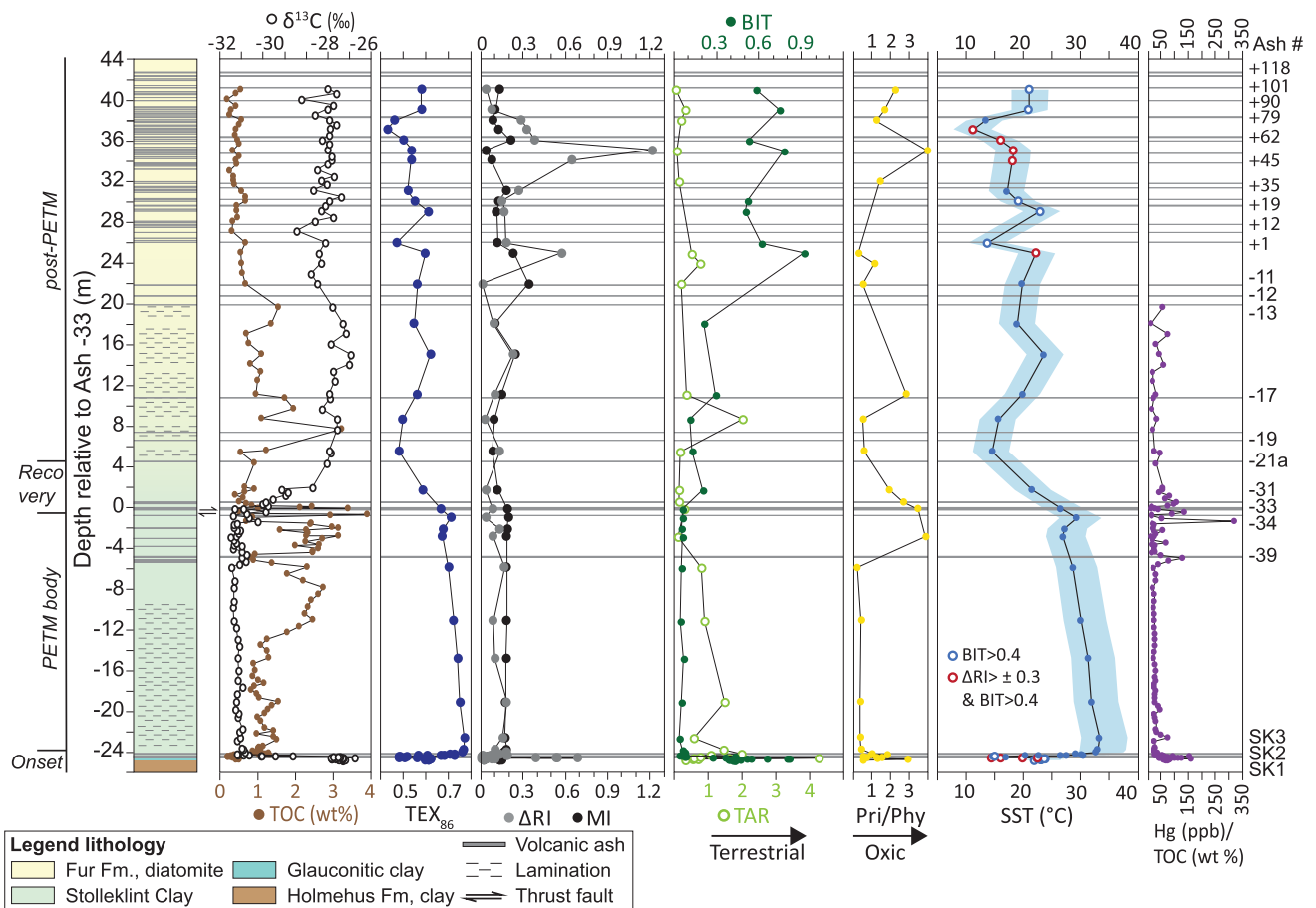


Fig. 4. Composite data from the island of Fur, combining samples from Stolleklint beach and three nearby quarries. Data includes $\delta^{13}\text{C}$ and TOC analyses, TEX_{86} values, BAYSPAR calibrated TEX_{86} SSTs with 1σ errorbars indicated by blue area, several organic biomarker ratios, and mercury/TOC from Jones et al. (2019). Hg values are included in the Supplementary data. Composite log of the local lithology and its relation to the interpreted PETM-onset, -body and -recovery, and post-PETM sections shown on the left. Grey lines indicate ash layers, with the ash stratigraphy indicated on the right. Legend shown at the base. TOC = Total Organic Carbon; SST = Sea Surface Temperature; ΔRI = Ring Index; MI = Methane Index; BIT = Branched and Isoprenoid Tetraether index; TAR = Terrigenous Aquatic Ratio; Pri/Phy = Pristane/Phytane.

3. Results and discussion

3.1. Shape and duration of the PETM at Fur

The Fur stratigraphy is an outstanding locality, comprising an uninterrupted PETM section of well-preserved marine clays. GC-MS measurements show that the *n*-alkanes have a constant high odd-over-even preference (OEP; Supplement), with $\text{OEP} > 1$ throughout indicating that the whole sequence is thermally immature and well suited for organic geochemical analyses (Peters et al., 2005).

The late Paleocene Holmehus/Østerrende Fm. show stable $\delta^{13}\text{C}_{\text{TOC}}$ values around -26‰ , and TOC concentrations of ~ 0.5 wt% (Figs. 4, 5). The C25r-C25n boundary (~ 57.7 Ma; Ogg, 2012) marks the top of the Holmehus Fm., but the duration of the overlying unconformity is undefined as it is unclear how much of the overlying Østerrende Fm. is present at Fur (Fig. 3; King, 2016). The $\delta^{13}\text{C}_{\text{TOC}}$ values in the overlying glauconitic unit remain stable at $\sim -26\text{‰}$ while TOC values drop to about 0.3 wt%. Neither the age nor duration of the glauconitic silt is well constrained, although it is most likely a part of the basal section of the Stolleklint clay, similar to that described at Ølst ~ 80 km to the southeast (Fig. 2; King, 2016; Schmitz et al., 2004). The glauconitic layer is ~ 5 m thick at the Store Bælt section but only ~ 5 cm thick at Ølst and Stolleklint (Fig. 2; Schmitz et al., 2004; Schoon et al., 2015), suggesting that it is highly condensed. An interstitial clay (between ashes SK1 and

SK2) with ~ 0.4 wt% TOC is found above the glauconitic silt prior to the PETM onset (Figs. 4, 5).

The PETM onset is defined by a sharp CIE of $\sim -4.5\text{‰}$ (from -26.5 to -31‰) immediately above Ash SK2, which is larger than average bulk marine OM records (McInerney and Wing, 2011). The CIE onset at Fur was concordant with the sudden dominance of the subtropical dinoflagellate *Apectodinium augustum* (Heilmann-Clausen et al., 1985; King, 2016). A pronounced increase in TOC from 0.45 to 1.5 wt% and a shift from bioturbated to laminated clays occur ~ 2 cm above the CIE onset (Figs. 4, 5), suggesting a shift to anoxic conditions. TOC concentrations remain relatively stable for the first half of the CIE body, before increasing up to 3.9 wt% in the upper half (Fig. 4). This large increase in TOC is followed by a shift from dark laminated clays to massive, black clays with abundant pyrite suggesting a highly anoxic environment. Just above Ash -33 at the start of the CIE recovery, TOC concentrations drop to < 1 wt%.

The CIE body is defined by an extended interval (~ 24 m) of sustained stable negative $\delta^{13}\text{C}_{\text{TOC}}$ values (Fig. 4). In contrast, the recovery phase is relatively sharp, starting at Ash -33 and returning to pre-PETM values by Ash -21 (~ 4.5 m thick; Fig. 4). The small thrust fault that cuts across Ash -33 in parts of the Stolleklint beach section likely leads to some uncertainty about the exact shape and duration of the $\delta^{13}\text{C}_{\text{TOC}}$ curve during the shift from CIE body to recovery (Fig. 4). The unusually thick CIE body at Fur most

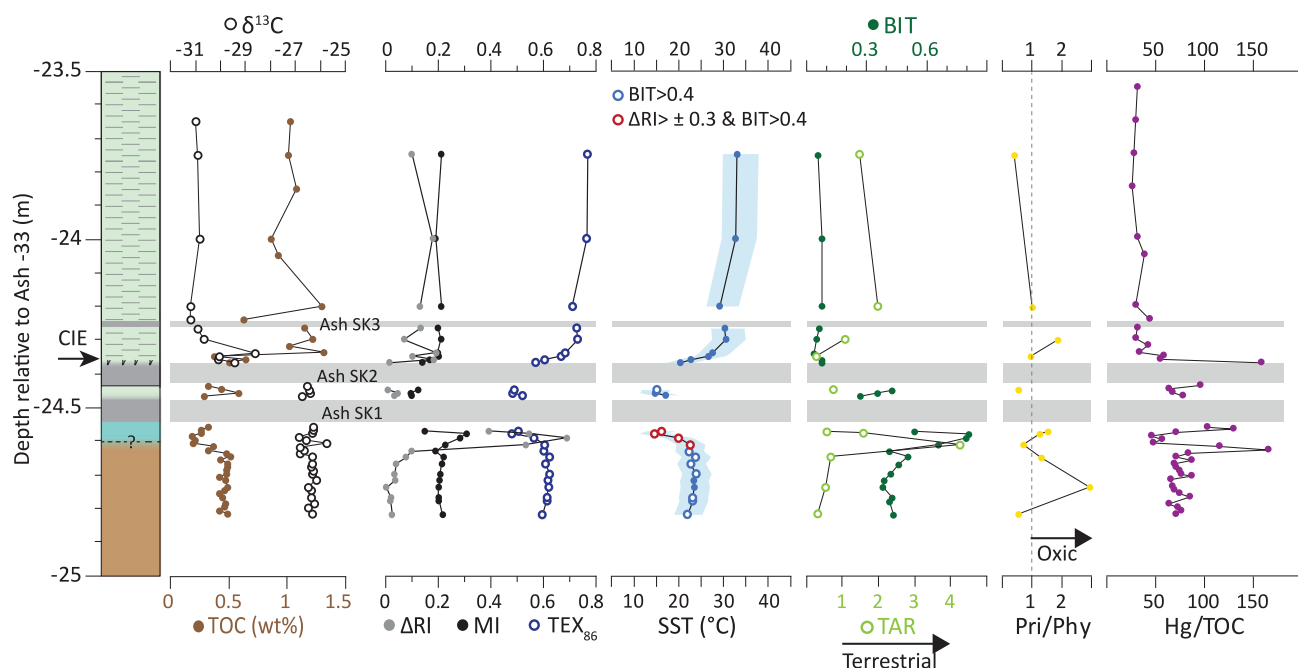


Fig. 5. Zoom-in of Fig. 4 showing data covering the PETM onset at Fur. Samples from the base of Stolleklint beach. Data include $\delta^{13}\text{C}$ and TOC analyses, TEX_{86} values, BAYSPAR calibrated TEX_{86} SSTs with 1σ errorbars indicated by blue area, several organic biomarker ratios, and mercury/TOC from Jones et al. (2019). Composite log of the local lithology and its relation to the interpreted PETM-onset shown on the left. Grey bands indicate ash layers SK1, SK2, and SK3. Legend shown in Fig. 4. TOC = Total Organic Carbon; SST = Sea Surface Temperature; ΔRI = Ring Index; MI = Methane Index; BIT = Branched and Isoprenoid Tetraether index; TAR = Terrigenous Aquatic Ratio; Pri/Phy = Pristane/Phytane.

likely reflects a large increase in sedimentation rates during the PETM CIE that wanes again during the recovery. Jones et al. (2019) estimated a 24.2 m ash-free thickness of the CIE body at Stolleklint. If we assume a 100 kyr for the PETM body (van de Meulen et al., 2020), the sediment accumulation rate for the Stolleklint Clay is about 24 cm/kyr (24.2 m/100 kyr). Considering the condensed and bioturbated nature of the underlying glauconitic silt, this indicates a considerable increase in sedimentation rate. The increasingly diatomite-dominated lithology suggests a decreasing sedimentation rate during the CIE recovery and post-PETM sections.

The post-PETM period section is characterised by $\delta^{13}\text{C}_{\text{TOC}}$ values that fluctuate between -26 and -28‰ (Fig. 4), typical for bulk marine OM records at this time (McInerney and Wing, 2011). The lower, laminated part of the post-PETM section ($\sim +4$ to $+20$ m in Fig. 4) is composed of a relatively clayey diatomite showing variable TOC concentrations (0.5 to 3.2 wt%). In contrast, the uppermost ~ 20 m of the stratigraphy, comprised almost entirely of diatomite, has stable low concentrations around 0.5 wt% TOC. The age control on the post-PETM Fur Fm. is limited as only the post-PETM Ash -17 is so far radioisotopically dated (Storey et al., 2007a), with a recalibrated Ar-Ar age of 55.6 ± 0.12 Ma (Jones et al., 2019). Westerhold et al. (2009) estimated a 200 kyr duration between Ash -17 and $+19$, placing Ash $+19$ at about 55.4 Ma (Fig. 6) and a total 300 kyr duration of the positive ash series. Stratigraphic correlations with the lower Balder Fm. places the top of the Fur Fm. at ≥ 54.6 Ma (King, 2016), prior to the onset of the Eocene Thermal Maximum 2 (ETM 2; Fig. 3).

3.2. Constraining PETM temperature changes

3.2.1. Apparent late Paleocene cooling

The late Paleocene interval comprises the lowermost ~ 65 cm of the stratigraphy (Figs. 4, 5). The Holmehus/Østerrende Fm. is characterised by relatively stable SSTs around $\sim 23^\circ\text{C}$ (Fig. 5). BAYSPAR

calibrated SSTs drop down to a minimum of $14.5 \pm 3[1\sigma]^\circ\text{C} \sim 2$ cm below Ash SK1 (Fig. 5), corresponding to a SST drop of $\sim 8^\circ\text{C}$ (Fig. 5). This corroborates the preliminary findings of Schoon et al. (2015), who found evidence of a pre-PETM cooling event from two samples at Stolleklint. However, the age of the late Paleocene strata below SK2 is poorly constrained. While there is no compelling evidence for hiatuses within the sediments above the glauconitic unit, considering the bioturbation in these sediments we cannot rule one out either. The timing of the cooling is therefore late Paleocene (< 57.7 Ma; King, 2016), although it could be just prior to the onset of the PETM.

This apparent cooling interval can be divided in two, with the lower part found in the glauconitic silt below Ash SK1 and the upper in the interstitial clay between Ashes SK1 and SK2. The entire cooling interval is characterised by low abundances of the Crenarchaeol isomer (Cren'; Supplement), suggesting a slightly different Thaumarchaeota population in this interval. The cooling onset coincides with increases in several overprinting signals that can bias TEX_{86} values (Fig. 5; Supplement). Firstly, ΔRI increases sharply and exceeds threshold values of $|0.3|$ at the start of the cooling, suggesting non-thermal factors likely control the GDGT distribution (Zhang et al., 2016). Both MI and GDGT-0/Crenarchaeol are elevated in the same interval (MI up to 0.3, GDGT-0/Cren up to 1.9; Fig. 5; Supplement) suggesting potential methanogenic influence (Blaga et al., 2009; Zhang et al., 2011). An abrupt increase in TAR (from 0.7 to 4.3) and BIT (up to 0.8) in the base of the glauconitic silt suggests a large increase in terrestrial input influencing TEX_{86} values (Fig. 5; Peters et al., 2005; Weijers et al., 2006). Preferential degradation of isoGDGTs due to oxic degradation could also have an influence, potentially resulting in increased BIT values and lower absolute temperatures (Hopmans et al., 2004). Bioturbation, low TOC concentration, and pristane/phytane partly > 1 indicate relatively oxygenated conditions below Ash SK1 (Fig. 5).

Low TEX_{86} values and inferred cooling continues in the upper part between Ashes SK1 and SK2. While the upper part is slightly

affected by elevated BIT values (from 0.27 to 0.43; Fig. 5), Δ RI decreases below threshold values and there is no compelling evidence of methanogenic influence (Fig. 5; Supplement). Despite the elevated BIT values, the low Δ RI suggests that the TEX_{86} values are likely to be robust. Schoon et al. (2015) observed a similar cooling in mean annual air temperatures (MAAT) from this interval, reconstructed from soil-derived brGDGTs. While brGDGTs may be produced *in-situ* (e.g. Peterse et al., 2009) and offset MAAT estimates, a separate corroborating proxy could support the presence of a cooling event before the CIE onset. Inglis et al. (2019) also describe a terrestrial cooling during the PETM onset in England, although they argue strongly that this is due to caveats with the brGDGT palaeothermometer. The presence of a cooling before the CIE is at odds with most other PETM sections, where temperatures are either stable (e.g. Sluijs et al., 2006) or even show a pre-CIE warming (Frieling et al., 2019). It is possible that the absence of any pre-PETM warming at Fur could be due to a regional cooling event affecting the North Sea. The interval between Ashes SK1 and SK2 is unlikely to be adversely affected by TEX_{86} bias, suggesting that the cooling observed is a real feature. However, the numerous overprinting factors and missing/condensed stratigraphy in the lower glauconitic silt indicates that more work is needed to constrain the likelihood and duration for such a cooling event.

3.2.2. PETM warming and recovery

The PETM onset, body and recovery show consistently low Δ RI, MI, and BIT indices, indicating TEX_{86} values are likely unbiased. While BIT values are consistently low (<1) throughout the CIE body, changing TAR values indicating variable input of long-chain *n*-alkanes from terrigenous sources during the PETM (Fig. 4). The $\sim -4.5\%$ CIE marking the PETM onset at Fur is followed closely by a SST increase to about 30°C (Fig. 5). Maximum PETM SSTs of $33.3 \pm 4 [1\sigma]^\circ\text{C}$ is reached only ~ 1.8 m above the CIE onset (Figs. 4, 5), suggesting a relatively rapid temperature response to carbon release. The temperature increase at Fur represents a minimum estimate of 10°C warming from late Paleocene values (Figs. 4, 5). The $\text{TEX}_{86}^{\text{H}}$ calibration is within the 1σ calibration error of BAYSPAR, and shows the same relative trend with lower maximum and higher minimum SSTs resulting in a minimum 7°C PETM warming (Supplement). A $7\text{--}10^\circ\text{C}$ SST warming is at the upper end of previous estimates for the PETM (Dunkley Jones et al., 2013; Frieling et al., 2017), although it is important to note that TEX_{86} typically yield slightly higher SSTs than other proxies (e.g. Inglis et al., 2020). The warming agrees relatively well with other mid-latitude shelf settings (Frieling et al., 2014; Zachos et al., 2006) and the Southern Ocean (Sluijs et al., 2011), but is higher than those observed in the Tropics (Frieling et al., 2017), the Arctic (Sluijs et al., 2006), and deeper mid-latitude settings (e.g. Bay of Biscay; Bornemann et al., 2014). However, spatial variability of warming and high latitude amplification have been described both from modelling and proxy studies during the PETM (Dunkley Jones et al., 2013; Frieling et al., 2017). The estimated temperature increase and estimated maximum PETM SSTs also agrees well with recently modelled Global Mean Surface Temperature for the PETM of 33°C and a temperature increase of $4\text{--}9^\circ\text{C}$ from latest Paleocene (Inglis et al., 2020).

The negative $\delta^{13}\text{C}_{\text{TOC}}$ values are near constant throughout the PETM body phase until Ash -33 (Fig. 4), indicating continued input of depleted carbon and little change to the carbon isotope composition of the surface carbon reservoir. However, after reaching maximum SSTs shortly after the onset, temperatures decline throughout the remainder of the PETM and return to late Paleocene values by the end of the CIE recovery (Fig. 4). This suggests that negative feedback mechanisms lowering temperatures were active during the PETM, such as increased silicate weathering and OM burial, removing CO_2 from the atmosphere (McInerney and

Wing, 2011). Sedimentation rates increase at Fur and globally during the PETM, reflecting enhanced weathering in response to a stronger hydrological cycle (Kender et al., 2012). Increased productivity and OM burial in shelf settings has also been demonstrated globally (Ma et al., 2014), and likely had an important role in atmospheric carbon drawdown (e.g. Gutjahr et al., 2017). John et al. (2008) suggested that due to drastically increased sedimentation rates and productivity during the PETM, mid-latitude shelves became highly efficient sinks for organic carbon burial. The substantial increase in sedimentation rate during the PETM and in OM burial in the upper half of the CIE body at Fur (Fig. 4), corroborates the important role for shelves in carbon drawdown and the final PETM CIE recovery.

3.3. Post-PETM temperature variations

Temperatures drop during the CIE recovery to a minimum of $15 \pm 3 [1\sigma]^\circ\text{C}$, 1 m above Ash -21a . An initial increase in SSTs up to $23.6 \pm 3.3 [1\sigma]^\circ\text{C}$ ($+15$ m in Fig. 4) is followed by varying SSTs ($11\text{--}23^\circ\text{C}$) during the post-PETM (Fig. 4). While the lower 15 m have low Δ RI, MI, and BIT indices indicating relatively robust TEX_{86} values, the upper 25 m are characterised by a number of overprinting factors. Δ RI values are high and exceeding $[0.3]$ in several samples, suggesting non-thermal factors are controlling isoGDGT distribution (Zhang et al., 2016). High BIT ratios prevail, with values >0.4 for all samples above $+21$ m height (Fig. 4). This may reflect inclusion of soil derived branched GDGTs (Hopmans et al., 2004; Weijers et al., 2006), although low TAR values suggest this section is dominated by marine-sourced short-chain *n*-alkanes (Fig. 4; Peters et al., 2005). Concentrations of brGDGTs are also low and sometimes below detection limit in the post-PETM section (Fig. 4; Supplement), which may compromise BIT values. Alternatively, the high BIT ratios could reflect preferential oxic degradation of marine isoGDGTs. This is supported by the low TOC concentrations and high pristane/phytane ratios (Fig. 4). While MI values are all <0.3 (Figs. 4, 5), the GDGT-0/Crenarchaeol ratio is relatively high in several samples post-PETM (>2 at $\sim +35$ m height; Supplement), suggesting a potential for limited methanogenesis (Blaga et al., 2009).

Although there are many possible factors affecting TEX_{86} values, the general trend of lower post-PETM temperatures is likely to be a real feature. The Fur Fm. was deposited during a ~ 1 Myr period before 54.6 Ma (King, 2016), thus predating ETM2 and the Early Eocene Climatic Optimum (Figs. 3, 6). Global temperatures show a general cooling after the PETM (Cramwinckel et al., 2018; Frieling et al., 2017; Inglis et al., 2020), although the post-PETM SSTs at Fur seem anomalously low compared to similar mid-latitude sites (Frieling et al., 2014; Bornemann et al., 2014). This is particularly true for the lowest SSTs recorded just above the CIE recovery ($15 \pm 3 [1\sigma]^\circ\text{C}$ at $+5.5$ m in Fig. 4), where potential TEX_{86} bias is least. A diversity reduction in plant communities in the Shetland basin has also been inferred to indicate lowered surface temperature in the period between the PETM and the ETM2 (Jolley and Widdowson, 2005). It is therefore possible that regional conditions led to enhanced cooling in the Danish region and possible larger parts of the Northeast Atlantic.

3.4. The role of North Atlantic Igneous Province volcanism

The NAIP is known to have been particularly active across the PETM. The dominant mode of eruption was effusive, building up huge continental flood basalts in Greenland and the Faroe Islands (Fig. 2). Constraints on timing and duration of the East Greenland lavas suggest that a 5–6 km thick lava pile was emplaced between 56.0 and 55.6 Ma (Jones et al., 2019; Larsen and Tegner, 2006). However, there is currently no data on whether these eruptions

were continuous, pulsed, or constrained to a much shorter time window. This has significant implications for the NAIP as a potential climate forcing. The main climatic impact of large eruptions is cooling, caused by sulphuric acid aerosols in the atmosphere increasing the planetary albedo (Robock, 2000). Atmospheric residence times for sulphur depend on whether it reaches the stratosphere (1–3 yr), or if it is released to the troposphere (weeks). This means that dominantly tropospheric emissions would result in a more regionally constrained cooling. A historic example is the 1783–84 eruption of Laki (Iceland) that caused a 2–3 yr of cooling largely constrained to the northern hemisphere (Thordarson and Self, 2003). However, the limited residence time of sulphur in the atmosphere restricts the duration of climatic impact to essentially syn-eruptive (Jones et al., 2016), which means transient cooling events from rapid explosive eruptions would not be preserved in the palaeotemperature record. Modelling has shown that the global climate can recover from perturbations during large effusive eruptions (4–6 °C cooling) within 50 yr of the eruption end (Schmidt et al., 2016). Therefore, the only potential method of preserving volcanic cooling in sedimentary sequences would be near-continuous eruptions over several centuries. The duration of periods of quiescence between eruptions is therefore a particularly important factor.

The hundreds of ash layers preserved in North Sea sediments indicate widespread explosive volcanism associated with the NAIP (Larsen et al., 2003). However, explosive eruptions are typically a minor volumetric component of LIPs. The unusual prevalence of basaltic tephra suggests that the explosiveness of eruptions was enhanced by magma-seawater interaction as Greenland and Eurasia broke apart (Larsen et al., 2003). Therefore, the increase in ash layers in the upper parts of the Fur stratigraphy likely reflect a change in eruptive style, rather than an increase in total volcanism. The positive ash series follows a period of long-lasting effusive flood basalt eruptions, which typically do not produce large amounts of ash, but do provide a constant supply of sulphur and other volcanic gases. While the volcanic ash layers mainly reflect periods of explosive volcanic activity, Hg/TOC anomalies indicate both the explosive and effusive activity.

Evidence from the Danish stratigraphy suggests at least four episodes of enhanced NAIP volcanism (Fig. 6). The first period occurs in the late Paleocene prior to the PETM onset, and is indicated by Hg/TOC anomalies (Jones et al., 2019) and the deposition of Ashes SK1 and SK2 (Figs. 5, 6). This period of prolonged and enhanced volcanic activity prior to the PETM onset coincides with the TEX₈₆ derived apparent cooling (Figs. 5, 6). Active NAIP volcanism is corroborated in the pre-PETM strata in Svalbard, where large Hg/TOC anomalies have been documented (Jones et al., 2019), together with low ¹⁸⁷Os/¹⁸⁸Os values suggesting weathering of substantial volumes of basaltic material (Wieczorek et al., 2013). The North Sea Basin is ideally placed to record potential volcanic cooling due to its close proximity to the NAIP and being downwind of the easterly polar jet stream. If effusive volcanism led to largely tropospheric degassing, then the surface cooling would be most prominent in the North Sea area and potentially absent from distal records, particularly in the tropics and southern hemisphere.

It is important to note that volcanic activity is one of several factors that could potentially explain the available SST proxy data. Thermal uplift from the NAIP led to the isolation of the North Sea during the latest Paleocene and earliest Eocene (Knox et al., 2010), which would have changed the oceanographic conditions. This could have affected the degree of mixing and therefore heat transport in the North Sea basin, potentially leading to slightly cooler SST conditions in the late Paleocene. A bolide impact has been identified at the Paleocene-Eocene transition that may have cooled surface temperatures through impact ejecta (Schaller et al., 2016). However, no indices of such an event have been found in

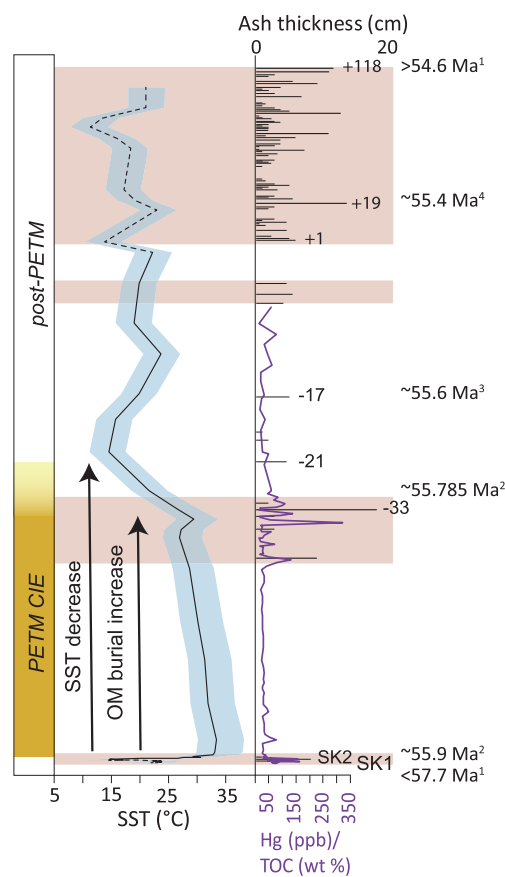


Fig. 6. Summary of temperature changes and volcanic proxies. Red bands show periods of active NAIP volcanism as indicated by high ash accumulation and Hg/TOC anomalies. Yellow band indicates duration of the PETM carbon isotope excursion (CIE). Black line shows BAYSPAR calibrated Sea Surface Temperatures (SST), where blue band indicates the associated 1σ error, and dashed line SSTs with high potential TEX₈₆ bias. OM = Organic Matter; TOC = Total Organic Carbon; ¹King (2016); ²Charles et al. (2011), assuming the timings of the Svalbard and Fur CIEs are coeval; ³Storey et al. (2007a); ⁴Westerhold et al. (2009).

Denmark (Schmitz et al., 2004) and the impact is placed at the CIE onset (Schaller et al., 2016), thereby post-dating the apparent cooling. If the observed cooling is a true indication of palaeotemperatures, then the most plausible explanation is that NAIP volcanism led to a regional cooling in the late Paleocene before the CIE onset in the interval between Ashes SK1 and SK2 (Fig. 5). However, temperature reconstructions from other areas proximal to the NAIP are sparse. More work is needed around the northeast Atlantic margins to confirm whether the apparent cooling is real, its exact timing and duration, and to constrain the potential regional distribution of cooling.

There is no compelling evidence for enhanced volcanism during most of the PETM body in the Danish strata (Fig. 6). This is noteworthy as the ~100 kyr CIE body interval occurs during the ~400 kyr (56.0–55.6 Ma) interval known for elevated NAIP volcanism (Gutjahr et al., 2017; Larsen and Tegner, 2006). This includes the important phase of sill emplacement and thermogenic degassing through hydrothermal vent complexes (Svensen et al., 2004; Frieling et al., 2016). The available proxies from Fur do not shed light on the timing nor duration of the thermogenic degassing phase of the NAIP. The cooling during the PETM recovery is coincident with the re-emergence of thick ash layers and Hg/TOC anomalies (Fig. 6). Temperatures decrease >10 °C during the CIE recovery (Fig. 4), and the abundance of volcanic proxies in the Danish strata toward the end of the CIE body and into the CIE recovery suggests

that the effects of volcanism (e.g. sulfate aerosols, weathering) may also have contributed to the cessation of hyperthermal conditions. The >140 ash layers present in post-PETM strata indicate intense and long-lasting explosive volcanism (Figs. 4, 6). These periods of enhanced volcanic activity coincide with the TEX₈₆ derived cool SSTs (Figs. 4, 6). A similar cooling is suggested within the exceptionally ash rich contemporaneous Balder Fm. (Fig. 3) of the Shetland basin (Jolley and Widdowson, 2005). It is possible that the period of exceptionally explosive volcanic activity following the PETM (Fig. 6) led to a period of regionally cooler temperatures in the North Sea and Northeast Atlantic region.

4. Conclusions

A $\sim -4.5\text{‰}$ change in $\delta^{13}\text{C}_{\text{TOC}}$ defines the PETM onset in an expanded section at Fur Island, Denmark. The CIE onset is accompanied by a marked lithological transition from bioturbated to laminated clays and a dramatic increase in both sedimentation rate and OM content. The late Paleocene section shows an apparent SST cooling of up to 8 °C, based on the TEX₈₆ proxy. While the large potential for TEX₈₆ bias during the first stage make validity of this cooling episode somewhat speculative, the potential TEX₈₆ bias decrease substantially suggesting the latest stage may represent a genuine cooling episode. This latest robust stage of apparent cooling coincides with deposition of two major ash layers (SK1 and SK2) and significant Hg/TOC anomalies, suggesting that regional cooling from voluminous volcanism may be the cause of temporally depressed SSTs in the North Sea during the late Paleocene.

TEX₈₆-derived SSTs yield a minimum temperature increase of $\sim 10\text{ °C}$ across the CIE onset, depending on the calibration method used. This temperature increase is within previous estimates for the PETM, though at the upper end. Maximum SST is reached relatively shortly after the CIE onset, followed by a shift to gradually declining temperatures. There is evidence for negative feedbacks to warming, such as silicate weathering and organic matter burial, occurring during the stable body phase of the PETM CIE. SSTs decreased substantially, reaching anomalously low temperatures by the end of the CIE recovery. A re-emergence of volcanic proxies during the end of the CIE body and the CIE recovery, suggest the effects of volcanism may have contributed to the cessation of hyperthermal conditions. During the post-PETM interval, TEX₈₆-derived SSTs are variable and partly anomalously low (11–23 °C). While overprinting factors could affect TEX₈₆-derived SSTs in parts of the stratigraphy, the effect of persistent explosive volcanic activity during this period is likely to have had some effect on SSTs in the North Sea region.

Declaration of competing interest

The authors declare that they have no known competing financial interests or personal relationships that could have appeared to influence the work reported in this paper.

Acknowledgements

We thank reviewer Dr. Peter Bijl, the anonymous reviewer, and editor Dr. Laura Robinson, for their very thorough and constructive comments. Prof. Emeritus Claus Heilmann-Clausen, Dr. Joost Frieling is sincerely thanked for good and helpful discussions. P. Sargent Bray, Bo Schultz, Dr. Sverre Planke, Prof. Christian Tegner, and Dr. Valentin Zuchuat are all warmly thanked for their assistance. This project was supported by the Research Council of Norway's funding schemes "Unge Forskертallenter" project number 263000 (project Ashlantic) and "Centres of Excellence" project number 223272, and their funding to the Norwegian Research School DEEP

with project number 249040/F60. J. Whiteside is thankful to support from an Annual Adventures in Research grant. J. Tierney acknowledges support from The David and Lucile Packard Foundation and The Heising-Simons Foundation Grant #2016-015.

Appendix A. Supplementary material

Supplementary material related to this article can be found online at <https://doi.org/10.1016/j.epsl.2020.116388>.

References

- Babila, T.L., Penman, D.E., Hönisch, B., Kelly, D.C., Bralower, T.J., Rosenthal, Y., Zachos, J.C., 2018. Capturing the global signature of surface ocean acidification during the Palaeocene-Eocene Thermal Maximum. *Philos. Trans. - Royal Soc., Math. Phys. Eng. Sci.* 376 (2130), 20170072.
- Blaga, C.I., Reichert, G.J., Heiri, O., Damsté, J.S.S., 2009. Tetraether membrane lipid distributions in water-column particulate matter and sediments: a study of 47 European lakes along a north-south transect. *J. Paleolimnol.* 41 (3), 523–540.
- Bornemann, A., Norris, R.D., Lyman, J.A., D'haenens, S., Groeneveld, J., Röhl, U., Speijer, R.P., 2014. Persistent environmental change after the Paleocene-Eocene Thermal Maximum in the eastern North Atlantic. *Earth Planet. Sci. Lett.* 394, 70–81.
- Charles, A.J., Condon, D.J., Harding, I.C., Pälike, H., Marshall, J.E., Cui, Y., Croudace, I.W., 2011. Constraints on the numerical age of the Paleocene-Eocene boundary. *Geochim. Geophys. Geosyst.* 12 (6).
- Cramer, B.S., Toggweiler, J.R., Wright, J.D., Katz, M.E., Miller, K.G., 2009. Ocean overturning since the Late Cretaceous: inferences from a new benthic foraminiferal isotope compilation. *Paleoceanography* 24 (4).
- Cramwinckel, M.J., Huber, M., Kocken, I.J., Agnini, C., Bijl, P.K., Bohaty, S.M., Peterse, F., 2018. Synchronous tropical and polar temperature evolution in the Eocene. *Nature* 559 (7714), 382–386.
- Dickens, G.R., O'Neil, J.R., Rea, D.K., Owen, R.M., 1995. Dissociation of oceanic methane hydrate as a cause of the carbon isotope excursion at the end of the Paleocene. *Paleoceanogr. Paleoclimatol.* 10 (6), 965–971.
- Dunkley Jones, T., Lunt, D.J., Schmidt, D.N., Ridgwell, A., Sluijs, A., Valdes, P.J., Maslin, M., 2013. Climate model and proxy data constraints on ocean warming across the Paleocene-Eocene Thermal Maximum. *Earth-Sci. Rev.* 125, 123–145.
- Fleming, L.E., Tierney, J.E., 2016. An automated method for the determination of the TEX₈₆ and U37K' paleotemperature indices. *Org. Geochem.* 92, 84–91.
- Frieling, J., Jakovleva, A.I., Reichert, G.J., Aleksandrova, G.N., Gnibidenko, Z.N., Schouten, S., Sluijs, A., 2014. Paleocene-Eocene warming and biotic response in the epicontinental West Siberian Sea. *Geology* 42 (9), 767–770.
- Frieling, J., Svensen, H.H., Planke, S., Cramwinckel, M.J., Selnes, H., Sluijs, A., 2016. Thermogenic methane release as a cause for the long duration of the PETM. *Proc. Natl. Acad. Sci.* 113 (43), 12059–12064.
- Frieling, J., Gebhardt, H., Huber, M., Adekeye, O.A., Akande, S.O., Reichert, G.J., Sluijs, A., 2017. Extreme warmth and heat-stressed plankton in the tropics during the Paleocene-Eocene Thermal Maximum. *Sci. Adv.* 3 (3), e1600891.
- Frieling, J., Peterse, F., Lunt, D.J., Bohaty, S.M., Sinninghe Damsté, J.S., Reichert, G.J., Sluijs, A., 2019. Widespread warming before and elevated barium burial during the Paleocene-Eocene Thermal Maximum: evidence for methane hydrate release? *Paleoceanogr. Paleoclimatol.* 34 (4), 546–566.
- Gutjahr, M., Ridgwell, A., Sexton, P.F., Anagnostou, E., Pearson, P.N., Pälike, H., Foster, G.L., 2017. Very large release of mostly volcanic carbon during the Palaeocene-Eocene Thermal Maximum. *Nature* 548 (7669), 573–577.
- Heilmann-Clausen, C., Nielsen, O.B., Gersner, F., 1985. Lithostratigraphy and depositional environments in the Upper Paleocene and Eocene of Denmark. *Bull. Geol. Soc. Den.* 33, 287–323.
- Hollis, C.J., Dunkley Jones, T., Wade, B.S., 2019. The DeepMIP contribution to PMIP4: methodologies for selection, compilation and analysis of latest Paleocene and early Eocene climate proxy data, incorporating version 0.1 of the DeepMIP database. *Geosci. Model Dev. Discuss.*
- Hopmans, E.C., Weijers, J.W., Schefuß, E., Herfort, L., Damsté, J.S.S., Schouten, S., 2004. A novel proxy for terrestrial organic matter in sediments based on branched and isoprenoid tetraether lipids. *Earth Planet. Sci. Lett.* 224 (1–2), 107–116.
- Hopmans, E.C., Schouten, S., Damsté, J.S.S., 2016. The effect of improved chromatography on GDGT-based palaeoproxies. *Org. Geochem.* 93, 1–6.
- Inglis, G.N., Farnsworth, A., Collinson, M.E., Carmichael, M.J., Naafs, B.D.A., Lunt, D.J., Pancost, R.D., 2019. Terrestrial environmental change across the onset of the PETM and the associated impact on biomarker proxies: a cautionary tale. *Glob. Planet. Change* 181, 102991.
- Inglis, G.N., Bragg, F., Burls, N., Evans, D., Foster, G.L., Huber, M., Lunt, D.J., Siler, N., Steinig, S., Wilkinson, R., Anagnostou, E., Cramwinckel, M., Hollis, C.J., Pancost, R.D., Tierney, J., 2020. Global mean surface temperature and climate sensitivity of the Eocene, PETM and latest Paleocene. *Clim. Past.* <https://doi.org/10.5194/cp-2019-167> (in press).

- John, C.M., Bohaty, S.M., Zachos, J.C., Sluijs, A., Gibbs, S., Brinkhuis, H., Bralower, T.J., 2008. North American continental margin records of the Paleocene-Eocene thermal maximum: implications for global carbon and hydrological cycling. *Paleoceanography* 23 (2).
- Jolley, D.W., Widdowson, M., 2005. Did Paleogene North Atlantic rift-related eruptions drive early Eocene climate cooling? *Lithos* 79, 355–366.
- Jones, M.T., Jerram, D.A., Svensen, H.H., Grove, C., 2016. The effects of large igneous provinces on the global carbon and sulphur cycles. *Palaeogeogr. Palaeoclimatol. Palaeoecol.* 441, 4–21.
- Jones, M.T., Percival, L.M., Stokke, E.W., Frieling, J., Mather, T.A., Riber, L., Svensen, H.H., 2019. Mercury anomalies across the Palaeocene–Eocene thermal maximum. *Clim. Past* 15 (1).
- Kender, S., Stephenson, M.H., Riding, J.B., Leng, M.J., Knox, R.W.B., Peck, V.L., Jamieson, R., 2012. Marine and terrestrial environmental changes in NW Europe preceding carbon release at the Paleocene–Eocene transition. *Earth Planet. Sci. Lett.* 353, 108–120.
- Kim, J.H., Van der Meer, J., Schouten, S., Helmke, P., Willmott, V., Sangiorgi, F., Damsté, J.S.S., 2010. New indices and calibrations derived from the distribution of crenarchaeal isoprenoid tetraether lipids: implications for past sea surface temperature reconstructions. *Geochim. Cosmochim. Acta* 74 (16), 4639–4654.
- King, C., 2016. A Revised Correlation of Tertiary Rocks in the British Isles and Adjacent Areas of NW Europe (Gale, A.S. & Barry, T.L., editors). Special Reports, vol. 27. The Geological Society, London.
- Knox, R.W.B., Bosch, J.H.A., Rasmussen, E.S., Heilmann-Clausen, C., Hiss, M., De Lugt, I.R., Kasinski, J., King, C., Köthe, A., Slodkowska, B., Standke, G., Vandenberghe, N., 2010. Cenozoic. In: Dornenbaal, H., Stevenson, A. (Eds.), *Petroleum Geological Atlas of the Southern Permian Basin Area*. EAGE Publications b.v., Houten, pp. 211–223.
- Larsen, R.B., Tegner, C., 2006. Pressure conditions for the solidification of the Skaergaard intrusion: eruption of East Greenland flood basalts in less than 300,000 years. *Lithos* 92 (1–2), 181–197.
- Larsen, L.M., Fitton, J.G., Pedersen, A.K., 2003. Paleogene volcanic ash layers in the Danish Basin: compositions and source areas in the North Atlantic Igneous Province. *Lithos* 71 (1), 47–80.
- Little, K., Röhl, U., Westerhold, T., Zachos, J.C., 2014. A high-resolution benthic stable-isotope record for the South Atlantic: implications for orbital-scale changes in Late Paleocene–Early Eocene climate and carbon cycling. *Earth Planet. Sci. Lett.* 401, 18–30.
- Ma, Z., Gray, E., Thomas, E., Murphy, B., Zachos, J., Paytan, A., 2014. Carbon sequestration during the Paleocene–Eocene Thermal Maximum by an efficient biological pump. *Nat. Geosci.* 7 (5), 382–388.
- McInerney, F.A., Wing, S.L., 2011. The Paleocene-Eocene Thermal Maximum: a perturbation of carbon cycle, climate, and biosphere with implications for the future. *Annu. Rev. Earth Planet. Sci.* 39, 489–516.
- Ogg, J., 2012. Geomagnetic polarity time scale. In: Gradstein, F., Ogg, J., Schmitz, M., Ogg, G. (Eds.), *The Geologic Time Scale 2012*. Elsevier, pp. 85–113.
- Peters, K.E., Peters, K.E., Walters, C.C., Moldowan, J.M., 2005. *The Biomarker Guide* (vol. 1). Cambridge University Press.
- Peterse, F., Kim, J.H., Schouten, S., Kristensen, D.K., Koç, N., Damsté, J.S.S., 2009. Constraints on the application of the MBT/CBT palaeothermometer at high latitude environments (Svalbard, Norway). *Org. Geochem.* 40 (6), 692–699.
- Robock, A., 2000. Volcanic eruptions and climate. *Rev. Geophys.* 38, 191–219.
- Schaller, M.F., Fung, M.K., Wright, J.D., Katz, M.E., Kent, D.V., 2016. Impact ejecta at the Paleocene–Eocene boundary. *Science* 354 (6309), 225–229.
- Schmidt, A., Skeffington, R.A., Thordarson, T., Self, S., Forster, P.M., Rap, A., Ridgwell, A., Fowler, D., Wilson, M., Mann, G.W., Wignall, P.B., Carslaw, K.S., 2016. Selective environmental stress from sulphur emitted by continental flood basalt eruptions. *Nat. Geosci.* 9, 77–82.
- Schmitz, B., Peucker-Ehrenbrink, B., Heilmann-Clausen, C., Åberg, G., Asaro, F., Lee, C.T.A., 2004. Basaltic explosive volcanism, but no comet impact, at the Paleocene–Eocene boundary: high-resolution chemical and isotopic records from Egypt, Spain and Denmark. *Earth Planet. Sci. Lett.* 225 (1–2), 1–17.
- Schoon, P.L., Heilmann-Clausen, C., Schultz, B.P., Damsté, J.S.S., Schouten, S., 2015. Warming and environmental changes in the eastern North Sea Basin during the Paleocene–Eocene Thermal Maximum as revealed by biomarker lipids. *Org. Geochem.* 78, 79–88.
- Schouten, S., Hopmans, E.C., Schefuß, E., Damsté, J.S.S., 2002. Distributional variations in marine crenarchaeotal membrane lipids: a new tool for reconstructing ancient sea water temperatures? *Earth Planet. Sci. Lett.* 204 (1–2), 265–274.
- Sluijs, A., Schouten, S., Pagani, M., Woltering, M., Brinkhuis, H., Damsté, J.S.S., Matthiessen, J., 2006. Subtropical Arctic Ocean temperatures during the Paleocene/Eocene thermal maximum. *Nature* 441 (7093), 610.
- Sluijs, A., Bijl, P.K., Schouten, S., Röhl, U., Reichert, G.J., Brinkhuis, H., 2011. Southern ocean warming, sea level and hydrological change during the Paleocene-Eocene thermal maximum. *Clim. Past* 7 (1), 47–61.
- Storey, M., Duncan, R.A., Swisher, C.C., 2007a. Paleocene-Eocene thermal maximum and the opening of the northeast Atlantic. *Science* 316 (5824), 587–589.
- Storey, M., Duncan, R.A., Tegner, C., 2007b. Timing and duration of volcanism in the North Atlantic Igneous Province: implications for geodynamics and links to the Iceland hotspot. *Chem. Geol.* 241 (3), 264–281.
- Svensen, H., Planke, S., Mørche, S., Mørche, S., Myklebust, R., Eidem, T.R., Rey, S.S., 2004. Release of methane from a volcanic basin as a mechanism for initial Eocene global warming. *Nature* 429 (6991), 542.
- Thordarson, T., Self, S., 2003. Atmospheric and environmental effects of the 1783–1784 Laki eruption: a review and reassessment. *J. Geophys. Res., Atmos.* 108 (D1), AAC-7.
- Tierney, J.E., Tingley, M.P., 2014. A Bayesian, spatially-varying calibration model for the TEX86 proxy. *Geochim. Cosmochim. Acta* 127, 83–106.
- van der Meulen, B., Gingerich, P.D., Lourens, L.J., Meijer, N., van Broekhuizen, S., van Ginneken, S., Abels, H.A., 2020. Carbon isotope and mammal recovery from extreme greenhouse warming at the Paleocene–Eocene boundary in astronomically-calibrated fluvial strata, Bighorn Basin, Wyoming, USA. *Earth Planet. Sci. Lett.* 534, 116044.
- Weijers, J.W., Schouten, S., Spaargaren, O.C., Sinninghe Damsté, J.S., 2006. Occurrence and distribution of Tetraether membrane lipids in soils: implications for the use of the TEX86 proxy and the BIT index. *Org. Geochem.* 37 (10), 1680–1693.
- Westerhold, T., Röhl, U., McCarren, H.K., Zachos, J.C., 2009. Latest on the absolute age of the Paleocene–Eocene Thermal Maximum (PETM): new insights from exact stratigraphic position of key ash layers +19 and –17. *Earth Planet. Sci. Lett.* 287 (3–4), 412–419.
- Westerhold, T., Röhl, U., Wilkens, R.H., Gingerich, P.D., Clyde, W.C., Wing, S.L., Bowen, G.J., Kraus, M.J., 2018. Synchronizing early Eocene deep-sea and continental records – cyclostratigraphic age models for the Bighorn Basin Coring Project drill cores. *Clim. Past* 14, 303–319.
- Wieczorek, R., Fantle, M.S., Kump, L.R., Ravizza, G., 2013. Geochemical evidence for volcanic activity prior to and enhanced terrestrial weathering during the Paleocene Eocene Thermal Maximum. *Geochim. Cosmochim. Acta* 119, 391–410.
- Zachos, J.C., Schouten, S., Bohaty, S., Quattlebaum, T., Sluijs, A., Brinkhuis, H., Bralower, T.J., 2006. Extreme warming of mid-latitude coastal ocean during the Paleocene-Eocene Thermal Maximum: inferences from TEX86 and isotope data. *Geology* 34 (9), 737–740.
- Zachos, J.C., McCarren, H., Murphy, B., Röhl, U., Westerhold, T., 2010. Tempo and scale of late Paleocene and early Eocene carbon isotope cycles: implications for the origin of hyperthermals. *Earth Planet. Sci. Lett.* 299 (1–2), 242–249.
- Zeebe, R.E., Lourens, L.J., 2019. Solar System chaos and the Paleocene–Eocene boundary age constrained by geology and astronomy. *Science* 365 (6456), 926–929.
- Zhang, Y.G., Zhang, C.L., Liu, X.L., Li, L., Hinrichs, K.U., Noakes, J.E., 2011. Methane index: a tetraether archaeal lipid biomarker indicator for detecting the instability of marine gas hydrates. *Earth Planet. Sci. Lett.* 307 (3–4), 525–534.
- Zhang, Y.G., Pagani, M., Wang, Z., 2016. Ring index: a new strategy to evaluate the integrity of TEX86 paleothermometry. *Paleoceanography* 31 (2), 220–232.

Supplementary Information

Temperature changes across the Paleocene-Eocene Thermal Maximum – a new high-resolution TEX₈₆ temperature record from the Eastern North Sea Basin

Ella W. Stokke^{a,*}, Morgan T. Jones^a, Jessica E. Tierney^b, Henrik H. Svensen^a, and Jessica H. Whiteside^c

^a Centre for Earth Evolution and Dynamics (CEED), University of Oslo, PO Box 1028 Blindern, 0315, Oslo, Norway. *e.w.stokke@geo.uio.no

^b The University of Arizona, Department of Geosciences, 1040 E 4th St Tucson, AZ 85721, USA.

^c School of Ocean and Earth Science, National Oceanography Centre Southampton, University of Southampton, Southampton SO14 3ZH, United Kingdom.

Included supplementary tables

Table 1: Stable carbon isotopes, total organic carbon and mercury concentrations.

Table 2: Peak areas of *iso*GDGT, Cren, Cren', and *br*GDGT.

Table 3: Fractional abundance of *iso*GDGTs, Cren, and Cren'. Biomarker ratios for TEX₈₆ quality control.

Table 4: TEX₈₆ and TEX^H₈₆ values and sea surface temperatures.

Table 5: Peak areas of pristane, phytane and n-alkanes.

Table 6: Biomarker ratios TAR, Pristane/Phytane and OEP.

Supplementary Table 1: Stable carbon isotopes ($\delta^{13}\text{C}$), total organic carbon (TOC) and mercury (Hg) analyses included Figures 4 and 5. Mercury data are from Jones et al. (2019).

Locality	Sample Name	Depth rel. to Ash -33 (m)	$\delta^{13}\text{C}$ (‰)	TOC (wt%)	Hg (ppb)	Hg/TOC
Stolleklint	SK17_-0.26 to -0.27	-24.82	-26.31	0.491	34.5	70.33
Stolleklint	SK17_-0.25 to -0.26	-24.81		0.420	32.0	76.19
Stolleklint	SK17_-0.24 to -0.25	-24.80	-26.48	0.466	33.5	71.88
Stolleklint	SK17_-0.23 to -0.24	-24.79	-26.25	0.472	29.5	62.49
Stolleklint	SK17_-0.21 to -0.22	-24.77	-26.39	0.451	38.0	84.34
Stolleklint	SK17_-0.20 to -0.21	-24.76		0.420	31.0	73.81
Stolleklint	SK17_-0.19 to -0.20	-24.75	-26.35	0.469	32.0	68.28
Stolleklint	SK17_-0.18 to -0.19	-24.74	-26.48	0.487	32.5	66.75
Stolleklint	SK17_-0.16 to -0.17	-24.72	-26.18	0.471	30.5	64.76
Stolleklint	SK17_-0.15 to -0.16	-24.71		0.420	36.0	85.71
Stolleklint	SK17_-0.14 to -0.15	-24.70	-26.34	0.479	36.5	76.23
Stolleklint	SK17_-0.13 to -0.14	-24.69	-26.30	0.485	36.0	74.16
Stolleklint	SK17_-0.12 to -0.13	-24.68	-26.36	0.493	35.0	70.96
Stolleklint	SK17_-0.11 to -0.12	-24.67	-26.32	0.487	33.5	68.76
Stolleklint	SK17_-0.10 to -0.11	-24.66		0.430	37.5	87.21
Stolleklint	SK17_-0.09 to -0.10	-24.65	-26.33	0.520	36.5	70.13
Stolleklint	SK17_-0.08 to -0.09	-24.64	-26.81	0.486	40.5	83.36
Stolleklint	SK17_-0.07 to -0.08	-24.63	-26.64	0.330	54.0	163.64
Stolleklint	SK17_-0.06 to -0.07	-24.62	-26.82	0.368	42.5	115.39
Stolleklint	SK17_-0.05 to -0.06	-24.61	-25.77	0.200	9.6	47.75
Stolleklint	SK17_-0.04 to -0.05	-24.60	-26.59	0.210	12.0	57.14
Stolleklint	SK17_-0.03 to -0.04	-24.59	-26.85	0.190	8.7	45.79
Stolleklint	SK17_-0.02 to -0.03	-24.58	-26.32	0.270	19.0	70.37
Stolleklint	SK17_-0.01 to -0.02	-24.57	-26.28	0.270	35.0	129.63
Stolleklint	SK17_0 to -0.01	-24.56	-26.30	0.330	34.0	103.03
Stolleklint	SK17_0.08-0.09	-24.47	-26.73	0.295	23	77.97
Stolleklint	SK17_0.09-0.10	-24.46	-26.43	0.589	39.5	67.02
Stolleklint	SK17_0.10-0.11	-24.45	-26.45	0.438	28.0	63.86
Stolleklint	SK17_0.11-0.12	-24.44	-26.54	0.330	31.5	95.45
Stolleklint	SK17_0.18-0.19	-24.37	-29.45	0.510	80.5	157.84
Stolleklint	SK17_0.19-0.20	-24.36	-30.09	0.644	35.0	54.37
Stolleklint	SK17_0.20-0.21	-24.35	-30.06	0.380	22.0	57.89
Stolleklint	SK17_0.21-0.22	-24.34	-28.62	1.309	44.0	33.61
Stolleklint	SK17_0.23-0.24	-24.32		1.020	42.5	41.67
Stolleklint	SK17_0.25-0.26	-24.30	-30.67	1.218	36.0	29.56
Stolleklint	SK17_0.284-0.292	-24.26	-30.94	1.151	36.5	31.72
Stolleklint	SK17_0.310-0.315	-24.24	-31.20	0.627	27.7	44.12
Stolleklint	SK17_0.350-0.355	-24.20	-31.21	1.294	38.5	29.76
Stolleklint	SK17_0.50-0.51	-24.05		0.920	36.0	39.13
Stolleklint	SK17_0.55-0.56	-24.00	-30.83	0.862	26.5	30.75
Stolleklint	SK17_0.70-0.71	-23.85		1.080	27.5	25.46
Stolleklint	SK17_0.80-0.81	-23.75	-30.91	1.007	27.5	27.32
Stolleklint	SK17-0.90_0.91	-23.65	-31.01	1.026	31.0	30.20
Stolleklint	SK17_0.100-0.101	-23.55		1.140	35.5	31.14
Stolleklint	SK17B-3.0	-22.86	-31.22	1.494	41.5	27.77
Stolleklint	SK17B-3.5	-22.58	-31.06	1.410	109.5	77.66
Stolleklint	SK17B-4	-22.30		0.960	50.0	52.08
Stolleklint	SK17B-4.5	-22.02	-31.10	1.409	50.0	35.50
Stolleklint	SK17B-5	-21.74	-30.95	1.174	37.5	31.95
Stolleklint	SK17B-6	-20.98		1.070	34.0	31.78
Stolleklint	SK17B-6.5	-20.60	-31.18	0.991	29.5	29.76
Stolleklint	SK17B-7	-20.22	-31.16	1.175	30.0	25.53
Stolleklint	SK17B-7.5	-19.84	-31.28	1.260	62.0	49.21
Stolleklint	SK17B-8	-19.46		1.380	58.5	42.39
Stolleklint	SK17B-8.5	-19.09	-31.27	1.551	45.5	29.34
Stolleklint	SK17B-9	-18.71		1.040	31.0	29.81
Stolleklint	SK17B-9.5	-18.33	-31.23	0.974	30.5	31.33
Stolleklint	SK17B-10	-17.95		0.820	27.5	33.54
Stolleklint	SK17B-10.5	-17.63	-30.97	0.911	25.0	27.44
Stolleklint	SK17B-11	-17.31		1.160	31.5	27.16

Supplement Paper I

Locality	Sample Name	Depth rel. to Ash -33 (m)	$\delta^{13}\text{C}$ (‰)	TOC (wt%)	Hg (ppb)	Hg/TOC
Stolleklint	SK17B-11.5	-16.99	-31.19	1.013	34.0	33.58
Stolleklint	SK17B-12	-16.68		0.870	26.0	29.89
Stolleklint	SK17B-13	-16.04	-31.15	0.914	31.0	33.91
Stolleklint	SK17B-14	-15.40		0.880	26.5	30.11
Stolleklint	SK17B-15	-14.77	-31.20	1.293	31.5	24.37
Stolleklint	SK17B-16	-14.17		1.250	33.5	26.80
Stolleklint	SK17B-17	-13.57	-31.11	1.081	33.0	30.51
Stolleklint	SK17B-18	-12.97	-31.19	1.251	38.5	30.78
Stolleklint	SK17B-19	-12.37		1.780	53.5	30.06
Stolleklint	SK17B-20	-11.77	-31.26	2.105	55.0	26.13
Stolleklint	SK17B-21	-11.13	-31.37	2.452	64.0	26.10
Stolleklint	SK17B-22	-10.48		2.240	59	26.34
Stolleklint	SK17B-23	-9.84	-31.38	2.332	57.0	24.44
Stolleklint	SK17B-24	-9.20	-31.35	2.408	62.5	25.95
Stolleklint	SK17B-25	-8.56		2.610	70	26.82
Stolleklint	SK17B-26	-7.90	-31.37	2.732	57.5	21.05
Stolleklint	SK17B-27	-7.24	-31.33	2.212	72.0	32.55
Stolleklint	SK17B-28	-6.58		1.780	58.5	32.87
Stolleklint	SK17B-29	-5.93	-31.49	2.309	55.5	24.04
Quarry FQ16	FQ16-01	-5.59	-31.11	1.374	60.5	44.03
Quarry FQ16	FQ16-04	-5.29	-30.83	0.889	73.0	82.13
Quarry FQ16	FQ16-07	-4.99	-30.99	0.806	105.5	130.86
Quarry FQ16	FQ16-10	-4.69	-30.77	0.933	47.5	50.92
Stolleklint	SK17B-31	-4.48		2.450	44	17.96
Quarry FQ16	FQ16-13	-4.39	-30.98	2.464	75.5	30.64
Quarry FQ16	FQ16-16	-4.09	-31.39	2.616	74.3	28.42
Quarry FQ16	FQ16-19	-3.79	-31.01	1.982	59.5	30.02
Stolleklint	SK17B-32	-3.70	-31.38	2.624	45.0	17.15
Quarry FQ16	FQ16-22	-3.49	-31.24	2.260	160.0	70.79
Quarry FQ16	FQ16-25	-3.19	-31.38	2.717	58.5	21.53
Stolleklint	SK17B-33	-2.91	-31.50	3.138	46.0	14.66
Quarry FQ16	FQ16-28	-2.89	-31.25	2.283	58.0	25.41
Quarry FQ16	FQ16-31	-2.59	-31.15	2.325	74.5	32.05
Quarry FQ16	FQ16-34	-2.29	-31.07	1.580	94.5	59.83
Stolleklint	SK16-B225	-2.25	-31.20	2.297	53.0	23.07
Stolleklint	SK17B-34	-2.12		3.140	66	21.02
Quarry FQ16	FQ16-37	-1.99	-31.36	2.965	66.5	22.43
Quarry FQ16	FQ16-40	-1.69	-31.35	2.400	63.5	26.45
Stolleklint	SK16-B165	-1.65	-31.21	2.423	47.5	19.60
Quarry FQ16	FQ16-43	-1.39	-30.27	0.700	226.5	323.63
Quarry FQ16	FQ16-46	-1.09	-30.66	0.857	48.0	55.98
Stolleklint	SK16-B86	-0.86	-31.42	2.938	47.0	16.00
Stolleklint	SK17B-36	-0.78		3.900	71	18.21
Quarry FQ16	FQ16-50	-0.69	-30.78	0.706	65.0	92.06
Quarry FQ16	FQ16-52	-0.49	-29.88	0.490	67.0	136.76
Quarry FQ16	FQ16-55	-0.19	-30.93	1.011	43.0	42.52
Stolleklint	SK16-B17	-0.17	-31.33	3.403	48.0	14.10
Stolleklint	SK17B-38	-0.11		2.110	65.5	31.04
Stolleklint	SK17B-38.5	0.01		2.440	45.5	18.65
Quarry FQ16	FQ16-58	0.11	-29.79	0.841	66.5	79.03
Quarry FQ16	FQ16-62	0.31	-30.05	0.696	70.5	101.34
Quarry FQ16	FQ16-64	0.51	-29.90	0.505	55.0	108.98
Quarry FQ16	FQ16-67	0.81	-29.54	0.605	41.0	67.74
Quarry FQ16	FQ16-70	1.11	-28.96	0.398	34.0	85.42
Quarry FQ16	FQ16-73	1.41	-28.87	0.647	29.5	45.56
Quarry FQ16	FQ16-76	1.71	-29.14	0.910	53.0	58.27
Quarry FQ16	FQ16-78	1.91	-27.73	0.648	39.0	60.19
Stolleklint	Fur15-4.30	4.30	-27.06	0.911	29.0	31.84
Stolleklint	Fur15-5.35	5.35	-26.88	0.542	26.0	47.94
Stolleklint	Fur15-5.50	5.50	-26.93	1.231	33.5	27.20
Stolleklint	Fur15-7.65	7.65	-26.58	3.220	64.0	19.88
Stolleklint	Fur15-8.65	8.65	-26.55	1.098	40.0	36.44
Stolleklint	Fur15-9.65	9.65	-27.27	1.945	31.5	16.19
Stolleklint	Fur15-10.7	10.70	-26.90	1.712	39.5	23.07

Supplement Paper I

Locality	Sample Name	Depth rel. to Ash -33 (m)	$\delta^{13}\text{C}$ (‰)	TOC (wt%)	Hg (ppb)	Hg/TOC
Stolleklint	Fur15-11.1	11.10	-26.93	0.944	30.0	31.80
Stolleklint	Fur15-12.4	12.40	-26.69	0.999	20.0	20.03
Stolleklint	Fur15-13.3	13.30	-26.74	1.082	22.5	20.79
Stolleklint	Fur15-14.0	14.00	-26.01	0.796	48.5	60.92
Stolleklint	Fur15-15.0	15.00	-25.94	1.091	48.5	44.44
Stolleklint	Fur15-16.0	16.00	-26.85	0.755	25.0	33.10
Stolleklint	Fur15-17.0	17.00	-26.15	0.699	55.0	78.68
Stolleklint	Fur15-18.0	18.00	-26.29	1.352	19.0	14.06
Stolleklint	Fur15-19.6	19.60	-26.79	1.547	90.5	58.51
Quarry PQ16	PQ16-1.0	21.90	-27.50	0.662		
Quarry PQ16	PQ16-2.0	22.90	-27.80	0.575		
Quarry PQ16	PQ16-3.0	23.90	-27.31	0.556		
Quarry PQ16	PQ16-4.0	24.90	-27.43	0.535		
Quarry PQ16	PQ16-5.0	25.9	-27.12	0.669		
Quarry JH17	JH17-0.05	27.05	-28.46	0.315		
Quarry JH17	JH17-1.0	28.00	-27.59	0.332		
Quarry JH17	JH17-1.4	28.40	-26.74	0.457		
Quarry JH17	JH17-2.0	29.00	-27.31	0.437		
Quarry JH17	JH17-2.5	29.50	-27.12	0.442		
Quarry JH17	JH17-3.0	30.00	-26.93	0.659		
Quarry JH17	JH17-3.4	30.40	-26.39	0.676		
Quarry JH17	JH17-4.0	31.00	-27.67	0.561		
Quarry JH17	JH17-4.6	31.60	-27.04	0.380		
Quarry JH17	JH17-5.0	32.00	-27.30	0.352		
Quarry JH17	JH17-5.4	32.40	-26.73	0.351		
Quarry JH17	JH17-6.0	33.00	-27.49	0.243		
Quarry JH17	JH17-6.6	33.60	-27.00	0.425		
Quarry JH17	JH17-7.0	34.00	-26.81	0.414		
Quarry JH17	JH17-7.4	34.40	-26.81	0.489		
Quarry JH17	JH17-8.0	35.00	-27.00	0.331		
Quarry JH17	JH17-8.6	35.60	-26.92	0.491		
Quarry JH17	JH17-9.0	36.00	-27.28	0.465		
Quarry JH17	JH17-9.5	36.50	-26.92	0.398		
Quarry JH17	JH17-10.1	37.10	-26.90	0.411		
Quarry JH17	JH17-10.5	37.50	-26.61	0.500		
Quarry JH17	JH17-11.0	38.00	-26.93	0.567		
Quarry JH17	JH17-11.5	38.50	-27.60	0.240		
Quarry JH17	JH17-12.0	39.00	-27.03	0.279		
Quarry JH17	JH17-12.4	39.40	-26.74	0.410		
Quarry JH17	JH17-13.0	40.00	-28.22	0.186		
Quarry JH17	JH17-13.6	40.60	-26.60	0.414		
Quarry JH17	JH17-14.0	41.00		0.536		

Supplementary Table 2: Relative abundance of Isoprenoid GDGT, Crenarchaeol and the Crenarchaeol isomer, and Branched GDGT peak areas from HPLC-MS analyses.

		Relative abundance										
Sample Name	Depth rel. to Ash -33 (m)	1302-GDGT0	1300-GDGT1	1298-GDGT2	1296-GDGT3	1292-GDGT4-cren	1292'	1050-5	1050-6	1036-5	1036-6	1022
SK17_-0.26 to -0.27	-24.82	157797	34122	28144	7011	235931	15196	6183	7260	11187	22618	131074
SK17_-0.22 to -0.23	-24.78	317489	63978	57731	12452	501548	31544	12140	16923	23313	45341	256304
SK17_-0.21 to -0.22	-24.77	217968	41999	38060	7912	329260	20936	8874	10249	14545	39333	171995
SK17_-0.18 to -0.19	-24.74	384487	75723	70633	15415	607965	37496	15382	19246	24498	49890	267722
SK17_-0.16 to -0.17	-24.72	255297	49432	45421	9977	383487	24273	10017	12455	14865	33069	175372
SK17_-0.14 to -0.15	-24.70	335161	66528	64723	13321	522671	33033	16538	19350	27123	48195	272746
SK17_-0.11 to -0.12	-24.67	285296	62593	56011	12385	454792	28304	17616	19129	25772	51390	276779
SK17_-0.09 to -0.10	-24.65	187972	37827	37078	7696	277566	18077	10584	16173	15629	36032	207315
SK17B-HC1_22-23	-24.63	394148	77796	65269	17447	653528	34760	21853	21104	27493	54434	331379
SK17B-HC1_25-26	-24.61	145233	15360	14944	4827	117460	3706	9830	37625	15153	18379	143136
SK17B-HC1_28-29	-24.59	44573	4969	4779	913	26288	756	4104	25374	6251	5889	60065
SK17_-0.02 to -0.03	-24.58	104680	14081	9123	2335	56385	1577	9885	41820	17817	10191	163966
SK17B-HC1_31-32	-24.57	357864	24114	15032	4749	250577	4935	17730	21305	31484	15358	210564
SK17B-HC1_36-37	-24.48	603152	40360	21737	7933	640934	13896	17917	23188	27109	19039	145762
SK17_0.09 to 0.10	-24.46	65227	4479	2135	761	68573	1294	2722	3362	4490	2408	25110
SK17_0.10 to 0.11	-24.45	149142	12363	6432	2659	151508	2751	7659	10562	10832	8609	75936
SK17_0.18 to 0.19	-24.37	433091	45779	35046	11823	570149	13796	6900	1931	5498	5365	29269
SK17_0.19 to 0.20	-24.36	967721	171570	159257	47656	1818429	57746	20592	8714	17883	15613	84291
SK17_0.20 to 0.21	-24.35	1061458	244141	301480	93029	2438089	98224	13087	6958	14796	14596	82735
SK17_0.21 to 0.22	-24.34	880096	234006	306622	98564	2515859	101361	10232	4329	11189	11129	62461
SK17_0.252 to 0.260	-24.30	2449054	714564	1142985	329995	7763652	468416	44931	16448	47014	52196	279832
SK17_0.284 to 0.292	-24.26	1522217	449901	683611	214160	5152133	299407	34241	11126	36539	36475	243531
SK17_0.350 to 0.355	-24.20	1769482	537567	760241	245000	5447566	313529	41089	15644	46321	45920	293296
SK17_0.55 to 0.66	-24.00	254295	95246	166521	54670	1271368	89726	4530	1883	10820	11307	76830
SK17_0.80 to 0.81	-23.75	1030259	391691	726850	235573	4719811	346459	15457	7934	30248	33330	201077
SK17B-3.5	-22.58	1103585	446795	763042	299000	5692458	464814	4818	3545	17202	22304	160896
SK17B-8.5	-19.09	469567	184903	299648	113300	2192572	151345	2669	2196	10679	13228	85931
SK17B-15	-14.77	1973363	678743	404285	7212958	7212958	519637	25380	11343	48572	58546	350461
SK17B-21	-11.13	1167401	376941	559171	216895	3718607	212139	5868	4594	17840	21807	128863
SK17B-29	-5.93	881371	299394	393865	155590	2798435	156082	4286	4848	14901	18642	115168
SK17B-33	-2.91	1587250	465452	538101	226103	3769061	199403	8850	9118	23760	28173	166332
SK17B-34	-2.12	1159386	377246	442476	181598	3042467	175370	4590	4583	15487	19584	115467
SK17B-35.5	-1.03	5110811	1651000	2269550	923491	14064171	896614	30031	32608	86274	102413	628085
SK16-B17	-0.17	817144	241395	282366	111098	1886425	91821	4639	4010	11367	14963	82180
FQ16-76	1.71	494083	81104	63428	24945	725959	28478	15411	12637	15347	14674	128546
Fur15-5.5	5.50	3697196	431795	218446	91116	4331660	91534	69617	47798	70632	60454	396561
Fur15-8.65	8.65	753888	95386	52903	20830	824132	21107	7831	8575	9590	7987	72006

Sample Name	Depth rel. to Ash -33 (m)	1302-GDGT0	1300-GDGT1	1298-GDGT2	1296-GDGT3	1292-GDGT4-cren	1292'	1050-5	1050-6	1036-5	1036-6	1022
Fur15-11.1	11.10	64571	11705	8341	4093	74881	2637	3598	456	7599	2154	17431
Fur15-15	15.00	62853	18948	22393	5945	82938	2811	75152	b.d.	57507	b.d.	110998
Fur15-18.0	18.00	47932	6399	4318	1675	64971	1805	1709	128	1834	627	12840
PQ16-1	21.90	5596	3511	3097	948	8606	484	b.d.	b.d.	b.d.	b.d.	33949
PQ16-4	24.90	11322	2571	2560	917	8468	373	4860	4147	28550	9509	46314
PQ16-5	25.9	39015	6823	3709	1297	47775	1056	4775	4137	9106	10404	48500
JH17-2	29.00	90298	15281	11192	5590	165792	7297	10269	12141	20655	9430	114815
JH17-3	30.00	53147	8258	5968	2063	55821	2125	2398	2117	5499	5916	43386
JH17-4	31.00	26599	8356	5548	1885	44021	1684	b.d.	b.d.	11548	3931	45165
JH17-7	34.00	26883	1794	1348	351	15383	376	1644	623	b.d.	b.d.	12403
JH17-8	35.00	40245	1199	622	310	11175	477	924	10374	2691	7421	16777
JH17-9	36.00	37399	16857	9200	4213	70774	3797	1312	31916	3032	15991	26077
JH17-10.1	37.10	15197	3161	1421	578	20231	403	b.d.	b.d.	3446	6687	27947
JH17-11	38.00	105310	13384	6035	2452	139100	3081	b.d.	b.d.	9932	11622	87853
JH17-12	39.00	7622	974	611	383	9363	356	329	6239	938	6732	12827
JH17-14	41.00	58525	11367	6685	3802	82766	5366	3812	30590	5188	26402	48567

Supplementary Table 3: First part include fractional abundance of isoGDGTs, Crenarchaeol and the Crenarchaeol isomer. Second part includes a set of biomarker indices calculated from peak areas, and indicating the reliability of the TEX₈₆ data. RI = Ring Index; BIT = Branched and Isoprenoid Tetraether index; MI = Methane Index; ¹Zhang et al. (2016); ²Hopmans et al. (2004); ³Zhang et al. (2011).

			Fractional abundance					Quality control							
Sample Name	Depth rel. to Ash -33 (m)	Cren	cren'	GDGT0	GDGT1	GDGT2	GDGT3	RI ¹	RI-TEX ¹	ΔRI ¹	BIT ²	MI ³	GDGT-2/3	Cren'/Cren'+Cren	GDGT0/Cren
SK17_-0.26 to -0.27	-24.82	0.493	0.032	0.330	0.071	0.059	0.015	2.334	2.311	0.023	0.430	0.216	4.014	0.061	0.669
SK17_-0.22 to -0.23	-24.78	0.509	0.032	0.322	0.065	0.059	0.013	2.386	2.369	0.017	0.414	0.201	4.636	0.059	0.633
SK17_-0.21 to -0.22	-24.77	0.502	0.032	0.332	0.064	0.058	0.012	2.351	2.370	0.019	0.427	0.201	4.810	0.060	0.662
SK17_-0.18 to -0.19	-24.74	0.510	0.031	0.323	0.064	0.059	0.013	2.387	2.389	0.001	0.383	0.200	4.582	0.058	0.632
SK17_-0.16 to -0.17	-24.72	0.499	0.032	0.332	0.064	0.059	0.013	2.346	2.379	0.033	0.391	0.205	4.553	0.060	0.666
SK17_-0.14 to -0.15	-24.70	0.505	0.032	0.324	0.064	0.063	0.013	2.375	2.407	0.032	0.423	0.206	4.859	0.059	0.641
SK17_-0.11 to -0.12	-24.67	0.506	0.031	0.317	0.070	0.062	0.014	2.384	2.346	0.038	0.462	0.213	4.522	0.059	0.627
SK17_-0.09 to -0.10	-24.65	0.490	0.032	0.332	0.067	0.065	0.014	2.327	2.403	0.076	0.507	0.218	4.818	0.061	0.677
SK17B-HC1_22-23	-24.63	0.526	0.028	0.317	0.063	0.053	0.014	2.425	2.328	0.096	0.411	0.189	3.741	0.051	0.603
SK17B-HC1_25-26	-24.61	0.390	0.012	0.482	0.051	0.050	0.016	1.805	2.338	0.532	0.656	0.225	3.096	0.031	1.236
SK17B-HC1_28-29	-24.59	0.320	0.009	0.542	0.060	0.058	0.011	1.525	2.214	0.689	0.795	0.283	5.234	0.028	1.696
SK17_-0.02 to -0.03	-24.58	0.300	0.008	0.556	0.075	0.048	0.012	1.441	1.987	0.546	0.812	0.306	3.907	0.027	1.857
SK17B-HC1_31-32	-24.57	0.381	0.008	0.544	0.037	0.023	0.007	1.659	2.051	0.392	0.542	0.147	3.165	0.019	1.428
SK17B-HC1_36-37	-24.48	0.483	0.010	0.454	0.030	0.016	0.006	2.053	2.085	0.032	0.267	0.097	2.740	0.021	0.941

Sample Name	Depth rel. to Ash -33 (m)	Cren	cren'	GDGT0	GDGT1	GDGT2	GDGT3	RI ¹	RI-TEX ¹	ΔRI ¹	BIT ²	MI ³	GDGT-2/3	Cren'/Cren'+Cren	GDGT0/Cren
SK17_0.09-0.10	-24.46	0.481	0.009	0.458	0.031	0.015	0.005	2.039	1.993	0.046	0.357	0.095	2.806	0.019	0.951
SK17_0.10-0.11	-24.45	0.466	0.008	0.459	0.038	0.020	0.008	2.002	2.008	0.006	0.429	0.122	2.419	0.018	0.984
SK17_0.18-0.19	-24.37	0.514	0.012	0.390	0.041	0.032	0.011	2.241	2.230	0.012	0.079	0.137	2.964	0.024	0.760
SK17_0.19-0.20	-24.36	0.564	0.018	0.300	0.053	0.049	0.015	2.525	2.345	0.181	0.075	0.168	3.342	0.031	0.532
SK17_0.20-0.21	-24.35	0.576	0.023	0.251	0.058	0.071	0.022	2.661	2.560	0.101	0.051	0.201	3.241	0.039	0.435
SK17_0.21-0.22	-24.34	0.608	0.025	0.213	0.057	0.074	0.024	2.807	2.617	0.191	0.038	0.196	3.111	0.039	0.350
SK17_0.252-0.260	-24.30	0.603	0.036	0.190	0.056	0.089	0.026	2.869	2.801	0.068	0.054	0.210	3.464	0.057	0.315
SK17_0.284-0.292	-24.26	0.619	0.036	0.183	0.054	0.082	0.026	2.916	2.784	0.132	0.066	0.198	3.192	0.055	0.295
SK17_0.350-0.355	-24.20	0.600	0.035	0.195	0.059	0.084	0.027	2.848	2.719	0.129	0.075	0.211	3.103	0.054	0.325
SK17_0.55-0.66	-24.00	0.658	0.046	0.132	0.049	0.086	0.028	3.125	2.946	0.179	0.077	0.189	3.046	0.066	0.200
SK17_0.80-0.81	-23.75	0.633	0.047	0.138	0.053	0.098	0.032	3.062	2.964	0.098	0.058	0.211	3.085	0.068	0.218
SK17B-3.5	-22.58	0.649	0.053	0.126	0.051	0.087	0.034	3.136	2.981	0.154	0.035	0.197	2.552	0.075	0.194
SK17B-8.5	-19.09	0.643	0.044	0.138	0.054	0.088	0.033	3.078	2.893	0.184	0.050	0.203	2.645	0.065	0.214
SK17B-15	-14.77	0.609	0.044	0.167	0.057	0.088	0.034	2.950	2.854	0.096	0.064	0.216	2.588	0.067	0.274
SK17B-21	-11.13	0.595	0.034	0.187	0.060	0.089	0.035	2.859	2.772	0.086	0.046	0.227	2.578	0.054	0.314
SK17B-29	-5.93	0.597	0.033	0.188	0.064	0.084	0.033	2.854	2.686	0.169	0.053	0.223	2.531	0.053	0.315
SK17B-33	-2.91	0.555	0.029	0.234	0.069	0.079	0.033	2.667	2.580	0.086	0.059	0.237	2.380	0.050	0.421
SK17B-34	-2.12	0.566	0.033	0.216	0.070	0.082	0.034	2.729	2.599	0.130	0.050	0.237	2.437	0.054	0.381
SK17B-35.5	-1.03	0.564	0.036	0.205	0.066	0.091	0.037	2.761	2.726	0.035	0.059	0.245	2.458	0.060	0.363
SK16-B17	-0.17	0.550	0.027	0.238	0.070	0.082	0.032	2.639	2.556	0.083	0.058	0.243	2.542	0.046	0.433
FQ16-76	1.71	0.512	0.020	0.348	0.057	0.045	0.018	2.328	2.292	0.035	0.204	0.183	2.543	0.038	0.681
Fur15-5.5	5.50	0.489	0.010	0.417	0.049	0.025	0.010	2.125	1.989	0.136	0.130	0.144	2.397	0.021	0.854
Fur15-8.65	8.65	0.466	0.012	0.426	0.054	0.030	0.012	2.061	2.031	0.030	0.114	0.167	2.540	0.025	0.915
Fur15-11.1	11.10	0.450	0.016	0.388	0.070	0.050	0.025	2.110	2.208	0.098	0.294	0.237	2.038	0.034	0.862
Fur15-15	15.00	0.423	0.014	0.321	0.097	0.114	0.030	2.167	2.395	0.227	0.746	0.355	3.767	0.033	0.758
Fur15-18.0	18.00	0.511	0.014	0.377	0.050	0.034	0.013	2.259	2.169	0.091	0.209	0.157	2.578	0.027	0.738
PQ16-1	21.90	0.387	0.022	0.252	0.158	0.139	0.043	2.199	2.210	0.011	0.798	0.454	3.267	0.053	0.650
PQ16-4	24.90	0.323	0.014	0.432	0.098	0.098	0.035	1.748	2.322	0.574	0.917	0.406	2.792	0.042	1.337
PQ16-5	25.9	0.479	0.011	0.391	0.068	0.037	0.013	2.142	1.963	0.179	0.617	0.195	2.860	0.022	0.817
JH17-2	29.00	0.561	0.025	0.306	0.052	0.038	0.019	2.528	2.361	0.166	0.502	0.156	2.002	0.042	0.545
JH17-3	30.00	0.438	0.017	0.417	0.065	0.047	0.016	2.027	2.175	0.149	0.515	0.219	2.893	0.037	0.952
JH17-4	31.00	0.500	0.019	0.302	0.095	0.063	0.021	2.360	2.092	0.268	0.579	0.257	2.943	0.037	0.604
JH17-7	34.00	0.333	0.008	0.583	0.039	0.029	0.008	1.486	2.132	0.645	0.488	0.181	3.840	0.024	1.748
JH17-8	35.00	0.207	0.009	0.745	0.022	0.012	0.006	0.925	2.143	1.218	0.774	0.155	2.006	0.041	3.601
JH17-9	36.00	0.498	0.027	0.263	0.119	0.065	0.030	2.434	2.048	0.385	0.525	0.289	2.184	0.051	0.528
JH17-10.1	37.10	0.494	0.010	0.371	0.077	0.035	0.014	2.202	1.876	0.326	0.653	0.200	2.458	0.020	0.751
JH17-11	38.00	0.516	0.011	0.391	0.050	0.022	0.009	2.233	1.947	0.287	0.440	0.133	2.461	0.022	0.757
JH17-12	39.00	0.485	0.018	0.395	0.050	0.032	0.020	2.187	2.263	0.076	0.743	0.168	1.595	0.037	0.814
JH17-14	41.00	0.491	0.032	0.347	0.067	0.040	0.023	2.307	2.268	0.039	0.581	0.199	1.758	0.061	0.707

Supplementary Table 4: TEX_{86} (Schouten et al., 2002) and TEX^H_{86} (Kim et al., 2010) values calculated from isoGDGT peak areas. Sea surface temperatures (SSTs) calculated following Tierney and Tingley (2014; 2015) and Kim et al. (2010).

Locality	Sample Name	Depth rel. to Ash -33 (m)	TEX ₈₆	SST BAYSPAR (°C) - (Tierney and Tingley, 2014; 2015)			SST (°C) TEX ₈₆ ^H - (Kim et al., 2010)	
			(Schouten et al., 2002)	0.05	0.50	0.095	TEX ₈₆ ^H	TEX ₈₆ ^H (°C)
Stolleklint	SK17_-0.26 to -0.27	-24.82	0.596	15.86	22.0	28.57	-0.225	23.23
Stolleklint	SK17_-0.22 to -0.23	-24.78	0.614	17.07	23.1	29.97	-0.212	24.11
Stolleklint	SK17_-0.21 to -0.22	-24.77	0.614	17.04	23.1	29.92	-0.212	24.13
Stolleklint	SK17_-0.18 to -0.19	-24.74	0.620	17.41	23.5	30.49	-0.208	24.40
Stolleklint	SK17_-0.16 to -0.17	-24.72	0.617	17.26	23.3	30.18	-0.210	24.26
Stolleklint	SK17_-0.14 to -0.15	-24.70	0.625	17.77	23.8	30.81	-0.204	24.66
Stolleklint	SK17_-0.11 to -0.12	-24.67	0.607	16.56	22.6	29.39	-0.217	23.77
Stolleklint	SK17_-0.09 to -0.10	-24.65	0.624	17.72	23.7	30.70	-0.205	24.60
Stolleklint	SK17B-HC1_22-23	-24.63	0.602	16.21	22.4	29.07	-0.221	23.50
Stolleklint	SK17B-HC1_25-26	-24.61	0.605	16.44	22.5	29.30	-0.219	23.65
Stolleklint	SK17B-HC1_28-29	-24.59	0.565	13.77	20.0	26.20	-0.248	21.63
Stolleklint	SK17_-0.02 to -0.03	-24.58	0.481	7.83	14.5	20.42	-0.318	16.84
Stolleklint	SK17B-HC1_31-32	-24.57	0.506	9.68	16.2	22.04	-0.296	18.37
Stolleklint	SK17B-HC1_36-37	-24.48	0.519	10.56	17.0	22.94	-0.285	19.12
Stolleklint	SK17_0.09_0.10	-24.46	0.483	7.98	14.7	20.60	-0.316	17.00
Stolleklint	SK17_0.10-0.11	-24.45	0.489	8.41	15.1	20.93	-0.310	17.36
Stolleklint	SK17_0.18_0.19	-24.37	0.570	14.10	20.3	26.63	-0.244	21.90
Stolleklint	SK17_0.19-0.20	-24.36	0.607	16.58	22.7	29.42	-0.217	23.76
Stolleklint	SK17_0.20-0.21	-24.35	0.669	20.59	26.6	34.30	-0.175	26.64
Stolleklint	SK17_0.21-0.22	-24.34	0.684	21.52	27.5	35.54	-0.165	27.32
Stolleklint	SK17_0.252-0.260	-24.30	0.731	24.41	30.5	39.38	-0.136	29.29
Stolleklint	SK17_0.284-0.292	-24.26	0.727	24.17	30.2	39.08	-0.139	29.12
Stolleklint	SK17_0.350-0.355	-24.20	0.710	23.16	29.2	37.66	-0.148	28.44
Stolleklint	SK17_0.55-0.66	-24.00	0.765	26.43	32.7	42.27	-0.116	30.66
Stolleklint	SK17_0.80-0.81	-23.75	0.770	26.73	33.0	42.60	-0.114	30.82
Stolleklint	SK17B-3.5	-22.58	0.774	26.96	33.3	42.99	-0.111	30.98
Stolleklint	SK17B-8.5	-19.09	0.753	25.74	31.9	41.25	-0.123	30.18
Stolleklint	SK17B-15	-14.77	0.744	25.22	31.3	40.49	-0.129	29.81
Stolleklint	SK17B-21	-11.13	0.724	24.01	30.1	38.82	-0.140	29.00
Stolleklint	SK17B-29	-5.93	0.702	22.64	28.7	37.02	-0.154	28.09
Stolleklint	SK17B-33	-2.91	0.674	20.91	26.9	34.68	-0.171	26.89
Stolleklint	SK17B-34	-2.12	0.679	21.22	27.2	35.11	-0.168	27.12
Stolleklint	SK17B-35.5	-1.03	0.712	23.28	29.3	37.81	-0.147	28.53
Stolleklint	SK16-B17	-0.17	0.668	20.54	26.5	34.20	-0.175	26.61
Quarry FQ16	FQ16-76	1.71	0.590	15.45	21.6	28.18	-0.229	22.94
Stolleklint	Fur15-5.5	5.50	0.482	7.92	14.6	20.50	-0.317	16.89
Stolleklint	Fur15-8.65	8.65	0.499	9.13	15.7	21.59	-0.302	17.92
Stolleklint	Fur15-11.1	11.10	0.563	13.62	19.9	26.13	-0.250	21.53
Stolleklint	Fur15-15	15.00	0.622	17.59	23.6	30.61	-0.206	24.48
Stolleklint	Fur15-18.0	18.00	0.549	12.67	18.9	25.09	-0.260	20.80
Quarry PQ16	PQ16-1	21.90	0.563	13.59	19.9	26.12	-0.249	21.55
Quarry PQ16	PQ16-4	24.90	0.600	16.15	22.2	28.87	-0.222	23.41
Quarry PQ16	PQ16-5	25.9	0.470	7.08	13.8	19.73	-0.327	16.20
Quarry JH17	JH17-2	29.00	0.612	16.88	23.0	29.77	-0.213	24.00
Quarry JH17	JH17-3	30.00	0.552	12.84	19.2	25.30	-0.258	20.92
Quarry JH17	JH17-4	31.00	0.522	10.78	17.2	23.19	-0.283	19.28
Quarry JH17	JH17-7	34.00	0.536	11.76	18.1	24.12	-0.271	20.09
Quarry JH17	JH17-8	35.00	0.540	12.06	18.4	24.40	-0.267	20.31
Quarry JH17	JH17-9	36.00	0.505	9.60	16.1	22.02	-0.297	18.32
Quarry JH17	JH17-10.1	37.10	0.432	4.24	11.4	17.39	-0.365	13.65
Quarry JH17	JH17-11	38.00	0.464	6.64	13.4	19.37	-0.334	15.76
Quarry JH17	JH17-12	39.00	0.581	14.84	21.0	27.43	-0.236	22.46
Quarry JH17	JH17-14	41.00	0.582	14.95	21.1	27.57	-0.235	22.54

Supplementary Table 5: Peak areas of pristane, phytane and n-alkanes. Data from GC-MS analyses of the aliphatic and aromatic fraction.

m/z=56 peak areas											
Sample Name	Depth rel. to Ash-33 (m)	Pristane	Phytane	C15	C17	C19	C27	C28	C29	C30	C31
SK17 -0.26 to -0.27	-24.82	29972314	54948184	37923757	147084628	56045538	19592923	25038099	21875262	8562284	36682344
SK17 -0.18 to -0.19	-24.74	28911519	9829194	9818151	42749976	15598660	12323233	5735437	14062934	6529078	10082940
SK17 -0.09 to -0.10	-24.65	2864342	2186099	4322805	8324591	10842230	6017632	3571677	6632462	2308030	3567495
SK17B-HC1-25-26	-24.61	5005536	7221077	2034197	9044268	20903175	51954801	38871218	47626229	31013658	37198423
SK17 -0.02 to -0.03	-24.58	5578435	4479327	4837379	14910987	16186669	18916849	12456421	22471513	15327325	16088361
SK17B-HC1-31-32	-24.57	5475078	3557777	622055	7670407	6144326	3566031	1836887	2925505	1324292	1956234
SK17 0.10 to 0.11	-24.45	824730	1511168	545889	10217751	15813265	5503353	1415041	5244819	1834158	9672680
SK17 0.20 to 0.21	-24.35	28223284	30075996	13993534	91447916	37846415	12421765	3641769	16856595	6205185	11423524
SK17 0.25 to 0.26	-24.30	7517444	4069014	1873823	16630970	7107828	11984373	2111746	10230628	2116508	5313669
SK17 0.350 to 0.355	-24.20	4632317	4600083	2764768	16166362	16759490	25393543	9594679	27295943	10221406	18123299
SK17 0.80 to 0.81	-23.75	1435487	3536674	578107	15594158	14015643	15114882	5285918	14377310	5475902	14563431
SK17B 3.5	-22.58	4369466	11879520	298525	28124406	15043545	8718658	2268928	9699736	3556271	6258313
SK17B 8.5	-19.09	922916	2568231	2464537	20266269	16243935	21331015	8254393	20185455	7287907	16660204
SK17B 21	-11.13	2336134	5629951	535826	14094151	20757075	9249047	4913041	10961904	8024044	10967334
SK17B 29	-5.93	796234	4253524	913525	15259728	15005808	5935794	3992890	10505819	6516291	8740012
SK17B 33	-2.91	12385787	3196091	5373222	88594883	20268905	1871246	1411939	4443428	3061700	4305574
SK16-B17	-0.17	7549165	2178376	625256	32539474	19384608	2426963	1466445	6969433	4968816	6279039
FQ16-64	0.51	88809898	33253058	349941008	147462341	47886713	18881451	9916535	22732751	19172443	24867709
FQ16-76	1.71	4015323	2084459	213261	27700814	13639504	1493778	992383	2227682	1220064	2372828
Fur15-5.50m	5.50	5962334	10437756	1037673	34967820	18379947	1215122	1411567	2975677	1123434	4844467
Fur15-8.65m	8.65	2490170	4803679	1983389	6232809	6645167	7132375	4187089	11082567	4800567	11714370
Fur15-11.1	11.10	9344259	3268333	2476593	43744545	14970583	5122420	961898	8233237	3870891	8670460
PQ16-1.0	21.90	14242811	27363100	5900733	69265855	19650870	7789510	1996404	2712561	1180276	9841818
PQ16-3.0	23.90	20477812	18172130	7663561	42596630	37897836	19436282	12903156	26066006	16763888	22020305
PQ16-4.0	24.90	2043574	7563656	888406	14034474	11463896	1616315	2794665	4210964	1430256	7569849
JH17 5.0	32	4811725	3385222	295358	31559777	17438947	2410553	1579372	2245089	1207589	2064822
JH17 8.0	35	19879775	4988736	927455	93063793	32041916	966432	894045	3622625	2184426	5363935
JH17 11.0	38	6727951	5461512	280635	32813031	20041867	2719611	1039510	3076577	983700	4446409
JH17 12.0	39	31579411	18994854	6668932	45859447	23292933	7967241	3467605	9181565	4222762	8144957
JH17 14.0	41	13022447	5797315	450736	62648424	28429188	991212	468366	1560570	800328	2059630

Supplementary Table 6: Biomarker ratios calculated with peak areas from the aliphatic and aromatic fraction. TAR = Terrigenous Aquatic Ratio; Pri/Phy = Pristane/Phytane; OEP = Odd over Even Predominance

Locality	Sample Name	Depth rel. to Ash -33 (m)	TAR (Bourbonniere & Meyers, 1996)	Pri/Phy	OEP (Scalan & Smith, 1970)
Stolleklint	SK17 -0.26 to -0.27	-24.82	0.3242	0.5455	1.3953
Stolleklint	SK17 -0.18 to -0.19	-24.74	0.5350	2.9414	2.1767
Stolleklint	SK17 -0.09 to -0.10	-24.65	0.6904	1.3103	2.0996
Stolleklint	SK17B-HC1-25-26	-24.61	4.2768	0.6932	1.3412
Stolleklint	SK17 -0.02 to -0.03	-24.58	1.5995	1.2454	1.5282
Stolleklint	SK17B-HC1-31-32	-24.57	0.5852	1.5389	1.8249
Stolleklint	SK17 0.10 to 0.11	-24.45	0.7684	0.5458	3.5890
Stolleklint	SK17 0.20 to 0.21	-24.35	0.2841	0.9384	3.1732
Stolleklint	SK17 0.25 to 0.26	-24.30	1.0748	1.8475	4.6521
Stolleklint	SK17 0.350 to 0.355	-24.20	1.9841	1.0070	2.6152
Stolleklint	SK17 0.80 to 0.81	-23.75	1.4594	0.4059	2.6934
Stolleklint	SK17B 3.5	-22.58	0.5677	0.3678	3.1405
Stolleklint	SK17B 8.5	-19.09	1.4927	0.3594	2.5592
Stolleklint	SK17B 21	-11.13	0.8811	0.4149	1.6617
Stolleklint	SK17B 29	-5.93	0.8076	0.1872	1.8486
Stolleklint	SK17B 33	-2.91	0.0930	3.8753	1.8350
Stolleklint	SK16-B17	-0.17	0.2983	3.4655	1.9627
Quarry FQ16	FQ16-64	0.51	0.1219	2.6707	1.5482
Quarry FQ16	FQ16-76	1.71	0.1467	1.9263	1.9472
Stolleklint	Fur15-5.50m	5.50	0.1661	0.5712	2.3583
Stolleklint	Fur15-8.65m	8.65	2.0139	0.5184	2.3739
Stolleklint	Fur15-11.1	11.10	0.3600	2.8590	3.2689
Quarry PQ16	PQ16-1.0	21.90	0.2146	0.5205	2.6684
Quarry PQ16	PQ16-3.0	23.90	0.7659	1.1269	1.6673
Quarry PQ16	PQ16-4.0	24.90	0.5077	0.2702	2.0386
Quarry JH17	JH17 5.0	32	0.1363	1.4214	1.6098
Quarry JH17	JH17 8.0	35	0.0790	3.9849	2.2792
Quarry JH17	JH17 11.0	38	0.1928	1.2319	3.1664
Quarry JH17	JH17 12.0	39	0.3336	1.6625	2.3146
Quarry JH17	JH17 14.0	41	0.0504	2.2463	2.4463

Supplementary references

- Bourbonniere, R. A., & Meyers, P. A. (1996). Sedimentary geolipid records of historical changes in the watersheds and productivities of Lakes Ontario and Erie. *Limnology and Oceanography*, 41(2), 352-359.
- Hopmans, E. C., Weijers, J. W., Schefuß, E., Herfort, L., Damsté, J. S. S., & Schouten, S. (2004). A novel proxy for terrestrial organic matter in sediments based on branched and isoprenoid tetraether lipids. *Earth and Planetary Science Letters*, 224(1-2), 107-116.
- Jones, M. T., Percival, L. M., Stokke, E. W., Frieling, J., Mather, T. A., Riber, L., ... & Svensen, H. H. (2019). Mercury anomalies across the Palaeocene–Eocene thermal maximum. *Climate of the Past*, 15(1).
- Kim, J. H., Van der Meer, J., Schouten, S., Helmke, P., Willmott, V., Sangiorgi, F., ... & Damsté, J. S. S. (2010). New indices and calibrations derived from the distribution of crenarchaeal isoprenoid tetraether lipids: Implications for past sea surface temperature reconstructions. *Geochimica et Cosmochimica Acta*, 74(16), 4639-4654.
- Scalan, E. S., & Smith, J. E. (1970). An improved measure of the odd-even predominance in the normal alkanes of sediment extracts and petroleum. *Geochimica et Cosmochimica Acta*, 34(5), 611-620.
- Schouten, S., Hopmans, E. C., Schefuß, E., & Damsté, J. S. S. (2002). Distributional variations in marine crenarchaeotal membrane lipids: a new tool for reconstructing ancient sea water temperatures?. *Earth and Planetary Science Letters*, 204(1-2), 265-274.
- Tierney, J. E., & Tingley, M. P. (2014). A Bayesian, spatially-varying calibration model for the TEX86 proxy. *Geochimica et Cosmochimica Acta*, 127, 83-106.
- Tierney, J. E., & Tingley, M. P. (2015). A TEX 86 surface sediment database and extended Bayesian calibration. *Scientific data*, 2, 150029.
- Zhang, Y. G., Zhang, C. L., Liu, X. L., Li, L., Hinrichs, K. U., & Noakes, J. E. (2011). Methane Index: a tetraether archaeal lipid biomarker indicator for detecting the instability of marine gas hydrates. *Earth and Planetary Science Letters*, 307(3-4), 525-534.
- Zhang, Y. G., Pagani, M., & Wang, Z. (2016). Ring Index: A new strategy to evaluate the integrity of TEX86 paleothermometry. *Paleoceanography*, 31(2), 220-232.

Evidence of explosive hydromagmatic eruptions during the emplacement of the North Atlantic Igneous Province

Ella W. Stokke, Emma J. Liu, and Morgan T. Jones

Volcanica (2020), 3(2), pp. 227-250.

Evidence of explosive hydromagmatic eruptions during the emplacement of the North Atlantic Igneous Province

Ella W. Stokke^{*α}, Emma J. Liu^{β, γ}, Morgan T. Jones^α

^αCentre for Earth Evolution and Dynamics (CEED), University of Oslo, PO Box 1028 Blindern, 0315, Oslo, Norway.

^βEarth Sciences, University College London, 5 Gower Place, London, WC1E 6BS, UK.

^γDepartment of Earth Sciences, University of Cambridge, Downing Street, Cambridge CB2 3EQ, UK.

ABSTRACT

Early Eocene sediments in northwest Denmark contain over 180 well-preserved volcanic ash layers, likely sourced from the North Atlantic Igneous Province (NAIP) between 56.0 and 54.6 Ma. Most of these ashes are basaltic, widespread, and represent a phase of unusually large and explosive eruptions that is coincident with the opening of the northeast Atlantic Ocean. Explosive basaltic eruptions of this magnitude are unheard of in historical times and in the current geological record. Here, we combine analyses of glass sulfur concentrations and variations in the morphology and vesicularity of pristine volcanic glass grains to explore the possible eruptive processes promoting such widespread basaltic ash dispersal. We suggest that these ashes formed in shallow subaqueous environments (<200 m water depth) where they fragmented and rapidly quenched during explosive hydromagmatic activity. We speculate that magma-water interaction during the opening of the northeast Atlantic Ocean was the main cause of this unusual explosive basaltic activity.

Keywords: Hydromagmatism; Large Igneous Province; Basaltic ash; Sulfur degassing;

1 INTRODUCTION

The North Atlantic Igneous Province (NAIP) is a vast complex composed of massive continental flood basalts, widespread sill intrusions, and large volcanic centres surrounding the margins of the present-day northeast Atlantic Ocean and Labrador Sea [Figure 1; Á Horni et al. 2017; Saunders et al. 1997; Storey, Duncan, and Tegner 2007]. The province began to form at ~63 Ma, but the bulk of the igneous material ($5\text{--}10 \times 10^6 \text{ km}^3$) was emplaced between 56 and 54 Ma, coincident with the breakup of Greenland from Eurasia and the formation of the northeast Atlantic Ocean [Larsen et al. 2016; Saunders 2016; Saunders et al. 1997; Storey, Duncan, and Tegner 2007; Wilkinson et al. 2017]. Most of the continental flood basalts in East Greenland, the sill intrusions in the Vøring and Møre basins (Figure 1), and the seaward dipping reflectors along the North Atlantic margins were emplaced during this time [Á Horni et al. 2017; Planke et al. 2005; Storey, Duncan, and Tegner 2007; Wilkinson et al. 2017]. The formation of the NAIP is of significant scientific interest because it coincides with both the breakup of the northeast Atlantic Ocean and the extreme climate perturbations of the late Paleocene and early Eocene, including the Paleocene-Eocene Thermal Maximum (PETM; [Saunders 2016; Schmitz et al. 2004; Storey, Duncan, and Swisher 2007; Storey, Duncan,

and Tegner 2007; Svensen et al. 2004]). Explosive volcanism played an integral part of the NAIP activity, as evidenced by the preservation of hundreds of tephra layers in the North Sea region [Knox and Morton 1988; Larsen et al. 2003; Morton and Knox 1990]. Tephra is especially abundant in the earliest Eocene stratigraphy, suggesting increased explosive activity during the later stages of NAIP emplacement and the start of seafloor spreading [e.g. Larsen et al. 2003]. To our knowledge, this is the first tephra sequence that traces the activity of a Large Igneous Province (LIP) during continental breakup that has been recognised in the geological record. The unique preservation of the NAIP compared to other LIPs enables us to recognize processes that are normally not observable, improving our understanding of the explosive components of LIPs.

Particularly well-preserved tephra layers from the NAIP are exposed subaerially in northwest Denmark (Figures 1 and 2) due to recent glaciotectionic activity [Pedersen 2008]. These layers are all within the ash fraction with grain sizes <2 mm, and will henceforth be referred to as ash. More than 180 individual ash layers are preserved in the earliest Eocene stratigraphy, comprising organic rich marine clays of the Stolleklint Clay (syn-PETM) gradually overlain by the diatomite-rich Fur Formation (post-PETM). The ashes are stratigraphically sorted into a negative (−39 to −1) and positive (+1 to +140) ash series [Bøggild 1918]. The negative series is composed of a heterogeneous range of ash compositions (from basalt to rhyolite) that are often heavily

*Corresponding author: e.w.stokke@geo.uio.no

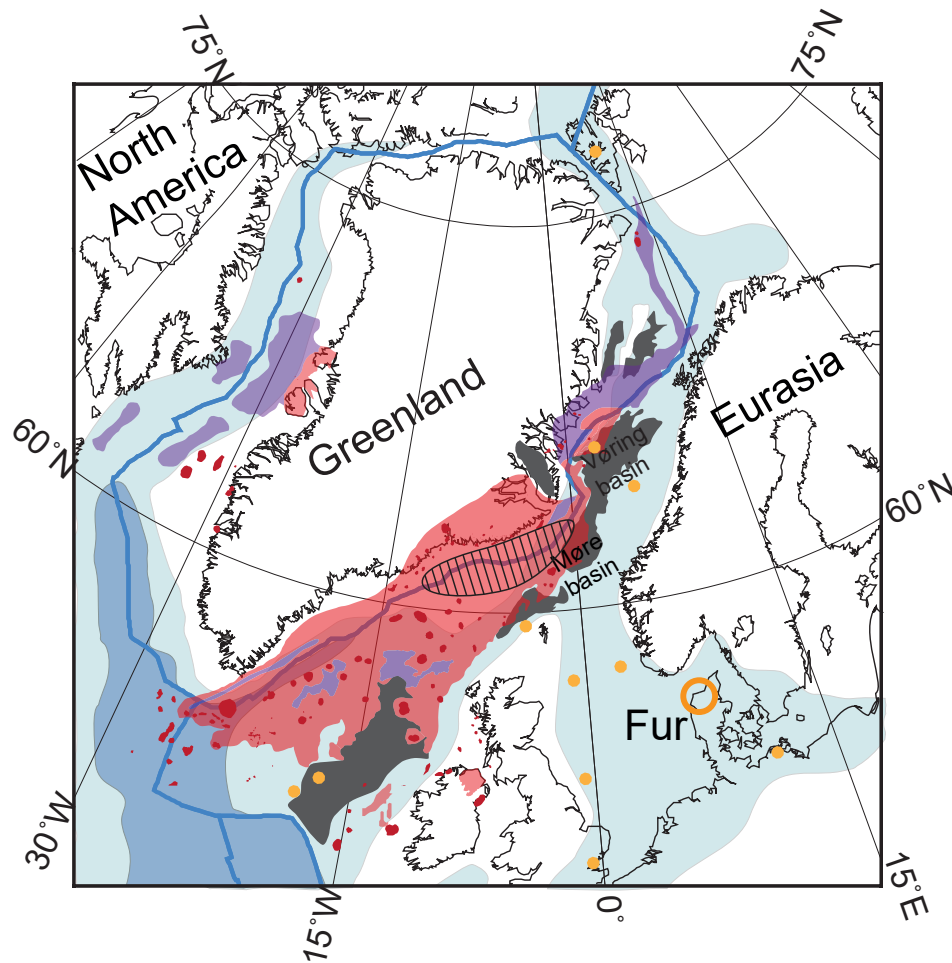


Figure 1: Map of the known extent of the North Atlantic Igneous Province (NAIP) in a regional palaeogeographic reconstruction from 56 Ma. The striped area indicates the most likely source area for the Danish ash layers based on [Larsen et al. \[2003\]](#). The yellow points show selected known localities of NAIP-derived ash (ash locations from [Haaland et al. \[2000\]](#), [Jolley and Widdowson \[2005\]](#), [Morton and Keene \[1984\]](#), and [Morton and Knox \[1990\]](#)), although NAIP-derived ash is also distributed far outside this map frame such as Goban Spur and in the Austrian Alps [e.g. [Egger et al. 2005](#)]. Dark red: volcanic centres. Red areas: the known extent of subaerial and submarine extrusive NAIP volcanism. Purple areas: the known extent of only submarine volcanism. Dark grey areas: known extent of NAIP sill intrusions. Blue lines: plate boundaries. Black lines: present-day coastlines. Light blue: shelf areas. Dark blue: ocean basins. Figure modified from [Abdelmalak et al. \[2016\]](#); [Á Horni et al. \[2017\]](#); [Jones et al. \[2019\]](#), and references therein.

altered. In contrast, the positive series is dominated by near-pristine tholeiitic basalts [[Larsen et al. 2003](#)]. All the ashes represent primary fall deposits with no evidence of post-depositional transport or redeposition [[Pedersen et al. 1975](#); [Pedersen and Surlyk 1983](#)]. Normal grading in the ash layers indicates that each layer is the product of a single explosive eruption ([Figure 3](#)).

It is generally accepted that the ashes are sourced from the NAIP, based on correlative chemistry and the lack of any other appropriate volcanic centres of the same age nearby [[Larsen et al. 2003](#); [Morton and Knox 1990](#)]. However, the NAIP source volcanoes were located between 700 and 1500 km from the depositional environment of the eastern North Sea at that time [[Figure 1](#); [Abdelmalak et al. 2016](#)]. These are exceptionally

large transport distances for basaltic eruptions, during which the bulk of erupted material is more commonly deposited close to source [e.g. [Parfitt 1998](#)]. If the source area of the volcanoes is correct ([Figure 1](#); [[Larsen et al. 2003](#)]), then each of these 180 ash layers represents an extremely large magnitude explosive eruption. For example, the Grímsvötn volcanic system in Iceland frequently produces explosive eruptions aided by hydromagmatic interactions with the overlying Vatnajökull ice cap. The early Holocene G10ka tephra series from Grímsvötn record several basaltic eruptions that are among the largest known Icelandic eruptions in the Neogene and covered an area of 2 million km² [[Óladóttir et al. 2020](#)]. However, only millimetre thick ash layers from the G10ka tephra series can be found at

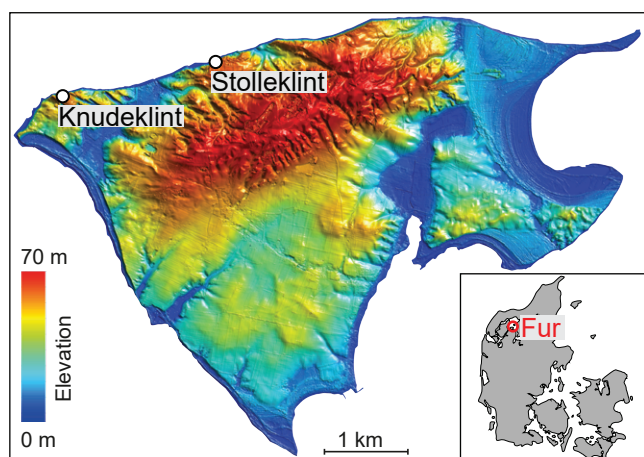


Figure 2: Topographic map of the island of Fur, Denmark. Ash samples are from two marked localities: Knudeklint (56°50'15"N, 8°57'30"E) and Stolleklint (56°50'29"N, 8°59'33"E). The high topography in the north of the island marks a partially overturned anticline of Fur Formation and upper Stolleklint Clay strata. Map courtesy of Egon Nørmark.

similar distances from the source as the Danish ash layers [Óladóttir et al. 2020]. By comparison, the largest basaltic ash in the Danish series is 16 cm thick [Bøggild 1918, 14 cm at Fur], and more than 20 of these tholeiitic basalts can be traced all the way to the Austrian Alps [Egger et al. 2005]. A key interval (Ash +19) has an estimated volume of 1200 km³ (dense rock equivalent; DRE) and an areal extent of 16 million km² [Egger and Brückl 2006]. This study focuses on the early Eocene tholeiitic ash layers preserved in the diatomitic Fur Formation, and explores the eruptive processes that promoted such widespread ash dispersal.

The large ash grain sizes (up to 500 µm), the thicknesses of the basaltic ash layers (2–160 mm), and the large distances from possible source volcanoes (700–1500 km) indicate that these were extremely explosive eruptions with high magma fluxes. Figure 4 shows the plume heights and wind speeds necessary to transport a 250 µm ash particle 750 km, based on the model of Stevenson et al. [2015]. This suggests that wind speeds need to be in the range of 35–60 m s⁻¹ and plume heights in the range of 15–30 km, or possibly higher (Figure 4). Therefore, it is only possible to transport basaltic ash grains of this size >750 km if the eruption was Plinian or similar, and if the stratospheric winds were in the right direction and at the upper end of present-day velocities. Note that the model assumes constant wind speeds at all altitudes, so given the lower average wind speeds in the troposphere, these values are likely to be minimum estimates. This strongly suggests that each of these ash layers represents a highly explosive (VEI 7–8) and large volume (M7–8; [Mason et al. 2004]) eruption. It is plausible that lateral stratospheric velocities were augmented by the high magnitudes and high intensities of the eruptions. Dynamical

modelling of the formation of giant umbrella clouds (>600 km diameter) suggests that radial spreading in the umbrella region enhances lateral transport in the stratosphere and leads to a more circular shape than for less violent eruptions [Baines and Sparks 2005; Mastin et al. 2014]. At mid- to high-latitudes, these giant ash clouds are inherently unstable due to internal differences in Coriolis forces, meaning that at least part of the cloud is drawn towards the equator [Baines et al. 2008]. In the case of the NAIP-derived eruptions, the North Sea region to the southeast would have been ideally positioned to receive additional ash fall through this effect. This would reduce the wind velocities needed to transport ash particles such great distances in the early Eocene, but requires that the eruptions be both high and sustained in intensity.

A review of bore holes in the Pacific Ocean shows that the magnitude of eruptions from volcanoes in Japan correlate with both tephra layer thicknesses and distance from the source volcano [Mahony et al. 2016]. The only tephra layers thicker than 1 cm and over 1000 km from the source in their dataset were M8 eruptions [Mahony et al. 2016] defined as eruptions with >400 km³ DRE magma volume [Mason et al. 2004]. Importantly, all known M8 eruptions have involved silica-rich magmas. The high viscosities of these magmas inhibit the escape of volatiles, enabling the generation of overpressure and eventually highly energetic fragmentation [Cashman and Scheu 2015; Dingwell 1996; Papale 1999; Wallace and Edmonds 2011]. In contrast, the low viscosities of silica-poor basaltic melts do not sufficiently restrict bubble growth and instead enable gas-melt separation and non-explosive degassing of exsolved volatiles [Cashman and Scheu 2015; Mangan and Cashman 1996]. Sub-Plinian and Plinian eruptions of basaltic magmas are therefore rare, and those that are known have largely been attributed to rapid ascent and syn-eruptive crystallisation of hydrous basalts, and the associated increase in magma viscosity [Arzilli et al. 2019; Costantini et al. 2010; Houghton et al. 2004; Sable et al. 2006; Walker et al. 1984; Williams 1983]. Critically, these rheological constraints imply that the tholeiitic basaltic ash layers in the positive ash series—which we show below are largely crystal-free—likely reflect a type and scale of explosive basaltic eruption not observed in the historical record.

Without historical examples as a reference, we need to consider the possible mechanisms for producing widespread basaltic tephra. Fundamentally, a high magma flux is required. However, enhanced explosivity and fine fragmentation of basaltic magma would also require either (1) increased viscosity due to rapid syn-eruptive crystallisation, enabling brittle fragmentation mechanisms more similar to that of silicic magmas, or (2) magma-water interactions amplifying brittle fragmentation and generating the heat transfer necessary to drive high plumes for widespread ash dispersal. The second option is conceivable, as the

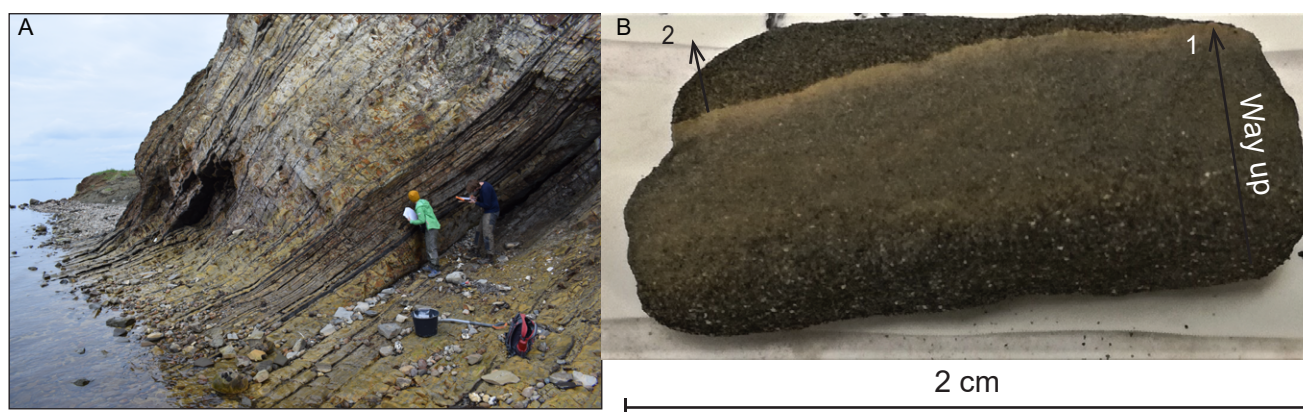


Figure 3: [A] Photo of the Knudeklint locality showing black ash layers of the positive series in light Fur Formation diatomite. [B] An example of the normally graded character of the ashes. The picture shows the double basaltic ash layer +16 where the first (1) upward fining ash layer is immediately overlain by the coarse base of a second (2) ash layer.

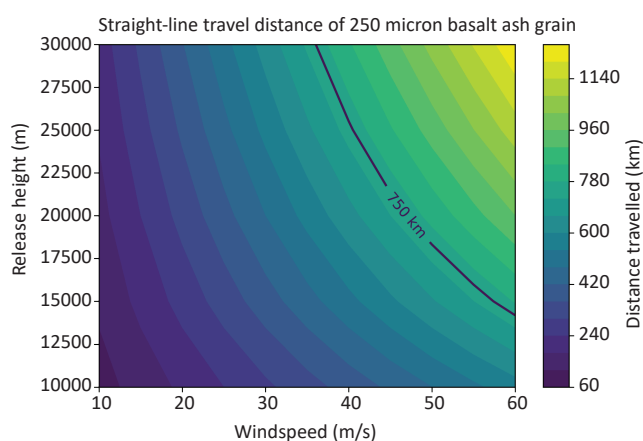


Figure 4: A model evaluation of the necessary plume heights and atmospheric wind speeds required for long distance ash dispersal, based on the method of Stevenson et al. [2015]. The model uses conservative estimates of 250 µm basaltic ash particle size and a 750 km transport distance (shown as a black line). The input parameters use a basaltic glass density of 2800 kg m⁻³, a grain sphericity of 0.7, a size-dependent density function [Bonadonna and Phillips 2003], and a Ganser fall velocity model. The model makes the unrealistic assumption of constant wind velocities at all altitudes and in a straight line from source to deposition, meaning that the output is a minimum estimate of the required plume heights/wind speeds to distribute ash particles these distances.

rupturing of Greenland from Eurasia led to seafloor spreading through the middle of the Greenland-Faroe continental flood basalt provinces in the early Eocene [Larsen et al. 2003; Storey, Duncan, and Swisher 2007; Storey, Duncan, and Tegner 2007]. This rifting would have allowed a seawater incursion at the heart of the elevated magmatic activity, which could have produced

the explosive basaltic ashes preserved in Denmark and the North Sea. A hydromagmatic origin for the ashes has been proposed previously by several authors, based on textural observations and the widespread ash distribution [Haaland et al. 2000; Morton and Evans 1988; Pedersen and Jørgensen 1981], but has yet to be rigorously tested.

Explosive hydromagmatic eruptions occur when erupting magma interacts with a body of external water, resulting in rapid quenching of the melt and extensive melt fragmentation [Büttner et al. 1999; Morrisey et al. 2000; Németh and Kósik 2020; Thórdarson et al. 1996]. Rapid quenching arrests the degassing process, leading to elevated residual volatile contents compared to magmatic tephra degassed to atmospheric pressure [Mastin et al. 2004; Németh and Kósik 2020; Óladóttir et al. 2007]. Therefore, one method that can potentially identify hydromagmatic eruptions is measuring the volatile contents of quenched glass, particularly late-stage degassing species such as sulfur and chlorine [Liu et al. 2018; Mastin et al. 2004; Óladóttir et al. 2007; Thórdarson et al. 2003]. Recent studies of basaltic eruptions in Iceland have used this approach to identify changes in glacial thickness above Katla volcano [Óladóttir et al. 2007] and to differentiate between coeval magmatic and hydromagmatic eruptions along a single fissure [Liu et al. 2017; Liu et al. 2018]. Coupled with volcanic glass morphology, Liu et al. [2018] demonstrated that glass sulfur concentrations were elevated in the hydromagmatic products due to quenching at pressures greater than atmospheric (1 atm). Although the Fur Formation ashes are considerably older (56.0–54.6 Ma) than these Holocene tephtras, they are remarkably well-preserved. We therefore measure glass volatile contents (S, Cl), in combination with component analysis of ash particle morphology, throughout the ash series to test the hypothesis that the NAIP tephtras were a product of hydromagmatic activity. We use these data to infer relative changes in the

pressure they were erupted under (i.e. depth below sea level) over time. Our results advance our understanding of the evolution of the NAIP and the physical volcanology of hydromagmatic eruptions more generally; an eruptive style that is currently under-represented in the literature, particularly for eruptions in deep time.

2 GEOLOGICAL SETTING

2.1 The island of Fur

Ash samples used for this study were collected on the island of Fur, northwest Denmark (Figures 1 and 2). During the Paleocene-Eocene transition and early Eocene, this area was part of a marginal basin within the eastern part of the larger semi-enclosed epicontinental North Sea Basin. The stratigraphy exposed at Fur reflects both small and large scale climatic and tectonic changes. A marine regression due to thermal uplift of the NAIP and the onset of PETM global warming marks the Paleocene-Eocene transition in Denmark. This caused a lithological shift from the latest Paleocene condensed, bioturbated clays of the Holmehus Formation, into the earliest Eocene dark, laminated Stolleklint Clay [Figure 5; Heilmann-Clausen 1995; Heilmann-Clausen et al. 1985]. The PETM onset has been identified at the base of the Stolleklint Clay by a 4.5 ‰ negative shift in organic $\delta^{13}\text{C}$ values [Jones et al. 2019]. Towards the end of the PETM the Stolleklint Clay grades upward into the 60 m thick Fur Formation (Figure 5), composed of diatomite with variable clay contents. The sediments are thermally immature and have experienced very little lithification and consolidation [Stokke et al. 2020]. However, Quaternary glacio-tectonic activity has generated large scale deformation in northern Denmark, creating abundant small scale folding and thrusting throughout the Fur stratigraphy [Pedersen 2008]. Despite this, ash layers are mostly laterally continuous and easy to trace, without any obvious overthickening.

2.2 The Danish ash series

More than 180 ash layers are interbedded in the stratigraphy, with the majority (~140) found within the diatomitic Fur Formation (Figure 3A; Figure 5). The volcanic ashes are grouped into a negative and positive ash series [Bøggild 1918], with additional ash layers [termed SK1, SK2, and SK3; Jones et al. 2019] within the base of the Stolleklint Clay (Figure 5). Numerous efforts have been made to constrain the timing of explosive activity preserved in Denmark. The lowermost ash layers (SK1 and SK2) are found stratigraphically just below the base of the PETM carbon isotope excursion (CIE), which is estimated to have begun between 56.0 and 55.9 Ma [Figure 5; Westerhold et al. 2017; Zeebe and Lourens 2019]. A bentonite layer found during the

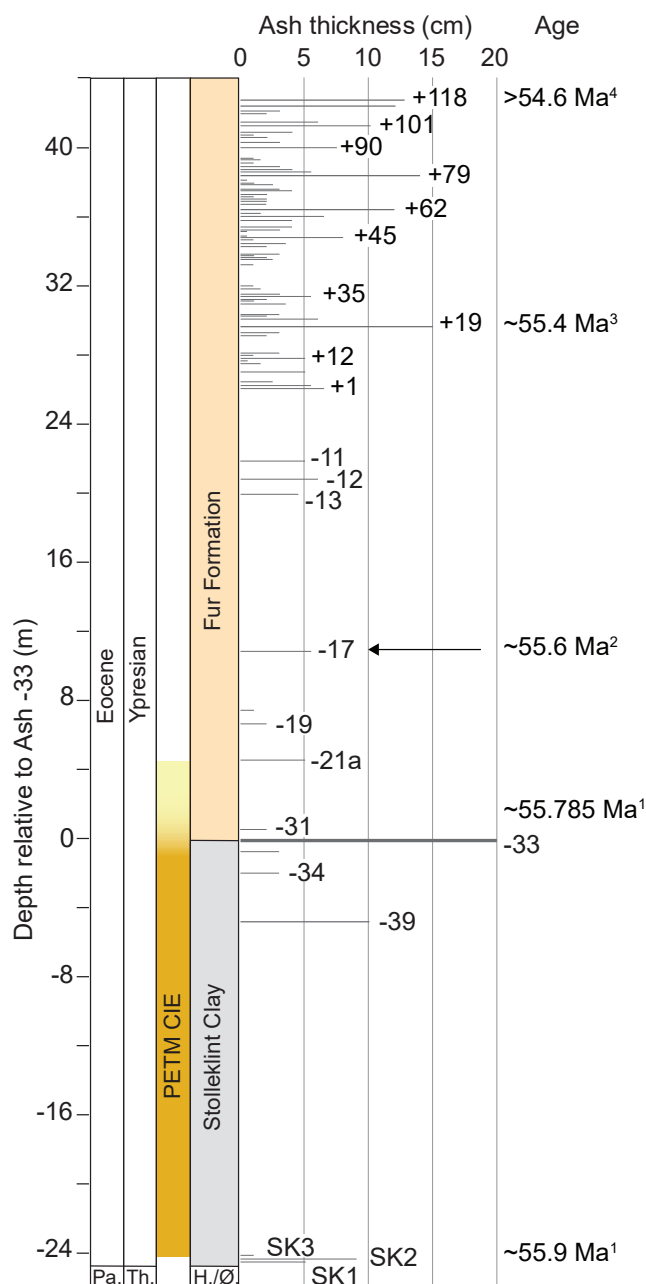


Figure 5: The relevant stratigraphy at Stolleklint and Knudeklint (locations shown in Figure 2). Pa. = Paleocene; Th. = Thanetian; H./Ø. = Holmehus/Østerrende Formation. For additional lithological information, see Stokke et al. [2020]. Extent of PETM carbon isotope excursion (CIE) taken from Stokke et al. [2020]. Grey lines indicate ash layers, with main ash layers labelled and maximum ash layer thickness measured at Fur indicated on the top. Note that there are some thickness variations within Denmark [Bøggild 1918]. ¹Charles et al. [2011], assuming the timings of the Svalbard and Fur CIEs are coeval; ²Storey, Duncan, and Tegner [2007]; ³Westerhold et al. [2009]; ⁴King [2016].

recovery of the PETM CIE has a U-Pb radioisotopic age of 55.785 ± 0.086 Ma [Charles et al. 2011]. If the Svalbard and Danish CIEs are coeval, this would be located stratigraphically about 1.5 m above Ash -33 in the Fur Formation [Figure 5; Stokke et al. 2020]. Approximately 10 m up the section, $^{40}\text{Ar}/^{39}\text{Ar}$ dating of Ash layer -17 gives a corrected absolute age of 55.60 ± 0.12 Ma [Figure 5; Jones et al. 2019; Storey, Duncan, and Swisher 2007]. Westerhold et al. [2009] estimated a 200 kyr duration between Ash -17 and +19, based on correlation to the orbital cyclostratigraphy of the DSDP 550 core at Goban Spur. The uppermost basaltic Ash +140 marks the top of the ~60 m thick Fur Formation [Bøggild 1918; Heilmann-Clausen et al. 1985]. There is no evidence of the magnetic reversal from C24r to C24n within the Fur Formation nor the second Eocene thermal maximum (ETM2; ~54.1 Ma; [King 2016; Stokke et al. 2020]). The positive series basalts correlates with subphase 2b of pyroclastic deposition in the lower Balder Formation [Knox and Morton 1988], which suggest that the top of the Fur Formation is no younger than 54.6 Ma (Figure 5; Heilmann-Clausen [pers. comm.]; [King 2016; Watson et al. 2017]). Therefore, the evidence of explosive volcanism in Denmark likely spans ~1.4 Myr from 56.0 to 54.6 Ma, with deposition of the basaltic positive series initiating sometime after 55.6 Ma (Figure 5).

The provenance of the Danish ash layers was a source of some contention. Earlier work assumed that the ashes were derived from a nearby volcanic source in the Skagerrak or North Sea [Nielsen and Heilmann-Clausen 1988; Pedersen et al. 1975]. However, subsequent geophysical and seismic surveys failed to find any volcanic centres in these areas, suggesting that the ashes originated from further afield. A strong geochemical correlation between North Sea ashes and NAIP volcanic centres [Larsen et al. 2003], coupled with widespread ash sequences across the North Sea and northern Europe [King 2016; Morton and Evans 1988; Morton and Knox 1990], strongly support the hypothesis that these ash layers originated from NAIP sources. A comprehensive attempt to correlate the ashes with different NAIP volcanic centres divided the ashes into four stages of volcanic activity [Larsen et al. 2003]. The first three stages involve ashes SK1-3 and the negative ash series. These include a heterogeneous mix of variably-preserved ashes, likely sourced from different volcanic centres on the British Isles, East Greenland, and around the northeast Atlantic margin [Larsen et al. 2003]. Stage 4 comprises the entire positive ash series, which temporally and chemically correlates to the offshore Balder Formation ashes and likely originated from the main rift zone during opening of the North Atlantic [Figure 1; Larsen et al. 2003; Morton and Knox 1990]. The positive ash series is composed of well-preserved, glassy tholeiitic basalts, with the exception of the rhyolitic layers Ash +13 and Ash +19 [Larsen et al. 2003; Pedersen and Jørgensen 1981].

3 MATERIALS AND METHODS

3.1 Sample description

A total of 21 ash layers are included in this study, all from the post-PETM Fur Formation and collected from two different outcrop exposures on Fur Island (Figure 2). Ash -19 was sampled at the Stolleklint beach ($56^{\circ}50'29''\text{N}$, $8^{\circ}59'33''\text{E}$), while Ash -13 and all of the positive series ashes from the Knudeklint beach locality ($56^{\circ}50'14''\text{N}$ $8^{\circ}57'26''\text{E}$). Additional ashes from the negative series were also sampled, but these turned out to be too altered to yield useful analyses and are therefore excluded from this study. The main part of the samples are therefore from the positive series, covering the interval from Ash +1 to Ash +118. The ash series does continue up to Ash +140, but these are thinner and difficult to sample due to poor exposure and preservation.

The ash layers are relatively distinct and easy to trace laterally. They vary in thickness from <1 to 20 cm (Figure 5) with grain sizes up to 500 μm . The ash layers typically have a sharp lower boundary followed by normally-graded bedding consistent with primary deposition (Figure 3); importantly, these properties suggest that no significant post-depositional overthickening has occurred. Except for bioturbation at the top of some of the ash beds and occasional fluid escape structures, there are no sedimentary structures within the ash, indicating there has been no later redeposition.

The ash layers are variably consolidated and cemented. Hard, cemented layers were sampled as solid blocks using a hammer and prepared as 30 μm thin sections at the University of Oslo. Samples that were consolidated but not cemented were carved into suitable pieces with a knife, then dried at 80 $^{\circ}\text{C}$ and glued with epoxy, before being prepared as 30 μm thin sections. Unconsolidated samples were oven dried at 80 $^{\circ}\text{C}$, then dry-sieved into six individual size fractions: >2 mm, 1-2 mm, 500 μm -1 mm, 250-500 μm , 125-250 μm , and <125 μm . The four smallest fractions were arranged in quadrants and mounted in epoxy grain mounts, which were then polished to intersect the ash grains.

3.2 Electron Probe Microanalysis (EPMA)

Polished and carbon coated grain mounts were analysed on a Cameca SX100 microprobe equipped with 5 wavelength dispersive spectrometers (WDS) at the University of Cambridge, UK. Analyses were conducted with 15 kV accelerating voltage and a 10 nA beam current using a defocused beam size of 10 μm . Counting times were 5 s for K, Na, and Si; 10 s for Ca and Fe; 15 s for P, Al, and Cl; 20 s for Ti, Mn, and Mg; and 60 s for S. A combination of mineral and glass standards were used for primary calibration. Repeat analyses of secondary standards were used to monitor instrumental drift during and between analytical sessions. Analyses were conducted in two sessions, each

comprising several batches of samples. For the two sessions, basaltic glass reference material yielded average values for sulfur of 1462 ± 13 [1 σ] ppm and 1422 ± 34 [1 σ] ppm for standard VG2 (Juan de Fuca Ridge, NMNH 111240-52), and 125 ± 9 [1 σ] ppm and 126 ± 21 [1 σ] ppm for standard VGA99 (Mahaopuhi lava lake, Hawai'i, NMNH 113498-1), respectively, indicating that no corrections for instrumental drift between analytical sessions or sample batches was necessary. See Table S2 in the [Supplementary Material](#) for a full table of precision and accuracy of the reference material.

For each ash layer, we analysed the matrix glass compositions of between 20 and 24 separate particles, distributed between the four size fractions. Most analyses were from ash particles within the 125–250 μm fraction; the 10- μm beam size made it difficult to ensure a sufficient area of clear glass in the smallest fraction and the larger size fractions were mostly composed of partly consolidated ash aggregates and smectite clay.

3.3 Image acquisition and textural analysis

Polished and carbon-coated grain mounts were imaged using a Quanta-650F Field Emission Gun Scanning Electron Microscope (FEG-SEM) at the University of Cambridge, UK, operating in backscattered electron (BSE) mode. We acquired images of individual ash particles at high vacuum and a 15kV accelerating voltage. Composite images of the 125–250 μm quadrant of the grain mounts (8×8 tiles) were acquired using MAPS 2.0 software (FEI, Thermo-Fischer), with a three-point focus interpolation and a zoom of $\sim 350\times$.

We analysed the morphology and texture of the ash particles using backscattered SEM image maps, by manually counting and classifying 400 particles within a defined area of each sample image. The degree of post-depositional alteration of the Fur ashes prevented reliable automated shape analysis [Dellino and Volpe 1996; Liu et al. 2015]. During manual classification, the ash particles were first categorised into four groups: altered particles, microcrystalline grains, lithic particles, and silicate glass ('glassy') grains (Figure 6). Altered particles include grains where the primary textures are no longer recognisable due to alteration and devitrification. Microcrystalline grains contain plagioclase microlites within a silicate glass matrix. Lithic particles are holocrystalline, and likely sourced from syn-eruptive erosion of conduit walls and surrounding rock material. Silicate glass particles are crystal-free, and the main focus of this study. These were further classified into three different categories based on their vesicle texture and external morphology: dense, vesicular, and shards (Figure 6). Dense, glassy grains are characterised by a blocky morphology with angular fracture surfaces and poor internal vesicularity (≤ 20 area %; hereafter we simply use % for area %). Shards are characterised by concave edges that comprise >50 % of the

perimeter of the grain (interpreted as portions of bubble walls) with few internal vesicles. Vesicular grains are characterised by >20 % internal vesicularity. Vesicles are generally circular (in cross-section) with relatively thick bubble walls.

4 RESULTS

4.1 Matrix glass major element chemistry

The ashes are all tholeiitic basalts (Figure 7), with an average glass composition of 49.6 ± 1.6 (2 σ) wt% SiO₂, 14.8 ± 1.4 (2 σ) wt% FeO, 5.2 ± 1.1 (2 σ) wt% MgO, and 3.6 ± 0.6 (2 σ) wt% TiO₂ (Table 1, [Supplementary Material](#)).

The two ash layers from the negative series, Ashes –19 and –13, have slightly different glass chemistries than the positive series. Ash –19 has lower SiO₂ and higher TiO₂ than the positive series (Figure 8), while Ash –13 is slightly outside the main trend with a marginally more alkaline composition (Table S1, [Supplementary Material](#)) and a large variance in glass oxide concentrations (Figure 8). However, Ash –13 is also the most affected by alteration of the analysed ashes, as indicated by the overall physical appearance (Figure 6A).

The positive ash series shows a stronger trend for both CaO vs MgO and Al₂O₃ vs MgO (Figure 8). The correlation is particularly evident between MgO and CaO, with the linear regression characterised by an r^2 of 0.90. This relationship suggests that the stratigraphically highest layers (Ash +94, +114, and +118) are the most evolved, with low MgO, CaO, and Al₂O₃, and high K₂O. However, the linear trend is not a simple function of stratigraphic depth, as the higher MgO concentrations of Ashes +54 and +102 suggest they are more primitive than the stratigraphically lower layers +18 and +46 (Figure 8). The linear trend in matrix glass chemistry involving plagioclase-compatible elements suggests that plagioclase fractionation is at least partly controlling the range of glass (melt) compositions. In contrast, the correlation is very weak between S and K₂O ($r^2 < 0.05$), even for the more chemically homogenous positive ash series (Figure 8). This suggests sulfur concentrations are controlled by a process other than crystal fractionation.

4.2 Mineralogy and texture

Although the partly consolidated nature of the layers inhibited a detailed grain size analysis, we find that the distribution is skewed towards finer grain sizes. Most of the grains within size fractions >500 μm are composed of aggregates of smaller glass grains and fragments, while the <125 μm fraction was difficult to analyse due to the small size, and abundance of clay and devitrified grains. The 125–250 μm fraction was therefore selected for morphological analysis, as this provided most information.

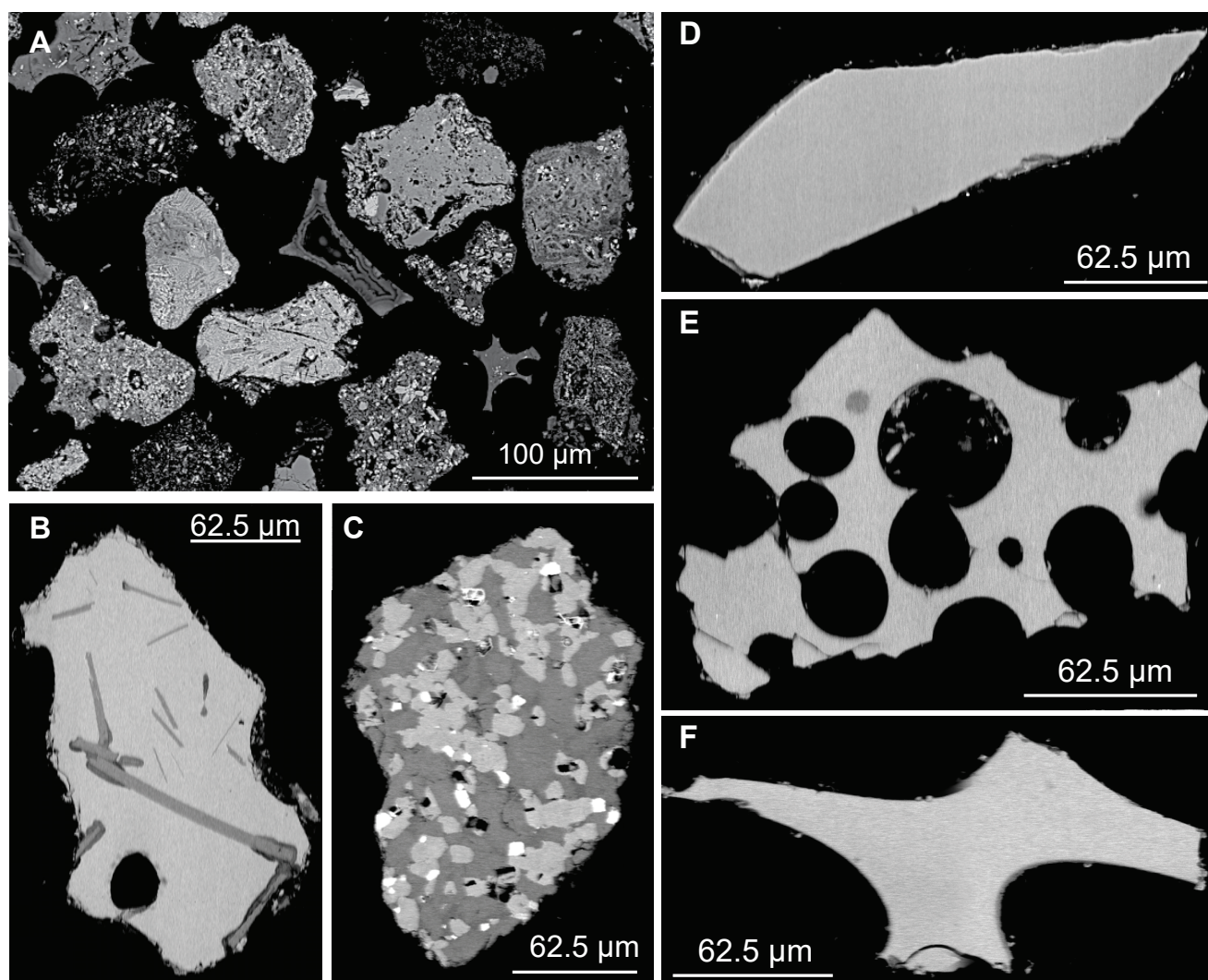


Figure 6: To the left, three examples of types of grains excluded from shape analysis in Figure 10. [A] Altered/devitrified glass from Ash -13. [B] Grain with microlites (Ash +46). [C] Lithic grain (Ash +36). To the right is shown an example of each type of glass texture. [D] Dense glass (Ash +1): blocky, poorly vesicular, [E] Vesicular glass: >20 % vesicularity, and [F] Shard (Ash +46).

Ash samples are predominantly composed of glass grains (altered or pristine; Figure 9). Altered and devitrified grains are common throughout; up to 75% of grains are altered in some layers, including Ashes +18 and +31 (Figure 9). The lowermost Ash -19 is the least altered sample, while the positive series shows an upward decrease in altered and devitrified glass grains (Figure 9). Microcrystalline and lithic particles are generally sparse and make up a negligible portion of the total particles, with only minor portions (<5 % combined) of lithics, microcrystalline glass, and crystals (Figure 9). The mineral assemblage is composed mostly of plagioclase and Fe-Ti oxides (mainly ilmenite), while pyroxenes and olivines are only observed occasionally.

Figure 10 shows how the texture and morphology of pristine glass grains (i.e. excluding altered grains) varies stratigraphically. The dense glassy fraction varies between 17 % and 52 %, with a minor overall

increase from Ash +18 upwards. Ash +1 deviates from this stratigraphic trend with a high fraction of dense glassy grains of about 50 %. The vesicular fraction varies between 12 % and 54 %. Although less distinct, it follows the dense fraction with an overall decrease up-section. The fraction of shards is more stable and shows no obvious stratigraphic variation, fluctuating between 18 % and 39 % (Figure 10).

4.3 Dissolved volatile contents

Average sulfur concentration for all analysed grains is 592 ± 381 (2 σ) ppm S, while all individual analyses vary between 171 and 1131 ppm S. Each individual analysed glass grain was also classified as dense, vesicular or shard, in order to investigate the relationship between morphology and residual volatiles in individual grains (Figure 11). Although the dense and vesicular

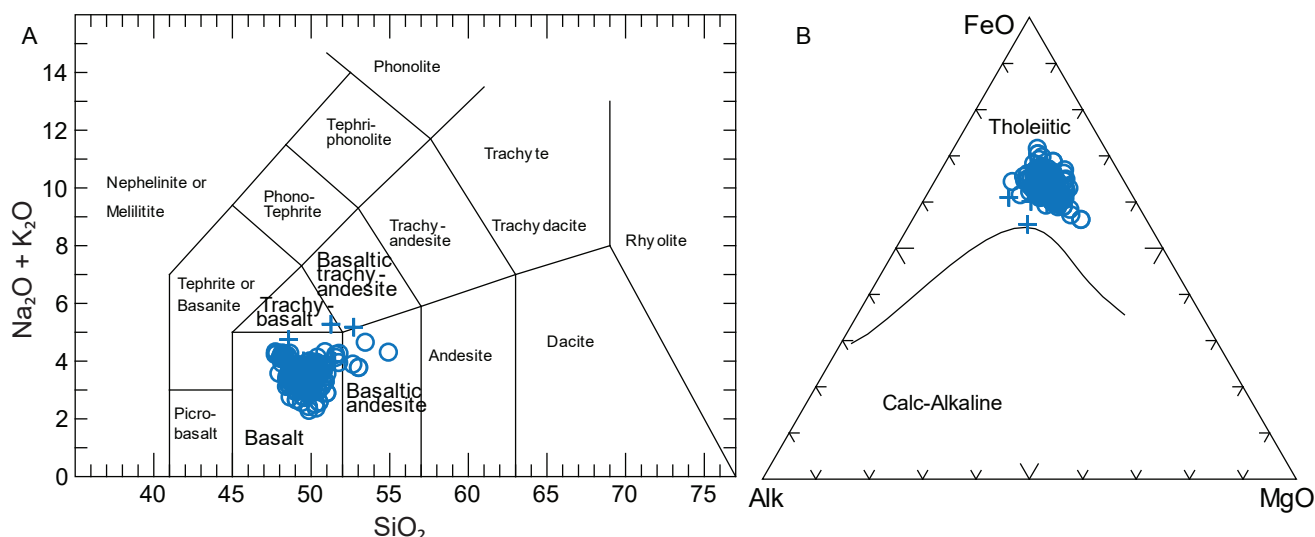


Figure 7: [A] Volatile-free total alkalis vs SiO₂ (TAS) diagram with the IUGS classification after Le Maitre et al. (1989). [B] Ternary AFM diagram plotting Alkalis (Na₂O+K₂O), FeO, and MgO. Tholeiitic and Calc-Alkaline boundary from Irvine and Baragar (1971). Both plots include all analyses, data in Table S1, [Supplementary Material](#).

fractions mostly overlap, there seems to be a slight tendency for higher sulfur concentrations within the dense fraction. The fraction of shards is under-represented as their narrow dimensions made them difficult to analyse.

Sulfur concentrations are plotted stratigraphically together with the textural analysis in [Figure 10](#), in order to evaluate the changes in residual sulfur over time. While the distribution of analyses within some samples are skewed towards higher or lower sulfur concentrations, most samples show a relatively normal distribution ([Figure 10](#)). Average sulfur concentrations (where averages are calculated from all analyses within an individual ash layer) show abundant stratigraphic variation between a minimum of 431 ± 191 (2 σ) ppm (Ash +90) and a maximum of 916 ± 120 (2 σ) ppm (Ash +118). There appears to be a slight overall stratigraphic increase in the mean sulfur concentrations from 476 ± 327 (2 σ) ppm S at the base (Ash -19) to 922 ± 239 (2 σ) ppm S at the top (Ash +118; [Figure 10](#)), although given the limitations of this dataset this observation is not statistically significant ($r^2_{\text{median}} = 0.12$; [Figure 10](#)).

The average chlorine concentration for all analyses is 139 ± 88 (2 σ) ppm Cl, with individual analyses varying between 43–371 ppm Cl. Mean chlorine concentrations for each ash sample vary between 88 ± 50 (2 σ) ppm (Ash +102) and 200 ± 77 (2 σ) ppm (Ash -19). Again, there is a strong division between the negative and positive ashes, with the negative Ashes -19 and -13 having comparatively higher chlorine concentrations than the positive series ([Figure 12](#)). There also seems to be a stronger linear correlation within the positive series, than when the negative series is included ([Figure 12](#)).

The opposite is true when chlorine is plotted as a function of K₂O ([Figure 12](#)), suggesting that the chlorine contents in the positive and negative ashes were initially different or controlled by different processes.

5 DISCUSSION

5.1 Eruption style

5.1.1 Morphological and textural evidence

Textural evidence shows that the proportions of dense glassy grains are generally high for a basaltic eruption throughout the stratigraphy. Most samples contain >30 % dense glassy grains, and in the uppermost 10 m of the stratigraphy (Ashes +46 to +118) there is consistently >40 %. Vesicles are macroscopic evidence of degassing, and typical vesicularities for basaltic tephra erupted in Hawaiian fountains generally range between 45 and 95 % [[Parcheta et al. 2013](#); [Porritt et al. 2012](#); [Stovall et al. 2012](#)]. Therefore, the high abundance of dense blocky glass morphologies with poor vesicularity suggests that degassing was arrested prematurely [[Cashman and Scheu 2015](#); [Graettinger et al. 2013](#); [Houghton and Gonnermann 2008](#)]. The blocky morphologies with brittle, angular surfaces and poor vesicularity are consistent with brittle fragmentation due to thermal fractures, rather than inertial fragmentation due to bubble expansion [[Houghton and Gonnermann 2008](#); [Mangan and Cashman 1996](#); [Morrissey et al. 2000](#)]. Pyroclastic textures and morphologies are often used to determine the fragmentation process during an eruption, primarily differentiating between “wet” hydromagmatic and “dry” magmatic eruptions, although

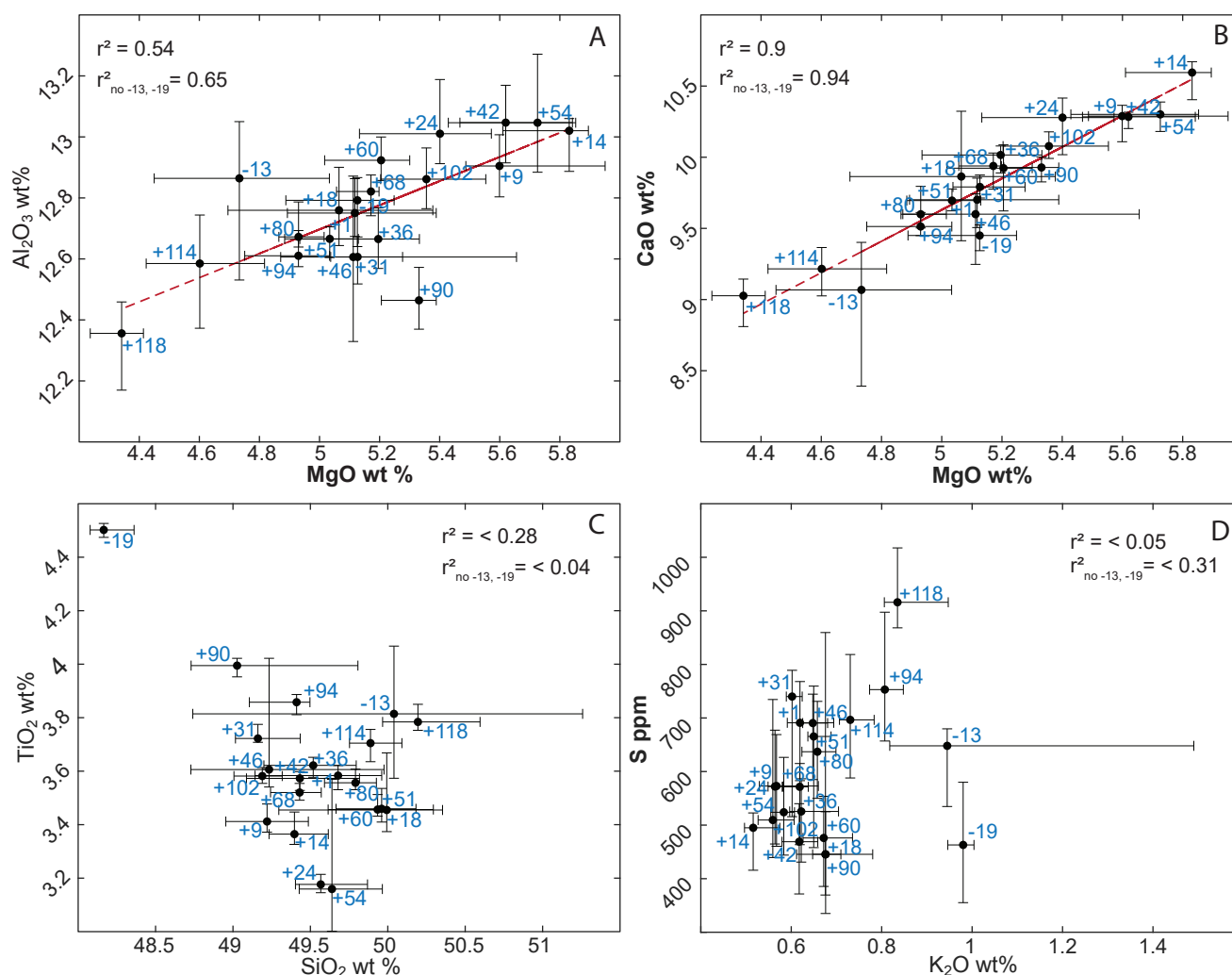


Figure 8: Major element crossplots. Each sample is labelled with ash number, with a dot showing median value and crosses indicating 25 and 75 quartile for X- and Y-axes. Red lines show linear regression for the median values, with the r^2 value noted both for all ashes, and for only the positive series. Data in Table S1, [Supplementary Material](#).

use of this morphological approach alone can be ambiguous [Mastin et al. 2004; White and Valentine 2016]. Volcanic particles resulting from brittle fragmentation due to magma-water interaction are generally characterised by dense and blocky fracture-bounded glass grains, with low but variable vesicularity [Büttner et al. 2002; Büttner et al. 1999; Dellino and Volpe 1996; Graettinger et al. 2013; Liu et al. 2017; Liu et al. 2015; Mastin et al. 2004; Morrissey et al. 2000]. Hydromagmatic explosions are associated with highly efficient fragmentation, and therefore the deposits are typically more fine-grained compared to basaltic “dry” magmatic deposits [Zimanowski et al. 2003]. Liu et al. [2015] found that the amount of dense glassy grains increased with decreasing grain size, and decreased with increasing distance to the source. The high abundance of dense glassy grains in the Fur ashes despite the long transport distance, coupled with the dominance of fine ash-sized material, strongly supports a hydromagmatic

origin for the ashes.

Highly explosive eruptions are generally associated with rapid magma ascent, such as during Plinian to ultra-Plinian eruptions [Cashman and Scheu 2015], but Plinian-type eruptions are rare for low viscosity basaltic magmas [Houghton and Gonnermann 2008]. The few examples in the geological record have been attributed to extensive syn-eruptive microlite crystallisation, such as the 122 BCE Mount Etna eruption [e.g. Sable et al. 2006] or the 1886 Tarawera eruption [e.g. Houghton et al. 2004]. The associated increase in melt viscosity will inhibit bubble expansion and promote rapid ascent and explosive fragmentation [Arzilli et al. 2019; Costantini et al. 2010; Szramek 2016]. However, the Fur ashes show relatively low crystallinities, with small fractions of both phenocrysts and microlites (Figure 9). This suggests that syn-eruptive crystallisation processes cannot be primarily responsible for the enhanced explosivity required to generate the Danish

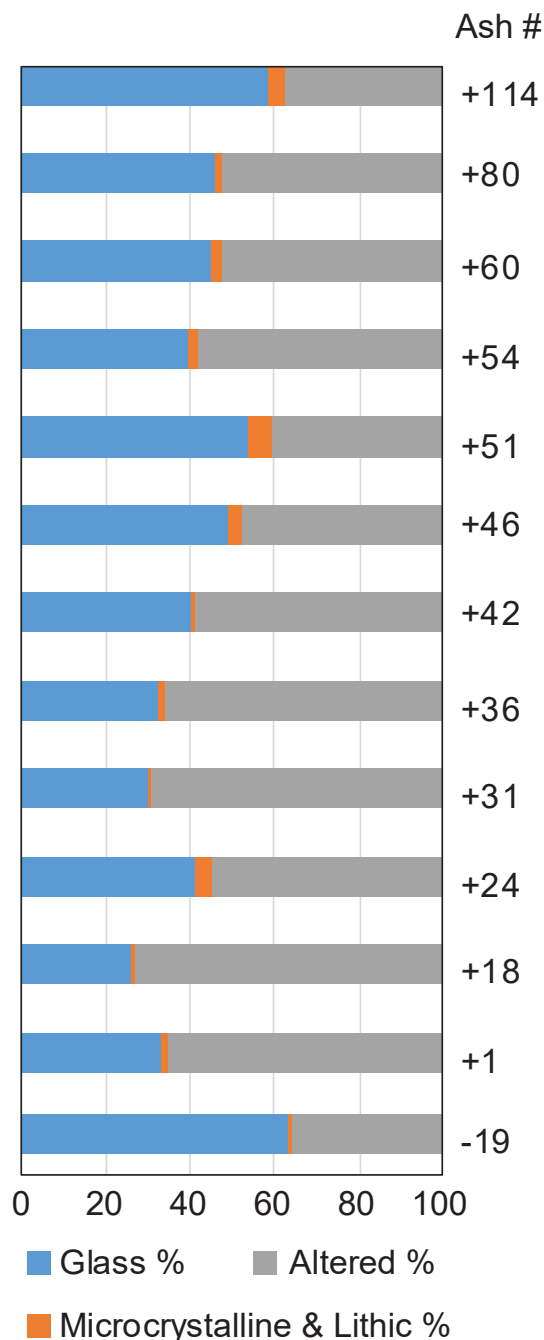


Figure 9: Graph showing relative amount (of total amount of grains counted in SEM images; e.g. Figure 6) of pristine glass, altered grains, and microcrystalline and lithics in each sample. Data in Table S4, [Supplementary Material](#).

ash layers.

While there is a high proportion (up to 50 %) of dense (probable) hydromagmatic glass grains, vesicular grains and shards are prevalent up-section indicating at least partial exsolution of a vapour phase (Figure 10). Importantly, however, the presence of vesicular glass grains does not exclude a hydromagmatic origin. Instead, it shows that magma-water interaction oc-

curred after the onset of decompression-driven exsolution. Several studies have demonstrated that solely using pyroclastic texture and morphology to differentiate between hydromagmatic and magmatic fragmentation, largely on the basis of vesicularity, may be too simplistic [Liu et al. 2017; White and Valentine 2016]. If the magma is quenched *during* rather than *prior to* vesiculation, then we would expect a spectrum of vesicularities and thus morphologies. In addition, the entire mass of erupted material will not be in direct contact with water during a hydromagmatic eruption, leading to variations in the resulting fragmented material [Houghton et al. 1996; Schipper and White 2016; White 1996]. The inner part of an eruption column can also be thermally insulated [e.g. Cole et al. 2001], leading to continued vesiculation and degassing during eruption. Overall, it is very likely, and even expected, that hydromagmatic erupted material will exhibit considerable variation in texture and morphology, even within a single eruption.

5.1.2 Evidence from volatile analyses

Additional diagnostic properties can be used to further elucidate the eruptive mechanisms and degassing histories of eruptions. Volatile analysis is an efficient tool to uncover the degassing history [Dixon et al. 1991; Edmonds 2008; Thórdarson et al. 2003; Thórdarson et al. 1996; Wallace and Edmonds 2011]. Elevated volatile concentrations in glass—above that expected in equilibrium with atmospheric pressures—indicate quenching before the melt is fully degassed. This would be most likely attributable to quenching under elevated pressures, such as during subaqueous or subglacial magma-water interactions [Dixon et al. 2002; Liu et al. 2018; Mastin et al. 2004; Métrich et al. 1991; Óladóttir et al. 2007]. Although most quantitative assessments of degassing histories have focussed on CO₂ and H₂O exsolution [e.g. Newman and Lowenstern 2002], sulfur in glass is more sensitive to small variations in quench pressure at shallow depths due to its greater solubility compared to CO₂ and H₂O in tholeiitic basaltic melts. However, there are many possible factors affecting the residual sulfur concentrations of volcanic glass [Mavrogenes and O'Neill 1999; Wallace and Carmichael 1992; Wallace and Edmonds 2011], and it does not necessarily reflect only variations in hydromagmatic activity. Here, we consider the various processes that could produce the observed trends in sulfur content.

- (a) Fractionation: In the absence of degassing or formation of a sulfur-rich phase (e.g. sulfide minerals), sulfur should behave like an incompatible element and increase with increasing magmatic fractionation [Wallace and Edmonds 2011]. A positive correlation between sulfur and K₂O would therefore indicate that the sulfur concentrations preserved in matrix glasses are controlled by fractionation rather than degassing. For the Fur ash samples there is a poor correlation between S and

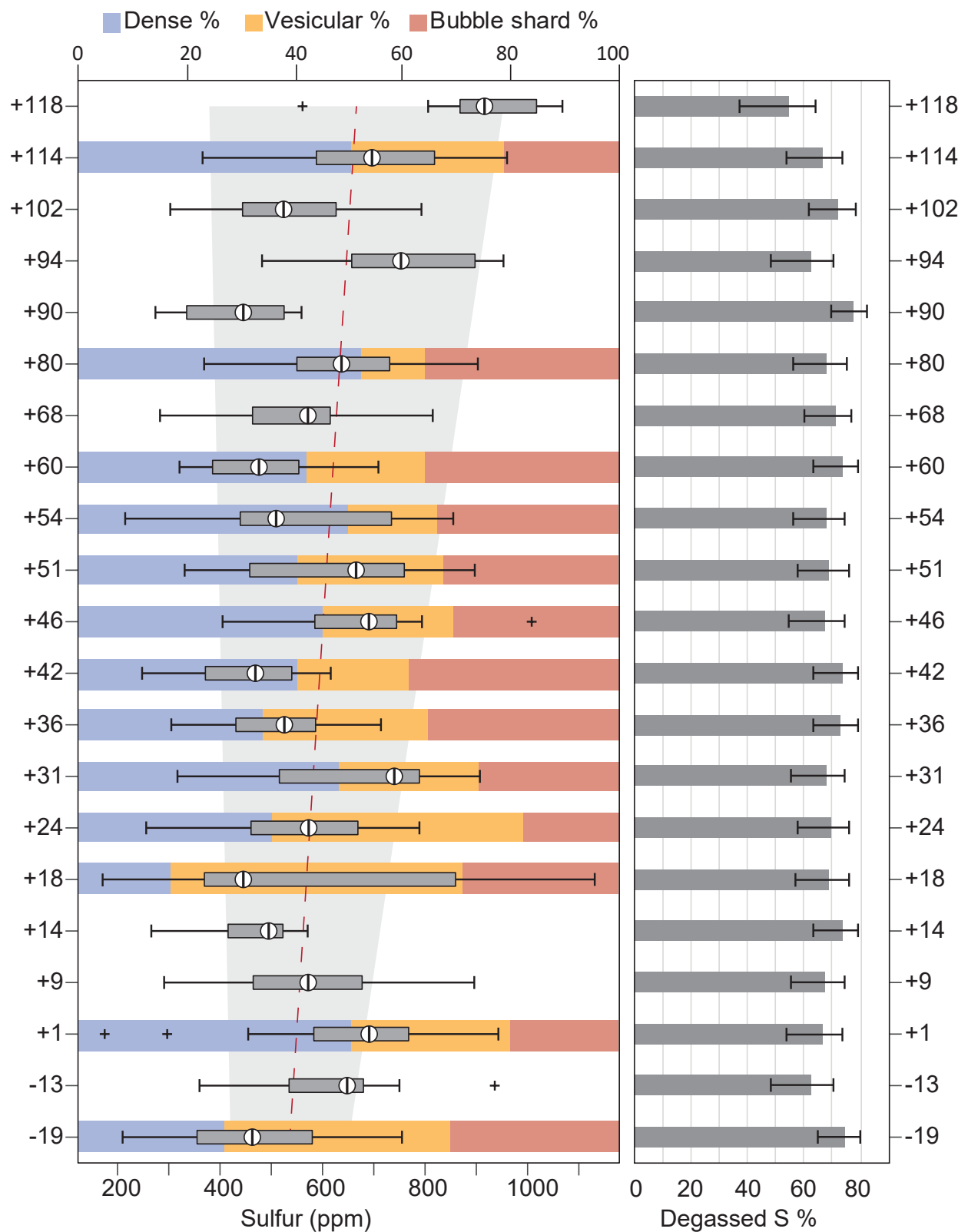


Figure 10: To the left: Bar chart of the morphological distribution and boxplots of sulfur concentrations, both stratigraphically sorted. In the boxplot, each box indicates the 25th and 75th percentiles of the ash sample, with the circle and line inside indicating the median value. Whiskers indicate 0.05 and 95 percentiles, and black crosses are outliers. The red line shows the linear regression ($r^2_{\text{median}} = 0.12$) of the median sulfur values, with grey band indicating 95 % confidence intervals. To the right: Percent degassed S, the calculation is discussed in detail in [Section 5.2.1](#). Data in Tables S1, S3, and S4, [Supplementary Material](#).

K₂O (Figure 8D), suggesting fractionation processes are not controlling sulfur concentrations.

- (b) Post-fragmentation degassing: Residual sulfur concentrations could also have been affected by post fragmentation degassing, depending on the time between fragmentation and quenching. However, this depends strongly on the cooling rate of individual glass grains [Lloyd et al. 2012]. Cooling duration is dependent on clast size and distance from the exterior surface [e.g. Mastin 2007]. Fast cooling rates of $10^{3.9}$ to $10^{5.1}$ K s⁻¹ is determined for 0.5 mm angular hyaloclastite particles [Helo et al. 2013], similar to that calculated for cooling of outer surfaces under water spray impact [Mastin 2007]. Glass grains analysed from the Fur ashes are all <500 µm, and most within the 125–250 µm fraction, suggesting they quenched rapidly and that significant post-fragmentation degassing of sulfur is unlikely.

Assuming that the range of residual sulfur concentrations in the Fur ash layers is indeed indicative of differences in quench pressure, we now consider what threshold separates hydromagmatic from magmatic erupted glass. A study of Hawaiian basalts found that the average dissolved sulfur of partially degassed hydromagmatic tephra was about 330 ppm S, compared to 100–150 ppm S expected for fully degassed Hawaiian tephra [Mastin et al. 2004]. However, Hawaiian basalts are generally lower in iron than typical Icelandic basalts, resulting in lower sulfur solubilities and subsequently lower initial sulfur concentrations [Liu et al. 2018; Wallace and Carmichael 1992]. The sulfur content expected for fully degassed Icelandic melts is therefore slightly higher, varying between 300–500 ppm depending on iron content [Thórdarson et al. 2001]. In order to interpret the Fur ash layers, some assumptions have to be made regarding their similarity to modern volcanic systems. Several previous studies have remarked on the similarity between the Fur ashes and Palaeogene and present-day

Icelandic basalts [Larsen et al. 2003; Morton and Knox 1990; Pedersen et al. 1975]. Morton and Knox [1990] noted how the Danish ashes resemble Icelandic tholeiites in the Th-Hf-Ta diagram of Wood [1980], both plotting within the E-type MORB and tholeiitic within-plate basalt field. Several studies have presented a summary of Icelandic glass volatile contents in the form of a S vs TiO₂/FeO scatter plot (Figure 13). This clearly shows (a) the progressive decrease in glass sulfur content from melt inclusions, to hydromagmatic glasses, to magmatic glasses, and finally to lava selvages, and (b) the effect of Fe on the initial sulfur content [Liu et al. 2018; Óladóttir et al. 2007; Thórdarson et al. 2001; Thórdarson et al. 2003]. The Fur ashes plot well within the typical TiO₂/FeO values for modern Icelandic basalts (Figure 13), with intermediate TiO₂ concentrations close to those of Laki [Thórdarson et al. 1996], Grímsvötn [Sigmarsson et al. 2013], and Surtsey [Schipper et al. 2015]. The median sulfur concentrations of the Fur ashes vary between ~445–753 ppm S, which overlap with both the hydromagmatic tephra of Surtsey and Grímsvötn, and the magmatic eruptions of Laki (Figure 13).

Chlorine concentrations are less diagnostic of degassing processes, as Cl is soluble until low pressures in basaltic magma [e.g. Sigvaldason and Óskarsson 1976]. Our analyses show that chlorine concentrations are quite variable (Figure 12); which may reflect some shallow post-fragmentation degassing. Chlorine is also an incompatible element, and has been shown to correlate strongly with K₂O [Davis et al. 2003; Sigvaldason and Óskarsson 1976], which we also see in our data (Figure 12). Previous studies on Icelandic tephtras have shown that the Cl contents of magmatic and hydromagmatic samples overlap, with the magmatic glasses extending to slightly lower Cl concentrations indicating partial degassing [Liu et al. 2018]. Liu et al. [2018] found that Icelandic hydromagmatic glasses generally had chlorine content above 140 ppm Cl, while a study of Hawaiian basalts found that subaerial basalts varied between 64 and 119 ppm Cl and submarine from 70 to 560 ppm Cl [Davis et al. 2003]. The positive series ashes have median values from about 80–170 ppm Cl, and correlate moderately well with sulfur contents particularly at higher sulfur concentrations (Figure 12). This may reflect some partial degassing potentially due to hydromagmatic activity. Ashes –19 and –13 have higher chlorine contents than any of the positive ashes, yet below average sulfur contents indicate that this is not due to arrested degassing. We show in Figure 7 that these two ashes have a different chemistry to the positive ash series. Indeed, they are older and likely erupted prior to the main rift phase, and therefore likely have different equilibrium Cl concentrations, though the high chlorine contents could also be due to some crustal contamination [e.g. Davis et al. 2003].

Considering variations in sulfur and morphology to

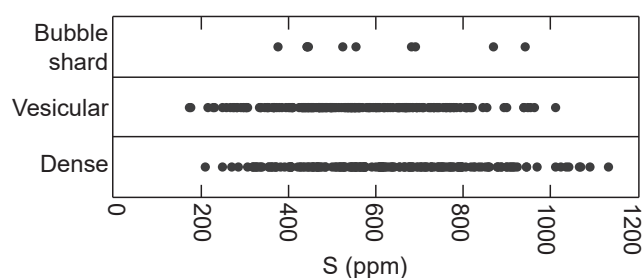


Figure 11: Sulfur concentration as a function of volcanic glass morphology. Diagram contains analyses of 10 Bubble shards, 192 Vesicular glass grains, and 189 Dense glass grains.

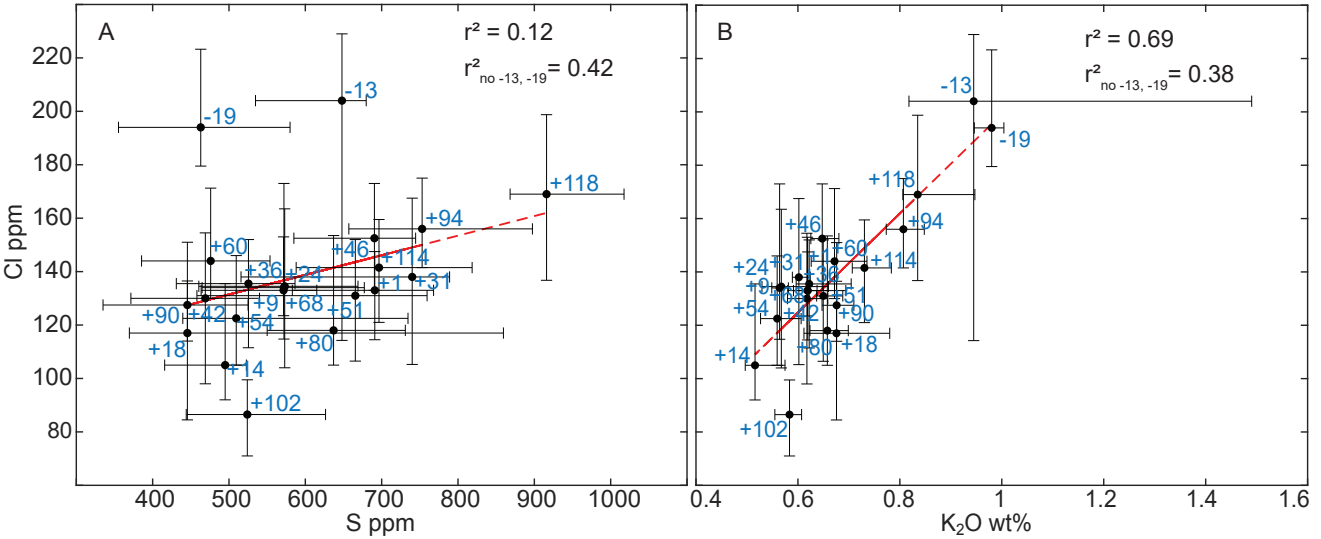


Figure 12: [A] Plot of chlorine as a function of sulfur. [B] Plot of chlorine as a function of K₂O. Each sample is labelled with ash number, with a dot showing median value and crosses indicating 25 and 75 quartile for X- and Y-axis. Red lines show linear regression for the median values. The r^2 value of the regression is noted both for all ashes, and for only the positive series. Data in Table S1, [Supplementary Material](#).

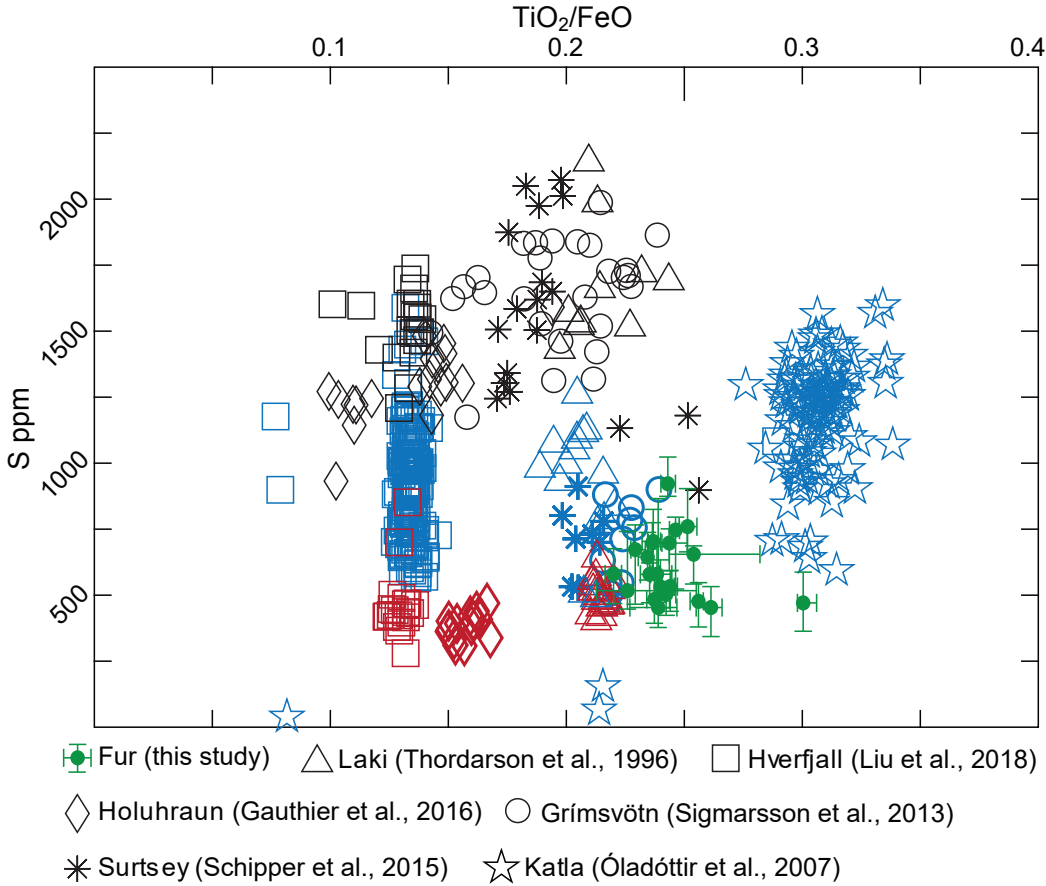


Figure 13: Compilation of sulfur concentrations in Icelandic basalts as a function of TiO₂/FeO. Different systems are represented, with melt inclusions in black, magmatic matrix glass in red, and hydromagmatic matrix glass in blue. Fur ashes are shown as green symbols.

gether (Figure 10), there seems to be a clear positive co-variation between the fraction of dense glassy grains and the median residual sulfur concentrations in glass. This suggests that residual sulfur concentrations are a function of the extent of degassing, where the least degassed melts are also the least vesicular, and vice versa. This supports the conclusions drawn from the morphological evidence that the Fur ash sequence quenched under varying pressures higher than 1 atm.

5.2 Total sulfur degassing

5.2.1 Relative degree of sulfur degassing

The residual sulfur in quenched silicate glasses can be used to indicate the total amount of sulfur degassing, if the initial sulfur concentration of the melt is known [Devine et al. 1984]. Melt inclusions in mineral phenocrysts are an ideal source to measure the initial sulfur concentration [Davis et al. 2017; Métrich and Wallace 2008; Thórdarson et al. 2003]. Unfortunately, no viable melt inclusions have been identified in the Fur ashes. Instead, we estimate the un-degassed sulfur content of the melt using theoretical models of the sulfur concentration at sulfide saturation [SCSS; Blake et al. 2010; Smythe et al. 2017; Wallace and Carmichael 1992]. A major assumption when applying SCSS models is that the magma was sulfide-saturated. Both MORB and Icelandic melts are thought to be sulfide-saturated for much of their ascent path [Edmonds and Wallace 2017]. Considering the geochemical similarity between Icelandic melts and the Fur ashes (Figure 13), we assume that the Fur ashes were similarly sulfide-saturated.

There are several available models for calculating the SCSS, most based on a linear function of sulfur and iron concentrations of the silicate melt [Blake et al. 2010; Wallace and Carmichael 1992]. This is largely due to the important role of iron in enhancing sulfur solubility by combining with S^{2-} to form an immiscible Fe-S-O sulfide liquid phase [Mavrogenes and O'Neill 1999; Wykes et al. 2015]. However, recent studies demonstrate that at fixed temperature, pressure, and silicate melt compositions, the SCSS also depends largely on the composition of the immiscible FeS-NiS-CuS_{0.5} sulfide liquid itself [Patten et al. 2013; Smythe et al. 2017]. Consequently, the relative input of Fe-Ni-Cu needs to be taken into account, and we therefore apply the SCSS model of Smythe et al. [2017]. In the absence of a known sulfide melt composition for the Fur ashes, we apply the average sulfide globule chemistry from the Northern Mid-Atlantic Ridge [Keith et al. 2017] as the closest available analogue for the NAIP. At temperatures >1100 °C and at pressures about 0.1 GPa, the sulfide melt is typically still a liquid phase “pre-crystallisation” [Patten et al. 2013]. We subsequently apply a pressure of 0.1 GPa, and a temperature of 1130 °C calculated with the glass/liquid thermometer

(Equation 1) of Montierth et al. [1995]:

$$T(^{\circ}\text{C}) = 23.0\text{MgO}_{\text{liq}} + 1012^{\circ}\text{C} \quad (1)$$

where MgO_{liq} is the average MgO content for Fur glasses of 5.14 wt % (Tables S1 and S3, Supplementary Material).

Figure 14 shows the modelled SCSS for each Fur ash sample plotted according to its average iron concentration. Using these values for the SCSS, which represent the theoretical un-degassed sulfur content of the melt, the total amount of sulfur degassed can be estimated by calculating the difference between the initial and the residual glass sulfur concentrations for each Fur ash layer (Figure 10). The ashes record total amounts of degassing between 55–80 % of the initial sulfur content, with the least sulfur degassing in the uppermost Ash +118 (Figure 10). Changes in pressure have a limited effect on the modelled SCSS, and within the tested temperature range of 1000–1500 °C the total degassing vary with no more than about ± 20 % (Table S3, Supplementary Material). Therefore, even if the NAIP source had anomalously high magma temperatures, the total degassing is unlikely to be more than 85 % of the initial sulfur content for any given sample (Table S3, Supplementary Material).

Comparing to other basaltic systems, Mastin et al. [2004] documented a similar 70–80 % degassing (relative to the initial sulfur content) in hydro-magmatic tephra from the Kilauea Volcano (Hawai'i), attributed to partial degassing due to quenching at higher than atmospheric pressures. Partial degassing was also observed in several Icelandic hydromagmatic systems, such as a 17–70 % degassing of the pre-eruptive sulfur content from the Hverfjall Fires [Liu et al. 2018] and the 18–75 % degassing from the subglacial 1783 Grímsvötn eruption [Métrich et al. 1991]. Highly variable volatile loss appears to be a general feature of hydromagmatic glasses, and may reflect variable degrees of magma-water interaction and quenching rates [e.g. White and Valentine 2016]. Overall, the consistent partial degassing of the Fur ashes is a strong indicator that the entire section is the result of hydromagmatic activity.

5.2.2 Estimated total mass of emitted SO_2

Using the modelled values for initial sulfur concentrations, we have also estimated the total mass of sulfur emitted into the atmosphere from each eruption. We do not consider the issue of excess sulfur, as this problem is negligible or absent in Hawaiian and Icelandic basaltic magmas [Sharma et al. 2004]. We calculate the total mass by taking the difference between initial and residual mass of sulfur and multiplying by the erupted volume, following the approach of Thórdarson et al. [1996] (Equation 2):

$$m_t = m_i - m_r = (V\rho v_{\text{SO}_2,i}) - (V\rho v_{\text{SO}_2,r}) \quad (2)$$

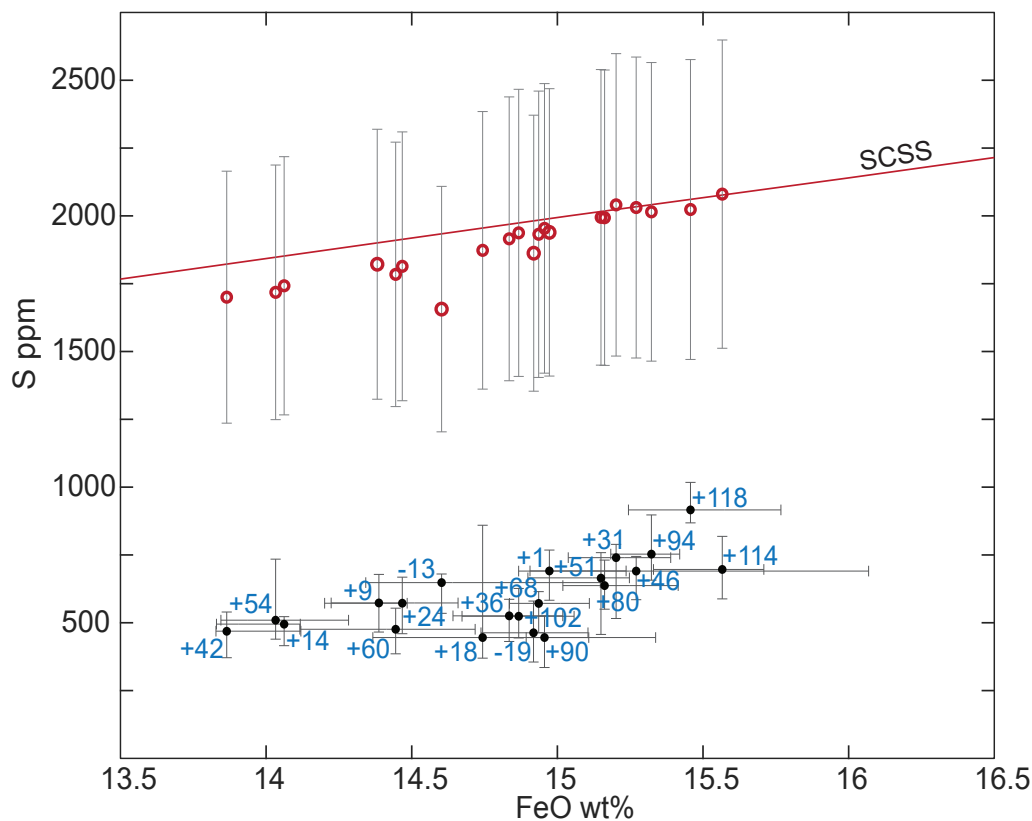


Figure 14: Sulfur concentrations (ppm) of the Fur ashes plotted as a function of FeO (wt %). Each sample is labelled with ash number, with a dot showing average value and crosses indicating 25 and 75 quantile for X- and Y-axis. Red circles indicate the modelled ideal value for SCSS for a FeS-NiS-CuS_{0.5} saturated MORB melt [Smythe et al. 2017]. Modelled using an average Northern Mid-Atlantic Ridge (NMAR) sulfide liquid composition [Keith et al. 2017], average silicate composition for each Fur ash layer, temperature of 1130 °C, and pressure 0.1 GPa. Vertical lines indicate error (1 σ) for each modelled SCSS. Data in Table S3, [Supplementary Material](#).

where m_t is the total emitted mass of SO₂, m_i the initial mass of SO₂, m_r the residual mass of SO₂, V the eruptive volume (DRE) of NAIP tephra, ρ the magma density (2750 kg m⁻³), and v_{SO_2} the initial (i) and residual (r) mass fraction of SO₂. We use the average content of sulfur for the whole dataset; converted to SO₂, which is the species assumed to be present in the magma. This amounts to a modelled initial sulfur content of 0.38 ± 0.10 wt% SO₂, and a measured residual sulfur content of 0.12 ± 0.04 wt% SO₂. The rhyolitic Ash +19 is one of the thickest (20 cm) and most widely distributed ashes, and has an estimated total volume of 1200 km³ [DRE; Egger and Brückl 2006]. Although this ash was rhyolitic and potentially more explosive, basaltic layers have been traced as far as the rhyolitic suggesting a similar distribution. We define Ash +19 as the upper limit for erupted volume, and apply a potential range of eruptive volumes (V) for each eruption of 100–1000 km³ (DRE). However, calculating DRE equivalents is complicated by the competing effects of vesicularity and post-depositional compaction, so these values need to be treated carefully. Keeping in mind the many uncertainties with these calculations,

this gives us a potential range of 0.72 ± 0.18 Gt to 7.2 ± 1.8 Gt SO₂ for each eruption. Using a similar approach, Blake et al. [2010] estimated a total yield of the Grande Ronde basalts of the Columbia River Basalts (a smaller and more recent LIP than the NAIP) of 1000 Gt delivered in intermittent bursts, each between <1 and 30 Gt SO₂. Considering that these estimates are from fully-degassed flood basalts, in contrast to the only partially degassed ashes of the NAIP, our results seem comparable to previous estimates.

On average over the past decade, the volcanic SO₂ sources consistently detected from space have discharged a total of ~ 63 kt d⁻¹ SO₂ during passive degassing, or $\sim 23 \pm 2$ Mt yr⁻¹ [Carn et al. 2017]. The estimated sulfur emissions from the NAIP would therefore significantly increase the total atmospheric sulfur content, with potentially large environmental consequences. A recent study also from the Fur Formation in Denmark has documented a potential sea surface temperature cooling using the organic palaeothermometer TEX₈₆ [Stokke et al. 2020]. Post-PETM cool conditions were initiated just below Ash -19 and persisted to varying degrees throughout the eruptions of the main

phase of explosive basaltic volcanism, raising the question whether there was a causal relationship. A modelling study of the Roza member of the Columbia River Basalts found that a decade long eruption with annual SO₂ emissions of 1.2 Gt could lead to a –3.0 K temperature decrease [Schmidt et al. 2016]. Considering the magnitude of the Fur Formation ashes and the estimated sulfur emissions up to 1.8 Gt per eruption transported to the stratosphere, it is likely that these eruptions would have instigated a powerful surface cooling [Jones et al. 2005]. However, it is important to stress that there are a lot of assumptions and uncertainties regarding these estimates, and they should therefore be interpreted with caution.

5.3 Eruption depth and implications for the NAIP

We have shown that the sulfur content preserved in Fur glasses is controlled by variable amounts of degassing, which can be explained by arrested volatile loss due to magma-water interaction and quenching. Most of the ash layers are therefore likely erupted during hydromagmatic activity. In addition, we have shown that there is stratigraphic variation with a potential minor overall upward increase in the proportion of dense glassy grains and in the total residual sulfur content (Figure 10). Assuming equilibrium degassing, and if the extent of degassing varies as a function of quench pressure, then these variations may reflect changes in the eruption depth [e.g. Moore and Schilling 1973]. However, the potential for disequilibrium degassing due to rapid ascent of clasts mean that other processes associated with thermal gradients in the eruptive jet could also explain these variations. During the 1963 eruption of Surtsey, uprush jets maintained hot magmatic temperatures in the core while cooling inwards from the margins [Moore 1985; Þórarinnsson 1967]. Differential clast quenching rates under these conditions would produce a range of residual glass S contents, even if the depth of magma-water interaction remained constant [Mastin 2007; Mastin et al. 2004]. Changes in the size or speed of eruptive jets through time, and thus changes in the extent of equilibrium versus disequilibrium degassing, could therefore also account for the stratigraphic variations in residual sulfur content observed in the Danish ash series. Though, keep in mind it is difficult to assess the importance of this effect for the Fur ashes, given the extreme differences in scale and intensity between these eruptions and Surtseyan events.

Several studies have shown a link between the residual volatile content and depth of magma-water interaction [Davis et al. 2003; Liu et al. 2018; Moore and Schilling 1973; Unni and Schilling 1978]. Even accounting for the likelihood of some degree of disequilibrium degassing, a quantitative assessment of volatile saturation pressures can provide an upper bound on eruption depth when combined with an appropriate

pressure gradient. Hydromagmatic activity can occur deep in the vent, in which case the residual volatiles would reflect both hydrostatic and lithostatic overpressure. If magma-water interaction involves a ground-water incursions into the volcanic conduit, then lithic particles are typically a large proportion of the erupted material due to explosive disruption and evacuation of subsurface country rock [Lorenz 1986; Morrissey et al. 2000]. The very low fraction of lithic clasts within the Fur ashes (<1 %; Figure 9) supports a shallow magma-water interaction involving surface water, rather than deep groundwater [e.g. Graettinger et al. 2013].

Quantitative assessments of eruption depth relies on thermodynamic modelling of residual H₂O and CO₂ contents, for which pressure- and temperature-dependent solubilities are well-constrained [Newman and Lowenstern 2002; Witham et al. 2012]. This multi-species approach was applied to the Hverfjall lavas in Iceland, where hydrostatic pressures corresponding to an average fragmentation depth of 210 ± 30 m (water depth) were estimated based on a combination of H₂O, CO₂, and S [Liu et al. 2018]. Due to a lack of H₂O or CO₂ measurements, we instead present a qualitative comparison to similar volcanic systems to infer an upper bound fragmentation (quench) depth. The Fur ashes have slightly lower sulfur concentrations than seen at Hverfjall (Figure 13), suggesting a potentially shallower water depth. Dredged basalts along the Reykjanes Ridge show that at a depths <200 m the sulfur concentrations decrease from 843 ppm S down to a minimum of 425 ppm S at 43 m depth [Moore and Schilling 1973]. This suggests that sulfur exsolution takes place very rapidly at low pressures in tholeiitic Icelandic basalts. Vesiculation is also increasingly variable with decreasing pressure, with some samples showing up to 50 % vesicularity at depths <200 m [Moore and Schilling 1973]. A similar shallow-marine subaqueous environment (water depths <200 m)—with variable vesiculation at the point of magma-water interaction and variation in quench rate following fragmentation—would together explain the range of elevated glass S contents and ash textures that we observe.

A shallow-marine subaqueous environment suggest that the ashes erupted during the opening of the northeast Atlantic Ocean. Gradual submergence of the NAIP through time is documented on both sides of the opening northeast Atlantic rift [Á Hórn et al. 2017]. Massive hyaloclastites within seaward dipping reflectors on the Vøring margin [Abdelmalak et al. 2016] (Figure 1) and offshore of the Faroe Islands [Jerram et al. 2009] reflect a gradual transition from subaerial to submarine basalt flows. The age of the positive ash series deposits (<55.6 to >54.6 Ma) also suggest that the Danish ashes coincide with the start of seafloor spreading, and post-date much of the voluminous flood basalts in East Greenland and the Faroes [Saunders 2016; Wilkinson et al. 2017]. The G10ka tephra series from Grímsvötn

in Iceland demonstrates that wide distribution of hydromagmatic ash (in this case subglacial) is plausible [Óladóttir et al. 2020]. However, while Larsen et al. [2003] suggest that the Danish ashes are sourced from somewhere within the opening rift (Figure 1), it is not possible to locate the exact source within this rift system. We still speculate that both the initiation and the eventual termination of explosive volcanic activity could at least partly be a result of a local marine transgression during seafloor spreading and opening of the northeast Atlantic Ocean. Indeed, the subtle increase in residual volatile contents (reduced degassing) and high fraction of dense glass grains toward the top of the stratigraphy (Figure 9) are consistent, at least conceptually, with gradually increasing overlying pressure arresting volatile degassing and thus suppressing explosive magma-water interaction. Evolving eruptive style with changing confining pressure has been reported elsewhere. Although on a much smaller scale, a reduction in overlying hydrostatic pressure was invoked to explain transitions from pillow basalts into voluminous basaltic tephra at Askja volcano in Iceland [Graettinger et al. 2013] and during the early stages of the 1963 Surtsey eruption [Moore 1985], with no evidence for changing geochemistry or magma flux.

Previous studies have argued that the early Eocene shift to explosive volcanic activity during the emplacement of the NAIP was caused primarily by an increased magma flux [e.g. Saunders 2016]. Substantial magma fluxes would no doubt be necessary to produce the observed volumes and large distribution of the ashes, but magmatic fluxes were already exceptionally high during the late Paleocene emplacement of the continental flood basalts in East Greenland [Larsen and Tegner 2006; Wotzlaw et al. 2012]. We argue that the shift to an overall explosive volcanic environment could have been caused by a change to a subaqueous hydromagmatic environment with no need for a sudden increase in magma flux. We hypothesize that large-scale magma-water interactions would in fact be essential to achieve the unusually wide distribution of tholeiitic basaltic tephra observed in our study.

6 CONCLUSION

In this study we analysed the matrix glass in basaltic ash layers deposited in early Eocene sedimentary strata in Denmark. These ashes were sourced from the North Atlantic Igneous Province during the opening of the northeast Atlantic Ocean. The thickness and form of the ash layers, coupled with the large distances from possible source volcanoes suggest they erupted during explosive eruptions of unusually large magnitude and intensity, especially for basaltic magma compositions. The exceptional preservation of these layers provides a unique insight into volcanic processes that occur during plate tectonic breakup and LIP activity. Image anal-

ysis of internal texture and external morphology show that the ashes are composed of 25–65 % well-preserved glass grains, with a minor amount (<5 %) of microcrystalline and lithic grains. The pristine glass fraction is dominated by dense, low vesicularity glass grains, relative to vesicular glass and shards. Geochemical analyses of pristine matrix glasses show an overall correlation between elevated residual sulfur concentrations and high fraction of dense glassy grains. Using initial sulfur concentrations calculated using theoretical models of sulfur content at sulfide saturation (SCSS), we find that these glasses are only partly degassed in sulfur (55–80 %). We also find that sulfur degassing during eruption of these ashes could potentially have led to emission of 0.72 ± 0.18 to 7.2 ± 1.8 Gt SO₂ for each eruption, with potentially large climatic consequences.

These data indicate that the glass quenched at pressures greater than expected for equilibration under atmospheric conditions, such as under hydrostatic pressure. Together, the fine grain size, dominance of dense angular ash morphologies, and elevated glass volatile contents suggest a hydromagmatic origin for the Danish ashes. Explosive hydromagmatic activity enhanced fine fragmentation and provided the high rates of heat transfer required to promote widespread distribution of large ash volumes. By comparing the residual sulfur concentrations with other basaltic hydromagmatic eruptions, we suggest that the eruptions likely occurred in a shallow marine subaqueous environment (<200 m water depth) during the opening of the northeast Atlantic Ocean. We propose that explosive hydromagmatic activity was the main driver of these unusually large explosive basaltic eruptions.

ACKNOWLEDGEMENTS

Penny E. Wieser, Dr. Iris Buisman, Bo Schultz, Gauti Trygvason Eliassen, Egon Nørmark, Dr. Henrik Svensen, and Dr. Sverre Planke are all warmly thanked for their assistance. Dr. John Stevenson is thanked for modelling plume height and producing Figure 4. We thank Dr. Larry Mastin and Dr. Karoly Nemeth for detailed and constructive reviews, and the editor Dr. Jamie Farquharson for efficient handling of this manuscript. This project was supported by the Research Council of Norway's funding schemes "Unge Forskертallenter" project number 263000 (project Ashlantic) and "Centres of Excellence" project number 223272. E.J.L. acknowledges support from a Leverhulme Early Career Fellowship.

AUTHOR CONTRIBUTIONS

Ella W. Stokke and Morgan T. Jones collected field data, while Ella W. Stokke and Emma J. Liu collected EMPA and SEM data. Ella W. Stokke conducted the grain counting, as well as modelling, calculations, and

statistical analyses of the analytical data. Morgan T. Jones and Emma J. Liu contributed in supervisory roles. All authors contributed to discussing and interpreting the data, and writing of the paper.

DATA AVAILABILITY

Supplementary Material including four tables is available alongside the online version of this article. Table S1: all EMPA analyses; Table S2: calculated precision and accuracy for secondary standards; Table S3: modelled values for SCSS; Table S4: summarised shape analysis.

COPYRIGHT NOTICE

© The Author(s) 2020. This article is distributed under the terms of the [Creative Commons Attribution 4.0 International License](#), which permits unrestricted use, distribution, and reproduction in any medium, provided you give appropriate credit to the original author(s) and the source, provide a link to the Creative Commons license, and indicate if changes were made.

REFERENCES

- Á Horni, J., J. R. Hopper, A. Blischke, W. H. Geisler, M. Stewart, K. McDermott, M. Judge, Ö. Erlendsson, and U. Ártíng (2017). “Regional distribution of volcanism within the North Atlantic Igneous Province”. *Geological Society, London, Special Publications* 447.1, pp. 105–125. DOI: [10.1144/sp447.18](#).
- Abdelmalak, M. M., S. Planke, J. I. Faleide, D. A. Jerram, D. Zastrozhnov, S. Eide, and R. Myklebust (2016). “The development of volcanic sequences at rifted margins: New insights from the structure and morphology of the Vøring Escarpment, mid-Norwegian Margin”. *Journal of Geophysical Research: Solid Earth* 121.7, pp. 5212–5236. DOI: [10.1002/2015jb012788](#).
- Arzilli, F. et al. (2019). “Magma fragmentation in highly explosive basaltic eruptions induced by rapid crystallization”. *Nature Geoscience* 12.12, pp. 1023–1028. DOI: [10.1038/s41561-019-0468-6](#).
- Baines, P. G. and R. S. J. Sparks (2005). “Dynamics of giant volcanic ash clouds from supervolcanic eruptions”. *Geophysical Research Letters* 32.24. DOI: [10.1029/2005gl024597](#).
- Baines, P. G., M. T. Jones, and R. S. J. Sparks (2008). “The variation of large-magnitude volcanic ash cloud formation with source latitude”. *Journal of Geophysical Research* 113.D21. DOI: [10.1029/2007jd009568](#).
- Blake, S., S. Self, K. Sharma, and S. Sephton (2010). “Sulfur release from the Columbia River Basalts and other flood lava eruptions constrained by a model of sulfide saturation”. *Earth and Planetary Science Letters* 299.3–4, pp. 328–338. DOI: [10.1016/j.epsl.2010.09.013](#).
- Bøggild, O. B. (1918). “Den vulkanske Aske i Moleret samt en Oversigt over Danmarks ældre Tertiærbjergarter”. *Bulletin of the Geological Society of Denmark* 33, pp. 1–159. [In Danish].
- Bonadonna, C. and J. C. Phillips (2003). “Sedimentation from strong volcanic plumes”. *Journal of Geophysical Research: Solid Earth* 108.B7. DOI: [10.1029/2002jb002034](#).
- Büttner, R., P. Dellino, L. L. Volpe, V. Lorenz, and B. Zimanowski (2002). “Thermohydraulic explosions in phreatomagmatic eruptions as evidenced by the comparison between pyroclasts and products from Molten Fuel Coolant Interaction experiments”. *Journal of Geophysical Research: Solid Earth* 107.B11, ECV 5–1–ECV 5–14. DOI: [10.1029/2001jb000511](#).
- Büttner, R., P. Dellino, and B. Zimanowski (1999). “Identifying magma–water interaction from the surface features of ash particles”. *Nature* 401.6754, pp. 688–690. DOI: [10.1038/44364](#).
- Carn, S. A., V. E. Fioletov, C. A. McLinden, C. Li, and N. A. Krotkov (2017). “A decade of global volcanic SO₂ emissions measured from space”. *Scientific Reports* 7.1. DOI: [10.1038/srep44095](#).
- Cashman, K. V. and B. Scheu (2015). “Magmatic Fragmentation”. *The Encyclopedia of Volcanoes*. Ed. by H. Sigurdsson. Elsevier, pp. 459–471. DOI: [10.1016/b978-0-12-385938-9.00025-0](#).
- Charles, A. J., D. J. Condon, I. C. Harding, H. Pälike, J. E. A. Marshall, Y. Cui, L. Kump, and I. W. Croudace (2011). “Constraints on the numerical age of the Paleocene-Eocene boundary”. *Geochemistry, Geophysics, Geosystems* 12.6. DOI: [10.1029/2010gc003426](#).
- Cole, P. D., J. E. Guest, A. M. Duncan, and J. A. M. Pacheco (2001). “Capelinhos 1957–1958, Faial, Azores: deposits formed by an emergent surtseyan eruption”. *Bulletin of Volcanology* 63.2–3, pp. 204–220. DOI: [10.1007/s004450100136](#).
- Costantini, L., B. Houghton, and C. Bonadonna (2010). “Constraints on eruption dynamics of basaltic explosive activity derived from chemical and microtextural study: The example of the Fontana Lapilli Plinian eruption, Nicaragua”. *Journal of Volcanology and Geothermal Research* 189.3–4, pp. 207–224. DOI: [10.1016/j.jvolgeores.2009.11.008](#).
- Davis, K. N., J. A. Wolff, M. C. Rowe, and O. K. Neill (2017). “Sulfur release from main-phase Columbia River Basalt eruptions”. *Geology* 45.11, pp. 1043–1046. DOI: [10.1130/g39371.1](#).
- Davis, M. G., M. O. Garcia, and P. Wallace (2003). “Volatiles in glasses from Mauna Loa Volcano, Hawai‘i: implications for magma degassing and contamination, and growth of Hawaiian volcanoes”. *Contributions to Mineralogy and Petrology* 144.5, pp. 570–591. DOI: [10.1007/s00410-002-0416-z](#).

- Dellino, P. and L. L. Volpe (1996). "Image processing analysis in reconstructing fragmentation and transportation mechanisms of pyroclastic deposits. The case of Monte Pilato-Rocche Rosse eruptions, Lipari (Aeolian islands, Italy)". *Journal of Volcanology and Geothermal Research* 71.1, pp. 13–29. doi: [10.1016/0377-0273\(95\)00062-3](https://doi.org/10.1016/0377-0273(95)00062-3).
- Devine, J. D., H. Sigurdsson, A. N. Davis, and S. Self (1984). "Estimates of sulfur and chlorine yield to the atmosphere from volcanic eruptions and potential climatic effects". *Journal of Geophysical Research: Solid Earth* 89.B7, pp. 6309–6325. doi: [10.1029/jb089ib07p06309](https://doi.org/10.1029/jb089ib07p06309).
- Dingwell, D. B. (1996). "Volcanic Dilemma—Flow or Blow?" *Science* 273.5278, pp. 1054–1055. doi: [10.1126/science.273.5278.1054](https://doi.org/10.1126/science.273.5278.1054).
- Dixon, J. E., D. A. Clague, and E. M. Stolper (1991). "Degassing History of Water, Sulfur, and Carbon in Submarine Lavas from Kilauea Volcano, Hawaii". *The Journal of Geology* 99.3, pp. 371–394. doi: [10.1086/629501](https://doi.org/10.1086/629501).
- Dixon, J. E., J. R. Filiberto, J. G. Moore, and C. J. Hickson (2002). "Volatiles in basaltic glasses from a subglacial volcano in northern British Columbia (Canada): implications for ice sheet thickness and mantle volatiles". *Geological Society, London, Special Publications* 202.1, pp. 255–271. doi: [10.1144/gsl.sp.2002.202.01.13](https://doi.org/10.1144/gsl.sp.2002.202.01.13).
- Edmonds, M. (2008). "New geochemical insights into volcanic degassing". *Philosophical Transactions of the Royal Society A: Mathematical, Physical and Engineering Sciences* 366.1885, pp. 4559–4579. doi: [10.1098/rsta.2008.0185](https://doi.org/10.1098/rsta.2008.0185).
- Edmonds, M. and P. Wallace (2017). "Volatiles and Exsolved Vapor in Volcanic Systems". *Elements* 13.1, pp. 29–34. doi: [10.2113/gselements.13.1.29](https://doi.org/10.2113/gselements.13.1.29).
- Egger, H. and E. Brückl (2006). "Gigantic volcanic eruptions and climatic change in the early Eocene". *International Journal of Earth Sciences* 95.6, pp. 1065–1070. doi: [10.1007/s00531-006-0085-7](https://doi.org/10.1007/s00531-006-0085-7).
- Egger, H., M. Homayoun, H. Huber, F. Rögl, and B. Schmitz (2005). "Early Eocene climatic, volcanic, and biotic events in the northwestern Tethyan Untersberg section, Austria". *Palaeogeography, Palaeoclimatology, Palaeoecology* 217.3–4, pp. 243–264. doi: [10.1016/j.palaeo.2004.12.006](https://doi.org/10.1016/j.palaeo.2004.12.006).
- Graettinger, A. H., I. Skilling, D. McGarvie, and Á. Höskuldsson (2013). "Subaqueous basaltic magmatic explosions trigger phreatomagmatism: A case study from Askja, Iceland". *Journal of Volcanology and Geothermal Research* 264, pp. 17–35. doi: [10.1016/j.jvolgeores.2013.08.001](https://doi.org/10.1016/j.jvolgeores.2013.08.001).
- Haaland, H. J., H. Furnes, and O. J. Martinsen (2000). "Paleogene tuffaceous intervals, Grane Field (Block 2511), Norwegian North Sea: their depositional, petrographical, geochemical character and regional implications". *Marine and Petroleum Geology* 17.1, pp. 101–118. doi: [10.1016/s0264-8172\(99\)00009-4](https://doi.org/10.1016/s0264-8172(99)00009-4).
- Heilmann-Clausen, C. (1995). "Palæogene aflejringer over Danskekalken". *Aarhus Geokompender No.1, Danmarks geologi fra Kridt til i dag*. Ed. by O. Nielsen. Vol. 1. Geologisk Institut Aarhus, pp. 69–114. [In Danish].
- Heilmann-Clausen, C., O. Nielsen, and F. Gersner (1985). "Lithostratigraphy and depositional environments in the Upper Paleocene and Eocene of Denmark". *Bulletin of the Geological Society of Denmark* 33.3–4, pp. 287–323.
- Helo, C., D. A. Clague, D. B. Dingwell, and J. Stix (2013). "High and highly variable cooling rates during pyroclastic eruptions on Axial Seamount, Juan de Fuca Ridge". *Journal of Volcanology and Geothermal Research* 253, pp. 54–64. doi: [10.1016/j.jvolgeores.2012.12.004](https://doi.org/10.1016/j.jvolgeores.2012.12.004).
- Houghton, B. F., C. J. N. Wilson, M. D. Rosenberg, I. E. M. Smith, and R. J. Parker (1996). "Mixed deposits of complex magmatic and phreatomagmatic volcanism: an example from Crater Hill, Auckland, New Zealand". *Bulletin of Volcanology* 58.1, pp. 59–66. doi: [10.1007/s004450050126](https://doi.org/10.1007/s004450050126).
- Houghton, B. and H. Gonnermann (2008). "Basaltic explosive volcanism: Constraints from deposits and models". *Geochemistry* 68.2, pp. 117–140. doi: [10.1016/j.chemer.2008.04.002](https://doi.org/10.1016/j.chemer.2008.04.002).
- Houghton, B., C. J. N. Wilson, P. Del Carlo, M. Coltelli, J. Sable, and R. Carey (2004). "The influence of conduit processes on changes in style of basaltic Plinian eruptions: Tarawera 1886 and Etna 122 BC". *Journal of Volcanology and Geothermal Research* 137.1–3, pp. 1–14. doi: [10.1016/j.jvolgeores.2004.05.009](https://doi.org/10.1016/j.jvolgeores.2004.05.009).
- Jerram, D. A., R. T. Single, R. W. Hobbs, and C. E. Nelson (2009). "Understanding the offshore flood basalt sequence using onshore volcanic facies analogues: an example from the Faroe–Shetland basin". *Geological Magazine* 146.3, pp. 353–367. doi: [10.1017/s0016756809005974](https://doi.org/10.1017/s0016756809005974).
- Jolley, D. W. and M. Widdowson (2005). "Did Paleogene North Atlantic rift-related eruptions drive early Eocene climate cooling?" *Lithos* 79.3–4, pp. 355–366. doi: [10.1016/j.lithos.2004.09.007](https://doi.org/10.1016/j.lithos.2004.09.007).
- Jones, G. S., J. M. Gregory, P. A. Stott, S. F. B. Tett, and R. B. Thorpe (2005). "An AOGCM simulation of the climate response to a volcanic super-eruption". *Climate Dynamics* 25.7–8, pp. 725–738. doi: [10.1007/s00382-005-0066-8](https://doi.org/10.1007/s00382-005-0066-8).
- Jones, M. T., L. M. E. Percival, E. W. Stokke, J. Frieling, T. A. Mather, L. Riber, B. A. Schubert, B. Schultz, C. Tegner, S. Planke, and H. H. Svensen (2019). "Mercury anomalies across the Palaeocene–Eocene Thermal Maximum". *Climate of the Past* 15.1, pp. 217–236. doi: [10.5194/cp-15-217-2019](https://doi.org/10.5194/cp-15-217-2019).
- Keith, M., K. M. Haase, R. Klemm, U. Schwarz-Schampera, and H. Franke (2017). "Systematic variations in magmatic sulphide chemistry from mid-ocean ridges, back-arc basins and island arcs". *Chemical Geology* 451, pp. 67–77. doi: [10.1016/j.chemgeo.2016.12.028](https://doi.org/10.1016/j.chemgeo.2016.12.028).

- King, C. (2016). *A revised correlation of Tertiary rocks in the British Isles and adjacent areas of NW Europe*. Ed. by A. S. Gale and T. L. Barry. The Geological Society of London. doi: 10.1144/sr27.
- Knox, R. W. O. and A. C. Morton (1988). "The record of early Tertiary N Atlantic volcanism in sediments of the North Sea Basin". *Geological Society, London, Special Publications* 39.1, pp. 407–419. doi: 10.1144/gsl.sp.1988.039.01.36.
- Larsen, L. M., J. Fitton, and A. K. Pedersen (2003). "Paleogene volcanic ash layers in the Danish Basin: compositions and source areas in the North Atlantic Igneous Province". *Lithos* 71.1, pp. 47–80. doi: 10.1016/j.lithos.2003.07.001.
- Larsen, L. M., A. K. Pedersen, C. Tegner, R. A. Duncan, N. Hald, and J. G. Larsen (2016). "Age of Tertiary volcanic rocks on the West Greenland continental margin: volcanic evolution and event correlation to other parts of the North Atlantic Igneous Province". *Geological Magazine* 153.3, pp. 487–511. doi: 10.1017/s0016756815000515.
- Larsen, R. B. and C. Tegner (2006). "Pressure conditions for the solidification of the Skaergaard intrusion: Eruption of East Greenland flood basalts in less than 300,000 years". *Lithos* 92.1-2, pp. 181–197. doi: 10.1016/j.lithos.2006.03.032.
- Liu, E. J., K. V. Cashman, A. C. Rust, and A. Höskuldsson (2017). "Contrasting mechanisms of magma fragmentation during coeval magmatic and hydro-magmatic activity: the Hverfjall Fires fissure eruption, Iceland". *Bulletin of Volcanology* 79.10. doi: 10.1007/s00445-017-1150-8.
- Liu, E. J., K. V. Cashman, A. Rust, and M. Edmonds (2018). "Insights into the dynamics of mafic magmatic-hydro-magmatic eruptions from volatile degassing behaviour: The Hverfjall Fires, Iceland". *Journal of Volcanology and Geothermal Research* 358, pp. 228–240. doi: 10.1016/j.jvolgeores.2018.05.016.
- Liu, E. J., K. V. Cashman, A. Rust, and S. Gislason (2015). "The role of bubbles in generating fine ash during hydro-magmatic eruptions". *Geology* 43.3, pp. 239–242. doi: 10.1130/g36336.1.
- Lloyd, A. S., T. Plank, P. Ruprecht, E. H. Hauri, and W. Rose (2012). "Volatile loss from melt inclusions in pyroclasts of differing sizes". *Contributions to Mineralogy and Petrology* 165.1, pp. 129–153. doi: 10.1007/s00410-012-0800-2.
- Lorenz, V. (1986). "On the growth of maars and diatremes and its relevance to the formation of tuff rings". *Bulletin of Volcanology* 48.5, pp. 265–274. doi: 10.1007/bf01081755.
- Mahony, S. H., R. S. J. Sparks, L. M. Wallace, S. L. Engwell, E. M. Scourse, N. H. Barnard, J. Kandlbauer, and S. K. Brown (2016). "Increased rates of large-magnitude explosive eruptions in Japan in the late Neogene and Quaternary". *Geochemistry, Geophysics, Geosystems* 17.7, pp. 2467–2479. doi: 10.1002/2016gc006362.
- Mangan, M. T. and K. V. Cashman (1996). "The structure of basaltic scoria and reticulite and inferences for vesiculation, foam formation, and fragmentation in lava fountains". *Journal of Volcanology and Geothermal Research* 73.1-2, pp. 1–18. doi: 10.1016/0377-0273(96)00018-2.
- Mason, B. G., D. M. Pyle, and C. Oppenheimer (2004). "The size and frequency of the largest explosive eruptions on Earth". *Bulletin of Volcanology* 66.8, pp. 735–748. doi: 10.1007/s00445-004-0355-9.
- Mastin, L. G. (2007). "Generation of fine hydro-magmatic ash by growth and disintegration of glassy rinds". *Journal of Geophysical Research* 112.B2. doi: 10.1029/2005jb003883.
- Mastin, L. G., R. L. Christiansen, C. Thornber, J. Lowenstern, and M. Beeson (2004). "What makes hydro-magmatic eruptions violent? Some insights from the Keanakāko'i Ash, Kīlauea Volcano, Hawai'i". *Journal of Volcanology and Geothermal Research* 137.1-3, pp. 15–31. doi: 10.1016/j.jvolgeores.2004.05.015.
- Mastin, L. G., A. R. Van Eaton, and J. B. Lowenstern (2014). "Modeling ash fall distribution from a Yellowstone supereruption". *Geochemistry, Geophysics, Geosystems* 15.8, pp. 3459–3475. doi: 10.1002/2014gc005469.
- Mavrogenes, J. A. and H. S. O'Neill (1999). "The relative effects of pressure, temperature and oxygen fugacity on the solubility of sulfide in mafic magmas". *Geochimica et Cosmochimica Acta* 63.7-8, pp. 1173–1180. doi: 10.1016/s0016-7037(98)00289-0.
- Métrich, N., H. Sigurdsson, P. S. Meyer, and J. D. Devine (1991). "The 1783 Lakagigar eruption in Iceland: geochemistry, CO₂ and sulfur degassing". *Contributions to Mineralogy and Petrology* 107.4, pp. 435–447. doi: 10.1007/bf00310678.
- Métrich, N. and P. Wallace (2008). "Volatile Abundances in Basaltic Magmas and Their Degassing Paths Tracked by Melt Inclusions". *Reviews in Mineralogy and Geochemistry* 69.1, pp. 363–402. doi: 10.2138/rmg.2008.69.10.
- Montierth, C., A. D. Johnston, and K. V. Cashman (1995). "An empirical glass-composition-based geothermometer for Mauna Loa Lavas". *Mauna Loa Revealed: Structure, Composition, History, and Hazards*. American Geophysical Union, pp. 207–217. doi: 10.1029/gm092p0207.
- Moore, J. G. (1985). "Structure and eruptive mechanisms at Surtsey Volcano, Iceland". *Geological Magazine* 122.6, pp. 649–661. doi: 10.1017/s0016756800032052.
- Moore, J. G. and J.-G. Schilling (1973). "Vesicles, water, and sulfur in Reykjanes Ridge basalts". *Contributions to Mineralogy and Petrology* 41.2, pp. 105–118. doi: 10.1007/bf00375036.

- Morrisey, M., B. Zimoriski, K. Wohletz, and R. Buettner (2000). "Phreatomagmatic fragmentation". *Encyclopedia of volcanoes*. Ed. by H. Sigurdsson, B. F. Houghton, H. Rymer, J. Stix, and S. McNutt. Academic Press, pp. 431–445.
- Morton, A. C. and J. A. Evans (1988). "Geochemistry of basaltic ash beds from the Fur Formation, Island of Fur, Denmark". *Bulletin of the Geological Society of Denmark* 37.1-2, pp. 1–9.
- Morton, A. C. and J. Keene (1984). "Paleogene Pyroclastic Volcanism in the Southwest Rockall Plateau". *Initial Reports of the Deep Sea Drilling Project*, 81. U.S. Government Printing Office. doi: [10.2973/dsdp.proc.81.119.1984](https://doi.org/10.2973/dsdp.proc.81.119.1984).
- Morton, A. C. and R. W. O. Knox (1990). "Geochemistry of late Palaeocene and early Eocene tephra from the North Sea Basin". *Journal of the Geological Society* 147.3, pp. 425–437. doi: [10.1144/gsjgs.147.3.0425](https://doi.org/10.1144/gsjgs.147.3.0425).
- Németh, K. and S. Kósik (2020). "Review of Explosive Hydrovolcanism". *Geosciences* 10.2, p. 44. doi: [10.3390/geosciences10020044](https://doi.org/10.3390/geosciences10020044).
- Newman, S. and J. B. Lowenstern (2002). "VolatileCalc: a silicate melt–H₂O–CO₂ solution model written in Visual Basic for excel". *Computers & Geosciences* 28.5, pp. 597–604. doi: [10.1016/S0098-3004\(01\)00081-4](https://doi.org/10.1016/S0098-3004(01)00081-4).
- Nielsen, O. B. and C. Heilmann-Clausen (1988). "Palaeogene volcanism: the sedimentary record in Denmark". *Geological Society, London, Special Publications* 39.1, pp. 395–405. doi: [10.1144/gsl.sp.1988.039.01.35](https://doi.org/10.1144/gsl.sp.1988.039.01.35).
- Óladóttir, B. A., T. Thordarson, Á. Geirsdóttir, G. E. Jóhannsdóttir, and J. Mangerud (2020). "The Sakunavratn Ash and the G10ka series tephra. Review and current state of knowledge". *Quaternary Geochronology* 56, p. 101041. doi: [10.1016/j.quageo.2019.101041](https://doi.org/10.1016/j.quageo.2019.101041).
- Óladóttir, B. A., T. Thordarson, G. Larsen, and O. Sigmarsson (2007). "Survival of the Mýrdalsjökull ice cap through the Holocene thermal maximum: evidence from sulphur contents in Katla tephra layers (Iceland) from the last ~8400 years". *Annals of Glaciology* 45, pp. 183–188. doi: [10.1017/S0022282282516](https://doi.org/10.1017/S0022282282516).
- Papale, P. (1999). "Modeling of the solubility of a two-component H₂O–CO₂ fluid in silicate liquids". *American Mineralogist* 84.4, pp. 477–492. doi: [10.2138/am-1999-0402](https://doi.org/10.2138/am-1999-0402).
- Parcheta, C., B. Houghton, and D. Swanson (2013). "Contrasting patterns of vesiculation in low, intermediate, and high Hawaiian fountains: A case study of the 1969 Mauna Ulu eruption". *Journal of Volcanology and Geothermal Research* 255, pp. 79–89. doi: [10.1016/j.jvolgeores.2013.01.016](https://doi.org/10.1016/j.jvolgeores.2013.01.016).
- Parfitt, E. A. (1998). "A study of clast size distribution, ash deposition and fragmentation in a Hawaiian-style volcanic eruption". *Journal of Volcanology and Geothermal Research* 84.3-4, pp. 197–208. doi: [10.1016/S0377-0273\(98\)00042-0](https://doi.org/10.1016/S0377-0273(98)00042-0).
- Patten, C., S.-J. Barnes, E. A. Mathez, and F. E. Jenner (2013). "Partition coefficients of chalcophile elements between sulfide and silicate melts and the early crystallization history of sulfide liquid: LA-ICP-MS analysis of MORB sulfide droplets". *Chemical Geology* 358, pp. 170–188. doi: [10.1016/j.chemgeo.2013.08.040](https://doi.org/10.1016/j.chemgeo.2013.08.040).
- Pedersen, A. K., J. Engell, and J. Rønsbo (1975). "Early tertiary volcanism in the Skagerrak: New chemical evidence from ash-layers in the mo-clay of northern Denmark". *Lithos* 8.4, pp. 255–268. doi: [10.1016/0024-4937\(75\)90009-2](https://doi.org/10.1016/0024-4937(75)90009-2).
- Pedersen, A. K. and K. A. Jørgensen (1981). "A Textural Study of Basaltic Tephra from Lower Tertiary Diatomites in Northern Denmark". *Tephra Studies*. Springer Netherlands, pp. 213–218. doi: [10.1007/978-94-009-8537-7_12](https://doi.org/10.1007/978-94-009-8537-7_12).
- Pedersen, G. K. and F. Surlyk (1983). "The Fur Formation, a late Paleocene ash-bearing diatomite from northern Denmark". *Bulletin of the Geological Society of Denmark* 32.1-2, pp. 43–65.
- Pedersen, S. A. S. (2008). "Palaeogene diatomite deposits in Denmark: geological investigations and applied aspects". *Geological Survey of Denmark and Greenland (GEUS) Bulletin* 15, pp. 21–24. doi: [10.34194/geusb.v15.5034](https://doi.org/10.34194/geusb.v15.5034).
- Planke, S., T. Rasmussen, S. S. Rey, and R. Myklebust (2005). "Seismic characteristics and distribution of volcanic intrusions and hydrothermal vent complexes in the Vøring and Møre basins". *Geological Society, London, Petroleum Geology Conference series* 6.1, pp. 833–844. doi: [10.1144/0060833](https://doi.org/10.1144/0060833).
- Porritt, L., J. Russell, and S. Quane (2012). "Pele's tears and spheres: Examples from Kilauea Iki". *Earth and Planetary Science Letters* 333-334, pp. 171–180. doi: [10.1016/j.epsl.2012.03.031](https://doi.org/10.1016/j.epsl.2012.03.031).
- Sable, J. E., B. F. Houghton, P. Del Carlo, and M. Coltelli (2006). "Changing conditions of magma ascent and fragmentation during the Etna 122 BC basaltic Plinian eruption: Evidence from clast microtextures". *Journal of Volcanology and Geothermal Research* 158.3-4, pp. 333–354. doi: [10.1016/j.jvolgeores.2006.07.006](https://doi.org/10.1016/j.jvolgeores.2006.07.006).
- Saunders, A. D. (2016). "Two LIPs and two Earth-system crises: the impact of the North Atlantic Igneous Province and the Siberian Traps on the Earth-surface carbon cycle". *Geological Magazine* 153.2, pp. 201–222. doi: [10.1017/S0016756815000175](https://doi.org/10.1017/S0016756815000175).
- Saunders, A. D., J. Fitton, A. C. Kerr, M. Norry, and R. Kent (1997). "The north Atlantic igneous province". *Large Igneous Provinces: Continental, Oceanic, and Planetary Flood Volcanism*. Ed. by J. J. Mahoney and M. L. Coffin. Vol. 100. American Geophysical Union, pp. 45–94.
- Schipper, C. I., S. P. Jakobsson, J. D. White, J. M. Palin, and T. Bush-Marcinowski (2015). "The Surtsey Magma Series". *Scientific Reports* 5.1. doi: [10.1038/srep11498](https://doi.org/10.1038/srep11498).

- Schipper, C. I. and J. D. White (2016). “Magma-slurry interaction in Surtseyan eruptions”. *Geology* 44.3, pp. 195–198. doi: 10.1130/g37480.1.
- Schmidt, A., R. A. Skeffington, T. Thórdarson, S. Self, P. M. Forster, A. Rap, A. Ridgwell, D. Fowler, M. Wilson, G. W. Mann, P. Wignall, and K. S. Carslaw (2016). “Selective environmental stress from sulphur emitted by continental flood basalt eruptions”. *Nature Geoscience* 9.1, pp. 77–82. doi: 10.1038/ngeo2588.
- Schmitz, B., B. Peucker-Ehrenbrink, C. Heilmann-Clausen, G. Åberg, F. Asaro, and C.-T. A. Lee (2004). “Basaltic explosive volcanism, but no comet impact, at the Paleocene–Eocene boundary: high-resolution chemical and isotopic records from Egypt, Spain and Denmark”. *Earth and Planetary Science Letters* 225.1–2, pp. 1–17. doi: 10.1016/j.epsl.2004.06.017.
- Sharma, K., S. Blake, S. Self, and A. J. Krueger (2004). “SO₂ emissions from basaltic eruptions, and the excess sulfur issue”. *Geophysical Research Letters* 31.13. doi: 10.1029/2004gl019688.
- Sigmarrsson, O., B. Haddadi, S. Carn, S. Moune, J. Gudnason, K. Yang, and L. Clarisse (2013). “The sulfur budget of the 2011 Grimsvötn eruption, Iceland”. *Geophysical Research Letters* 40.23, pp. 6095–6100. doi: 10.1002/2013gl057760.
- Sigvaldason, G. E. and N. Óskarsson (1976). “Chlorine in basalts from Iceland”. *Geochimica et Cosmochimica Acta* 40.7, pp. 777–789. doi: 10.1016/0016-7037(76)90030-2.
- Smythe, D. J., B. J. Wood, and E. S. Kiseeva (2017). “The S content of silicate melts at sulfide saturation: New experiments and a model incorporating the effects of sulfide composition”. *American Mineralogist* 102.4, pp. 795–803. doi: 10.2138/am-2017-5800ccby.
- Stevenson, J. A., S. C. Millington, F. M. Beckett, G. T. Swindles, and T. Thórdarson (2015). “Big grains go far: understanding the discrepancy between tephrochronology and satellite infrared measurements of volcanic ash”. *Atmospheric Measurement Techniques* 8.5, pp. 2069–2091. doi: 10.5194/amt-8-2069-2015.
- Stokke, E. W., M. T. Jones, J. E. Tierney, H. H. Svensen, and J. H. Whiteside (2020). “Temperature changes across the Paleocene-Eocene Thermal Maximum – a new high-resolution TEX86 temperature record from the Eastern North Sea Basin”. *Earth and Planetary Science Letters* 544, p. 116388. doi: 10.1016/j.epsl.2020.116388.
- Storey, M., R. A. Duncan, and C. C. Swisher (2007). “Paleocene-Eocene Thermal Maximum and the Opening of the Northeast Atlantic”. *Science* 316.5824, pp. 587–589. doi: 10.1126/science.1135274.
- Storey, M., R. A. Duncan, and C. Tegner (2007). “Timing and duration of volcanism in the North Atlantic Igneous Province: Implications for geodynamics and links to the Iceland hotspot”. *Chemical Geology* 241.3–4, pp. 264–281. doi: 10.1016/j.chemgeo.2007.01.016.
- Stovall, W. K., B. F. Houghton, J. E. Hammer, S. A. Fagents, and D. A. Swanson (2012). “Vesiculation of high fountaining Hawaiian eruptions: episodes 15 and 16 of 1959 Kilauea Iki”. *Bulletin of Volcanology* 74.2, pp. 441–455. doi: 10.1007/s00445-011-0531-7.
- Svensen, H., S. Planke, A. Malthe-Sørenssen, B. Jamtveit, R. Myklebust, T. R. Eidem, and S. S. Rey (2004). “Release of methane from a volcanic basin as a mechanism for initial Eocene global warming”. *Nature* 429.6991, pp. 542–545. doi: 10.1038/nature02566.
- Szramek, L. A. (2016). “Mafic Plinian eruptions: Is fast ascent required?” *Journal of Geophysical Research: Solid Earth* 121.10, pp. 7119–7136. doi: 10.1002/2016jb013208.
- Thórdarson, T., D. Miller, G. Larsen, S. Self, and H. Sigurdsson (2001). “New estimates of sulfur degassing and atmospheric mass-loading by the 934 AD Eldgjá eruption, Iceland”. *Journal of Volcanology and Geothermal Research* 108.1–4, pp. 33–54. doi: 10.1016/s0377-0273(00)00277-8.
- Thórdarson, T., S. Self, D. J. Miller, G. Larsen, and E. G. Vilmundardóttir (2003). “Sulphur release from flood lava eruptions in the Veidivötn, Grimsvötn and Katla volcanic systems, Iceland”. *Geological Society, London, Special Publications* 213.1, pp. 103–121. doi: 10.1144/gsl.sp.2003.213.01.07.
- Thórdarson, T., S. Self, N. Óskarsson, and T. Hulsebosch (1996). “Sulfur, chlorine, and fluorine degassing and atmospheric loading by the 1783–1784 AD Laki (Skaftár Fires) eruption in Iceland”. *Bulletin of Volcanology* 58.2–3, pp. 205–225. doi: 10.1007/s004450050136.
- Unni, C. K. and J.-G. Schilling (1978). “Cl and Br degassing by volcanism along the Reykjanes Ridge and Iceland”. *Nature* 272.5648, pp. 19–23. doi: 10.1038/272019a0.
- Walker, G. P., S. Self, and L. Wilson (1984). “Tarawera 1886, New Zealand — A basaltic plinian fissure eruption”. *Journal of Volcanology and Geothermal Research* 21.1–2, pp. 61–78. doi: 10.1016/0377-0273(84)90016-7.
- Wallace, P. and I. S. Carmichael (1992). “Sulfur in basaltic magmas”. *Geochimica et Cosmochimica Acta* 56.5, pp. 1863–1874. doi: 10.1016/0016-7037(92)90316-b.
- Wallace, P. and M. Edmonds (2011). “The Sulfur Budget in Magmas: Evidence from Melt Inclusions, Submarine Glasses, and Volcanic Gas Emissions”. *Reviews in Mineralogy and Geochemistry* 73.1, pp. 215–246. doi: 10.2138/rmg.2011.73.8.
- Watson, D., N. Schofield, D. Jolley, S. Archer, A. J. Finlay, N. Mark, J. Hardman, and T. Watton (2017). “Stratigraphic overview of Palaeogene tuffs in the Faroe–Shetland Basin, NE Atlantic Margin”. *Journal of the Geological Society* 174.4, pp. 627–645. doi: 10.1144/jgs2016-132.

- Westerhold, T., U. Röhl, T. Frederichs, C. Agnini, I. Raffi, J. C. Zachos, and R. H. Wilkens (2017). "Astro-nomical calibration of the Ypresian timescale: implications for seafloor spreading rates and the chaotic behavior of the solar system?" *Climate of the Past* 13.9, pp. 1129–1152. doi: [10.5194/cp-13-1129-2017](https://doi.org/10.5194/cp-13-1129-2017).
- Westerhold, T., U. Röhl, H. K. McCarren, and J. C. Zachos (2009). "Latest on the absolute age of the Paleocene–Eocene Thermal Maximum (PETM): New insights from exact stratigraphic position of key ash layers 19 and -17". *Earth and Planetary Science Letters* 287.3–4, pp. 412–419. doi: [10.1016/j.epsl.2009.08.027](https://doi.org/10.1016/j.epsl.2009.08.027).
- White, J. D. (1996). "Impure coolants and interaction dynamics of phreatomagmatic eruptions". *Journal of Volcanology and Geothermal Research* 74.3–4, pp. 155–170. doi: [10.1016/s0377-0273\(96\)00061-3](https://doi.org/10.1016/s0377-0273(96)00061-3).
- White, J. D. and G. A. Valentine (2016). "Magmatic versus phreatomagmatic fragmentation: Absence of evidence is not evidence of absence". *Geosphere* 12.5, pp. 1478–1488. doi: [10.1130/ges01337.1](https://doi.org/10.1130/ges01337.1).
- Wilkinson, C. M., M. Ganerød, B. W. H. Hendriks, and E. A. Eide (2017). "Compilation and appraisal of geochronological data from the North Atlantic Igneous Province (NAIP)". *Geological Society, London, Special Publications* 447.1, pp. 69–103. doi: [10.1144/sp447.10](https://doi.org/10.1144/sp447.10).
- Williams, S. N. (1983). "Plinian airfall deposits of basaltic composition". *Geology* 11.4, p. 211. doi: [10.1130/0091-7613\(1983\)11<211:padobc>2.0.co;2](https://doi.org/10.1130/0091-7613(1983)11<211:padobc>2.0.co;2).
- Witham, F., J. Blundy, S. C. Kohn, P. Lesne, J. Dixon, S. V. Churakov, and R. Botcharnikov (2012). "SolEx: A model for mixed COHSCI-volatile solubilities and exsolved gas compositions in basalt". *Computers & Geosciences* 45, pp. 87–97. doi: [10.1016/j.cageo.2011.09.021](https://doi.org/10.1016/j.cageo.2011.09.021).
- Wood, D. A. (1980). "The application of a ThHfTa diagram to problems of tectonomagmatic classification and to establishing the nature of crustal contamination of basaltic lavas of the British Tertiary Volcanic Province". *Earth and Planetary Science Letters* 50.1, pp. 11–30. doi: [10.1016/0012-821x\(80\)90116-8](https://doi.org/10.1016/0012-821x(80)90116-8).
- Wotzlaw, J.-F., I. N. Bindeman, U. Schaltegger, C. K. Brooks, and H. R. Naslund (2012). "High-resolution insights into episodes of crystallization, hydrothermal alteration and remelting in the Skaergaard intrusive complex". *Earth and Planetary Science Letters* 355–356, pp. 199–212. doi: [10.1016/j.epsl.2012.08.043](https://doi.org/10.1016/j.epsl.2012.08.043).
- Wykes, J. L., H. S. C. O'Neill, and J. A. Mavrogenes (2015). "The Effect of FeO on the Sulfur Content at Sulfide Saturation (SCSS) and the Selenium Content at Selenide Saturation of Silicate Melts". *Journal of Petrology* 56.7, pp. 1407–1424. doi: [10.1093/petrology/egv041](https://doi.org/10.1093/petrology/egv041).
- Zeebe, R. E. and L. J. Lourens (2019). "Solar System chaos and the Paleocene–Eocene boundary age constrained by geology and astronomy". *Science* 365.6456, pp. 926–929. doi: [10.1126/science.aax0612](https://doi.org/10.1126/science.aax0612).
- Zimanowski, B., K. Wohletz, P. Dellino, and R. Büttner (2003). "The volcanic ash problem". *Journal of Volcanology and Geothermal Research* 122.1–2, pp. 1–5. doi: [10.1016/s0377-0273\(02\)00471-7](https://doi.org/10.1016/s0377-0273(02)00471-7).
- Pórarinnsson, S. (1967). *Surtsey: the new island in the North Atlantic*. Viking Press.

Supplementary material

Evidence of explosive hydromagmatic eruptions during the emplacement of the North Atlantic Igneous Province

Ella W. Stokke^{1,*}, Emma J. Liu^{2,3}, and Morgan T. Jones¹

¹Centre for Earth Evolution and Dynamics (CEED), University of Oslo, PO Box 1028 Blindern, 0315, Oslo, Norway. *e.w.stokke@geo.uio.no

²Earth Sciences, University College London, 5 Gower Place, London, WC1E 6BS, UK.

³Department of Earth Sciences, University of Cambridge, Downing Street, Cambridge CB2 3EQ, UK.

Included supplementary tables

Table 1: Data from microprobe analyses of matrix glass.

Table 2: Precision and accuracy of secondary standards.

Table 3: Modelled values of the Sulfur Concentration at Sulfur Saturation

Table 4: Textural analysis and classification of the volcanic material.

Supplementary references

Keith, M., Haase, K. M., Klemm, R., Schwarz-Schampera, U., & Franke, H. (2017). Systematic variations in magmatic sulphide chemistry from mid-ocean ridges, back-arc basins and island arcs. *Chemical Geology*, 451, 67-77. <https://doi.org/10.1016/j.chemgeo.2016.12.028>

Smythe, D. J., Wood, B. J., & Kiseeva, E. S. (2017). The S content of silicate melts at sulfide saturation: new experiments and a model incorporating the effects of sulfide composition. *American Mineralogist*, 102(4), 795-803. <https://doi.org/10.2138/am-2017-5800CCBY>

Supplementary Table 1: Data from microprobe analyses of matrix glass. First part (orange) show anhydrous major element oxides, SO₂ and Cl. Second part (yellow) show sulfur and chlorine from the total weight % element composition recalculated to parts per million (ppm). Analyses were conducted in two sessions (a and b in the sample names).

Sample Name	Depth relative to Ash -33 (m)	Anhydrous Oxides (wt%)														PPM	
		SiO2	TiO2	Al2O3	MgO	MnO	FeO	CaO	Na2O	K2O	P2O5	SO2	Cl	S	Cl		
SK17_19_a_1	6.6	47.80	4.54	12.60	5.85	0.21	14.62	9.39	3.20	1.040	0.5826	0.1342	0.0210	668	209		
SK17_19_a_2	6.6	48.08	4.49	12.79	5.19	0.31	14.93	9.49	3.12	0.960	0.5463	0.0705	0.0219	352	218		
SK17_19_a_3	6.6	48.17	4.48	12.87	5.25	0.22	14.73	9.40	3.24	1.004	0.5126	0.1042	0.0193	517	191		
SK17_19_a_4	6.6	48.08	4.50	12.80	5.11	0.19	15.09	9.46	3.12	0.927	0.5507	0.1346	0.0253	664	249		
SK17_19_a_5	6.6	48.17	4.42	12.88	5.23	0.24	14.92	9.32	3.17	0.976	0.5775	0.0928	0.0188	463	188		
SK17_19_a_6	6.6	47.71	4.53	12.88	5.23	0.32	15.11	9.25	3.28	1.004	0.5104	0.1524	0.0238	755	236		
SK17_19_a_7	6.6	48.37	4.57	12.81	5.34	0.21	14.65	9.31	3.08	0.971	0.5582	0.1174	0.0220	583	218		
SK17_19_a_8	6.6	48.14	4.49	12.55	5.29	0.29	15.32	9.35	2.88	1.015	0.5520	0.0932	0.0272	468	273		
SK17_19_a_9	6.6	47.75	4.59	12.79	5.13	0.20	15.38	9.34	3.21	0.986	0.5569	0.0496	0.0175	247	174		
SK17_19_a_10	6.6	48.04	4.50	12.97	5.24	0.21	15.06	9.31	3.15	0.922	0.4907	0.0845	0.0179	419	177		
SK17_19_a_11	6.6	48.13	4.52	12.78	5.30	0.24	14.69	9.52	3.15	1.006	0.5756	0.0593	0.0172	296	172		
KD17_19_b_1	6.6	48.11	4.51	12.55	4.88	0.20	15.23	9.68	3.24	0.944	0.5339	0.1127	0.0194	551	190		
KD17_19_b_2	6.6	48.73	4.53	12.82	4.78	0.23	14.76	9.52	3.09	0.895	0.5456	0.0743	0.0198	365	194		
KD17_19_b_4	6.6	48.50	4.47	12.69	4.92	0.24	14.79	9.62	3.16	0.995	0.4988	0.0909	0.0245	449	242		
KD17_19_b_5	6.6	48.27	4.47	12.65	4.84	0.26	15.04	9.56	3.21	0.980	0.5433	0.1512	0.0227	752	225		
KD17_19_b_6	6.6	48.68	4.54	12.64	4.73	0.21	14.88	9.45	3.25	0.992	0.5757	0.0426	0.0115	210	114		
KD17_19_b_7	6.6	48.29	4.47	12.84	4.96	0.18	14.88	9.44	3.20	1.012	0.5913	0.1165	0.0191	571	187		
KD17_19_b_8	6.6	48.35	4.51	12.56	4.91	0.19	15.15	9.52	3.15	0.951	0.5919	0.0885	0.0216	440	214		
KD17_19_b_9	6.6	48.96	4.37	13.38	4.47	0.21	14.23	9.90	2.97	0.855	0.5829	0.0560	0.0135	280	135		
KD17_13_a_2	19.9	47.78	4.51	12.78	5.77	0.27	14.64	9.43	3.15	0.987	0.5233	0.1320	0.0235	653	232		
KD17_13_a_3	19.9	52.60	3.43	13.18	3.47	0.25	13.49	7.40	3.50	1.658	0.7934	0.1886	0.0374	936	371		
KD17_13_a_4	19.9	51.20	3.63	12.87	5.13	0.24	12.80	8.32	1.65	3.618	0.4128	0.1089	0.0103	543	103		
KD17_13_a_5	19.9	51.45	3.53	13.00	4.40	0.25	14.48	8.31	3.04	0.945	0.4732	0.1071	0.0146	532	145		
KD17_13_a_6	19.9	48.42	4.13	13.07	5.06	0.21	14.95	9.33	3.11	0.945	0.6039	0.1513	0.0358	750	355		
KD17_13_a_12	19.9	50.19	3.74	12.45	4.95	0.25	15.21	9.17	2.79	0.711	0.4212	0.1185	0.0095	586	94		
KD17_13_b_3	19.9	49.99	3.87	12.02	4.60	0.24	15.90	9.06	3.03	0.787	0.4179	0.0726	0.0105	360	104		
KD17_13_b_4	19.9	50.04	3.81	12.43	4.65	0.23	15.60	9.07	2.87	0.689	0.4635	0.1320	0.0208	648	204		
KD17_13_b_7	19.9	48.51	4.02	13.07	4.89	0.20	14.50	9.50	2.70	2.037	0.4201	0.1371	0.0209	673	205		
KD17_13_b_8	19.9	49.43	4.08	12.82	4.73	0.26	14.30	9.56	3.08	0.910	0.6614	0.1380	0.0223	682	220		
KD17_13_b_9	19.9	51.28	3.55	12.86	4.16	0.20	14.76	8.61	3.04	0.946	0.4817	0.1046	0.0164	514	161		
KD17_+1_a_1	26	49.15	3.64	12.73	5.29	0.23	15.13	9.93	2.71	0.622	0.3976	0.1555	0.0097	776	97		
KD17_+1_a_2	26	49.07	3.60	12.81	5.37	0.28	14.97	9.87	2.92	0.617	0.3630	0.1250	0.0125	618	123		
KD17_+1_a_3	26	50.61	3.18	13.01	5.27	0.20	14.02	9.51	2.99	0.693	0.4451	0.0594	0.0155	297	155		
KD17_+1_a_4	26	48.95	3.61	12.77	5.13	0.28	15.24	9.81	2.93	0.672	0.4481	0.1558	0.0117	774	116		
KD17_+1_a_5	26	49.82	3.99	12.53	4.77	0.27	15.19	9.03	3.04	0.797	0.5051	0.0352	0.0112	175	111		
KD17_+1_a_6	26	49.72	3.68	12.78	5.11	0.24	14.91	9.35	2.95	0.695	0.4286	0.1344	0.0145	668	144		
KD17_+1_a_7	26	49.13	3.58	12.88	5.56	0.25	14.87	9.84	2.77	0.587	0.3572	0.1539	0.0155	762	153		
KD17_+1_a_8	26	49.30	3.63	12.79	5.44	0.22	15.03	9.53	2.86	0.578	0.4112	0.1902	0.0128	943	127		

Sample Name	Depth relative to Ash -33 (m)	SiO2	TiO2	Al2O3	MgO	MnO	FeO	CaO	Na2O	K2O	P2O5	SO2	Cl	S	Cl
KD17_+1_a_9	26	49.14	3.58	12.90	5.31	0.25	15.18	9.81	2.69	0.584	0.3862	0.1727	0.0144	853	142
KD17_+1_a_10	26	49.16	3.59	12.70	5.41	0.23	15.20	9.70	2.79	0.599	0.4659	0.1413	0.0103	706	103
KD17_+1_a_11	26	48.97	3.60	12.74	5.48	0.23	15.33	9.70	2.81	0.600	0.3458	0.1775	0.0114	884	113
KD17_+1_b_1	26	49.41	3.42	12.84	4.82	0.17	15.27	10.11	2.68	0.760	0.3477	0.1620	0.0099	711	187
KD17_+1_b_2	26	49.64	3.58	12.68	4.94	0.23	14.97	9.69	3.06	0.596	0.4606	0.1411	0.0090	742	137
KD17_+1_b_3	26	50.04	3.25	12.67	5.69	0.24	13.76	10.57	2.80	0.462	0.4159	0.1097	0.0053	614	139
KD17_+1_b_4	26	50.16	3.54	12.88	4.91	0.23	14.20	9.97	3.18	0.478	0.3262	0.1106	0.0109	693	184
KD17_+1_b_5	26	49.81	3.53	12.67	4.93	0.16	15.29	9.51	2.89	0.673	0.4145	0.1143	0.0139	474	127
KD17_+1_b_6	26	51.00	3.53	12.98	4.51	0.20	14.90	9.48	2.23	0.632	0.4182	0.1108	0.0109	552	129
KD17_+1_b_7	26	49.89	3.53	12.49	5.07	0.20	15.06	9.74	2.85	0.615	0.4659	0.0742	0.0127	649	144
KD17_+1_b_8	26	50.51	3.70	12.68	4.65	0.24	15.70	9.50	1.77	0.773	0.3682	0.0946	0.0105	689	151
KD17_+1_b_9	26	49.79	3.53	12.65	4.88	0.25	15.23	9.65	2.69	0.761	0.3733	0.1823	0.0158	455	93
KD17_+9_a_1	27	48.98	3.51	12.81	5.79	0.23	14.42	10.44	2.67	0.581	0.4255	0.1359	0.0107	675	106
KD17_+9_a_2	27	48.59	3.42	13.57	5.67	0.24	14.47	10.34	2.57	0.548	0.3822	0.1838	0.0176	896	171
KD17_+9_a_3	27	48.84	3.35	12.72	6.96	0.22	14.15	10.12	2.62	0.567	0.3302	0.1079	0.0149	545	151
KD17_+9_a_5	27	49.22	3.44	12.90	6.06	0.22	14.03	10.34	2.67	0.564	0.3961	0.1282	0.0181	637	180
KD17_+9_a_6	27	49.01	3.41	12.96	5.88	0.16	14.65	10.02	2.70	0.582	0.4338	0.1763	0.0165	877	164
KD17_+9_a_8	27	48.88	3.48	13.03	5.95	0.20	14.44	10.24	2.77	0.577	0.3034	0.1216	0.0146	599	144
KD17_+9_a_9	27	48.69	3.38	12.81	7.16	0.25	13.87	10.08	2.75	0.553	0.3424	0.1013	0.0114	507	114
KD17_+9_a_10	27	49.47	3.38	12.89	5.96	0.19	14.25	10.14	2.75	0.513	0.3135	0.1159	0.0121	572	119
KD17_+9_b_1	27	49.21	3.41	13.09	5.42	0.17	14.42	10.40	2.79	0.565	0.3922	0.1121	0.0114	554	113
KD17_+9_b_2	27	49.47	3.86	12.44	4.91	0.27	15.31	9.84	2.71	0.607	0.4880	0.0893	0.0182	440	179
KD17_+9_b_3	27	49.64	3.32	13.00	5.53	0.22	14.09	10.30	2.82	0.552	0.3758	0.1389	0.0117	684	115
KD17_+9_b_4	27	49.49	3.35	12.81	5.55	0.22	14.39	10.45	2.58	0.583	0.3894	0.1659	0.0202	822	200
KD17_+9_b_5	27	49.38	3.34	13.06	5.46	0.17	14.32	10.29	2.95	0.549	0.3746	0.0950	0.0117	472	116
KD17_+9_b_6	27	49.49	3.41	12.99	5.60	0.19	14.20	10.21	2.87	0.551	0.4178	0.0587	0.0135	291	134
KD17_+9_b_7	27	49.92	3.71	12.79	4.94	0.21	14.49	9.65	3.02	0.666	0.4450	0.1324	0.0184	654	182
KD17_+9_b_8	27	49.55	3.48	12.71	5.57	0.28	14.22	10.50	2.71	0.513	0.3670	0.0899	0.0125	443	123
KD17_+9_b_9	27	49.18	3.47	12.91	5.50	0.29	14.76	10.35	2.57	0.548	0.3479	0.0713	0.0111	353	110
KD17_+14_1	28.05	49.38	3.31	13.02	5.81	0.20	13.90	10.58	2.77	0.485	0.4233	0.1044	0.0106	518	105
KD17_+14_2	28.05	49.33	3.33	12.95	6.10	0.29	13.95	10.63	2.48	0.483	0.3777	0.0678	0.0090	336	89
KD17_+14_3	28.05	49.24	3.34	12.87	5.98	0.20	14.15	10.68	2.55	0.514	0.3541	0.1095	0.0137	544	136
KD17_+14_4	28.05	49.41	3.46	12.98	5.81	0.20	13.91	10.60	2.71	0.480	0.3438	0.0922	0.0105	451	103
KD17_+14_5	28.05	49.92	3.84	12.75	4.79	0.29	14.53	9.47	3.04	0.757	0.5198	0.0822	0.0118	404	116
KD17_+14_7	28.05	49.59	3.36	13.02	5.83	0.16	13.90	10.60	2.59	0.516	0.3183	0.1024	0.0122	508	121
KD17_+14_8	28.05	52.68	3.28	13.50	4.03	0.23	13.53	8.42	2.76	1.102	0.3849	0.0537	0.0202	266	200
KD17_+14_9	28.05	49.62	3.31	13.04	5.78	0.20	13.82	10.67	2.61	0.512	0.3560	0.0794	0.0080	393	79
KD17_+14_10	28.05	49.29	3.62	12.39	5.53	0.27	14.70	10.35	2.72	0.591	0.4261	0.1155	0.0099	571	98
KD17_+14_11	28.05	49.83	3.64	12.82	5.56	0.17	14.63	10.38	1.86	0.538	0.4524	0.1038	0.0134	520	134
KD17_+14_12	28.05	49.08	3.84	12.50	5.07	0.20	15.41	9.87	1.61	1.854	0.4498	0.1004	0.0081	495	80
KD17_+14_13	28.05	49.66	3.35	13.08	5.87	0.26	13.56	10.66	2.68	0.500	0.3161	0.0547	0.0106	271	105
KD17_+14_14	28.05	49.40	3.37	13.03	5.90	0.25	13.82	10.58	2.72	0.489	0.3358	0.0941	0.0106	464	105
KD17_+14_15	28.05	49.11	3.32	13.05	5.85	0.26	13.97	10.73	2.69	0.517	0.3713	0.1083	0.0109	541	109
KD17_+14_16	28.05	49.15	3.40	13.06	5.83	0.22	14.03	10.78	2.58	0.510	0.3197	0.1052	0.0140	522	139
KD17_+14_17	28.05	49.44	3.37	13.00	5.87	0.23	13.71	10.85	2.61	0.496	0.3141	0.0949	0.0151	471	150

Sample Name	Depth relative to Ash -33 (m)	SiO2	TiO2	Al2O3	MgO	MnO	FeO	CaO	Na2O	K2O	P2O5	SO2	Cl	S	Cl
KD17_+14_18	28.05	49.01	3.34	13.09	5.91	0.19	13.85	10.67	2.88	0.564	0.3847	0.1069	0.0090	534	90
KD17_+14_19	28.05	49.23	3.37	13.06	6.02	0.19	13.90	10.51	2.68	0.578	0.3529	0.0907	0.0065	453	65
KD17_+14_20	28.05	49.40	3.32	13.10	5.88	0.23	13.91	10.49	2.71	0.531	0.3184	0.1049	0.0147	523	147
KD17_+18_a_2	29.28	49.43	3.82	12.71	4.18	0.26	15.56	9.87	2.81	0.719	0.4949	0.1379	0.0082	670	80
KD17_+18_a_3	29.28	48.43	3.80	12.73	5.13	0.28	15.55	9.96	2.78	0.657	0.4551	0.2070	0.0129	1009	126
KD17_+18_a_5	29.28	48.67	3.75	12.73	5.81	0.29	14.59	10.85	2.13	0.588	0.4670	0.1108	0.0145	542	142
KD17_+18_a_6	29.28	48.45	3.31	13.10	5.66	0.18	15.11	10.68	2.08	1.007	0.3223	0.0880	0.0091	429	89
KD17_+18_a_7	29.28	48.54	3.13	13.11	6.10	0.21	14.32	10.94	2.71	0.467	0.3824	0.0880	0.0111	435	110
KD17_+18_a_8	29.28	51.54	3.32	12.79	3.87	0.28	14.59	8.67	3.01	1.181	0.5917	0.1371	0.0236	666	229
KD17_+18_a_9	29.28	49.16	3.81	12.63	4.82	0.25	15.31	9.86	2.79	0.680	0.4579	0.2306	0.0108	1131	106
KD17_+18_b_1	29.28	49.93	3.43	12.93	5.78	0.15	13.24	10.70	2.51	0.787	0.3975	0.1280	0.0146	1088	153
KD17_+18_b_2	29.28	50.07	3.03	13.49	5.49	0.16	13.36	10.49	2.90	0.585	0.3435	0.0820	0.0133	936	131
KD17_+18_b_3	29.28	49.77	3.43	12.87	5.21	0.19	14.57	9.92	2.95	0.612	0.3684	0.0730	0.0129	408	125
KD17_+18_b_4	29.28	50.40	3.59	12.87	4.85	0.23	14.41	9.31	2.96	0.768	0.5027	0.0931	0.0149	325	66
KD17_+18_b_5	29.28	50.07	3.45	12.86	5.16	0.22	14.11	10.09	2.95	0.644	0.3593	0.0789	0.0160	366	143
KD17_+18_b_6	29.28	50.53	3.45	12.82	4.63	0.23	14.70	9.41	2.90	0.773	0.4544	0.0692	0.0200	282	128
KD17_+18_b_7	29.28	50.01	3.45	12.65	5.26	0.16	14.27	10.16	2.93	0.672	0.3533	0.0688	0.0132	171	67
KD17_+18_b_8	29.28	50.75	3.46	12.56	5.01	0.21	14.61	9.41	2.64	0.611	0.3397	0.0815	0.3077	400	90
KD17_+18_b_9	29.28	50.30	3.85	12.93	4.46	0.30	14.75	8.86	2.90	1.020	0.4782	0.1462	0.0158	796	90
KD17_+18_b_10	29.28	49.97	3.22	12.64	5.12	0.25	14.91	9.85	3.12	0.420	0.4330	0.0720	0.0075	923	151
KD17_+18_b_11	29.28	49.68	3.47	12.38	4.09	0.22	17.26	9.20	2.47	0.753	0.4008	0.0672	0.0111	373	75
KD17_+18_b_12	29.28	50.20	3.48	12.66	5.01	0.22	15.10	9.61	2.36	0.835	0.3919	0.1135	0.0120	230	71
KD17_+18_b_13	29.28	50.51	3.55	12.48	4.76	0.28	14.55	9.81	2.83	0.627	0.5021	0.0890	0.0112	456	124
KD17_+24_a_1	30.36	49.85	3.09	13.26	5.37	0.17	14.14	10.31	2.69	0.640	0.3658	0.0913	0.0193	452	191
KD17_+24_a_2	30.36	50.88	3.39	13.32	4.40	0.29	14.17	8.66	3.28	1.008	0.4797	0.1083	0.0208	537	206
KD17_+24_a_3	30.36	49.36	3.17	13.12	5.34	0.25	14.76	10.09	2.89	0.554	0.3150	0.1412	0.0136	701	135
KD17_+24_a_4	30.36	49.08	3.17	13.29	5.69	0.29	14.72	10.40	2.36	0.555	0.3207	0.1238	0.0101	617	101
KD17_+24_a_5	30.36	49.52	3.26	12.76	5.57	0.27	14.57	10.24	2.75	0.580	0.3297	0.1351	0.0100	664	98
KD17_+24_a_6	30.36	49.39	3.20	13.20	5.63	0.28	14.74	10.60	2.00	0.533	0.3016	0.1004	0.0135	500	134
KD17_+24_a_7	30.36	49.73	3.24	13.15	5.38	0.20	14.40	9.92	2.92	0.583	0.3490	0.0955	0.0203	469	199
KD17_+24_a_8	30.36	49.81	3.22	12.94	5.16	0.31	14.58	9.65	3.08	0.684	0.4235	0.1205	0.0173	597	171
KD17_+24_a_9	30.36	49.10	3.15	13.17	5.69	0.27	14.28	10.43	2.84	0.518	0.3894	0.1500	0.0087	741	86
KD17_+24_a_10	30.36	49.51	3.18	13.17	4.72	0.18	14.71	10.71	2.83	0.540	0.3035	0.1364	0.0132	674	130
KD17_+24_a_11	30.36	49.52	3.20	12.97	5.51	0.24	14.50	10.24	2.82	0.541	0.3554	0.0817	0.0145	405	144
KD17_+24_b_1	30.36	50.21	3.14	13.22	4.94	0.25	14.05	10.00	3.02	0.679	0.3448	0.1259	0.0145	620	143
KD17_+24_b_2	30.36	49.61	3.15	12.89	5.11	0.29	14.91	10.03	2.78	0.616	0.4373	0.1591	0.0135	789	134
KD17_+24_b_3	30.36	49.42	3.14	13.05	5.57	0.22	14.35	10.31	2.86	0.517	0.4170	0.1232	0.0157	612	156
KD17_+24_b_4	30.36	49.73	3.17	12.94	5.46	0.20	14.60	10.17	2.81	0.526	0.2893	0.0961	0.0125	477	124
KD17_+24_b_5	30.36	49.89	3.13	12.96	5.36	0.24	14.12	10.37	2.87	0.600	0.3681	0.0756	0.0108	374	107
KD17_+24_b_6	30.36	50.30	3.19	12.89	5.89	0.27	14.13	10.39	1.96	0.524	0.4057	0.0517	0.0084	256	83
KD17_+24_b_7	30.36	49.36	3.19	12.94	5.42	0.18	14.52	10.46	2.90	0.519	0.3311	0.1468	0.0183	721	180
KD17_+24_b_8	30.36	49.41	3.10	12.89	5.49	0.19	14.50	10.73	2.43	0.783	0.3487	0.1113	0.0145	549	143
KD17_+24_b_9	30.36	51.03	3.40	12.77	4.49	0.21	14.60	9.45	2.83	0.704	0.4463	0.0718	0.0082	355	81
KD17_+31_a_1	30.95	49.32	3.72	12.72	5.37	0.23	14.80	9.92	2.79	0.602	0.4659	0.0638	0.0105	317	104
KD17_+31_a_2	30.95	48.78	3.75	12.58	5.60	0.27	15.28	9.71	2.86	0.635	0.3625	0.1518	0.0118	743	115

Supplement Paper II

Sample Name	Depth relative to Ash -33 (m)	SiO2	TiO2	Al2O3	MgO	MnO	FeO	CaO	Na2O	K2O	P2O5	SO2	Cl	S	Cl
KD17_+31_a_3	30.95	48.97	3.79	12.70	5.50	0.19	14.95	9.87	2.89	0.588	0.3989	0.1384	0.0101	684	100
KD17_+31_a_4	30.95	49.13	3.71	12.62	5.29	0.28	15.14	9.78	2.85	0.624	0.4468	0.1167	0.0139	578	138
KD17_+31_a_5	30.95	49.62	3.70	12.61	5.23	0.37	14.93	9.60	2.78	0.593	0.3970	0.1552	0.0213	771	211
KD17_+31_a_6	30.95	49.10	3.79	12.58	5.22	0.24	15.28	9.74	2.91	0.607	0.3843	0.1354	0.0153	661	149
KD17_+31_a_7	30.95	48.43	3.77	12.46	5.52	0.34	15.65	9.81	2.73	0.631	0.4616	0.1835	0.0110	907	109
KD17_+31_a_8	30.95	49.20	3.78	12.71	4.80	0.26	15.32	9.79	2.91	0.588	0.4500	0.1827	0.0120	891	117
KD17_+31_a_9	30.95	49.10	3.76	12.72	5.11	0.28	15.19	9.82	2.84	0.592	0.4028	0.1639	0.0206	805	202
KD17_+31_a_10	30.95	49.10	3.68	12.66	5.13	0.27	15.47	9.71	2.81	0.577	0.4328	0.1524	0.0093	757	92
KD17_+31_a_11	30.95	48.99	3.78	12.65	5.09	0.23	15.41	9.70	2.89	0.672	0.3907	0.1724	0.0182	842	178
KD17_+31_b_1	30.95	50.24	3.74	12.68	4.95	0.24	14.73	9.71	2.56	0.640	0.4037	0.1009	0.0143	495	140
KD17_+31_b_2	30.95	49.44	3.72	12.49	5.02	0.28	15.27	9.68	2.85	0.584	0.4958	0.1602	0.0161	795	160
KD17_+31_b_3	30.95	49.45	3.71	12.41	5.20	0.22	15.18	9.96	2.78	0.592	0.4333	0.0708	0.0049	354	49
KD17_+31_b_4	30.95	49.16	3.88	12.16	5.02	0.24	15.51	9.95	2.94	0.624	0.4253	0.0875	0.0101	431	99
KD17_+31_b_6	30.95	49.51	3.71	12.63	4.99	0.27	15.03	9.78	2.88	0.613	0.4097	0.1502	0.0173	740	170
KD17_+31_b_7	30.95	49.43	3.72	12.50	5.10	0.22	15.05	9.86	2.99	0.573	0.4526	0.0828	0.0154	405	151
KD17_+31_b_8	30.95	49.38	3.68	12.59	5.10	0.23	15.23	9.88	2.82	0.603	0.3500	0.1176	0.0173	583	171
KD17_+31_b_9	30.95	48.98	3.71	12.56	5.16	0.23	15.41	9.97	2.74	0.600	0.4749	0.1498	0.0128	751	128
KD17_+36_a_1	31.48	49.34	3.76	12.78	4.92	0.28	14.96	9.80	2.85	0.723	0.4585	0.1106	0.0153	542	150
KD17_+36_a_2	31.48	49.11	3.66	12.75	5.40	0.19	14.84	10.05	2.85	0.650	0.3767	0.1095	0.0112	534	109
KD17_+36_a_5	31.48	49.45	3.61	12.63	5.35	0.17	14.82	10.02	2.79	0.618	0.4411	0.0861	0.0151	424	148
KD17_+36_a_6	31.48	49.16	3.63	12.57	5.22	0.27	15.30	9.96	2.69	0.651	0.4359	0.0869	0.0127	432	126
KD17_+36_a_7	31.48	49.03	3.55	12.56	5.68	0.23	14.81	9.98	2.95	0.592	0.4943	0.1097	0.0180	542	178
KD17_+36_a_8	31.48	49.66	3.70	12.51	5.17	0.26	14.82	9.59	2.96	0.708	0.4799	0.1213	0.0105	599	104
KD17_+36_a_9	31.48	49.78	3.64	12.73	4.95	0.24	14.78	9.97	2.76	0.601	0.4007	0.1443	0.0138	704	135
KD17_+36_a_10	31.48	48.54	3.45	12.61	5.32	0.28	15.45	10.34	2.86	0.589	0.3896	0.1439	0.0150	708	148
KD17_+36_a_11	31.48	49.24	3.60	12.71	5.38	0.22	14.94	9.93	2.76	0.588	0.4835	0.1456	0.0095	714	93
KD17_+36_b_1	31.48	49.29	3.63	12.57	5.10	0.31	15.81	9.85	2.33	0.610	0.3977	0.1003	0.0114	497	113
KD17_+36_b_2	31.48	50.44	3.61	12.87	5.18	0.24	14.20	10.08	2.32	0.602	0.3614	0.0767	0.0133	382	132
KD17_+36_b_3	31.48	53.03	3.29	13.48	3.73	0.20	13.78	8.17	2.39	1.361	0.4972	0.0627	0.0225	305	219
KD17_+36_b_4	31.48	49.08	3.64	12.56	5.22	0.16	15.05	10.08	2.28	1.372	0.4262	0.1170	0.0174	574	171
KD17_+36_b_5	31.48	50.13	3.68	12.57	4.76	0.25	14.99	9.56	2.80	0.719	0.3968	0.1106	0.0226	545	222
KD17_+36_b_6	31.48	49.43	3.58	12.48	5.26	0.25	15.16	10.02	2.80	0.576	0.3466	0.0972	0.0146	483	145
KD17_+36_b_7	31.48	49.81	3.82	12.74	4.89	0.28	14.38	10.15	2.84	0.616	0.3707	0.0902	0.0138	447	136
KD17_+36_b_8	31.48	49.98	3.58	12.87	5.15	0.19	14.46	10.36	2.17	0.701	0.4151	0.1210	0.0111	602	110
KD17_+36_b_9	31.48	49.79	3.62	12.86	5.30	0.23	14.86	10.06	2.24	0.649	0.3356	0.0611	0.0124	306	124
KD17_+36_b_10	31.48	49.72	3.63	12.70	4.89	0.27	14.67	10.01	2.90	0.626	0.4623	0.1046	0.0156	517	154
KD17_+36_b_11	31.48	49.59	3.58	12.26	5.95	0.29	14.61	10.50	2.14	0.567	0.4347	0.0857	0.0051	430	51
KD17_+42_a_1	33.54	48.84	3.59	13.20	5.73	0.22	14.06	10.22	3.02	0.627	0.4192	0.0503	0.0101	248	99
KD17_+42_a_2	33.54	49.12	3.62	13.05	5.99	0.24	14.08	10.20	2.56	0.591	0.4214	0.1237	0.0090	616	90
KD17_+42_a_3	33.54	48.73	3.57	13.29	5.68	0.22	14.27	10.13	2.94	0.642	0.4114	0.0990	0.0140	485	137
KD17_+42_a_5	33.54	49.97	3.68	13.25	5.13	0.17	13.83	9.75	3.00	0.688	0.4404	0.0675	0.0181	331	177
KD17_+42_a_6	33.54	49.43	3.65	13.24	5.26	0.23	14.18	9.89	2.90	0.689	0.4439	0.0708	0.0113	351	112
KD17_+42_a_7	33.54	50.50	3.49	12.87	4.75	0.18	14.58	9.48	2.64	0.862	0.5191	0.1224	0.0183	603	180
KD17_+42_a_8	33.54	49.31	3.52	13.18	5.88	0.24	14.13	10.31	2.34	0.618	0.3983	0.0745	0.0116	369	115
KD17_+42_a_9	33.54	49.35	3.52	13.05	5.54	0.28	13.92	10.28	2.89	0.603	0.4523	0.1102	0.0083	545	82

Supplement Paper II

Sample Name	Depth relative to Ash -33 (m)	SiO2	TiO2	Al2O3	MgO	MnO	FeO	CaO	Na2O	K2O	P2O5	SO2	Cl	S	Cl
KD17_+42_a_11	33.54	48.89	3.50	13.15	6.14	0.18	13.83	10.24	2.94	0.606	0.4356	0.0898	0.0099	445	98
KD17_+42_b_1	33.54	49.82	3.61	12.96	6.02	0.13	13.09	10.70	2.58	0.555	0.4604	0.0538	0.0088	268	88
KD17_+42_b_2	33.54	48.82	3.55	12.93	5.69	0.21	14.05	10.77	2.74	0.734	0.4036	0.0937	0.0140	469	140
KD17_+42_b_3	33.54	49.96	3.53	13.10	5.62	0.21	13.77	10.36	2.42	0.575	0.3553	0.0825	0.0172	404	168
KD17_+42_b_4	33.54	49.53	3.53	12.91	5.49	0.24	14.09	10.31	2.76	0.579	0.4447	0.1065	0.0100	525	98
KD17_+42_b_5	33.54	49.63	3.59	12.93	5.40	0.20	13.92	10.23	2.94	0.618	0.4232	0.1132	0.0157	559	155
KD17_+42_b_6	33.54	49.92	3.58	13.06	5.72	0.18	13.56	10.32	2.58	0.638	0.3561	0.0771	0.0137	379	135
KD17_+42_b_7	33.54	49.80	3.55	12.78	5.61	0.25	13.87	10.22	2.84	0.580	0.3816	0.1117	0.0155	552	153
KD17_+42_b_8	33.54	49.08	3.53	12.83	6.87	0.24	12.09	12.20	2.19	0.431	0.4304	0.0992	0.0048	493	48
KD17_+42_b_9	33.54	49.62	3.59	12.90	5.46	0.30	13.89	10.29	2.89	0.557	0.3866	0.0982	0.0175	484	173
KD17_+42_b_10	33.54	49.27	3.60	13.02	5.51	0.18	14.21	10.32	2.75	0.664	0.3773	0.0892	0.0131	444	130
KD17_+46_a_1	34.21	48.73	4.05	12.33	4.86	0.32	16.43	9.13	2.83	0.654	0.5054	0.1512	0.0149	748	147
KD17_+46_a_2	34.21	48.97	4.14	12.44	4.47	0.27	16.20	9.31	2.92	0.686	0.4569	0.1152	0.0180	562	176
KD17_+46_a_3	34.21	49.76	3.60	12.85	4.57	0.29	15.19	9.65	2.85	0.644	0.4462	0.1245	0.0122	614	120
KD17_+46_a_4	34.21	49.32	3.58	12.92	5.11	0.27	15.06	9.61	2.95	0.626	0.4150	0.1140	0.0162	563	160
KD17_+46_a_5	34.21	48.56	4.02	12.47	5.03	0.31	16.17	9.23	2.89	0.662	0.4727	0.1586	0.0202	785	200
KD17_+46_a_6	34.21	49.15	4.03	12.17	5.19	0.23	15.97	9.28	2.80	0.604	0.4239	0.1466	0.0171	730	170
KD17_+46_a_7	34.21	47.93	3.84	12.26	6.47	0.31	15.89	9.20	2.92	0.623	0.3942	0.1463	0.0176	741	178
KD17_+46_a_8	34.21	48.91	3.79	12.15	5.78	0.27	15.78	9.26	2.79	0.657	0.4246	0.1582	0.0135	794	135
KD17_+46_a_9	34.21	48.73	3.80	12.33	6.13	0.22	15.45	9.22	2.81	0.702	0.4759	0.1203	0.0225	607	227
KD17_+46_a_10	34.21	48.55	4.03	12.38	5.17	0.29	16.24	9.20	2.85	0.675	0.4429	0.1582	0.0142	782	140
KD17_+46_a_11	34.21	48.46	4.08	12.29	5.11	0.29	16.29	9.51	2.52	0.781	0.4432	0.2024	0.0142	1008	141
KD17_+46_b_1	34.21	50.29	3.36	12.66	5.14	0.29	14.38	9.92	2.77	0.646	0.4243	0.0956	0.0138	701	158
KD17_+46_b_2	34.21	50.22	3.37	12.89	4.79	0.22	14.68	9.71	2.82	0.699	0.4489	0.1394	0.0167	552	160
KD17_+46_b_3	34.21	50.22	3.34	12.64	4.89	0.18	15.24	9.68	2.69	0.625	0.4074	0.0728	0.0162	731	120
KD17_+46_b_4	34.21	49.65	3.60	12.57	4.88	0.22	15.22	9.78	2.93	0.633	0.4105	0.1037	0.0105	607	108
KD17_+46_b_5	34.21	50.02	3.45	12.67	4.93	0.24	15.06	9.62	2.85	0.643	0.3878	0.1242	0.0103	650	140
KD17_+46_b_6	34.21	49.99	3.60	12.73	4.79	0.23	15.26	9.59	2.60	0.649	0.4002	0.1529	0.0142	680	174
KD17_+46_b_7	34.21	49.82	3.61	12.96	6.02	0.13	13.09	10.70	2.58	0.555	0.4604	0.0538	0.0088	444	131
KD17_+46_b_8	34.21	48.82	3.55	12.93	5.69	0.21	14.05	10.77	2.74	0.734	0.4036	0.0937	0.0140	405	172
KD17_+46_b_9	34.21	49.96	3.53	13.10	5.62	0.21	13.77	10.36	2.42	0.575	0.3553	0.0825	0.0172	725	129
KD17_+51_a_1	34.76	49.81	3.56	12.46	5.05	0.27	15.20	9.63	2.71	0.674	0.4634	0.1435	0.0198	705	194
KD17_+51_a_2	34.76	49.38	3.52	12.70	5.15	0.23	15.43	9.56	2.76	0.697	0.3926	0.1566	0.0139	768	136
KD17_+51_a_3	34.76	49.72	3.55	12.71	4.97	0.21	15.51	9.66	2.38	0.688	0.4347	0.1537	0.0140	759	138
KD17_+51_a_4	34.76	49.70	3.42	12.68	5.06	0.20	15.14	9.78	2.76	0.688	0.4403	0.1307	0.0096	640	94
KD17_+51_a_5	34.76	49.42	3.42	12.67	5.39	0.29	15.00	9.69	2.82	0.677	0.4331	0.1789	0.0166	878	163
KD17_+51_a_6	34.76	49.45	3.53	12.64	5.03	0.28	15.44	9.70	2.69	0.650	0.4044	0.1811	0.0127	897	126
KD17_+51_a_7	34.76	49.95	3.43	12.81	5.17	0.24	14.62	9.77	2.81	0.640	0.3812	0.1583	0.0147	771	143
KD17_+51_a_8	34.76	50.17	3.44	12.70	5.04	0.23	14.89	9.77	2.64	0.655	0.3811	0.0833	0.0074	409	73
KD17_+51_a_9	34.76	50.13	3.40	12.50	5.20	0.27	14.97	9.86	2.52	0.640	0.3482	0.1461	0.0124	716	121
KD17_+51_a_11	34.76	49.45	3.52	12.85	5.11	0.29	15.14	9.69	2.61	0.634	0.5439	0.1419	0.0183	691	178
KD17_+51_b_1	34.76	49.97	3.22	12.64	5.12	0.25	14.91	9.85	3.12	0.420	0.4330	0.0720	0.0075	364	76
KD17_+51_b_2	34.76	49.68	3.47	12.38	4.09	0.22	17.26	9.20	2.47	0.753	0.4008	0.0672	0.0111	331	109
KD17_+51_b_3	34.76	50.20	3.48	12.66	5.01	0.22	15.10	9.61	2.36	0.835	0.3919	0.1135	0.0120	556	117
KD17_+51_b_4	34.76	50.51	3.55	12.48	4.76	0.28	14.55	9.81	2.83	0.627	0.5021	0.0890	0.0112	442	111

Supplement Paper II

Sample Name	Depth relative to Ash -33 (m)	SiO2	TiO2	Al2O3	MgO	MnO	FeO	CaO	Na2O	K2O	P2O5	SO2	Cl	S	Cl
KD17_+51_b_5	34.76	50.29	3.36	12.66	5.14	0.29	14.38	9.92	2.77	0.646	0.4243	0.0956	0.0138	474	137
KD17_+51_b_6	34.76	50.22	3.37	12.89	4.79	0.22	14.68	9.71	2.82	0.699	0.4489	0.1394	0.0167	692	166
KD17_+51_b_7	34.76	50.22	3.34	12.64	4.89	0.18	15.24	9.68	2.69	0.625	0.4074	0.0728	0.0162	361	161
KD17_+51_b_8	34.76	49.65	3.60	12.57	4.88	0.22	15.22	9.78	2.93	0.633	0.4105	0.1037	0.0105	512	104
KD17_+51_b_9	34.76	50.02	3.45	12.67	4.93	0.24	15.06	9.62	2.85	0.643	0.3878	0.1242	0.0103	621	103
KD17_+51_b_10	34.76	49.99	3.60	12.73	4.79	0.23	15.26	9.59	2.60	0.649	0.4002	0.1529	0.0142	760	141
KD17_+54_a_1	35.14	49.42	2.98	13.33	5.94	0.23	13.89	10.42	2.84	0.527	0.2692	0.1404	0.0148	692	146
KD17_+54_a_2	35.14	50.45	3.56	12.74	5.14	0.19	14.94	9.49	2.27	0.706	0.3799	0.1283	0.0152	635	150
KD17_+54_a_3	35.14	49.90	2.98	13.12	5.73	0.30	14.06	10.16	2.76	0.530	0.3629	0.0942	0.0086	469	85
KD17_+54_a_4	35.14	49.44	3.03	13.35	6.00	0.27	14.37	10.31	2.19	0.548	0.3276	0.1507	0.0124	745	123
KD17_+54_a_5	35.14	49.64	3.03	13.31	5.78	0.24	13.92	10.36	2.75	0.512	0.3001	0.1468	0.0122	724	120
KD17_+54_a_6	35.14	49.05	3.01	13.30	6.03	0.27	13.96	10.54	2.90	0.580	0.2704	0.0827	0.0133	409	131
KD17_+54_a_7	35.14	50.01	2.93	13.24	5.74	0.21	14.02	10.20	2.70	0.527	0.3031	0.0925	0.0155	462	155
KD17_+54_a_8	35.14	50.33	3.02	13.21	5.92	0.25	13.54	10.34	2.49	0.525	0.2700	0.0911	0.0205	452	203
KD17_+54_a_9	35.14	49.44	3.03	13.02	5.76	0.29	14.40	10.26	2.78	0.536	0.3498	0.1102	0.0146	550	146
KD17_+54_a_10	35.14	49.91	2.97	13.21	5.72	0.25	13.82	10.44	2.75	0.518	0.3055	0.0881	0.0089	439	89
KD17_+54_a_11	35.14	49.23	3.00	13.03	5.76	0.26	14.53	10.50	2.70	0.562	0.2415	0.1717	0.0137	855	136
KD17_+54_b_1	35.14	49.53	3.53	12.91	5.49	0.24	14.09	10.31	2.76	0.579	0.4447	0.1065	0.0100	228	122
KD17_+54_b_2	35.14	49.63	3.59	12.93	5.40	0.20	13.92	10.23	2.94	0.618	0.4232	0.1132	0.0157	440	143
KD17_+54_b_3	35.14	49.92	3.58	13.06	5.72	0.18	13.56	10.32	2.58	0.638	0.3561	0.0771	0.0137	443	93
KD17_+54_b_4	35.14	49.80	3.55	12.78	5.61	0.25	13.87	10.22	2.84	0.580	0.3816	0.1117	0.0155	316	115
KD17_+54_b_5	35.14	49.08	3.53	12.83	6.87	0.24	12.09	12.20	2.19	0.431	0.4304	0.0992	0.0048	767	153
KD17_+54_b_6	35.14	49.62	3.59	12.90	5.46	0.30	13.89	10.29	2.89	0.557	0.3866	0.0982	0.0175	604	117
KD17_+54_b_8	35.14	49.29	3.63	12.57	5.10	0.31	15.81	9.85	2.33	0.610	0.3977	0.1003	0.0114	803	106
KD17_+54_b_9	35.14	50.44	3.61	12.87	5.18	0.24	14.20	10.08	2.32	0.602	0.3614	0.0767	0.0133	794	104
KD17_+54_b_10	35.14	53.03	3.29	13.48	3.73	0.20	13.78	8.17	2.39	1.361	0.4972	0.0627	0.0225	215	59
KD17_+60_a_1	35.98	49.60	3.15	13.67	5.43	0.14	13.81	10.32	2.83	0.614	0.3294	0.1024	0.0122	504	120
KD17_+60_a_2	35.98	50.21	3.43	12.97	5.26	0.18	14.14	9.88	2.79	0.635	0.3860	0.1007	0.0145	499	144
KD17_+60_a_3	35.98	50.41	3.34	13.01	5.12	0.20	14.08	9.69	2.88	0.744	0.3672	0.1435	0.0100	709	99
KD17_+60_a_4	35.98	49.93	3.63	13.14	4.84	0.27	14.26	10.03	2.62	0.711	0.4320	0.1231	0.0106	608	105
KD17_+60_a_5	35.98	49.47	3.50	12.93	5.22	0.24	14.72	9.93	2.94	0.634	0.3238	0.0782	0.0145	384	142
KD17_+60_a_6	35.98	49.54	3.50	13.05	5.03	0.23	14.72	10.07	2.78	0.623	0.3405	0.1072	0.0169	526	166
KD17_+60_a_7	35.98	49.67	3.53	12.84	5.90	0.20	14.21	9.77	2.53	0.748	0.4669	0.1141	0.0136	563	134
KD17_+60_a_8	35.98	49.23	3.70	12.92	4.13	0.32	16.65	8.93	2.97	0.680	0.3886	0.0642	0.0186	321	186
KD17_+60_a_9	35.98	49.35	3.48	12.92	5.20	0.21	14.89	9.83	2.93	0.683	0.3744	0.1183	0.0138	579	135
KD17_+60_a_10	35.98	49.79	3.52	12.94	5.18	0.21	14.85	9.60	2.71	0.699	0.3943	0.0962	0.0175	476	173
KD17_+60_a_11	35.98	50.32	3.47	12.86	5.31	0.25	14.85	10.04	1.67	0.664	0.4369	0.1007	0.0190	499	188
KD17_+60_b_1	35.98	49.93	3.43	12.93	5.78	0.15	13.24	10.70	2.51	0.787	0.3975	0.1280	0.0146	631	144
KD17_+60_b_2	35.98	50.07	3.03	13.49	5.49	0.16	13.36	10.49	2.90	0.585	0.3435	0.0820	0.0133	402	130
KD17_+60_b_3	35.98	49.77	3.43	12.87	5.21	0.19	14.57	9.92	2.95	0.612	0.3684	0.0730	0.0129	362	128
KD17_+60_b_4	35.98	50.40	3.59	12.87	4.85	0.23	14.41	9.31	2.96	0.768	0.5027	0.0931	0.0149	464	148
KD17_+60_b_5	35.98	50.07	3.45	12.86	5.16	0.22	14.11	10.09	2.95	0.644	0.3593	0.0789	0.0160	390	158
KD17_+60_b_6	35.98	50.53	3.45	12.82	4.63	0.23	14.70	9.41	2.90	0.773	0.4544	0.0692	0.0200	343	198
KD17_+60_b_7	35.98	50.01	3.45	12.65	5.26	0.16	14.27	10.16	2.93	0.672	0.3533	0.0688	0.0132	338	130
KD17_+60_b_8	35.98	50.75	3.46	12.56	5.01	0.21	14.61	9.41	2.64	0.611	0.3397	0.0815	0.3077	399	3014

Supplement Paper II

Sample Name	Depth relative to Ash -33 (m)	SiO2	TiO2	Al2O3	MgO	MnO	FeO	CaO	Na2O	K2O	P2O5	SO2	Cl	S	Cl
KD17_+68_1	37.4	49.23	3.55	12.73	5.35	0.32	14.87	9.99	2.81	0.635	0.4196	0.0965	0.0130	480	129
KD17_+68_6	37.4	49.41	3.56	12.70	5.19	0.21	15.09	9.79	2.83	0.632	0.4379	0.1253	0.0089	614	87
KD17_+68_7	37.4	49.09	3.60	12.75	5.20	0.23	15.13	10.08	2.86	0.576	0.3565	0.1159	0.0129	569	127
KD17_+68_8	37.4	50.92	3.29	12.66	4.55	0.22	14.74	9.08	2.95	0.896	0.5694	0.1131	0.0201	567	202
KD17_+68_9	37.4	49.07	3.53	12.69	5.25	0.27	15.01	10.12	2.85	0.614	0.4486	0.1455	0.0127	724	126
KD17_+68_10	37.4	49.47	3.50	12.85	5.17	0.20	14.85	9.99	2.93	0.574	0.3402	0.1084	0.0174	538	173
KD17_+68_11	37.4	49.48	3.52	12.81	5.01	0.23	15.01	9.89	2.85	0.624	0.4465	0.1241	0.0106	616	105
KD17_+68_12	37.4	49.89	3.49	13.08	5.08	0.23	14.26	9.76	3.07	0.696	0.3710	0.0573	0.0147	283	145
KD17_+68_13	37.4	49.11	3.50	12.86	5.20	0.20	15.17	10.06	2.33	1.090	0.3744	0.0910	0.0145	447	142
KD17_+68_14	37.4	49.25	3.45	12.91	5.24	0.27	15.05	9.85	2.88	0.578	0.3841	0.1156	0.0132	575	131
KD17_+68_15	37.4	49.47	3.52	12.85	5.05	0.25	14.61	10.04	2.98	0.602	0.4536	0.1492	0.0164	731	161
KD17_+68_16	37.4	49.28	3.54	12.78	5.20	0.26	15.05	10.01	2.78	0.636	0.3565	0.0877	0.0141	438	141
KD17_+68_17	37.4	49.45	3.49	12.83	5.11	0.21	15.13	9.86	2.74	0.609	0.4322	0.1175	0.0089	588	89
KD17_+68_18	37.4	49.76	3.68	13.06	5.06	0.26	15.20	9.59	2.28	0.580	0.3527	0.1627	0.0180	815	180
KD17_+68_19	37.4	49.66	3.56	12.76	5.04	0.27	14.82	9.72	2.92	0.639	0.4702	0.1165	0.0137	574	135
KD17_+68_20	37.4	49.26	3.48	12.89	5.17	0.28	14.99	10.02	2.78	0.580	0.4459	0.0879	0.0122	434	121
KD17_+80_a_1	38.57	49.89	3.62	12.79	4.19	0.21	15.41	9.96	2.82	0.671	0.3388	0.0929	0.0116	452	113
KD17_+80_a_2	38.57	49.61	3.63	12.68	4.95	0.21	15.71	9.55	2.42	0.672	0.4097	0.1373	0.0119	681	118
KD17_+80_a_3	38.57	49.96	3.59	12.66	4.85	0.27	14.97	9.45	3.10	0.653	0.3685	0.1131	0.0120	557	118
KD17_+80_a_4	38.57	49.57	3.52	12.84	4.97	0.23	15.16	9.57	2.88	0.639	0.4459	0.1577	0.0184	778	181
KD17_+80_a_5	38.57	49.80	3.54	12.61	5.04	0.23	15.41	9.45	2.84	0.593	0.3125	0.1557	0.0171	768	168
KD17_+80_a_6	38.57	49.67	3.61	12.67	5.10	0.23	15.49	9.53	2.51	0.638	0.4082	0.1390	0.0154	684	151
KD17_+80_a_7	38.57	49.35	3.55	12.78	4.91	0.23	15.42	9.61	2.91	0.696	0.4048	0.1302	0.0106	636	103
KD17_+80_a_8	38.57	49.38	3.63	12.68	5.00	0.30	15.33	9.59	2.77	0.722	0.4734	0.1106	0.0184	546	181
KD17_+80_a_9	38.57	49.85	3.61	12.63	4.92	0.24	15.19	9.66	2.62	0.702	0.3971	0.1646	0.0204	813	201
KD17_+80_a_10	38.57	49.65	3.58	12.56	5.03	0.23	15.12	9.85	2.77	0.644	0.4166	0.1381	0.0109	677	107
KD17_+80_a_11	38.57	49.43	3.56	12.60	4.93	0.29	15.64	9.43	2.96	0.662	0.3535	0.1294	0.0140	638	138
KD17_+80_b_1	38.57	49.41	3.42	12.84	4.82	0.17	15.27	10.11	2.68	0.760	0.3477	0.1620	0.0099	808	99
KD17_+80_b_2	38.57	49.64	3.58	12.68	4.94	0.23	14.97	9.69	3.06	0.596	0.4606	0.1411	0.0090	694	88
KD17_+80_b_3	38.57	50.04	3.25	12.67	5.69	0.24	13.76	10.57	2.80	0.462	0.4159	0.1097	0.0053	551	53
KD17_+80_b_4	38.57	50.16	3.54	12.88	4.91	0.23	14.20	9.97	3.18	0.478	0.3262	0.1106	0.0109	549	108
KD17_+80_b_5	38.57	49.81	3.53	12.67	4.93	0.16	15.29	9.51	2.89	0.673	0.4145	0.1143	0.0139	563	137
KD17_+80_b_6	38.57	51.00	3.53	12.98	4.51	0.20	14.90	9.48	2.23	0.632	0.4182	0.1108	0.0109	551	108
KD17_+80_b_7	38.57	49.89	3.53	12.49	5.07	0.20	15.06	9.74	2.85	0.615	0.4659	0.0742	0.0127	369	126
KD17_+80_b_8	38.57	50.51	3.70	12.68	4.65	0.24	15.20	9.50	1.77	0.773	0.3682	0.0946	0.0105	465	103
KD17_+80_b_9	38.57	49.79	3.53	12.65	4.88	0.25	15.23	9.65	2.69	0.761	0.3733	0.1823	0.0158	903	156
KD17_+90_1	39.95	49.28	3.99	13.09	5.16	0.29	14.25	10.22	2.45	0.672	0.5122	0.0673	0.0111	335	110
KD17_+90_2	39.95	48.84	4.01	12.57	5.28	0.23	15.35	9.97	2.49	0.715	0.4323	0.1060	0.0111	529	111
KD17_+90_3	39.95	49.87	4.08	12.41	5.37	0.29	15.33	9.83	1.55	0.714	0.4344	0.1066	0.0159	525	156
KD17_+90_4	39.95	49.18	4.05	12.37	5.25	0.23	15.20	9.97	2.40	0.867	0.3779	0.0816	0.0120	402	118
KD17_+90_5	39.95	48.73	4.05	12.36	5.46	0.24	15.29	10.00	2.76	0.665	0.3762	0.0615	0.0152	302	149
KD17_+90_6	39.95	48.57	4.01	12.33	5.42	0.27	15.06	10.21	2.89	0.629	0.5026	0.0939	0.0076	471	76
KD17_+90_7	39.95	48.62	3.99	12.60	5.33	0.15	15.34	9.92	2.89	0.682	0.3812	0.0926	0.0147	457	145
KD17_+90_8	39.95	50.79	3.57	12.91	4.88	0.24	14.00	9.54	2.89	0.710	0.4052	0.0658	0.0137	325	135
KD17_+90_9	39.95	48.77	3.98	12.47	5.30	0.17	15.43	9.94	2.79	0.611	0.4482	0.0868	0.0151	434	151

Supplement Paper II

Sample Name	Depth relative to Ash -33 (m)	SiO2	TiO2	Al2O3	MgO	MnO	FeO	CaO	Na2O	K2O	P2O5	SO2	Cl	S	Cl
KD17_+90_10	39.95	49.81	3.72	12.51	5.21	0.24	14.65	9.90	2.82	0.700	0.3772	0.0651	0.0115	323	114
KD17_+90_11	39.95	48.97	4.03	12.37	5.33	0.25	15.54	10.00	2.31	0.647	0.4250	0.1050	0.0145	523	144
KD17_+90_12	39.95	48.94	4.02	12.46	5.39	0.25	14.89	10.01	2.83	0.647	0.4260	0.1113	0.0111	552	110
KD17_+90_13	39.95	49.20	4.00	12.30	5.39	0.29	15.21	9.97	2.40	0.680	0.4481	0.1061	0.0118	529	118
KD17_+90_14	39.95	48.68	4.02	12.54	5.39	0.23	15.23	9.88	2.83	0.702	0.3866	0.0858	0.0119	426	118
KD17_+90_16	39.95	48.67	3.95	12.45	5.38	0.23	15.57	9.76	2.79	0.632	0.4651	0.0927	0.0120	465	120
KD17_+90_18	39.95	54.93	2.79	13.08	3.66	0.19	12.59	7.96	2.89	1.377	0.4511	0.0546	0.0323	274	323
KD17_+90_19	39.95	49.90	3.46	12.54	4.95	0.24	15.04	9.72	2.93	0.650	0.4409	0.1125	0.0161	559	160
KD17_+90_20	39.95	49.08	3.99	12.27	5.33	0.26	15.22	9.88	2.77	0.672	0.4380	0.0672	0.0177	335	176
KD17_+94_a_1	40.79	49.44	3.89	12.63	4.89	0.28	15.15	9.39	2.85	0.809	0.4942	0.1506	0.0189	738	185
KD17_+94_a_2	40.79	49.08	3.88	12.71	4.99	0.21	15.47	9.61	1.98	1.348	0.5638	0.1390	0.0152	677	148
KD17_+94_a_3	40.79	49.46	3.84	12.67	5.07	0.29	14.93	9.45	2.86	0.757	0.4691	0.1843	0.0108	913	107
KD17_+94_a_4	40.79	48.85	3.86	12.62	5.03	0.26	15.34	9.57	2.95	0.805	0.5328	0.1711	0.0142	841	139
KD17_+94_a_5	40.79	49.38	3.83	12.43	4.92	0.26	15.36	9.49	2.75	0.826	0.5646	0.1580	0.0160	787	159
KD17_+94_a_6	40.79	48.59	3.86	12.66	5.20	0.31	15.50	9.52	2.85	0.764	0.5483	0.1923	0.0161	947	158
KD17_+94_a_7	40.79	48.95	3.87	12.58	5.04	0.32	15.27	9.51	2.83	0.877	0.5500	0.1703	0.0177	834	173
KD17_+94_a_8	40.79	49.58	3.90	12.71	4.79	0.27	15.06	9.45	2.73	0.790	0.6126	0.0978	0.0183	486	182
KD17_+94_a_9	40.79	49.08	3.90	12.59	4.83	0.23	15.22	9.58	3.00	0.837	0.5279	0.1942	0.0229	953	225
KD17_+94_a_10	40.79	49.50	3.91	12.63	4.96	0.27	15.39	9.47	2.10	1.059	0.5294	0.1555	0.0146	768	144
KD17_+94_a_11	40.79	49.45	3.80	12.58	4.94	0.25	15.38	9.22	2.92	0.798	0.5210	0.1314	0.0152	653	151
KD17_+94_b_1	40.79	49.13	3.74	12.74	4.78	0.27	15.23	9.52	2.58	1.251	0.5576	0.1785	0.0183	885	181
KD17_+94_b_2	40.79	49.26	3.75	12.75	4.72	0.29	15.38	9.51	2.87	0.829	0.5007	0.1311	0.0152	661	153
KD17_+94_b_3	40.79	49.64	3.83	12.53	4.96	0.26	15.06	9.61	2.60	0.859	0.5044	0.1448	0.0133	719	132
KD17_+94_b_4	40.79	49.53	3.81	12.57	4.70	0.25	15.11	9.76	2.88	0.769	0.4893	0.1233	0.0162	610	160
KD17_+94_b_5	40.79	49.27	3.86	12.58	4.66	0.19	15.35	9.73	2.87	0.810	0.4678	0.1820	0.0154	910	160
KD17_+94_b_6	40.79	49.63	3.81	12.74	4.61	0.28	15.24	9.34	2.94	0.787	0.4683	0.1362	0.0178	676	177
KD17_+94_b_7	40.79	49.37	3.88	12.60	4.44	0.23	16.10	9.43	2.59	0.695	0.5277	0.1214	0.0131	606	131
KD17_+94_b_8	40.79	49.50	3.97	12.00	5.12	0.19	15.45	10.13	2.37	0.683	0.4757	0.0973	0.0110	482	109
KD17_+94_b_9	40.79	49.44	3.72	12.23	5.14	0.21	15.47	9.94	2.37	0.778	0.4988	0.1895	0.0171	942	170
KD17_+102_a_1	41.46	49.22	3.63	12.95	5.50	0.23	14.65	10.06	2.75	0.531	0.3576	0.1022	0.0118	501	116
KD17_+102_a_2	41.46	49.97	3.46	12.80	4.86	0.26	15.06	9.28	2.92	0.715	0.5666	0.1022	0.0085	505	84
KD17_+102_a_3	41.46	49.00	3.55	13.08	5.52	0.29	14.89	9.80	2.76	0.557	0.3896	0.1421	0.0137	698	134
KD17_+102_a_4	41.46	48.90	3.60	13.01	5.58	0.27	14.61	10.21	2.76	0.586	0.3713	0.0879	0.0044	433	43
KD17_+102_a_5	41.46	49.12	3.52	12.96	5.43	0.30	14.88	9.95	2.81	0.508	0.3884	0.1265	0.0100	625	99
KD17_+102_a_6	41.46	48.45	3.60	12.89	5.42	0.29	15.51	10.00	2.76	0.578	0.3747	0.1099	0.0053	543	52
KD17_+102_a_7	41.46	48.82	3.61	12.92	5.36	0.26	15.05	9.98	2.92	0.576	0.3991	0.0929	0.0070	455	68
KD17_+102_a_8	41.46	49.01	3.55	12.59	5.68	0.25	15.13	10.35	1.96	0.957	0.4165	0.0856	0.0087	426	87
KD17_+102_a_9	41.46	49.21	3.55	12.79	5.75	0.21	14.87	9.78	2.74	0.613	0.3647	0.1106	0.0086	552	86
KD17_+102_a_10	41.46	49.02	3.58	12.83	5.67	0.28	14.77	10.04	2.66	0.592	0.4251	0.1187	0.0083	593	83
KD17_+102_a_11	41.46	49.12	3.58	13.00	5.65	0.26	14.51	10.17	2.75	0.539	0.3575	0.0614	0.0054	303	53
KD17_+102_b_1	41.46	49.16	3.56	12.89	5.19	0.23	14.85	10.08	2.95	0.581	0.3770	0.1138	0.0099	558	97
KD17_+102_b_2	41.46	49.31	3.64	12.77	4.97	0.29	15.16	10.29	2.33	0.751	0.4100	0.0754	0.0134	372	132
KD17_+102_b_3	41.46	49.36	3.61	12.76	5.23	0.26	14.89	10.08	2.66	0.601	0.3950	0.1277	0.0096	628	94
KD17_+102_b_4	41.46	49.33	3.57	12.97	5.21	0.33	14.56	10.08	2.83	0.601	0.3590	0.1491	0.0065	730	64
KD17_+102_b_5	41.46	49.58	3.61	12.78	5.11	0.22	14.73	10.09	2.84	0.549	0.3896	0.0987	0.0102	484	100

Supplement Paper II

Sample Name	Depth relative to Ash -33 (m)	SiO2	TiO2	Al2O3	MgO	MnO	FeO	CaO	Na2O	K2O	P2O5	SO2	Cl	S	Cl
KD17_+102_b_6	41.46	48.91	3.63	12.58	5.19	0.27	15.23	10.19	2.86	0.627	0.4138	0.0966	0.0075	476	74
KD17_+102_b_7	41.46	49.23	3.59	13.00	5.35	0.23	14.47	10.16	2.88	0.552	0.3702	0.1596	0.0092	777	90
KD17_+102_b_8	41.46	49.40	3.65	12.70	5.29	0.23	14.70	10.03	2.85	0.575	0.4036	0.1621	0.0119	793	116
KD17_+102_b_9	41.46	49.22	3.54	12.74	5.28	0.25	14.83	10.22	2.87	0.589	0.3624	0.0815	0.0081	402	80
KD17_+114_a_1	42.39	50.10	3.72	12.95	4.09	0.23	16.06	9.21	2.20	0.726	0.5225	0.1643	0.0129	804	126
KD17_+114_a_2	42.39	49.72	3.81	12.59	4.66	0.30	15.22	9.37	2.84	0.792	0.5186	0.1583	0.0142	791	142
KD17_+114_a_3	42.39	50.63	3.77	12.86	3.97	0.27	15.72	9.01	2.29	0.789	0.5047	0.1810	0.0148	896	146
KD17_+114_a_4	42.39	48.88	3.64	12.49	5.79	0.23	15.87	9.19	2.72	0.731	0.2662	0.1577	0.0173	788	173
KD17_+114_a_5	42.39	49.93	3.68	12.58	4.74	0.28	15.27	9.13	2.95	0.727	0.5022	0.1717	0.0183	848	181
KD17_+114_a_6	42.39	50.07	3.57	12.78	4.63	0.24	15.35	8.87	2.85	0.970	0.5219	0.1475	0.0210	724	206
KD17_+114_a_7	42.39	49.73	3.77	12.28	4.85	0.18	15.73	9.22	2.92	0.773	0.4106	0.1066	0.0158	528	156
KD17_+114_a_8	42.39	49.89	3.79	12.38	4.58	0.30	15.63	9.02	3.06	0.777	0.4671	0.0950	0.0119	470	118
KD17_+114_a_9	42.39	49.57	3.61	12.71	4.92	0.25	15.54	9.56	2.49	0.723	0.4284	0.1924	0.0124	960	124
KD17_+114_a_10	42.39	50.70	3.52	12.69	4.36	0.27	15.61	8.96	2.44	0.797	0.4675	0.1719	0.0102	854	101
KD17_+114_a_11	42.39	50.02	3.71	12.69	4.69	0.25	15.70	9.22	2.22	0.811	0.5390	0.1343	0.0118	659	116
KD17_+114_b_1	42.39	49.78	3.65	12.80	4.57	0.20	15.38	9.36	2.97	0.709	0.4326	0.1333	0.0191	654	187
KD17_+114_b_2	42.39	49.89	3.63	12.33	4.79	0.25	15.31	9.50	2.95	0.704	0.4675	0.1669	0.0104	817	102
KD17_+114_b_3	42.39	49.49	3.70	12.94	4.85	0.14	14.99	9.87	2.85	0.614	0.4056	0.1370	0.0145	667	141
KD17_+114_b_4	42.39	50.09	3.71	12.35	4.57	0.18	15.41	9.32	3.04	0.730	0.4607	0.1258	0.0157	611	152
KD17_+114_b_5	42.39	49.86	3.99	12.67	3.82	0.30	17.09	8.67	2.25	0.774	0.4900	0.0736	0.0152	366	151
KD17_+114_b_6	42.39	49.84	3.32	12.58	5.61	0.19	14.50	9.96	2.97	0.465	0.4362	0.1088	0.0141	534	138
KD17_+114_b_7	42.39	50.24	3.75	12.28	4.53	0.25	15.64	9.30	2.79	0.700	0.3937	0.1147	0.0120	565	118
KD17_+114_b_8	42.39	50.14	3.74	12.36	4.41	0.27	15.64	9.03	3.08	0.691	0.4460	0.1663	0.0165	820	163
KD17_+114_b_9	42.39	49.80	3.70	12.57	4.43	0.27	15.66	9.20	3.00	0.778	0.4382	0.1365	0.0131	669	128
KD17_+118_a_1	42.71	49.38	3.85	12.44	4.66	0.29	15.95	9.08	2.88	0.793	0.4941	0.1601	0.0241	806	243
KD17_+118_a_2	42.71	49.91	3.81	12.46	4.56	0.23	15.47	8.96	3.16	0.806	0.5257	0.1133	0.0096	561	95
KD17_+118_a_3	42.71	49.96	3.86	12.52	4.30	0.30	15.76	8.81	2.91	0.813	0.5299	0.2171	0.0178	1064	174
KD17_+118_b_1	42.71	50.01	3.78	12.28	4.33	0.19	15.54	9.34	2.99	0.816	0.5437	0.1795	0.0117	882	115
KD17_+118_b_2	42.71	50.36	3.75	12.16	4.33	0.16	15.64	8.82	2.70	1.401	0.4845	0.1853	0.0091	916	90
KD17_+118_b_3	42.71	50.19	3.75	12.20	4.39	0.24	15.57	9.05	3.08	0.806	0.4988	0.2021	0.0181	990	177
KD17_+118_b_4	42.71	50.18	3.86	12.47	4.36	0.22	15.45	9.03	2.89	0.801	0.5582	0.1758	0.0135	878	135
KD17_+118_b_5	42.71	49.95	3.79	12.40	4.38	0.20	15.66	9.27	2.76	0.821	0.5435	0.2019	0.0154	1010	154
KD17_+118_b_6	42.71	50.28	3.78	12.31	4.40	0.26	15.95	8.88	2.55	0.844	0.5480	0.1831	0.0170	914	169
KD17_+118_b_7	42.71	51.53	3.62	12.59	3.97	0.19	14.77	8.44	3.11	0.977	0.6148	0.1762	0.0128	866	126
KD17_+118_b_8	42.71	51.68	3.51	12.46	3.84	0.22	14.99	8.44	2.89	1.014	0.7295	0.2077	0.0203	1034	202
KD17_+118_b_9	42.71	50.12	3.79	12.36	4.42	0.18	15.50	9.19	2.95	0.783	0.5299	0.1787	0.0149	875	146
KD17_+118_b_11	42.71	50.64	3.95	11.79	4.25	0.23	15.77	9.11	2.77	0.840	0.4560	0.1764	0.0194	859	189
KD17_+118_b_12	42.71	51.70	3.74	12.05	3.82	0.21	15.17	8.26	3.20	1.034	0.5770	0.2131	0.0208	1038	202
KD17_+118_b_14	42.71	49.68	3.84	12.10	4.51	0.22	15.82	9.14	3.16	0.750	0.5732	0.1919	0.0168	941	165
KD17_+118_b_15	42.71	49.97	3.87	12.18	4.34	0.34	15.63	9.14	2.92	0.835	0.5304	0.2172	0.0175	1068	172
KD17_+118_b_16	42.71	50.47	3.78	12.17	4.23	0.28	15.77	8.81	2.86	0.845	0.5473	0.2055	0.0217	1020	215
KD17_+118_b_17	42.71	53.41	3.17	12.62	3.28	0.26	14.17	7.63	3.38	1.227	0.6596	0.1681	0.0241	826	237
KD17_+118_b_18	42.71	50.33	3.77	12.36	4.44	0.23	15.10	9.16	3.04	0.859	0.4826	0.1980	0.0146	967	142

Supplementary Table 2: Precision and accuracy for EPMA analyses of matrix glasses and mineral phases. Precision and accuracy was estimated from repeat measurements of VG2 (basaltic glass) and A99 (basaltic glass) secondary standards. Precision is reported as the “(standard deviation of all repeats/mean) x 100”. Accuracy is reported as the “(mean of all repeats/standard reference) x 100”

Session	Standard	Number of repeats		CaO	P2O5	K2O	TiO2	FeO	MnO	Na2O	Al2O3	SiO2	MgO	SO2	Cl
February 2019	VG2	7	Precision (%)	0.94	15.31	13.03	0.63	1.20	21.94	2.66	0.97	0.86	3.39	0.85	4.11
			Accuracy (%)	100.49	102.98	96.89	99.90	100.62	108.40	100.63	99.04	99.78	103.71	97.35	104.10
	A99	6	Precision (%)	0.78	6.62	2.62	0.80	0.90	12.99	2.97	1.11	1.67	6.11	7.19	7.63
			Accuracy (%)	99.54	97.57	100.27	100.53	101.66	80.33	99.20	99.43	99.23	101.76	82.89	112.75
	VG2	16	Precision (%)	1.20	15.69	11.10	1.59	1.85	22.42	1.96	1.19	0.57	1.30	2.39	13.05
			Accuracy (%)	101.58	99.05	102.42	100.03	101.00	94.35	102.69	99.13	102.23	99.51	95.71	105.38
November 2019	A99	16	Precision (%)	1.21	12.88	4.11	0.75	1.54	16.88	3.21	1.32	0.44	1.30	16.85	16.26
			Accuracy (%)	103.28	101.05	97.96	100.93	100.25	85.09	102.18	100.84	101.38	99.34	85.44	116.69

Supplementary Table 3: The Sulfur Concentration at Sulfur Saturation (SCSS) modelled following Smythe et al. (2017) with five different pressure and temperatures scenarios (indicated at the top for each predicted SCSS). Average sulfide liquid composition applied in the model indicated in the yellow box. Degassed S indicate the estimated amount of sulfur degassed for each ash layer. Degassed S in parts per million (ppm) calculated as “Ideal SCSS (ppm)–Average Fur glass S”. Percentage degassed calculated as “(Degassed S (ppm)/Ideal SCSS (ppm))*100”.

Sample	T=1130 °C P=0.1GPa					T=1130 °C P=0.01 GPa				
	Predicted SCSS					Predicted SCSS				
	Ideal		Non-Ideal			Ideal		Non-Ideal		
	[S] (ppm)	σ [S] (ppm)	[S] (ppm)	σ [S] (ppm)	Degassed S (ppm)	[S] (ppm)	σ [S] (ppm)	[S] (ppm)	σ [S] (ppm)	Degassed S (ppm)
KD17_-19	1862.41	508.76	1792.50	479.13	1386.10	1894.88	517.62	1823.22	487.34	1418.56
KD17_-13	1656.30	452.45	1599.47	427.54	1031.12	1685.17	460.34	1626.88	434.86	1059.99
KD17_+1	1939.18	529.73	1854.14	495.61	1287.43	1972.98	538.96	1885.91	504.10	1321.23
KD17_+9	1821.70	497.63	1731.35	462.79	1232.23	1853.45	506.31	1761.01	470.72	1263.98
KD17_+14	1742.29	475.94	1654.87	442.35	1279.92	1772.65	484.24	1683.22	449.92	1310.28
KD17_+18	1872.96	511.64	1789.60	478.36	1291.16	1905.60	520.55	1820.26	486.55	1323.80
KD17_+24	1814.03	495.54	1724.82	461.04	1258.53	1845.65	504.18	1754.37	468.94	1290.15
KD17_+31	2040.62	557.44	1952.22	521.83	1382.20	2076.19	567.15	1985.66	530.77	1417.77
KD17_+36	1915.37	523.22	1830.95	489.41	1401.02	1948.76	532.34	1862.32	497.80	1434.41
KD17_+42	1700.29	464.47	1615.36	431.79	1249.24	1729.93	472.56	1643.04	439.18	1278.88
KD17_+46	2030.76	554.74	1944.96	519.89	1359.31	2066.15	564.41	1978.29	528.79	1394.70
KD17_+51	1994.59	544.86	1908.69	510.19	1377.24	2029.35	554.36	1941.39	518.93	1412.00
KD17_+54	1718.11	469.33	1631.61	436.13	1166.01	1748.05	477.52	1659.57	443.60	1195.95
KD17_+60	1784.34	487.43	1702.25	455.01	1310.81	1815.44	495.92	1731.42	462.81	1341.91
KD17_+68	1932.20	527.82	1845.63	493.34	1370.13	1965.88	537.02	1877.25	501.79	1403.81
KD17_+80	1993.23	544.49	1907.88	509.97	1359.08	2027.98	553.98	1940.57	518.71	1393.83
KD17_+90	1953.91	533.75	1871.58	500.27	1522.47	1987.97	543.05	1903.65	508.84	1556.52
KD17_+94	2014.85	550.40	1936.26	517.56	1260.45	2049.96	559.99	1969.43	526.43	1295.56
KD17_+102	1937.38	529.23	1847.65	493.88	1394.68	1971.15	538.46	1879.31	502.34	1428.45
KD17_+114	2080.15	568.23	2000.92	534.84	1378.90	2116.41	578.14	2035.20	544.01	1415.16
KD17_+118	2023.46	552.75	1954.80	522.52	1101.62	2058.73	562.38	1988.29	531.47	1136.89
Mean	1896.58	518.09	1814.17	484.93		1929.63	527.12	1845.25	493.23	
SD	121.21	33.11	120.21	32.13		123.32	33.69	122.27	32.68	

		T=1000 °C P=0.1 GPa				
		Predicted SCSS				
		Ideal		Non-Ideal		
Sample	[S] (ppm)	σ [S] (ppm)	[S] (ppm)	σ [S] (ppm)	Degassed S(ppm)	Degassed S%
KD17_-19	1501.41	410.14	1400.99	374.48	1025.09	68.3
KD17_-13	1316.70	359.68	1233.18	329.63	691.52	52.5
KD17_+1	1570.62	429.04	1454.97	388.91	918.87	58.5
KD17_+9	1459.42	398.67	1343.02	358.99	869.95	59.6
KD17_+14	1386.36	378.71	1274.93	340.79	923.99	66.6
KD17_+18	1509.22	412.27	1397.04	373.43	927.42	61.5
KD17_+24	1453.71	397.11	1338.41	357.76	898.21	61.8
KD17_+31	1564.07	454.57	1542.49	412.30	1005.65	60.4
KD17_+36	1548.03	422.88	1433.69	383.22	1033.68	66.8
KD17_+42	1347.46	368.09	1239.48	331.31	896.41	66.5
KD17_+46	1656.01	452.37	1536.91	410.82	984.56	59.5
KD17_+51	1622.35	443.18	1504.25	402.09	1005.00	61.9
KD17_+54	1364.84	372.83	1254.90	335.43	812.74	59.5
KD17_+60	1427.47	389.94	1319.09	352.59	953.94	66.8
KD17_+68	1563.88	427.20	1447.15	386.82	1001.82	64.1
KD17_+80	1621.30	442.89	1503.71	401.94	987.15	60.9
KD17_+90	1583.80	432.65	1470.09	392.95	1152.36	72.8
KD17_+94	1642.73	448.75	1530.29	409.04	888.33	54.1
KD17_+102	1567.65	428.24	1448.11	387.08	1024.95	65.4
KD17_+114	1704.42	465.60	1589.41	424.85	1003.17	58.9
KD17_+118	1552.25	451.34	1548.11	413.81	730.41	44.2
	Mean	1531.60	418.39	1419.53	379.44	
	SD	112.43	30.71	108.00	28.87	

		T=1250 °C P=0.1 GPa				
		Predicted SCSS				
		Ideal		Non-Ideal		
	[S] (ppm)	σ [S] (ppm)	[S] (ppm)	σ [S] (ppm)	Degassed S(ppm)	Degassed S%
	2215.12	605.10	2183.52	583.65	1738.80	78.50
	1991.35	543.98	1969.00	526.31	1366.17	68.61
	2298.12	627.78	2251.64	601.86	1646.37	71.64
	2177.17	594.74	2121.34	567.03	1587.70	72.92
	2093.20	571.80	2038.37	544.86	1630.83	77.91
	2228.44	608.74	2182.00	583.25	1646.64	73.89
	2167.51	592.10	2112.78	564.74	1612.01	74.37
	2405.67	657.16	2358.21	630.35	1747.25	72.63
	2273.63	621.09	2227.18	595.32	1759.28	77.38
	2049.16	559.77	1995.92	533.51	1598.11	77.99
	2394.06	653.98	2349.26	627.96	1722.61	71.95
	2356.07	643.61	2310.16	617.50	1738.72	73.80
	2066.81	564.59	2012.34	537.90	1514.71	73.29
	2134.85	583.18	2087.35	557.95	1661.33	77.82
	2291.06	625.85	2242.67	599.46	1729.00	75.47
	2354.41	643.15	2309.09	617.22	1720.26	73.07
	2314.16	632.16	2271.10	607.06	1882.71	81.36
	2375.63	648.95	2338.45	625.07	1621.23	68.24
	2297.68	627.66	2245.87	600.32	1754.98	76.38
	2443.25	667.42	2407.12	643.42	1742.00	71.30
	2383.02	650.97	2357.13	630.06	1461.17	61.32
	2252.88	615.42	2208.12	590.23		
	127.46	34.82	129.57	34.63		

Northern Mid Atlantic Ridge
Sulfide composition
(Keith et al., 2017)

S % = 35.60
Fe % = 48.30
Ni % = 15.90
Cu % = 0.30

Sample		T=1500 °C P=0.1 GPa					
		Predicted SCSS					
		Ideal		Non-Ideal			
	[S] (ppm)	σ [S] (ppm)	[S] (ppm)	σ [S] (ppm)	Degassed S (ppm)	Degassed 5%	Average Fur glass S (ppm)
KD17_-19	2998.87	819.20	3074.85	821.91	2522.56	84.12	476.32
KD17_-13	2744.33	749.67	2821.32	754.14	2119.15	77.22	625.18
KD17_+1	3092.81	844.86	3154.69	843.25	2441.06	78.93	651.75
KD17_+9	2971.07	811.61	3016.10	806.20	2381.60	80.16	589.47
KD17_+14	2881.24	787.07	2923.51	781.45	2418.87	83.95	462.37
KD17_+18	3018.66	824.61	3077.40	822.59	2436.86	80.73	581.80
KD17_+24	2956.76	807.70	3002.63	802.60	2401.26	81.21	555.50
KD17_+31	3209.62	876.77	3275.27	875.48	2551.20	79.49	658.42
KD17_+36	3068.15	838.13	3128.97	836.37	2553.80	83.24	514.35
KD17_+42	2835.24	774.50	2877.36	769.12	2384.18	84.09	451.05
KD17_+46	3194.18	872.55	3262.41	872.04	2522.73	78.98	671.45
KD17_+51	3153.76	861.51	3218.96	860.42	2536.41	80.42	617.35
KD17_+54	2850.94	778.79	2892.35	773.12	2298.84	80.63	552.10
KD17_+60	2918.56	797.26	2971.66	794.32	2445.04	83.78	473.53
KD17_+68	3086.02	843.01	3145.29	840.73	2523.96	81.79	562.06
KD17_+80	3151.42	860.87	3217.21	859.96	2517.27	79.88	634.15
KD17_+90	3111.25	849.90	3178.01	849.48	2679.81	86.13	431.44
KD17_+94	3170.32	866.04	3246.73	867.85	2415.92	76.20	754.40
KD17_+102	3095.99	845.73	3151.50	842.39	2553.29	82.47	542.70
KD17_+114	3240.03	885.08	3320.62	887.60	2538.78	78.36	701.25
KD17_+118	3174.09	867.06	3264.15	872.50	2252.24	70.96	921.84
	Mean	3043.97	831.52	3105.76	830.17		
	SD	135.46	37.00	143.38	38.32		

Supplementary Table 4: Data from textural analysis of Secondary Electron Microscope images. Manual classification of first the whole sample, and then only the Crystal-free glass.

Sample	Whole sample			Crystal-free glass		
	Crystal-free glass (%)	Microcrystalline and lithics (%)	Altered (%)	Dense (%)	Vesicular (%)	Bubble shard (%)
KD17 +114	58.75	3.75	37.5	50.64	28.51	20.85
KD17 +80	45.5	2	52.5	52.2	12.09	35.71
KD17 +60	45	2	53	42.22	22.22	35.56
KD17 +54	39.75	2	58.25	49.69	16.98	33.33
KD17 +51	53.5	6	40.5	40.65	27.1	32.24
KD17 +46	48.75	3.25	48	45.13	24.1	30.77
KD17 +42	40	1.25	58.75	40.63	20.63	38.75
KD17 +36	32.5	1.5	66	33.85	30.77	35.38
KD17 +31	30	0.75	69.25	48.33	25.83	25.83
KD17 +24	41.25	3.5	55.25	35.76	46.67	17.58
KD17 +18	26.25	0.5	73.25	17.14	54.29	28.57
KD17 +1	33	1.25	65.75	50.76	29.55	19.7
SK17B -19	63.25	0.75	36	26.88	41.9	31.23

Rapid and sustained environmental response to global warming:
The Paleocene-Eocene Thermal Maximum in Denmark

*Ella W. Stokke, Morgan T. Jones, Lars Riber, Haflidi Haflidason, Ivar
Midtkandal, Bo Pagh Schultz, and Henrik H. Svensen*

Unpublished

3

Rapid and sustained environmental response to global warming: The Paleocene-Eocene Thermal Maximum in Denmark

Ella W. Stokke^{1*}, Morgan T. Jones¹, Lars Riber², Haflidi Haflidason^{3,4}, Ivar Midtkandal², Bo Pagh Schultz⁵, and Henrik H. Svensen¹

¹CEED, University of Oslo, PO Box 1028, 0315 Oslo, Norway (*Correspondence: e.w.stokke@geo.uio.no)

²Department of Geosciences, University of Oslo, P.O. Box 1047, Blindern, NO 0316 Oslo, Norway

³Department of Earth Science, University of Bergen, Allégt. 41, N-5007 Bergen, Norway

⁴Bjerknes Centre for Climate Research, Jahnebakken 5, 5007 Bergen, Norway

⁵Museum Salling, Fur Museum, Nederby 28, 7884 Fur, Denmark

Abstract

The Paleocene-Eocene Thermal Maximum (PETM; ~55.9 Ma) was a period of rapid and sustained global warming associated with significant carbon emissions. It coincided with the opening of the North Atlantic Ocean and the North Atlantic Igneous Province (NAIP) emplacement, suggesting a possible causal relationship. Only a very limited number of PETM studies exist from the North Sea, despite its ideal position for tracking the impact of both changing climate and the NAIP explosive and effusive activity. Here we present sedimentological, mineralogical, and geochemical proxy data from Denmark in the eastern North Sea, exploring the environmental response to the PETM. An increase in kaolinite content of up to 50 %, and in the chemical index of alteration, indicate an influx of terrestrial input occurred shortly after the PETM onset and during the recovery, likely due to an intensified hydrological cycle. The volcanically derived minerals zeolite and smectite comprise up to 36 % and 90 % of the bulk and clay mineralogy respectively during the PETM body. This emphasises the NAIPs important role as a sediment source for the North Sea and in increasing the rate of silicate weathering during the PETM. XRF element core scans also reveal possible hitherto unknown NAIP ash deposition both prior to and during the PETM. Geochemical proxies show that an anoxic environment persisted during the PETM body, possibly reaching euxinic conditions in the upper half with high concentrations of Mo (>30 ppm), S (~4 wt%), and pyrite (~7 % of bulk), and low Th/U (<2 ppm). At the same time, export productivity and organic matter burial reached its maximum intensity. These new records reveal that negative feedback mechanisms to the atmospheric carbon increase – including silicate weathering and organic carbon drawdown – rapidly began to counteract the global carbon cycle perturbations and temperature increase, and remained active throughout the PETM. This study highlights the importance

of shelf sections in tracking the environmental response to the PETM climatic changes, and as carbon sinks driving the PETM recovery.

1. Introduction

The early Cenozoic was a period characterized by long-term warming, punctuated by transient periods of rapid global hyperthermal events (Zachos et al., 2008; Hollis et al., 2012; Cramwinckel et al., 2018). The most pronounced of these periods was the Paleocene-Eocene Thermal Maximum (PETM; ~55.9 Ma; Kennett and Stott, 1991; Thomas and Shackleton, 1996; Westerhold et al., 2018), during which global surface temperatures rose rapidly by 4–5 °C (Dunkley Jones et al., 2013; Frieling et al., 2017). The PETM is associated with a large input of ¹²C-rich carbon to the ocean-atmosphere system resulting in a 2.5–8 ‰ negative carbon isotope excursion (CIE) in the terrestrial and marine sedimentary record (McInerney and Wing, 2011). The PETM CIE lasted up to 200 kyr (Westerhold et al., 2018), and is characterised by a rapid onset (~1–5 kyr; Kirtland-Turner et al., 2017), followed by a stable body (~100 kyr; van der Meulen et al., 2020) and a gradual recovery towards background conditions (McInerney and Wing, 2011). There were a number of smaller-magnitude hyperthermals in the early Eocene, but the PETM differs from these events with both higher magnitude and longer duration (Zachos et al., 2010; Bowen, 2013). However, there is still no consensus on the ultimate cause of the PETM, or whether several mechanisms contributed to prolong the PETM duration (e.g. Zeebe et al., 2009; Bowen et al., 2015). Several ¹²C-enriched carbon sources may have contributed to the PETM CIE; the dissociation of methane clathrates triggered by increasing temperatures (Dickens et al., 1995), a bolide impact activating terrestrial carbon reservoirs (Kent et al., 2003; Schaller et al., 2016), and volcanic and thermogenic degassing triggered by the emplacement of the North Atlantic Igneous Province (NAIP; Fig. 1; Eldholm and Thomas, 1993; Svensen et al., 2004; Storey et al., 2007a).

Marine uptake of increased atmospheric CO₂ altered the ocean chemistry, leading to deep ocean acidification and substantial deep-sea carbonate dissolution (Zachos et al., 2005; Babila et al., 2018). The temperature increase and ocean acidification were accompanied by transient ocean circulation changes, increased halocline stratification and a global reduction in bottom water oxygen (Kennett and Stott, 1991; Nunes and Norris, 2006; Kender et al., 2012; Pälike et al., 2014). This led to the extinction of 30–50 % of all benthic foraminifera species (Koch et al., 1992; Thomas & Shackleton, 1996; Alegret et al., 2009; Nagy et al., 2013). Anoxic conditions were less extensive during the PETM than in previous ocean anoxic events (Jenkyns, 2010), and there were large regional variations in ocean oxicity (Pälike et al., 2014). Still, globally widespread ocean deoxygenation has been recognised (Pälike et al., 2014; Zhou et al., 2014; Yao et al., 2018), with particularly prevalent anoxic to euxinic conditions observed in semi-enclosed shelf areas such as in the Tethys Ocean (Egger et al., 2003; Khozyem et al., 2013), Peri-

Tethys Basin (Gavrilov et al., 2003; Dickson et al., 2014), the North Sea (Schoon et al., 2015), and the Arctic Ocean (Stein et al., 2006; Harding et al., 2011).

The spread of marine anoxia was accompanied by increased productivity in shelf areas, linked to the increased input of nutrients from enhanced erosion and runoff in the terrestrial realm (Bains et al., 2000; John et al., 2008; Ma et al., 2014). The hydrological cycle changed substantially during the PETM (e.g. Carmichael et al., 2017), with modelling studies suggesting an overall increase in extreme weather events (Carmichael et al., 2018). Proxy evidence indicates a more humid climate, particularly in higher latitudes and marginal marine areas such as Antarctica (Robert and Kennett, 1994), the northeast US coast (Gibson et al., 2000; John et al., 2012), the Tethys (Bolle et al., 2000; Egger et al., 2003; Khozyem et al., 2013), North Atlantic (Bornemann et al., 2014), North Sea (Kender et al., 2012; Kemp et al., 2016), and the Arctic (Dypvik et al., 2011; Harding et al., 2011). In contrast, areas such as the Pyrenees (Schmitz and Pujalte, 2003) and the US interior (Kraus and Riggins, 2007) show evidence of arid climates. There seems to be considerable regional and temporal variation in the hydrological changes, with an increased meridional transport of water vapour from low to high latitudes leading to an overall dry-drier, wet-wetter climate response to the global warming (Carmichael et al., 2017).

The 4–5 °C PETM temperature increase (Dunkley Jones et al., 2013; Frieling et al., 2017) is comparable to that predicted in response to the current anthropogenic carbon emissions (e.g. Riahi et al., 2017). The PETM is therefore an important natural analogue for future greenhouse conditions, as the environmental and ecological response may hold clues for the consequences of present day global warming (Zachos et al., 2010; Alley, 2016; Penman and Zachos, 2018; Svensen et al., 2019). Model predictions suggest that the current global warming will lead to an enhanced hydrological cycle, akin to that indicated by PETM proxy records (Held and Soden, 2006; Seager et al., 2010; Trenberth, 2011). The intensification of both droughts and extreme weather events are already occurring in parts of the world, with substantial consequences for human settlements (e.g. Riahi et al., 2017). Similarly, a decrease in ocean oxygenation has been observed for the last 50 years, most likely caused by the current global warming (Bograd et al., 2008; Stramma et al., 2012). The spread of marine anoxia is a well-known consequence of global warming, negatively affecting marine ecosystems as a whole (Stramma et al., 2008; Gilly et al., 2013). Understanding the timing and regional distribution of the environmental response to global warming in the past is therefore vital to meet future challenges.

The Stolleklint section on the island of Fur in northwest Denmark offers an excellent opportunity to study the environmental response to temperature changes during the PETM in detail (Fig. 1). Denmark is placed in the eastern part of the epicontinental North Sea, which during the latest Paleocene became a highly restricted basin due to NAIP thermal uplift (Knox et al., 2010). During the PETM the North Sea

was characterised by bottom-water deoxygenation (Schoon et al., 2015), and a high sedimentary input, significant surface water freshening, and development of halocline stratification reflecting an intensified hydrological cycle (Zacke et al., 2009; Kender et al., 2012; Kemp et al., 2016). At Stolleklint, the PETM is recognized by a 4.5 ‰ CIE and the diagnostic dinoflagellate *Apectodinium augustum* appearing at the base of the earliest Eocene Stolleklint Clay (Fig. 2; Heilmann-Clausen, 1994; Schmitz et al., 2004; Schoon et al., 2013; Jones et al., 2019). The Stolleklint Clay – which covers the PETM interval in Denmark – is a thermally immature and expanded clay-dominated section, making this a unique and particularly well-suited section for detailed geochemical analyses. Located in a downwind direction and within proximity to the NAIP, Denmark was also ideally placed to record the distal extent of the contemporary volcanic activity from the NAIP (Fig. 1; Jones et al., 2019; Stokke et al., 2020b). This is evidenced by the hundreds of NAIP tephra layers interbedded in the Danish and North Sea stratigraphy (Bøggild, 1918; Knox and Morton, 1988; Larsen et al., 2003). The importance of the NAIP in the PETM initiation and termination is a topic of much discussion (Svensen et al., 2004; Jolley and Widdowson, 2005; Storey et al., 2007a; Frieling et al., 2016; Saunders, 2016; Gutjahr et al., 2017). To refine this relationship, better constraints on the relative timings of volcanic activity and climatic and environmental changes are needed.

In our previous paper from Stolleklint, we presented a high resolution sea surface temperature (SST) reconstruction based on the organic palaeo-thermometer TEX₈₆ (Stokke et al., 2020a). We found that SSTs increased by 7 – 10 °C across the CIE onset, and then gradually decreased during the CIE body and recovery (Fig. 2; Stokke et al., 2020a). Here, we combine mineralogical, sedimentological, and geochemical proxies to investigate the relationship between changes in temperature and variations in both basin oxicity and sediment input; the latter typically inferred to indicate changes in terrestrial erosion and runoff. Both increased weathering of siliciclastic rocks and enhanced sequestration of organic carbon have been proposed as important negative feedback mechanisms, potentially driving the PETM recovery (Bowen and Zachos, 2010; Ma et al., 2014; Penman, 2016; Dunkley-Jones et al., 2018). Better constraints on the timing and global extent of increased silicate weathering and organic matter drawdown are therefore vital for understanding the PETM termination.

2. Field area and stratigraphy

Stolleklint is located on the northern shore of the island of Fur in northwest Denmark (Fig. 1). In the Palaeogene, Fur was part of the Norwegian-Danish Basin, a marginal basin in the eastern semi-enclosed epicontinental North Sea Basin (Rasmussen et al., 2008; Knox et al., 2010). The Norwegian-Danish Basin forms a NW to SE striking depression, bounded by the Fennoscandian Shield and the Sorgenfrei-Tornquist Zone to the NE and basement blocks in the Ringkøbing-Fyn High to the SW

(Schiøler et al., 2007). Salt diapirs of Zechsten salt creates additional restricting structures within the Norwegian-Danish Basin (e.g. Petersen et al., 2008).

The base of the section at Stolleklint likely comprises the Holmehus Formation, which correspond to the Lista Formation offshore in the North Sea (Figs. 2, 3, 4). This is a hemipelagic bioturbated fine-grained mudstone, representing the culmination of a long period of transgression in the upper Paleocene Denmark (Heilmann-Clausen, 1995). In the latest Paleocene, a combination of thermal uplift around the NAIP (Knox, 1996) and tectonic uplift along the Sorgenfrei-Tornquist Zone (Clausen et al., 2000) led to a relative sea-level fall and almost complete North Sea Basin isolation (Knox et al., 2010). In Denmark, this resulted in either erosion of the latest Paleocene strata, a hiatus in deposition, or deposition of the informal Østerrende Clay unit at the top of the Holmehus Formation. However, the Østerrende Clay unit has a very limited distribution, and it is uncertain how much is present at Stolleklint despite its presence further south in Denmark (Schmitz et al., 2004; King, 2016). Schoon et al. (2015) correlated the top of the Paleocene stratigraphy at Fur with the Østerrende Clay similar to that seen at Store Bælt (Fig. 1). However, the Østerrende Clay is absent in cores drilled at Mors ~20 km to the west and at Ølst ~80 km to the SE (Fig. 1A; Heilmann-Clausen, 1995), suggesting that a hiatus of uncertain duration followed the Holmehus Formation at Stolleklint. Still, due to the uncertainty of this boundary, we will henceforth refer to the lowermost unit as the Holmehus/Østerrende Formation.

The Paleocene-Eocene transition is seen as a lithological shift from the Holmehus/Østerrende Formation bioturbated clays, into the Stolleklint Clay dark, laminated clays (Fig. 4; Heilmann-Clausen et al., 1985; Heilmann-Clausen, 1995; King, 2016). The lithological shift is accompanied by the almost complete absence of benthic fauna and preferential dissolution of remaining calcareous organisms within the Stolleklint Clay (Heilmann-Clausen, 1995; Mitlehner, 1996). The Stolleklint Clay is an informal unit, representing the lower part of the Ølst Formation in northern Denmark and correlating with the offshore Sele Formation (Fig. 3; Heilmann-Clausen, 1995). A condensed, glauconite-rich silty horizon marks the base of the Stolleklint Clay (Heilmann-Clausen, 1995, Schmitz et al., 2004; Schoon et al., 2015). This glauconite-rich silt contains mainly authigenic and biogenic grains and was likely deposited in an upper bathyal to outer neritic environment with low sedimentation rates (Nielsen et al., 1986; Schoon et al., 2015). A relative sea level rise is observed in PETM sections in the Atlantic, Pacific, Tethyan, and Arctic Ocean (Sluijs et al., 2008; Harding et al., 2011; Pujalte et al., 2014; Sluijs et al., 2014). It was likely caused by thermal expansion of seawater due to global warming (Sluijs et al., 2008), and may pre-date the PETM up to 20–200 kyr (John et al., 2012). Although this transgression was overprinted by regional tectonically forced regression in the latest Paleocene, the earliest Eocene Stolleklint Clay is deposited in an outer neritic environment (between 100–200 m; Knox et al., 2010; Schoon et al., 2015) during a gradual transgression (Heilmann-Clausen, 1995). The Stolleklint Clay is

overlain by the ~60 m thick Fur Formation clay-rich diatomites (Figs. 2, 4), correlating to the offshore Sele and Balder Formations (Fig. 3). At Stolleklint, the PETM is defined by a negative CIE of -4.5 ‰; characterized by a sharp onset above Ash SK2 at the base of the Stolleklint Clay, a thick stable body phase (~24 m), and a gradual recovery (~4.5 m) from about Ash -33 to around Ash -21a (Fig. 2, 4). The PETM at Stolleklint is associated with a substantially increased sedimentation rate from the condensed glauconitic base to a maximum sediment accumulation rate in the Stolleklint Clay of about 24 cm/kyr (Stokke et al., 2020a).

More than 180 tephras with thicknesses up to 20 cm have been identified in the stratigraphy exposed at Fur, with the majority (~140) within the post-PETM Fur Formation (Fig. 3; Bøggild, 1918; Pedersen and Surlyk, 1983). Tephra is a general term for all air-borne volcanic fragmented material, but the grain sizes of all the Fur tephras are <2 mm and therefore within the ash fraction. Heavily altered ashes are called bentonites, and while this applies to some of the lowermost ashes we will for simplicity use the term ash for all. The volcanic ashes are grouped in a negative and positive ash series based on variations on outcrop appearance and geochemistry (Bøggild, 1918), with additional ash layers SK1–4 found later at the base of the Stolleklint Clay (Schmitz et al., 2004; Jones et al., 2019). The SK ashes and the negative series are a heterogeneous mix of ash compositions, whereas the positive series are largely comprised of tholeiitic basalts (Morton and Evans, 1988; Larsen et al., 2003). All the ashes are believed to be sourced from NAIP explosive volcanism during the opening of the Northeast Atlantic (Larsen et al., 2003; Storey et al., 2007a; Stokke et al., 2020b). These ash layers are found throughout the North Sea and North Atlantic (Knox and Morton, 1988; Haaland et al., 2000) with some of the major layers traced all the way to Austria, suggesting that ash was occasionally distributed all over Northern Europe (Egger et al., 2000).

3. Materials and methods

3.1 Sampling

Samples were mostly collected from the Stolleklint beach (56°50'29"N, 8°59'33"E; Figs. 1B, 4), with some additional samples from a quarry near Fur Camping (Quarry FQ16 at 56°49'51"N, 8°58'45"E; Fig. 1B). At Stolleklint, the Stolleklint Clay and the Fur Formation are exposed in the cliff side (Fig. 4). However, the base of the Stolleklint Clay and the Paleocene-Eocene transition were not exposed at the time of field work due to coastal erosion (Fig. 4C). We therefore excavated a 43 m long and 0.5 m deep trench along the beach (Fig. 4B). Recent glaciotectonic activity has resulted in a relatively steep bedding with internal small scale folding and thrusting (Pedersen, 2008), complicating stratigraphic thickness estimates. Jones et al. (2019) used trigonometry to estimate a local true thickness of 24.4 ± 2 m (24.2 m excluding ash layers) for the PETM onset and body at the Stolleklint beach; from the top

of Ash SK2 to the base of Ash -33 within the excavated trench. This estimated true thickness is used as the depth scale when presenting the results stratigraphically (e.g. Fig. 2), measured as positive and negative depth relative to the base of the main marker bed Ash -33. As the PETM was the main target, samples are collected at highest resolution across the PETM onset, then at lower resolution within the PETM interval and in the post-PETM section: Discrete samples were collected at 1 cm intervals from ~25 cm below to ~90 cm above Ash SK1 (in estimated true thickness), and then at 0.5 m intervals (0.2–0.3 m when converted to the estimated true thickness) up to Ash -33. Samples above ash -33 were collected from the cliff face at Stolleklint at ~10–20 cm intervals. Additional samples from -5.6 to +1.9 m relative to the base of Ash -33 were included from the quarry FQ16, sampled at ~30 cm intervals. All samples were oven dried at ≤50 °C and powdered in an agate hand mortar or an agate disc mill before further analysis.

The sediments unconsolidated character enabled the collection of 4 box-cores up section. The box-cores were collected in 50 cm long, 5 cm wide and deep aluminium boxes. These were pushed into the sediments before surrounding material was removed and the box cut away with its content intact using a steel wire. Box-cores were collected in order to get complete recovery of selected intervals for XRF core scanning (Fig. 5). Two box-cores were collected across the PETM onset (-24.90 to -24.40 m and -24.63 to -24.20 m stratigraphic depth intervals), and two from the PETM body with one from the lower laminated part (-14.47 to -14.17 m) and one from the non-laminated upper part (-10.81 to -10.48 m).

3.2 XRD bulk and clay mineralogy

Bulk rock mineralogy was conducted on 8 samples from -24.81 to +5.35 m depth, while 13 samples were analysed for clay minerals. The mineralogy of both bulk rock and clay fraction (< 2 µm) of Fur sediment samples were determined by X-ray diffraction (XRD) analyses on a Bruker D8 ADVANCE diffractometer with a Lynxeye 1-dimensional position-sensitive detector (PSD) and CuKα radiation ($\lambda = 0.154$ nm; 40mA and 40kV) at the Department of Geosciences, University of Oslo. The bulk-rock fraction was wet milled in a McCrone Micronizing Mill, prepared as randomly oriented samples, and analysed with a step size of 0.01° from 2° to 65° (2 θ) at a count time of 0.3 s (2 θ). The software DIFFRAC-EVA (v. 2.0) was used for phase determination, and phase quantities were determined by Rietveld refinement (Rietveld, 1969) using PROFEX (v. 3.13.0; Doebelin and Kleeberg, 2015).

The clay fraction (< 2 µm) was separated from the crushed whole-rock sample (before wet milling) by gravity settling, and then prepared as oriented aggregate mounts using the Millipore filter transfer method (Moore and Reynolds, 1997). As the dried samples had to be powdered prior to separation, they contain some minor contribution from the coarser fraction. XRD clay data were recorded with a step size of 0.01° from 2° to 65° (2 θ) at a count time of 0.3s (2 θ) in air-dried samples, and a step size

of 0.01° from 2° to 34° (2 θ) at a count time of 0.3s (2 θ) on treated samples. Three rounds of treatments were applied: 24h of ethylene glycol saturation, 1h heating at 350 °C, and 1h heating at 550 °C. The software NewMod II (Reynolds and Reynolds, 2012) was used for semi-quantification of the XRD-patterns of inter-stratified clay minerals.

3.3 XRF core scanning

Non-destructive geochemical measurements and radiographic images were obtained from the box-cores with an ITRAX X-ray fluorescence (XRF) Core Scanner (Croudace et al., 2006) from Cox Analytical Systems at the EARTHLAB facilities, Department of Earth Science, University of Bergen. The core scanner was fitted with a molybdenum X-ray tube run with power settings at 30 kV and 30 mA. The box-cores were scanned with 10 s exposure time at 0.5 mm sampling intervals.

3.4 Rock-Eval pyrolysis

The bulk organic-carbon characteristics including the hydrogen index (HI), oxygen index (OI), and T_{MAX} were investigated by Rock-Eval analyses. These were conducted at the University of Oxford on a Rock-Eval 6 (Vinci Technologies SA, Nanterre, France; Behar et al., 2001) with pyrolysis and oxidation ovens, a flame ionization detector, and infra-red cell. About 50 mg powder aliquots were weighed into crucibles and heated first at a temperature profile of 300 – 650 °C in a pyrolysis furnace and then at 300-850 °C in an oxidation oven. For a detailed methodology on the Rock-Eval 6 application, see Lafargue et al. (1998).

The HI corresponds to the quantity of hydrocarbons per gram TOC, and reflects the relative distribution of terrestrially and marine derived organic matter. A HI <100 indicates a dominantly terrigenous source, while a HI >>100 indicates the presence of significant amount of aquatic algae (marine and/or freshwater) and/or microbial biomass (e.g. Stein et al., 2006).

3.5 ICP-MS and Element Analyser

Analyses were conducted on 24 samples between -24.82 to +5.50 m depth. Dried and crushed marine sediment samples were digested in a mixture of 16M HNO₃ and 27M HF over several days at 100 °C, then twice in 2 % HNO₃, followed by HNO₃/18Mohm grade water overnight, all to a constant volume of 10 ml to give a total dilution of ~4 x 10⁶-fold by volume. Major and trace element analyses of digested bulk sediment samples were performed on a PerkinElmer NexION 350D ICP-MS. Total sulfur concentrations were analysed on a Coulomat 702 coulometric analyser. Sample digestion and analyses were all conducted at the Department of Earth Sciences, University of Oxford. The method detection limit is indicated in Supplementary Table 4. P₂O₅, Ba, Cu, Ni, and V have all been normalized to Al₂O₃ to

account for the potential detrital influx, as Al_2O_3 indicates the aluminosilicate fraction of the sediments (Tribovillard et al., 2006).

ICP-MS analyses of major elements were used to calculate the chemical index of alteration (CIA; Nesbitt and Young, 1982). The CIA is a measure of weathering intensity based on the relative distribution of mobile cations relative to aluminium oxide, and indicates the extent of conversion of feldspars (which dominate the upper crust) to clays such as kaolinite (Nesbitt and Young, 1982). While the CIA may directly represent the rate of weathering when measured *in situ*, when measured in marine sediments it becomes more complex as it also reflects the type of sediment and transport sorting processes (Nesbitt and Young, 1982). The CIA is expressed as:

$$CIA = \left(\frac{Al_2O_3}{Al_2O_3 + CaO + K_2O + Na_2O} \right) * 100$$

Where Al_2O_3 , CaO, K_2O , and Na_2O are given as whole-rock molecular proportions.

4. Results

4.1 Sedimentology

The base of the beach section comprises the Holmehus/Østerrende Formation (Figs. 4, 5), which is composed of dark, blueish clay with pervasive bioturbation. It is overlain by a greenish silty layer indicative of glauconite (marked with G in Fig. 6), with up to coarse sand-sized aggregates of glauconite scattered within the clay. The silt layers lower boundary is unclear, but it appears conformable and possibly gradational. The 5 cm thick ash layer SK1 is deposited on top of the glauconitic silt, with a sharp undulating lower boundary (Fig. 6). About 4.5 cm of structureless, grey clay conformably overlies SK1, and is followed by the ~8 cm thick ash layer SK2 (Fig. 6). Both ashes are light grey and seems to be heavily altered, almost bentonites. They are upward fining from medium sand to clay-sized particles. Both ashes are relatively reworked and become gradually more clay-rich toward the top, with the highest bioturbation intensity at the top of Ash SK2 (Fig. 6). About 2 cm of strongly bioturbated and ash-rich clay overlying the ash is abruptly ended by the initiation of dark laminations (Fig. 6 section B). The Stolleklint Clay bases exact level is uncertain as the boundary is blurred by ashes SK1 and SK2, but it includes the base of the laminations, placing the boundary no higher than here (Fig. 6 section B). Laminated dark clay continues for ~10 cm before deposition of two ash layers SK3 & SK4, ~1 cm and ~0.4 cm thick respectively (Fig. 6 section B). They are separated by 2 cm of clay with slightly undulating lamination. Above the ash, laminated clay continues about half-way up the beach (Fig. 5), with increasingly folded and disturbed layering (Fig. 7 section C).

The PETM body is dominated by hemipelagic clay, but appears to have a lower laminated part and an upper part (from about -10 m depth) comprising very dark grey clay with no visible laminations in field exposures (Fig. 5). However, the XRF radiographic image reveals that there are occasional diffuse laminations and patchy structures/colour differences within the clay (Fig. 8 section D). The cause of these colour patches is uncertain, but could be a result of depositional variations and/or post-depositional deformation. Between about -6 and -2 m depth there are some highly pyritized concretions, or likely broken up concreted layers (Fig. 5). Ash layers reappear from about -5 m depth with deposition of the thin (~2 cm), black Ash -39 (Fig. 5). Ashes -34, -33, -32, and -31 are deposited relatively closely spaced between -0.85 to +0.05 m depth, with thicknesses of 2, 20, 2 and 3 cm respectively. The thickest layer Ash -33 is repeated at the Stolleklint Beach, due to a small glaciotectionic thrust fault (Fig. 5). The boundary between the Stolleklint Clay and the Fur Formation is formally placed at Ash -33, although there is no sharp lithological boundary (Figs. 4, 5). Dark clays continue upward with a gradually increasing diatomite content. Laminations re-appear at about +6 m depth, as the lithology become dominated by clay-rich diatomite (Fig. 5).

4.2 Mineralogy

The bulk mineralogy comprises six main phases: zeolites, mica, clay (including smectite, chlorite, kaolin minerals, and glauconite), feldspars, quartz, and pyrite (Fig. 5). Phyllosilicates dominate the bulk mineralogy in the lower laminated part of the stratigraphy. While the mica fraction remains relatively stable throughout, the clay fraction reaches its maximum of 50.6 % at ~13 cm above Ash SK2 and the CIE onset (-24.24 m depth), before decreasing substantially upward from about -22 m depth (Fig. 5). Zeolites (of the heulandite-clinoptilolite type) dominate the CIE body, comprising up to 36 % of the bulk mineralogy at -10.48 m depth (Fig. 5). The fraction of feldspars is largest within the Holmehus/Østerende Formation (37 % at -24.81 m depth) and during the CIE recovery (35 % at +5.35 m depth), while quartz increases up to 26 % in the stratigraphically upper part (-0.28 m depth; Fig. 5). Pyrite makes up the smallest fraction of the bulk mineralogy (Fig. 5). It increases from 1.9 % in the lower Holmehus/Østerende Formation (-24.81 m depth) to 5.3 % ~13 cm above the CIE onset (-24.24 m depth). The highest fraction of pyrite (6.1-7.5 %) is reached during the CIE body, before values decrease during the PETM recovery to a minimum of 0.11 % at +5.35 m depth.

The clay fraction XRD analyses identified four major clay mineral phases: kaolinite, chlorite, mixed-layer illite-smectite with only minor illite layers indicating almost pure smectite, and illite + fine-grained mica (Fig. 5). From the base of the studied section and up to 13 cm above the CIE onset (-24.24 m depth), illite-smectite is the dominating clay mineral, increasing from 84 % to 90 % of the total clay within the interval, with only minor amounts of kaolinite and illite + fine-grained mica (Fig. 5). The lowest amount of illite-smectite in the studies section is 32 % about 1.5 m above the CIE onset (-22.86

m depth), before the illite-smectite content increases throughout the CIE body and recovery (Fig. 5). Illite + fine-grained mica comprises a smaller part of the total clay fraction, with 10 % during the CIE onset, and a maximum of 33 % at -5.93 m depth (Fig. 5). Kaolinite increases substantially from 5 % at 13 cm above the CIE onset (-24.24 m depth) to 37 % at 62 cm above the CIE onset (-23.75 m depth). Kaolinite dominates the clay fraction in the lower laminated PETM body with a maximum of 52 % at -20.60 m depth, before disappearing in the upper PETM body and re-emerging with 11 % during the recovery phase (+5.35 m depth; Fig. 5). Chlorite only appear in 4 of 13 samples and makes up the smallest part of the clay fraction, with a maximum of 7 % at -10.48 m depth (Fig. 5).

4.3 XRF core scanning

Two box-cores cross the PETM onset, covering the transition from Holmehus/Østerrende Formation into Stolleklint Clay, and the three ash layers SK1, SK2, and SK3 (Fig. 6). Sulfur counts show a slight overall increase from below to above the ashes, suggesting gradually more suboxic conditions above the ashes. Low K/Ti and Fe/Ti ratios suggest that the ashes are Ti-rich basalts. The gradual decrease in both K/Ti and Fe/Ti below Ash SK1 may subsequently suggests a potential gradual increase in volcanic-derived material before the appearance of the first ash layers in the Danish Basin (Fig. 6). Peaks in S counts indicate particularly S-rich parts of the ashes, although when correlating with Fe/Ti peaks it is more likely due to suboxic formation. Above Ash SK3, peaks of S, Fe/Ti, and Fe/K (although the latter signal is swamped by the iron-rich ashes in Fig. 6 section B) correlate with the dark lamination, suggesting at least periods of decreased oxicity.

Principal component analysis reveal a distinct difference in chemistry between the Holmehus/Østerrende Formation and the Stolleklint Clay (Fig. 8). It also indicates that both the clay between ashes SK1 and SK2 and parts of the glauconitic silt likely include a large ash component. While the glauconitic silt is chemically closer to the underlying Holmehus/Østerrende Formation than the Stolleklint Clay, the less ash-rich inter-ash clay appears to have a composition closest to the Stolleklint Clay. This suggests that this is indeed a part of the Stolleklint Clay base, and we therefore propose that Ash SK1 marks the lower Stolleklint Clay boundary. The correlation circle indicate that differences in Ca and Ti on one hand and K on the other is the main controlling factors (Fig. 8).

The box core in Figure 7 section C, covering the lower part of the Stolleklint Clay, shows that the sediments are strongly laminated and slightly folded. A relative elevation of S concentrations and Fe/Ti and Fe/K ratios compared to pre-PETM values indicate a possible decrease in basin oxicity. Correlations between these peaks in anoxia and dark laminations (Fig. 7 section C) suggest that there were regular variations in bottom-water oxicity. The K/Ti ratio remains relatively stable, suggesting no dramatic lithological changes. Figure 7 section D shows the non-laminated upper part of the Stolleklint Clay,

which displays relatively minor elemental variations. However, drops in the K/Ti ratio could indicate areas of increased volcanically-derived material, potentially as cryptotephra (Fig. 7 section D); defined as volcanic tephra deposits not visible to the naked eye. The presence of cryptotephra layers is particularly likely when low K/Ti ratios correlate with increases in Fe/Ti and Ca, and to some extent S (Rothwell and Croudace, 2015). Relative changes in Fe/Ti – and to some extent Ca – depend strongly on the source of the volcanic material. The biplot of S and Fe (Fig. 9) shows that the variability of S measurements decreases upward, and that there is an overall increase in S upward from the pre-PETM Holmehus/Østerrende Formation and throughout the Stolleklint Clay.

4.4 Major and trace elements of single samples

4.4.1 Detrital input

The CIA in pre-PETM sediments is generally at around 75, but has one peak of 85 just before the pre-PETM cooling event (-24.64 m depth; Fig. 10) indicating a relative rise in the influx of terrestrially weathered material. Following the onset, the CIA increases to a maximum of about 83 at -20.60 m depth, before returning to pre-PETM values in the upper half of the PETM body (Fig. 11). The recovery phase shows increasing CIA values again towards Ash -19, with 86 at +5.50 m depth.

The sediments thermal immaturity was verified by the low RockEval T_{max} values of <422 °C (Supplementary Table 3). The HI peaks up to 150 mgHC/gC in the glauconitic silt between -24.61 to -24.59 m depth, but is otherwise <100 mgHC/gC pre-PETM (Fig. 10). The HI increases >100 mgHC/gC about 13 cm above the CIE onset at -24.05 m depth. A second major increase in HI occurs above -14 m depth, after which values remain high and reaches maximum values of 303 mgHC/gC at -0.78 m depth (Fig. 11).

4.4.2 Productivity

The TOC data shows a pronounced increase from ~0.45 to ~1.3 wt% TOC about 2 cm above the PETM CIE onset (Fig. 10). TOC concentrations remain relatively stable for the first half of the CIE body, before increasing again in the upper half of the CIE body (from about -13 m depth) up to a maximum of 3.9 wt% at -0.78 m depth (Fig. 11). At the start of the CIE recovery, TOC drops down again to around 1 wt%.

Before the CIE onset Ba/Al₂O₃ decreases from at the base of the glauconitic silt, while Cu/Al₂O₃ increases, and Ni/Al₂O₃ and P₂O₅/Al₂O₃ remain relatively stable (Fig. 10). Both Cu and Ni are elements typically associated with volcanic ash, and both remain relatively high within the ash-rich interval. The main increase in productivity proxies occurs within the uppermost CIE body between about -8.56 m depth and Ash -33 (Fig. 11). This trend is most notable in Ba/Al₂O₃ and P₂O₅/Al₂O₃, reaching maximum

values of 49.8 and 0.017 respectively at -4.48 m depth. $\text{Cu}/\text{Al}_2\text{O}_3$ shows a similar although less distinct trend with the main increase in the upper CIE body, while $\text{Ni}/\text{Al}_2\text{O}_3$ decreases much earlier at about -5 m depth. During the recovery $\text{Ba}/\text{Al}_2\text{O}_3$ and $\text{P}_2\text{O}_5/\text{Al}_2\text{O}_3$ decreases, while $\text{Cu}/\text{Al}_2\text{O}_3$ and $\text{Ni}/\text{Al}_2\text{O}_3$ remain relatively stable (Fig. 11).

4.4.3 Redox

Both S and pyrite concentrations start to rise before Ash SK1 and the CIE onset, with S increasing from about 1 wt% in the Holmehus/Østerrende Formation to about 3 wt% in the glauconitic silt (Fig. 10). Sulfur concentrations remain high throughout the CIE body, with maximum values of 4.6 wt% reached at -8.6 m depth (Fig. 11). Th/U shows a relatively similar pattern as S, decreasing below Ash SK1 and reaching values below 2 before the CIE onset (Fig. 10). In the lower CIE body between -20.60 to -16.68 m depth Th/U increases up to 3, coinciding with slightly lowered S concentrations (Fig. 11). Th/U values decreases again and persist below 2 for the remainder of the CIE body (Fig. 11), as U concentrations are enriched up to 11.4 ppm (Supplementary Table 4), well above average crustal values of 2.8 ppm (Taylor and McLennan, 1995).

Molybdenum concentrations vary between 0.7–3.0 ppm below the CIE onset, before increasing to ~15 ppm about 2 cm above the CIE onset (Fig. 10). Molybdenum concentrations continue between 11–43 ppm indicating anoxic conditions prevail throughout the CIE body and recovery, with euxinic conditions (>30 ppm Mo) indicated in the upper part of the CIE body between -12.4 to -0.1 m depth (Fig. 11; Scott and Lyons, 2012).

$\text{V}/\text{Al}_2\text{O}_3$ increases in the glauconitic silt and remain relatively high in the ash interval (Fig. 10). Vanadium enrichments can also be associated with ash deposition, which might affect V concentrations in this particularly ash-rich interval. $\text{V}/\text{Al}_2\text{O}_3$ values increase gradually throughout the CIE body, reaching maximum just below Ash -33 at -0.11 m depth, and decreases again in the recovery (Fig. 11).

5. Discussion

5.1 Changing sediment input – tectonic and climatic influence

5.1.1 Illite-Smectite – importance and origin

Smectite is the dominant clay mineral within the pre-PETM and most of the earliest Eocene strata at both Fur (Fig. 5) and generally in the North Sea (Nielsen et al., 2015). Clay mineral assemblages have been used as indicators of palaeoclimate, most commonly using kaolinite as a proxy for humid tropical climates and smectite for warm climates with seasonal humidity and longer dry spells (e.g. Thiry, 2000). However, soil formation is a slow processes, and the subsequent long duration between formation and

deposition in a marine basin suggests that clay mineralogy is an unreliable palaeoclimate proxy at resolutions shorter than 1 Myr (Thiry, 2000). Changes in the clay mineral assemblage in the marine sediments may therefore instead indicate changes in source area and intensity of sediment transport, reflecting the climatic conditions at the time of continental soil formation rather than at the time of deposition (Thiry, 2000; Nielsen et al., 2015). Smectite is a common weathering product of mafic volcanic material (Stefánsson and Gíslason, 2001), and previous studies have suggested that smectites in the Danish stratigraphic record are of predominantly volcanic origin (Nielsen and Heilmann-Clausen, 1988; Pedersen et al., 2004). Although smectite may precipitate *in situ* from hydrothermal fluids, this has largely been discounted in the North Sea due to the wide geographic extent of smectite and the overall lack of indices of hydrothermal influence (Huggett and Knox, 2006; Kemp et al., 2016). Post-depositional alteration of volcanic ash also probably contributed only minor amounts of smectite, as the ashes are mostly relatively well-preserved (Nilsen et al., 2015). While clay minerals make up a small fraction of the bulk mineralogy in the upper part of the PETM (4–8 %), zeolites comprise up to 36 % (Fig. 5). Zeolites are another typical weathering product of volcanic materials, supporting a volcanic provenance (Stefánsson and Gíslason, 2001; Nielsen et al., 2015).

The volcanic source is likely to be the NAIP. Major flood basalts erupted in East Greenland, the Faroe Islands, and the British Isles across the Paleocene-Eocene boundary, producing large uplifted areas several km high of easily eroded material (Larsen and Tegner, 2006; Storey et al., 2007b; Wilkinson et al., 2017). This is reflected in Os isotopes and CIA records in the Arctic Ocean, which record an influx of weathered volcanic material both prior to and during the PETM (Wieczorek et al., 2013; Dickson et al., 2015). Moreover, the first phase of ash deposition was identified within Late Paleocene strata in the North Sea, well before the PETM onset (Knox and Morton, 1988; Haaland et al., 2000), which constitutes a highly important source for the weathered volcanic material in the North Sea (Pedersen et al., 2004; Nielsen et al., 2015; Kemp et al., 2016). Smectite is found in abundance throughout the North Sea stratigraphic record, and decreases as ash deposition ceases upward in the Eocene (Nielsen et al., 2015; Kemp et al., 2016). It seems likely that the dominance of smectite and abundance of zeolites reflect this extensive extrusive volcanism around the NAIP (Nielsen et al., 2015; Kemp et al., 2016).

5.1.2 Kaolinite and changes in weathering across the PETM onset

An important deviation from the smectite dominance is the substantial influx of kaolinite in the lowermost 10 m of the PETM CIE (Fig. 5). The abundance of kaolinite at Fur rises shortly after the CIE onset and again in the CIE recovery, in both instances concordant with an increase in the CIA and the overall clay fraction (Figs. 5, 11). An increase in kaolinite content during the PETM is observed globally (Robert and Kennett, 1994; Dypvik et al., 2011; John et al., 2012; Khozyem et al., 2013; Bornemann et

al., 2014; Kemp et al., 2016). While it was initially attributed to a warmer and more humid climate (e.g. Bolle et al., 2000), it is now generally acknowledged that the formation of kaolinite requires too much time (1–2 Myr; Thiry, 2000) to be a direct result of climate on such short timescales (Carmichael et al., 2017). The increase in kaolinite is therefore most likely due to an intensified hydrological cycle, leading to enhanced erosion and sediment transport of older deeply weathered bedrock and soils (Schmitz and Pujalte, 2003; John et al., 2012; Bornemann et al., 2014).

Although the kaolinite pulse appears to be global, the timing and magnitude varies a great deal even within the North Sea (Kender et al., 2012; Kemp et al., 2016). In the western North Sea, the kaolinite content increases earlier before and during the CIE onset and again similarly during the CIE recovery, but is relatively low in the CIE body (Kender et al., 2012; Kemp et al., 2016). However, at Fur a kaolinite content increase is not observed until after the CIE onset (Fig. 5), and southward in the Bay of Biscay in the North Atlantic the kaolinite content does not rise at all until the PETM recovery (Bornemann et al., 2014). It would be expected that changes in the climate and the hydrological cycle would be broadly similar within such a narrow region. It is therefore reasonable to assume that the timing and extent of kaolinite deposition depends just as much on the availability and proximity to potential source areas as the climatic conditions.

During the Paleocene and Early Eocene, the major sediment transport direction in the North Sea were from the west and northwest due to the thermal uplift of source areas around the NAIP such as the Faroe-Shetland platform (Fig. 12; Knox, 1996; Anell et al., 2012). Kender et al. (2012) subsequently suggested that the kaolinite pulse before the CIE in the central North Sea was due to the thermal uplift and short-lived regression in the latest Paleocene. At Fur, there is no pre-PETM pulse of kaolinite and the HI index is >100 within the glauconitic silt (Fig. 10), indicating an increase in aquatic organic matter deposition. However, it seems there is also an augmented CIA just below the glauconitic silt (~28 cm below the CIE onset at -24.64 m depth; Fig. 10), which suggests some increase in the fluxes of terrestrially-derived material could have occurred also prior to the CIE onset at Fur. Stokke et al. (2020a) similarly observed a peak in terrestrially-derived long chain *n*-alkanes and in soil-derived branched GDGTs (*br*GDGTs) around the base of the glauconitic silt, which could reflect a tectonically-forced regression due to the NAIP thermal uplift. The reduced response to this tectonic event in Denmark compared to the Central North Sea seems reasonable considering comparably distal position to the NAIP (Figs. 1, 12).

The influx of kaolinite at Fur correlates with a major increase in the CIA and starts minimum 12 cm above the CIE onset, and up to 22 cm (excluding Ash SK2) above the Stolleklint Clay base (Figs. 5, 11) – If we assume the boundary is placed at Ash SK1. Nielsen et al. (2015) found that deposition of kaolinite

in the Paleocene-Eocene North Sea thickens substantially towards the Fennoscandian shield, and suggest that this as the main source area for the Danish sediments. The Fennoscandian shield was characterised by deeply weathered bedrocks in the Paleogene, reflecting the Mesozoic warm tropical climate (Nielsen et al., 2015), and would therefore be enriched in kaolinite. Kaolinite is typically deposited closer to the source than finer clays such as smectite (Gibbs, 1977). Considering again the Danish areas distal position in relation to the NAIP (Figs. 1, 12) it is therefore likely that the main source of kaolinite was from the Fennoscandian Shield to the north and northeast, despite the main sediment source for the North Sea during this period being from the west and northwest (Fig. 12; Jordt et al., 2000; Anell et al., 2012). A drop in sea level exposes larger areas to erosion and brings river mouths closer to the marginal marine areas, subsequently triggering an influx of terrestrially derived material that could explain the early Eocene kaolinite and CIA increase in the Danish area. However, the increase post-dates sea level fall and major tectonic uplift in the latest Paleocene, and occurs after the CIE and major temperature increase (Fig. 11). It therefore seems reasonable that it at least partially reflects an intensified hydrological cycle due to climatic changes rather than purely tectonic forcing. Furthermore, a North Sea surface water freshening is suggested from palynology and shark-tooth apatite $\delta^{18}\text{O}$ values in the central North Sea (Zacke et al., 2009; Kender et al., 2012). The observed influx of kaolinite, increased CIA, and rapid intensification of sedimentation rates after the CIE onset at Fur are therefore likely to be the result of increased runoff due to an enhanced hydrological cycle.

5.2 Volcanic indices

Although the principal component analysis indicate that the glauconitic silt is most like the Holmehus/Østerrende Formation (Fig. 8), the gradual increase in Ti relative to Fe and K shown by the XRF element core scans suggest a gradual change in lithology towards Ash SK1 (Fig. 6). Variations in the major elements Fe, Ti, and K in marine sediments typically indicate changes in the terrigenous fraction (Rothwell and Croudace, 2015). Titanium is considered a stable element directly reflecting the coarse-grained terrigenous fraction, and the gradual increase could therefore reflect an influx of terrestrially-derived material within the glauconitic silt. This is supported by a slightly coarser grain size, the augmented CIA (Fig. 10), and an influx of terrestrially derived organic matter (Stokke et al., 2020a). However, this influx seems to decline prior to Ash SK1 in contrast to the increase in Ti. Titanium can also be used to indicate volcanic provenance, where K and Ti reflect felsic and mafic sources respectively (Rothwell and Croudace, 2015). In fact, the K/Ti ratio has been applied as a useful proxy for felsic/mafic provenance in the North Atlantic (Richter et al., 2006). The SK ashes are all highly titanium rich (Figs. 6), and it could be that we see a gradual rise in mafic volcanic activity before the main ash deposition. This is corroborated by the East Greenland lava eruptions timing and duration,

which suggest that a 5–6 km thick lava pile was emplaced between 56.0 and 55.6 Ma (Larsen and Tegner, 2006).

An amplified influx of weathered basaltic material such as smectite could also cause the gradually increased Ti flux. However, smectite is already the dominant clay phase in the Holmehus/Østerrende Formation (Fig. 5), and does not show a significant rise in the glauconitic clay. It therefore seems that the augmented Ti concentrations within the glauconitic silt might be caused by an increased ash component, rather than from basaltic weathering. The trace metals Cu, Ni, and V are also found to increase within the glauconitic silt (Fig. 10), all of which are typically associated with volcanic material and maintain high concentrations within the SK1–SK2 interval. Such volcanic ash deposits that are not visible to the naked eye are called cryptotephra, and typically include glass shards and crystals together with non-volcanic deposits (Cassidy et al., 2014). It is possible that the glauconitic silt includes an increasing portion of cryptotephra prior to the large eruptions producing ashes SK1 and SK2. In our previous study, we found that SSTs cooled prior to the PETM onset in Denmark (Stokke et al., 2020a). Although the cooling started within the glauconitic silt below Ash SK1 (Fig. 10), we proposed that it could be a result of volcanic cooling induced by SO₂ aerosols from NAIP eruptions (Stokke et al., 2020a). The observation of a potentially increasing ash component already within this glauconitic unit would be supportive of a volcanically induced cooling.

The identified tephra layers in Denmark represent explosive eruptions with an unusually large magnitude in order to be transported such a long distance (Stokke et al., 2020b). The absence of visible tephra layers therefore does not automatically mean that there was no tephra producing eruptions during the PETM. Besides two thin ash layers about 10 and 12 cm above Ash SK2, there are no visible ash layers during the PETM body until the deposition of Ash -39 at about -5 m depth (Fig. 5). However, the box cores allow for a detailed and high resolution overview that might reveal the presence of ash rich intervals earlier. Figure 7 section D shows correlating changes in S, Ca, Fe/Ti, Fe/K, and K/Ti between about -10.81 to -10.48 m depth. These indicate four possible ash rich horizons within the dark clays, which could be cryptotephra of slightly variable chemistry (Fig. 7 section D). This suggests that explosive volcanic eruptions at a scale substantial enough for some material to reach Denmark may also have occurred during the PETM body. However, much more detailed work is needed in order to confirm the presence or absence of tephra fall deposits during this interval.

5.3 Changes in basin oxicity

5.3.1 Oxic-anoxic shift across the PETM onset

The PETM CIE is concordant with a lithological shift from the bioturbated Holmehus/Østerrende Formation to the laminated Stolleklint Clay, reflecting a shift to a suboxic to anoxic bottom water

environment. An increase in S, pyrite, V/Al, and U (seen as a decrease in Th/U) within the glauconitic silt could indicate reducing conditions prior to the CIE onset (Fig. 10). The NAIP uplift led to the closing of ocean seaways and North Sea Basin restriction prior to the CIE, resulting in increased halocline stratification that could explain this early deoxygenation (Kender et al., 2012). However, this is contrary to the low organic content, abundant bioturbation, and high content of glauconite, suggesting that an oxygenated environment prevailed pre-PETM. An oxic environment has also been indicated by the relatively high organic biomarker pristane/phytane values indicating oxidation of phytol to pristane (Stokke et al., 2020a). Sluijs et al. (2014) explained a similar co-occurrence of oxic and euxinic proxies within a section in the Gulf of Mexico as the result of seasonal to decadal variations in basin oxicity. Alternatively, the increase in S, U, and V could be attributed to an increased ash component within the glauconitic silt, as volcanic tephra deposits can reduce the sediment pore water oxygen levels (Hembury et al., 2012). An increase in the sedimentary ash component has already been suggested based on the high resolution XRF element core scans (Fig. 6), and the increase in ICP-MS analyses of Ni and Cu (Fig. 10). However, the highly redox-sensitive element Mo does not show a similar increase below the CIE (Fig. 10). The burial rate of Mo increases three orders of magnitude in sulfidic environments relative to oxic, as Mo becomes highly reactive in the presence of hydrogen sulfide (Tribouillard et al., 2004; Scott and Lyons, 2012). Molybdenum enrichment above bulk crustal values (1–2 ppm; Taylor and McLennan, 1995) indicates suboxic to anoxic conditions, and enrichments >30 ppm are argued to indicate euxinic conditions (Scott and Lyons, 2012; Dickson et al., 2014). Molybdenum concentrations at Stolleklint do not increase substantially above 3 ppm until after the CIE, suggesting that a substantial decrease in oxicity does not occur until after the PETM onset.

Laminations occur rapidly after the CIE onset, together with an increase in TOC and Mo concentrations, as well as continued low Th/U values (Fig. 11). The XRF element core scans also show an increase in S and Fe/Ti at base of the laminated sediments (Fig. 6 section B). Iron and Ti in marine sediments commonly co-vary, and elevated Fe/Ti ratios therefore indicate excess Fe over basaltic lithogenic values (Marsh et al., 2007). While Ti is considered a stable element that directly reflects the coarse-grained terrigenous fraction, Fe is redox-sensitive and may also reflect changes in basin oxicity post-deposition (Rothwell and Croudace, 2015). An increase of Fe relative to Ti or K may therefore indicate suboxic conditions, particularly in concert with increased S content (e.g. Sluijs et al., 2009). We therefore conclude that the start of laminations about 2 cm above Ash SK2 and the CIE onset indicate the initiation of fully anoxic conditions at Stolleklint. In addition, photic zone euxinia may have occurred just after the CIE onset, as indicated by the presence of sulfur bound isorenieratane; a diagenetic product of green sulfur bacteria (Schoon et al., 2015).

5.3.2 Redox and productivity changes during the PETM body

Schoon et al. (2015) argued that photic zone euxinia prevailed during the entire PETM interval in two sedimentary sections in Denmark. Unfortunately, their data from Fur only covers the lowermost 2.5 m and uppermost 0.5 m of the Stolleklint Clay, and therefore excludes most of the PETM body. All proxies from our continuous record through the PETM body suggest that anoxia prevailed throughout (Fig. 10), but the proxies also indicate distinct stratigraphic variations in basin oxicity. The XRF element core scans document a direct correlation between elevated S and Fe/Ti, and the dark laminations (Fig. 7 section C), suggesting regular fluctuations in basin oxicity (approximately every 2 cm). Variations in basin anoxia is also indicated for longer periods. The biplot of S data from XRF element core scans (Fig. 9) indicate an overall stratigraphic upward increase in basin anoxia. The upward decrease in scatter in the S measurements also indicates that anoxic conditions becomes gradually more continuous with time (Fig. 9).

While Th is sourced from continental weathering and unreactive to redox changes, U has minimal detrital influence and is enriched in the sediments under reducing conditions (Tribovillard et al., 2006). The Th/U ratio therefore reflects U enrichment above crustal values, and is typically employed to assess basin oxicity (Wignall and Myers, 1988; Dypvik et al., 2011; Elrick et al., 2017). Th/U is about 4 in the average upper crust, and typically <2 in anoxic environments with substantial authigenic U enrichment (Wignall and Twitchett, 1996). An increase in Th/U above 2 correlates with a decrease in Mo concentrations well below 30 ppm around -17 to -18 m depth in the lower laminated part, indicating a period of less anoxic conditions in the lower part of the PETM body (Fig. 11). Both U and Mo concentrations increase substantially in the upper part of the PETM, with Th/U <2 and Mo well above 30 ppm indicating euxinic conditions (Fig. 11). Maximum values of S, pyrite and V/Al within this interval also indicate highly reducing conditions, with high TOC of 4 wt% indicating increased organic matter burial rate.

The North Sea Basin became very restricted in the latest Paleocene prior to initiation of seafloor spreading and basin subsidence, resulting in poor circulation in the basin (Knox et al., 2010). While this could explain the initial decrease in basin oxicity, there is no further evidence supporting regional uplift and North Sea basin restriction associated with the CIE onset. On the contrary, high HI (Fig. 11), and low input of *br*GDGTs and long-chained *n*-alkanes (Stokke et al., 2020a) suggest that marine-derived organic matter increases up stratigraphy, as the Stolleklint Clay was likely deposited during a relative sea level rise (Heilmann-Clausen, 1995). Barium is closely related to export productivity, as it precipitates from decaying organic matter (Paytan and Griffith, 2007; Ma et al., 2014). The sedimentary Ba content is at its highest during the upper PETM body, as is P₂O₅ (an essential macronutrient), indicating that export productivity was at its highest at this point (Fig. 11; Supplementary Table 4).

Possible remobilisation of Ba and P needs to be considered, particularly in sulfidic environments (Tribovillard et al., 2006). However, the dark massive clay in the upper part of the PETM body is also highly enriched in organic matter (TOC up to 3.9 wt%). An increase in TOC could reflect declining terrestrial influx, possibly due to the increasing sea level, which is expected to lead to a decrease in terrestrial sediment transport to marginal areas (e.g. Carmichael et al., 2017). Still, the combined elevation of TOC, Ba/Al, and P_2O_5/Al , as well as to some extent Ni/Al and Cu/Al (Fig. 11), are all in support of an increase in export productivity. Kender et al. (2012) found evidence of low surface water salinity and extensive stratification in the North Sea, and suggested this as the main cause of anoxia during the PETM. A combination of ocean stratification and increased productivity would efficiently contribute to the increase in basin anoxia toward the upper half of the PETM body.

5.4 The PETM recovery

The PETM carbon cycle perturbations are unusual both in magnitude and duration, and likely a result of a combination of triggers and feedback mechanisms that are not yet fully understood (McInerney and Wing, 2011; Komar and Zeebe, 2017). Continuous emissions from a light carbon source such as thermogenic degassing around the NAIP could have contributed to the long duration (Svensen et al., 2004; Frieling et al. 2016). Another suggestion is that an initial pulse of light carbon led to warming (e.g. Frieling et al., 2019), subsequently activating positive feedback mechanisms producing continued input of light carbon emissions from sources such as methane clathrates (Dickens et al. 1995) or terrestrial organic carbon (Bowen 2013). Another key feature of the PETM is the rapidity of the PETM recovery (e.g. Bowen and Zachos, 2010). The carbon cycle recovery occurs through a combination of natural carbon sequestration and negative feedback mechanisms reducing the atmospheric CO_2 content (McInerney and Wing, 2011). Silicate weathering and denudation is one of the most important negative feedback mechanisms driving CO_2 drawdown (Gislason and Oelkers, 2011), and has been proposed as one of the most important PETM recovery drivers (Kelly et al., 2005; Torfstein et al., 2010; Penman, 2016).

Silicate weathering is highly sensitive to runoff, temperature, and topography (Gislason and Oelkers, 2011). Temperatures rose globally both before and during the PETM onset (Frieling et al., 2017; Frieling et al., 2019). At Stolleklint, temperatures rose about 10 °C reaching maximum SSTs of ~33 °C shortly after the CIE onset, followed by a shift to gradually decreasing SSTs throughout the PETM body and recovery (Stokke et al., 2020a). The warming combined with the increased runoff, indicated in the North Sea by enhanced surface water freshening (Kender et al., 2012), would result in a warm and humid climate ideal for increased silicate weathering and denudation. This is supported by the large increase in sedimentation rate, kaolinite influx, and the CIA at Stolleklint (Figs. 5, 11), suggesting a rapid response in weathering to changes in carbon cycle and temperature. Fresh basaltic volcanic terrains

are particularly prone to weathering, and constitute one of the most important sources of weathered suspended material in the world's oceans (Gislason and Oelkers, 2011). While both the kaolinite content and the CIA decreased in the upper part of the PETM body, the sedimentation rate likely remained high, suggesting a relatively rapid influx of other minerals such as the volcanically-derived smectite and zeolite. The extensive NAIP flood basalt volcanism occurring before and during the PETM (e.g. Larsen and Tegner, 2006) may therefore have played an important role in facilitating the enhanced silicate weathering, as reflected in the dominance of smectite within the North Sea (Nilsen et al., 2015). A second increase in both the CIA and the kaolinite content occurred during the CIE recovery at Fur (Figs. 5, 11), as well as further west in the North Sea (Kender et al., 2012; Kemp et al., 2016). This supports the important role of enhanced silicate weathering in driving the PETM recovery suggested both for the North Atlantic (Penman, 2016) and globally (e.g. Kelly et al., 2005).

We have documented a relatively rapid rise in silicate weathering as a response to carbon emissions, but a major increase in productivity and organic carbon burial is delayed until the upper part of the PETM body. An enhanced terrestrial sediment influx would bring substantial nutrients to the basin, but the decrease in the CIA and kaolinite, as well as the dominance of marine organic matter ($HI > 100$; Fig. 11), rather suggest a decrease in the terrigenous influx upwards in the PETM body. However, the deposition of volcanic ash can work as a fertilizer, supplying key nutrients to the marine environment resulting in augmented productivity (Jones and Gislason, 2008). Substantial increases in Ba and P_2O_5 occur after the deposition of Ash -39 at the end of the PETM body (Fig. 11; Supplementary Table 4). Additional ash deposition below Ash -39 have now been revealed by the possible cryptotephra in XRF element core scans (Fig. 7 section D), which could have had an added fertilizing effect.

Bowen and Zachos (2010) suggested that the rate of recovery is an order of magnitude faster than expected for carbon drawdown by silicate weathering alone. Similarly, Penman and Zachos (2018) found that the $\delta^{11}B$ and B/Ca records of ocean acidification recovers within a similar time frame as the $\delta^{13}C$ record, and far more rapid than suggested by carbon cycle models that rely on silicate weathering alone (e.g. Zeebe et al., 2009). We have documented a rise in nutrient supply and enhanced primary production, which could lead to the increased organic carbon sequestration attributed to the accelerated PETM recovery (Bowen and Zachos, 2010; Komar and Zeebe, 2017; Bridgestock et al., 2019). Enhanced export productivity has also been observed in PETM sites globally (Bains et al., 2000; Egger et al., 2003; Stein et al., 2006; Soliman et al., 2011; Ma et al., 2014; Bridgestock et al., 2019), and average Ba burial rates approximately tripled during the PETM (Frieling et al., 2019). Our results show that negative feedback mechanisms responded rapidly to changes in carbon cycle and SSTs, and remained highly active from PETM onset to recovery. While the $\delta^{13}C$ values remained low until the PETM recovery, SSTs decreased gradually throughout the PETM body and recovery. This dual response

may reflect that while continued input of ^{12}C -enriched maintained a negative CIE (e.g. Frieling et al., 2016), it was not sufficient to completely counteract the continued carbon drawdown by the alternating increases in both silicate weathering and export productivity during the PETM leading to a gradual temperature decline.

Conclusions

We present new mineralogical and geochemical data from an expanded marine section at Fur in northwest Denmark covering the PETM onset, body and recovery. Here, the PETM is defined by a negative 4.5 ‰ CIE and at least 10 °C temperature rise across the PETM onset. The study focuses on a section at Stolleklint, where the PETM onset is seen as lithological shift from the Holmehus/Østerrende Formation bioturbated clays into the Stolleklint Clay laminated clays. The sediments are composed of marine clays, dominated by volcanogenic minerals such as smectite and zeolite, reflecting the NAIPs important role as a source area during this period.

The CIE onset is quickly followed by an increase in kaolinite content, the chemical index of alteration, and substantially enhanced sedimentation rates. This reflects a rapid response in silicate weathering to changes in the carbon cycle and elevated temperatures, likely due to an enhanced hydrological cycle. Large volumes of easily weathered NAIP flood basalts and widespread tephra deposits likely contributed to accelerate the degree of silicate weathering and carbon drawdown. Proxy evidence shows augmented export productivity and organic matter burial towards the upper part of the PETM body, coinciding with the reappearance of volcanic ash in XRF element core scans and in field exposures. Such a correlation highlights the fertilizing effect of volcanic nutrients, and its potential importance in increasing primary productivity. Pervasive basin deoxygenation also occurs shortly after the PETM onset, with anoxic to euxinic bottom-water conditions prevailing throughout the PETM body. The continued deoxygenation was likely caused by the already restricted nature of the basin combined with amplified terrestrial runoff leading to ocean stratification, and intensified export productivity.

The results presented in this study show the potentially rapid environmental response to changes in carbon cycle and temperature. Our data also show that negative feedback mechanisms were active throughout the PETM. The increased export productivity in the upper part of the PETM body and the renewed rise in kaolinite content and the CIA during the PETM recovery reflect the important role of enhanced silicate weathering and organic matter burial in carbon drawdown leading to the PETM recovery. This highlights the importance of such marginal marine areas in carbon sequestration and recovery from carbon cycle perturbations.

Acknowledgement

Claus Heilmann-Clausen, Sverre Planke, Christian Tegner, Tanusha Naidoo, Phil Holdship, Stephen Wyatt, Lina Hedvig Line, and Valentin Zuchuat are all warmly thanked for their assistance. This project was supported by the Research Council of Norway's funding schemes "Unge Forskертallenter" project number 263000 (project Ashlantic) and "Centres of Excellence" project number 223272.

References

- Abdelmalak, M. M., Planke, S., Faleide, J. I., Jerram, D. A., Zastrozhnov, D., Eide, S., & Myklebust, R. (2016). The development of volcanic sequences at rifted margins: New insights from the structure and morphology of the Vøring Escarpment, mid-Norwegian Margin. *Journal of Geophysical Research: Solid Earth*, 121(7), 5212-5236.
- Alegret, L., Ortiz, S., & Molina, E. (2009). Extinction and recovery of benthic foraminifera across the Paleocene–Eocene Thermal Maximum at the Alamedilla section (Southern Spain). *Palaeogeography, Palaeoclimatology, Palaeoecology*, 279(3-4), 186-200.
- Alley, R. B. (2016). A heated mirror for future climate. *Science*, 352(6282), 151-152.
- Anell, I., Thybo, H., & Rasmussen, E. (2012). A synthesis of Cenozoic sedimentation in the North Sea. *Basin Research*, 24(2), 154-179.
- Babila, T. L., Penman, D. E., Hönlisch, B., Kelly, D. C., Bralower, T. J., Rosenthal, Y., & Zachos, J. C. (2018). Capturing the global signature of surface ocean acidification during the Palaeocene–Eocene Thermal Maximum. *Philosophical Transactions of the Royal Society A: Mathematical, Physical and Engineering Sciences*, 376(2130), 20170072.
- Bains, S., Norris, R. D., Corfield, R. M., & Faul, K. L. (2000). Termination of global warmth at the Palaeocene/Eocene boundary through productivity feedback. *Nature*, 407(6801), 171-174.
- Behar, F., Beaumont, V., & Penteado, H. D. B. (2001). Rock-Eval 6 technology: performances and developments. *Oil & Gas Science and Technology*, 56(2), 111-134.
- Bograd, S. J., Castro, C. G., Di Lorenzo, E., Palacios, D. M., Bailey, H., Gilly, W., & Chavez, F. P. (2008). Oxygen declines and the shoaling of the hypoxic boundary in the California Current. *Geophysical Research Letters*, 35(12), L12607.
- Bolle, M. P., Tantawy, A. A., Pardo, A., Adatte, T. H. E. R. R. Y., Burns, S., & Kassab, A. (2000). Climatic and environmental changes documented in the upper Paleocene to lower Eocene of Egypt. *Eclogae Geologicae Helvetiae*, 93(1), 33-52.
- Bornemann, A., Norris, R. D., Lyman, J. A., D'haenens, S., Groeneveld, J., Röhl, U., ... & Speijer, R. P. (2014). Persistent environmental change after the Paleocene–Eocene Thermal Maximum in the eastern North Atlantic. *Earth and Planetary Science Letters*, 394, 70-81.
- Bowen, G. J. (2013). Up in smoke: A role for organic carbon feedbacks in Paleogene hyperthermals. *Global and Planetary Change*, 109, 18-29.
- Bowen, G. J., & Zachos, J. C. (2010). Rapid carbon sequestration at the termination of the Palaeocene–Eocene Thermal Maximum. *Nature Geoscience*, 3(12), 866-869.

- Bowen, G. J., Maibauer, B. J., Kraus, M. J., Röhl, U., Westerhold, T., Steimke, A., ... & Clyde, W. C. (2015). Two massive, rapid releases of carbon during the onset of the Palaeocene–Eocene thermal maximum. *Nature Geoscience*, 8(1), 44-47.
- Bridgestock, L., Hsieh, Y. T., Porcelli, D., & Henderson, G. M. (2019). Increased export production during recovery from the Paleocene–Eocene thermal maximum constrained by sedimentary Ba isotopes. *Earth and Planetary Science Letters*, 510, 53-63.
- Bøggild, O.B. (1918). Den vulkanske Aske i Moleret samt en Oversigt over Danmarks ældre Tertiærbjergarter. *Bulletin of the Geological Society of Denmark*, 33, 1-159.
- Carmichael, M. J., Inglis, G. N., Badger, M. P., Naafs, B. D. A., Behrooz, L., Remmelzwaal, S., ... & Dickson, A. J. (2017). Hydrological and associated biogeochemical consequences of rapid global warming during the Paleocene-Eocene Thermal Maximum. *Global and Planetary Change*, 157, 114-138.
- Carmichael, M. J., Pancost, R. D., & Lunt, D. J. (2018). Changes in the occurrence of extreme precipitation events at the Paleocene–Eocene thermal maximum. *Earth and Planetary Science Letters*, 501, 24-36.
- Cassidy, M., Watt, S. F., Palmer, M. R., Trofimovs, J., Symons, W., Maclachlan, S. E., & Stinton, A. J. (2014). Construction of volcanic records from marine sediment cores: A review and case study (Montserrat, West Indies). *Earth-Science Reviews*, 138, 137-155.
- Charles, A. J., Condon, D. J., Harding, I. C., Pälike, H., Marshall, J. E., Cui, Y., ... & Croudace, I. W. (2011). Constraints on the numerical age of the Paleocene-Eocene boundary. *Geochemistry, Geophysics, Geosystems*, 12(6).
- Clausen, O. R., Nielsen, O. B., Huuse, M., & Michelsen, O. (2000). Geological indications for Palaeogene uplift in the eastern North Sea Basin. *Global and Planetary Change*, 24(3-4), 175-187.
- Cramer, B. S., Toggweiler, J. R., Wright, J. D., Katz, M. E., & Miller, K. G. (2009). Ocean overturning since the Late Cretaceous: Inferences from a new benthic foraminiferal isotope compilation. *Paleoceanography*, 24(4).
- Cramwinckel, M. J., Huber, M., Kocken, I. J., Agnini, C., Bijl, P. K., Bohaty, S. M., ... & Peterse, F. (2018). Synchronous tropical and polar temperature evolution in the Eocene. *Nature*, 559(7714), 382-386.
- Croudace, I. W., Rindby, A., & Rothwell, R. G. (2006). ITRAX: description and evaluation of a new multi-function X-ray core scanner. *Geological Society, London, Special Publications*, 267(1), 51-63.
- Dickens, G. R., O'Neil, J. R., Rea, D. K., & Owen, R. M. (1995). Dissociation of oceanic methane hydrate as a cause of the carbon isotope excursion at the end of the Paleocene. *Paleoceanography and Paleoclimatology*, 10(6), 965-971.
- Dickson, A. J., Rees-Owen, R. L., März, C., Coe, A. L., Cohen, A. S., Pancost, R. D., ... & Shcherbinina, E. (2014). The spread of marine anoxia on the northern Tethys margin during the Paleocene-Eocene Thermal Maximum. *Paleoceanography*, 29(6), 471-488.
- Dickson, A. J., Cohen, A. S., Coe, A. L., Davies, M., Shcherbinina, E. A., & Gavrilov, Y. O. (2015). Evidence for weathering and volcanism during the PETM from Arctic Ocean and Peri-Tethys osmium isotope records. *Palaeogeography, Palaeoclimatology, Palaeoecology*, 438, 300-307.
- Doebelin, N., & Kleeberg, R. (2015). Profex: a graphical user interface for the Rietveld refinement program BGMN. *Journal of Applied Crystallography*, 48(5), 1573-1580.
- Dunkley Jones, T., Lunt, D. J., Schmidt, D. N., Ridgwell, A., Sluijs, A., Valdes, P. J., & Maslin, M. (2013). Climate model and proxy data constraints on ocean warming across the Paleocene–Eocene Thermal Maximum. *Earth-Science Reviews*, 125, 123-145.

- Dunkley Jones, T., Manners, H. R., Hoggett, M., Kirtland Turner, S., Westerhold, T., Leng, M. J., ... & Grimes, S. T. (2018). Dynamics of sediment flux to a bathyal continental margin section through the Paleocene–Eocene Thermal Maximum. *Climate of the Past*, 14(7), 1035-1049.
- Dypvik, H., Riber, L., Burca, F., R  ther, D., Jargvoll, D., Nagy, J., & Jochmann, M. (2011). The Paleocene–Eocene thermal maximum (PETM) in Svalbard—clay mineral and geochemical signals. *Palaeogeography, Palaeoclimatology, Palaeoecology*, 302(3-4), 156-169.
- Egger, H., Heilmann-Clausen, C., & Schmitz, B. (2000). The Paleocene/Eocene-boundary interval of a Tethyan deep-sea section (Austria) and its correlation with the North Sea Basin. *Bulletin de la Soci  t   g  ologique de France*, 171(2), 207-216.
- Egger, H., R  gl, F., & Schmitz, B. (2003). Paleoproductivity of the northwestern Tethyan margin. *Causes and consequences of globally warm climates in the early Paleogene*, 369, 133.
- Eldholm, O., & Thomas, E. (1993). Environmental impact of volcanic margin formation. *Earth and Planetary Science Letters*, 117(3-4), 319-329.
- Elrick, M., Polyak, V., Algeo, T. J., Romaniello, S., Asmerom, Y., Herrmann, A. D., ... & Chen, Z. Q. (2017). Global-ocean redox variation during the middle-late Permian through Early Triassic based on uranium isotope and Th/U trends of marine carbonates. *Geology*, 45(2), 163-166.
- Frieling, J., Svensen, H. H., Planke, S., Cramwinckel, M. J., Selnes, H., & Sluijs, A. (2016). Thermogenic methane release as a cause for the long duration of the PETM. *Proceedings of the National Academy of Sciences*, 113(43), 12059-12064.
- Frieling, J., Gebhardt, H., Huber, M., Adekeye, O. A., Akande, S. O., Reichart, G. J., ... & Sluijs, A. (2017). Extreme warmth and heat-stressed plankton in the tropics during the Paleocene-Eocene Thermal Maximum. *Science Advances*, 3(3), e1600891.
- Frieling, J., Peterse, F., Lunt, D. J., Bohaty, S. M., Sinninghe Damst  , J. S., Reichart, G. J., & Sluijs, A. (2019). Widespread warming before and elevated barium burial during the Paleocene-Eocene Thermal Maximum: Evidence for methane hydrate release?. *Paleoceanography and Paleoclimatology*, 34(4), 546-566.
- Gavrilov, Y. O., Shcherbinina, E. A., & Oberhansli, H. (2003). Paleocene-Eocene boundary events in the northeastern Peri-Tethys. *Special Papers, Geological Society of America*, 147-168.
- Gibbs, R. J. (1977). Clay mineral segregation in the marine environment. *Journal of Sedimentary Research*, 47(1), 237-243.
- Gibson, T. G., Bybell, L. M., & Mason, D. B. (2000). Stratigraphic and climatic implications of clay mineral changes around the Paleocene/Eocene boundary of the northeastern US margin. *Sedimentary Geology*, 134(1-2), 65-92.
- Gilly, W. F., Beman, J. M., Litvin, S. Y., & Robison, B. H. (2013). Oceanographic and biological effects of shoaling of the oxygen minimum zone. *Annual Review of Marine Science*, 5, 393-420.
- Gislason, S. R., & Oelkers, E. H. (2011). Silicate rock weathering and the global carbon cycle. *Frontiers in Geochemistry: Contribution of Geochemistry to the Study of the Earth*, 84-103.
- Gutjahr, M., Ridgwell, A., Sexton, P. F., Anagnostou, E., Pearson, P. N., P  like, H., ... & Foster, G. L. (2017). Very large release of mostly volcanic carbon during the Palaeocene–Eocene Thermal Maximum. *Nature*, 548(7669), 573-577.
- Haaland, H.J., Furnes, H., & Martinsen, O.J. (2000). Paleogene tuffaceous intervals, Grane Field (Block 25/11), Norwegian North Sea: their depositional, petrographical, geochemical character and regional implications. *Marine and Petroleum Geology*, 17(1), 101-118.

- Harding, I. C., Charles, A. J., Marshall, J. E., Pälike, H., Roberts, A. P., Wilson, P. A., ... & Pearce, R. B. (2011). Sea-level and salinity fluctuations during the Paleocene–Eocene thermal maximum in Arctic Spitsbergen. *Earth and Planetary Science Letters*, 303(1-2), 97-107.
- Heilmann-Clausen C. (1994) Review of Paleocene dinoflagellates from the North Sea region. *GFF* 116, 51–53.
- Heilmann-Clausen, C. (1995). Palæogene aflejringer over Danskekalken. In: Nielsen, O.B. (Ed.), *Aarhus Geokompender No. 1, Danmarks geologi fra Kridt til i dag*, pp. 69-114.
- Heilmann-Clausen, C., Nielsen, O. B., & Gersner, F. (1985). Lithostratigraphy and depositional environments in the Upper Paleocene and Eocene of Denmark. *Bulletin of the Geological Society of Denmark*, 33, 287-323.
- Held, I. M., & Soden, B. J. (2006). Robust responses of the hydrological cycle to global warming. *Journal of Climate*, 19(21), 5686-5699.
- Hembury, D. J., Palmer, M. R., Fones, G. R., Mills, R. A., Marsh, R., & Jones, M. T. (2012). Uptake of dissolved oxygen during marine diagenesis of fresh volcanic material. *Geochimica et Cosmochimica Acta*, 84, 353-368.
- Hollis, C. J., Taylor, K. W., Handley, L., Pancost, R. D., Huber, M., Creech, J. B., ... & Gibbs, S. (2012). Early Paleogene temperature history of the Southwest Pacific Ocean: Reconciling proxies and models. *Earth and Planetary Science Letters*, 349-350, 53-66.
- Horni, J.A., Hopper, J.R., Blischke, A., Geisler, W.H., Stewart, M., McDermott, K., Judge, M., Elerlendsson, O., & Arting, U.E. (2017). Regional distribution of volcanism within the North Atlantic Igneous Province. In: Peron-Pinvidic, G., Hopper, J.R., Stoker, M.S., Gaina, C., Doornenbal, J.C., Funck, T., & Arting, U.E. (Eds.), *A Reappraisal of Crustal Structure, Tectonostratigraphy and Magmatic Evolution*. Geological Society, London, special publications.
- Huggett, J. M., & Knox, R. O. B. (2006). Clay mineralogy of the Tertiary onshore and offshore strata of the British Isles. *Clay minerals*, 41(1), 5-46.
- Jenkyns, H. C. (2010). Geochemistry of oceanic anoxic events. *Geochemistry, Geophysics, Geosystems*, 11(3).
- John, C. M., Bohaty, S. M., Zachos, J. C., Sluijs, A., Gibbs, S., Brinkhuis, H., & Bralower, T. J. (2008). North American continental margin records of the Paleocene-Eocene thermal maximum: Implications for global carbon and hydrological cycling. *Paleoceanography*, 23(2).
- John, C. M., Banerjee, N. R., Longstaffe, F. J., Sica, C., Law, K. R., & Zachos, J. C. (2012). Clay assemblage and oxygen isotopic constraints on the weathering response to the Paleocene-Eocene thermal maximum, east coast of North America. *Geology*, 40(7), 591-594.
- Jolley, D.W. & Widdowson, M. (2005). Did Paleogene North Atlantic rift-related eruptions drive early Eocene climate cooling? *Lithos*, 79, 355-366.
- Jones, M. T., & Gislason, S. R. (2008). Rapid releases of metal salts and nutrients following the deposition of volcanic ash into aqueous environments. *Geochimica et Cosmochimica Acta*, 72(15), 3661-3680.
- Jones, M. T., Percival, L. M., Stokke, E. W., Frieling, J., Mather, T. A., Riber, L., ... & Svensen, H. H. (2019). Mercury anomalies across the Palaeocene–Eocene thermal maximum. *Climate of the Past*, 15(1).
- Jordt, H., Thyberg, B. I., & Nøttvedt, A. (2000). Cenozoic evolution of the central and northern North Sea with focus on differential vertical movements of the basin floor and surrounding clastic source areas. *Geological Society, London, Special Publications*, 167(1), 219-243.

- Kelly, D. C., Zachos, J. C., Bralower, T. J., & Schellenberg, S. A. (2005). Enhanced terrestrial weathering/runoff and surface ocean carbonate production during the recovery stages of the Paleocene-Eocene thermal maximum. *Paleoceanography*, 20(4).
- Kemp, S. J., Ellis, M. A., Mounteney, I., & Kender, S. (2016). Palaeoclimatic implications of high-resolution clay mineral assemblages preceding and across the onset of the Palaeocene–Eocene Thermal Maximum, North Sea Basin. *Clay Minerals*, 51(5), 793-813.
- Kender, S., Stephenson, M. H., Riding, J. B., Leng, M. J., Knox, R. W. B., Peck, V. L., ... & Jamieson, R. (2012). Marine and terrestrial environmental changes in NW Europe preceding carbon release at the Paleocene–Eocene transition. *Earth and Planetary Science Letters*, 353, 108-120.
- Kennett, J. P., & Stott, L. D. (1991). Abrupt deep-sea warming, palaeoceanographic changes and benthic extinctions at the end of the Palaeocene. *Nature*, 353(6341), 225-229.
- Kent, D. V., Cramer, B. S., Lanci, L., Wang, D., Wright, J. D., & Van der Voo, R. (2003). A case for a comet impact trigger for the Paleocene/Eocene thermal maximum and carbon isotope excursion. *Earth and Planetary Science Letters*, 211(1-2), 13-26.
- Khozyem, H., Adatte, T., Spangenberg, J. E., Tantawy, A. A., & Keller, G. (2013). Palaeoenvironmental and climatic changes during the Palaeocene–Eocene Thermal Maximum (PETM) at the Wadi Nukhul Section, Sinai, Egypt. *Journal of the Geological Society*, 170(2), 341-352.
- King C. (2016). *A Revised Correlation of Tertiary Rocks in the British Isles and Adjacent Areas of NW Europe* (Gale, A.S. & Barry, T.L., editors). Special reports, 27. The Geological Society, London.
- Kirtland Turner, S., Hull, P. M., Kump, L. R., & Ridgwell, A. (2017). A probabilistic assessment of the rapidity of PETM onset. *Nature communications*, 8(1), 1-10.
- Knox, R.O.B. & Morton, A.C. (1988). The record of early Tertiary N Atlantic volcanism in sediments of the North Sea Basin. *Geological Society, London, Special Publications*, 39(1), 407-419.
- Knox, R. W. B. (1996). Tectonic controls on sequence development in the Palaeocene and earliest Eocene of southeast England: implications for North Sea stratigraphy. *Geological Society, London, Special Publications*, 103(1), 209-230.
- Knox, R.W.O'B., Bosch, J.H.A., Rasmussen, E.S., Heilmann-Clausen, C., Hiss, M., De Lugt, I.R., Kasinski, J., King, C., Köthe, A., Slodkowska, B., Standke, G., Vandenberghe, N. (2010). Cenozoic. In: Dornenbaal, H., Stevenson, A. (Eds.), *Petroleum Geological Atlas of the Southern Permian Basin Area*. EAGE Publications b.v, Houten, pp. 211–223.
- Koch, P. L., Zachos, J. C., & Gingerich, P. D. (1992). Correlation between isotope records in marine and continental carbon reservoirs near the Palaeocene/Eocene boundary. *Nature*, 358(6384), 319-322.
- Komar, N., & Zeebe, R. E. (2017). Redox-controlled carbon and phosphorus burial: A mechanism for enhanced organic carbon sequestration during the PETM. *Earth and Planetary Science Letters*, 479, 71-82.
- Kraus, M. J., & Riggins, S. (2007). Transient drying during the Paleocene–Eocene Thermal Maximum (PETM): analysis of paleosols in the Bighorn Basin, Wyoming. *Palaeogeography, Palaeoclimatology, Palaeoecology*, 245(3-4), 444-461.
- Lafargue, E., Marquis, F., & Pillot, D. (1998). Rock-Eval 6 applications in hydrocarbon exploration, production, and soil contamination studies. *Revue de l'institut français du pétrole*, 53(4), 421-437.
- Larsen, L. M., Fitton, J. G., & Pedersen, A. K. (2003). Paleogene volcanic ash layers in the Danish Basin: compositions and source areas in the North Atlantic Igneous Province. *Lithos*, 71(1), 47-80.

- Larsen, R. B., & Tegner, C. (2006). Pressure conditions for the solidification of the Skaergaard intrusion: eruption of East Greenland flood basalts in less than 300,000 years. *Lithos*, 92(1-2), 181-197.
- Littler, K., Röhl, U., Westerhold, T., & Zachos, J.C. (2014). A high-resolution benthic stable-isotope record for the South Atlantic: Implications for orbital-scale changes in Late Paleocene–Early Eocene climate and carbon cycling. *Earth and Planetary Science Letters*, 401, 18-30.
- Ma, Z., Gray, E., Thomas, E., Murphy, B., Zachos, J., & Paytan, A. (2014). Carbon sequestration during the Palaeocene–Eocene Thermal Maximum by an efficient biological pump. *Nature Geoscience*, 7(5), 382-388.
- Marsh, R., Mills, R. A., Green, D. R., Salter, I., & Taylor, S. (2007). Controls on sediment geochemistry in the Crozet region. *Deep Sea Research Part II: Topical Studies in Oceanography*, 54(18-20), 2260-2274.
- McInerney, F. A., & Wing, S. L. (2011). The Paleocene-Eocene Thermal Maximum: A perturbation of carbon cycle, climate, and biosphere with implications for the future. *Annual Review of Earth and Planetary Sciences*, 39, 489-516.
- van der Meulen, B., Gingerich, P. D., Lourens, L. J., Meijer, N., van Broekhuizen, S., van Ginneken, S., & Abels, H. A. (2020). Carbon isotope and mammal recovery from extreme greenhouse warming at the Paleocene–Eocene boundary in astronomically-calibrated fluvial strata, Bighorn Basin, Wyoming, USA. *Earth and Planetary Science Letters*, 534, 116044.
- Mitlehner, A. G. (1996). Palaeoenvironments in the North Sea Basin around the Paleocene-Eocene boundary: evidence from diatoms and other siliceous microfossils. *Geological Society, London, Special Publications*, 101(1), 255-273.
- Moore, D.M., & Reynolds, R.C. (1997). *X-ray Diffraction and the Identification and Analysis of Clay Minerals*. Oxford University Press, Oxford.
- Morton, A. C., & Evans, J. A. (1988). Geochemistry of basaltic ash beds from the Fur Formation, Island of Fur, Denmark. *Bulletin of the Geological Society of Denmark*, 37(1-2), 1-9.
- Nagy, J., Jargvoll, D., Dypvik, H., Jochmann, M., & Riber, L. (2013). Environmental changes during the Paleocene–Eocene Thermal Maximum in Spitsbergen as reflected by benthic foraminifera. *Polar Research*, 32(1), 19737.
- Nesbitt, H., & Young, G. M. (1982). Early Proterozoic climates and plate motions inferred from major element chemistry of lutites. *Nature*, 299(5885), 715-717.
- Nielsen, O.B. & Heilmann-Clausen, C. (1988). Palaeogene volcanism: the sedimentary record in Denmark. *Geological Society, London, Special Publications*, 39(1), 395-405.
- Nielsen, O. B., Sørensen, S., Thiede, J., & Skarbø, O. (1986). Cenozoic differential subsidence of North Sea. *AAPG bulletin*, 70(3), 276-298.
- Nielsen, O. B., Rasmussen, E. S., & Thyberg, B. I. (2015). Distribution of clay minerals in the northern North Sea Basin during the Paleogene and Neogene: a result of source-area geology and sorting processes. *Journal of Sedimentary Research*, 85(6), 562-581.
- Nunes, F., & Norris, R. D. (2006). Abrupt reversal in ocean overturning during the Palaeocene/Eocene warm period. *Nature*, 439(7072), 60-63.
- Ogg, J., (2012). Geomagnetic Polarity Time Scale, in: Gradstein, F., Ogg, J., Schmitz, M., Ogg, G. (Eds.), *The Geologic Time Scale 2012*. Elsevier, pp. 85-113.

- Paytan, A., & Griffith, E. M. (2007). Marine barite: Recorder of variations in ocean export productivity. *Deep Sea Research Part II: Topical Studies in Oceanography*, 54(5-7), 687-705.
- Pedersen, G. K., & Surlyk, F. (1983). The Fur Formation, a late Paleocene ash-bearing diatomite from northern Denmark. *Bulletin of the Geological Society of Denmark*, 32(1-2), 43-65.
- Pedersen, G. K., Pedersen, S. A. S., Steffensen, J., & Pedersen, C. S. (2004). Clay content of a clayey diatomite, the Early Eocene Fur Formation, Denmark. *Bulletin of the Geological Society of Denmark*, (51), 159-177.
- Pedersen, S. A. S. (2008). Palaeogene diatomite deposits in Denmark: geological investigations and applied aspects. *Geological Survey of Denmark and Greenland (GEUS) Bulletin*, 15, 21-24.
- Penman, D. E. (2016). Silicate weathering and North Atlantic silica burial during the Paleocene-Eocene thermal maximum. *Geology*, 44(9), 731-734.
- Penman, D. E., & Zachos, J. C. (2018). New constraints on massive carbon release and recovery processes during the Paleocene-Eocene Thermal Maximum. *Environmental Research Letters*, 13(10), 105008.
- Petersen, H. I., Nielsen, L. H., Bojesen-Koefoed, J. A., Mathiesen, A., Kristensen, L., & Dalhoff, F. (2008). Evaluation of the quality, thermal maturity and distribution of potential source rocks in the Danish part of the Norwegian–Danish Basin. *Geological Survey of Denmark and Greenland Bulletin*, 16, 1-27.
- Pujalte, V., Schmitz, B., & Baceta, J. I. (2014). Sea-level changes across the Paleocene–Eocene interval in the Spanish Pyrenees, and their possible relationship with North Atlantic magmatism. *Palaeogeography, Palaeoclimatology, Palaeoecology*, 393, 45-60.
- Pälike, C., Delaney, M. L., & Zachos, J. C. (2014). Deep-sea redox across the Paleocene-Eocene thermal maximum. *Geochemistry, Geophysics, Geosystems*, 15(4), 1038-1053.
- Rasmussen, E. S., Heilmann-Clausen, C., Waagstein, R., & Eidvin, T. (2008). The tertiary of Norden. *Episodes*, 31(1), 66.
- Reynolds III, R. C., & Reynolds Jr, R. C. (2012). NEWMOD II a computer program for the calculation of one-dimensional diffraction patterns of mixed-layered clays. 1526 Farlow Avenue. *Crofton, MD*, 21114.
- Riahi, K., Van Vuuren, D. P., Kriegler, E., Edmonds, J., O'Neill, B. C., Fujimori, S., ... & Lutz, W. (2017). The shared socioeconomic pathways and their energy, land use, and greenhouse gas emissions implications: an overview. *Global Environmental Change*, 42, 153-168.
- Richter, T. O., Van der Gaast, S., Koster, B., Vaars, A., Gieles, R., de Stigter, H. C., ... & van Weering, T. C. (2006). The Avaatech XRF Core Scanner: technical description and applications to NE Atlantic sediments. *Geological Society, London, Special Publications*, 267(1), 39-50.
- Rietveld, H. (1969). A profile refinement method for nuclear and magnetic structures. *Journal of applied Crystallography*, 2(2), 65-71.
- Robert, C., & Kennett, J. P. (1994). Antarctic subtropical humid episode at the Paleocene-Eocene boundary: Clay-mineral evidence. *Geology*, 22(3), 211-214.
- Rothwell, R. G. & Croudace, I. W. (2015). Twenty Years of XRF Core Scanning Marine Sediments: What Do Geochemical Proxies Tell Us? In: Croudace I., Rothwell R. (eds) *Micro-XRF Studies of Sediment Cores*. Developments in Paleoenvironmental Research, vol 17. Springer, Dordrecht, 25-102.
- Saunders, A.D. (2016). Two LIPs and two Earth-system crises: the impact of the North Atlantic Igneous Province and the Siberian Traps on the Earth-surface carbon cycle. *Geological Magazine*, 153, 201-222,

- Schaller, M. F., Fung, M. K., Wright, J. D., Katz, M. E., & Kent, D. V. (2016). Impact ejecta at the Paleocene-Eocene boundary. *Science*, 354(6309), 225-229.
- Schiøler, P., Andsbjerg, J., Clausen, O. R., Dam, G., Dybkjær, K., Hamberg, L., ... & Rasmussen, J. A. (2007). Lithostratigraphy of the Palaeogene, Lower Neogene Succession of the Danish North Sea (Vol. 12). *Geological Survey of Denmark and Greenland*.
- Schmitz, B., & Pujalte, V. (2003). Sea-level, humidity, and land-erosion records across the initial Eocene thermal maximum from a continental-marine transect in northern Spain. *Geology*, 31(8), 689-692.
- Schmitz, B., Peucker-Ehrenbrink, B., Heilmann-Clausen, C., Åberg, G., Asaro, F., & Lee, C. T. A. (2004). Basaltic explosive volcanism, but no comet impact, at the Paleocene–Eocene boundary: high-resolution chemical and isotopic records from Egypt, Spain and Denmark. *Earth and Planetary Science Letters*, 225(1-2), 1-17.
- Schoon, P. L., Heilmann-Clausen, C., Schultz, B. P., Sluijs, A., Damsté, J. S. S., & Schouten, S. (2013). Recognition of Early Eocene global carbon isotope excursions using lipids of marine Thaumarchaeota. *Earth and Planetary Science Letters*, 373, 160-168.
- Schoon, P. L., Heilmann-Clausen, C., Schultz, B. P., Damsté, J. S. S., & Schouten, S. (2015). Warming and environmental changes in the eastern North Sea Basin during the Palaeocene–Eocene Thermal Maximum as revealed by biomarker lipids. *Organic Geochemistry*, 78, 79-88.
- Scott, C., & Lyons, T. W. (2012). Contrasting molybdenum cycling and isotopic properties in euxinic versus non-euxinic sediments and sedimentary rocks: Refining the paleoproxies. *Chemical Geology*, 324, 19-27.
- Seager, R., Naik, N., & Vecchi, G. A. (2010). Thermodynamic and dynamic mechanisms for large-scale changes in the hydrological cycle in response to global warming. *Journal of Climate*, 23(17), 4651-4668.
- Sluijs, A., Brinkhuis, H., Crouch, E. M., John, C. M., Handley, L., Munsterman, D., ... & Pancost, R. D. (2008). Eustatic variations during the Paleocene-Eocene greenhouse world. *Paleoceanography*, 23(4).
- Sluijs, A., Schouten, S., Donders, T. H., Schoon, P. L., Röhl, U., Reichert, G. J., ... & Brinkhuis, H. (2009). Warm and wet conditions in the Arctic region during Eocene Thermal Maximum 2. *Nature Geoscience*, 2(11), 777-780.
- Sluijs, A., Van Roij, L., Harrington, G. J., Schouten, S., Sessa, J. A., LeVay, L. J., ... & Slomp, C. P. (2014). Warming, euxinia and sea level rise during the Paleocene–Eocene Thermal Maximum on the Gulf Coastal Plain: implications for ocean oxygenation and nutrient cycling. *1foldr Import 2019-10-08 Batch 7*.
- Soliman, M. F., Aubry, M. P., Schmitz, B., & Sherrell, R. M. (2011). Enhanced coastal paleoproductivity and nutrient supply in Upper Egypt during the Paleocene/Eocene Thermal Maximum (PETM): Mineralogical and geochemical evidence. *Palaeogeography, Palaeoclimatology, Palaeoecology*, 310(3-4), 365-377.
- Stefánsson, A., & Gíslason, S. R. (2001). Chemical weathering of basalts, Southwest Iceland: effect of rock crystallinity and secondary minerals on chemical fluxes to the ocean. *American Journal of Science*, 301(6), 513-556.
- Stein, R., Boucsein, B., & Meyer, H. (2006). Anoxia and high primary production in the Paleogene central Arctic Ocean: First detailed records from Lomonosov Ridge. *Geophysical Research Letters*, 33(18).

- Stokke, E. W., Jones, M. T., Tierney, J. E., Svensen, H. H., & Whiteside, J. H. (2020a). Temperature changes across the Paleocene-Eocene Thermal Maximum—a new high-resolution TEX86 temperature record from the Eastern North Sea Basin. *Earth and Planetary Science Letters*, 544, 116388.
- Stokke, E. W., Liu, E. J., & Jones, M. T. (2020b). Evidence of explosive hydromagmatic eruptions during the emplacement of the North Atlantic Igneous Province. *Volcanica*
- Storey, M., Duncan, R. A., & Swisher, C. C. (2007a). Paleocene-Eocene thermal maximum and the opening of the northeast Atlantic. *Science*, 316 (5824), 587-589.
- Storey, M., Duncan, R.A., & Tegner, C. (2007b). Timing and duration of volcanism in the North Atlantic Igneous Province: Implications for geodynamics and links to the Iceland hotspot. *Chemical Geology*, 241(3), 264-281.
- Stramma, L., Johnson, G. C., Sprintall, J., & Mohrholz, V. (2008). Expanding oxygen-minimum zones in the tropical oceans. *Science*, 320(5876), 655-658.
- Stramma, L., Prince, E. D., Schmidtko, S., Luo, J., Hoolihan, J. P., Visbeck, M., ... & Körtzinger, A. (2012). Expansion of oxygen minimum zones may reduce available habitat for tropical pelagic fishes. *Nature Climate Change*, 2(1), 33-37.
- Svensen, H., Planke, S., Maltte-Sørensen, A., Jamtveit, B., Myklebust, R., Eidem, T. R., & Rey, S. S. (2004). Release of methane from a volcanic basin as a mechanism for initial Eocene global warming. *Nature*, 429(6991), 542.
- Svensen, H. H., Bjærke, M. R., & Kverndokk, K. (2019). The Past as a Mirror: Deep Time Climate Change Exemplarity in the Anthropocene. *Culture Unbound*, 11(3-4), 330-352.
- Taylor, S. R., & McLennan, S. M. (1995). The geochemical evolution of the continental crust. *Reviews of Geophysics*, 33(2), 241-265.
- Thiry, M. (2000). Palaeoclimatic interpretation of clay minerals in marine deposits: an outlook from the continental origin. *Earth-Science Reviews*, 49(1-4), 201-221.
- Thomas, E., & Shackleton, N. J. (1996). The Paleocene-Eocene benthic foraminiferal extinction and stable isotope anomalies. *Geological Society, London, Special Publications*, 101(1), 401-441.
- Torfstein, A., Winckler, G., & Tripathi, A. (2010). Productivity feedback did not terminate the Paleocene-Eocene Thermal Maximum (PETM). *Climate of the Past*, 6(2), 265-272.
- Trenberth, K. E. (2011). Changes in precipitation with climate change. *Climate Research*, 47(1-2), 123-138.
- Tribovillard, N., Riboulleau, A., Lyons, T., & Baudin, F. (2004). Enhanced trapping of molybdenum by sulfurized marine organic matter of marine origin in Mesozoic limestones and shales. *Chemical Geology*, 213(4), 385-401.
- Tribovillard, N., Algeo, T. J., Lyons, T., & Riboulleau, A. (2006). Trace metals as paleoredox and paleoproductivity proxies: an update. *Chemical Geology*, 232(1-2), 12-32.
- Westerhold, T., Röhl, U., Wilkens, R. H., Gingerich, P. D., Clyde, W. C., Wing, S. L., Bowen, G. J., and Kraus, M. J. (2018). Synchronizing early Eocene deep-sea and continental records – cyclostratigraphic age models for the Bighorn Basin Coring Project drill cores, *Climate of the Past*, 14, 303-319.
- Wieczorek, R., Fantle, M. S., Kump, L. R., & Ravizza, G. (2013). Geochemical evidence for volcanic activity prior to and enhanced terrestrial weathering during the Paleocene Eocene Thermal Maximum. *Geochimica et Cosmochimica Acta*, 119, 391-410.

- Wignall, P. B., & Myers, K. J. (1988). Interpreting benthic oxygen levels in mudrocks: a new approach. *Geology*, 16(5), 452-455.
- Wignall, P. B., & Twitchett, R. J. (1996). Oceanic anoxia and the end Permian mass extinction. *Science*, 272(5265), 1155-1158.
- Wilkinson, C. M., Ganerød, M., Hendriks, B. W., & Eide, E. A. (2017). Compilation and appraisal of geochronological data from the North Atlantic Igneous Province (NAIP). *Geological Society, London, Special Publications*, 447(1), 69-103.
- Yao, W., Paytan, A., & Wortmann, U. G. (2018). Large-scale ocean deoxygenation during the Paleocene-Eocene Thermal Maximum. *Science*, 361(6404), 804-806.
- Zachos, J. C., Röhl, U., Schellenberg, S. A., Sluijs, A., Hodell, D. A., Kelly, D. C., ... & McCarren, H. (2005). Rapid acidification of the ocean during the Paleocene-Eocene thermal maximum. *Science*, 308(5728), 1611-1615.
- Zachos, J. C., Dickens, G. R., & Zeebe, R. E. (2008). An early Cenozoic perspective on greenhouse warming and carbon-cycle dynamics. *Nature*, 451(7176), 279-283.
- Zachos, J. C., McCarren, H., Murphy, B., Röhl, U., & Westerhold, T. (2010). Tempo and scale of late Paleocene and early Eocene carbon isotope cycles: Implications for the origin of hyperthermals. *Earth and Planetary Science Letters*, 299(1-2), 242-249.
- Zacke, A., Voigt, S., Joachimski, M. M., Gale, A. S., Ward, D. J., & Tütken, T. (2009). Surface-water freshening and high-latitude river discharge in the Eocene North Sea. *Journal of the Geological Society*, 166(5), 969-980.
- Zeebe, R. E., Zachos, J. C., & Dickens, G. R. (2009). Carbon dioxide forcing alone insufficient to explain Palaeocene–Eocene Thermal Maximum warming. *Nature Geoscience*, 2(8), 576-580.
- Zhou, X., Thomas, E., Rickaby, R. E., Winguth, A. M., & Lu, Z. (2014). I/Ca evidence for upper ocean deoxygenation during the PETM. *Paleoceanography*, 29(10), 964-975.

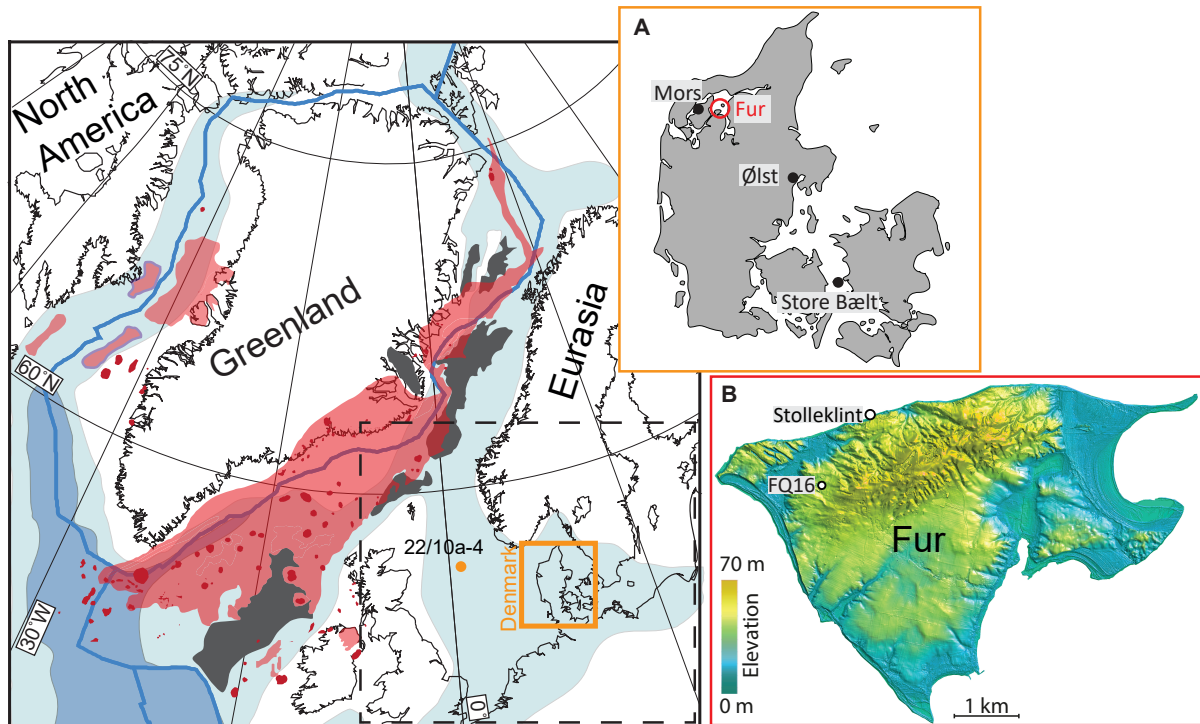


Figure 1: Plate tectonic reconstruction from 56 Ma with the known extent of the NAIP indicated (modified from Abdelmalak et al., 2016, Horni et al., 2017, and Jones et al., 2019). The orange dot notes the position of core 22/10a-4 described by Kender et al. (2012) and Kemp et al. (2016). Blue lines: plate boundaries. Black lines: present day coastlines. Light and dark blue areas: shelf and deep marine areas, respectively. Light red areas: Known extent of subaerial and submarine extrusive volcanism from the NAIP. Dark red: individual volcanic centres. Black areas: extent of known NAIP sill intrusions in sedimentary basins. The total extent of intrusions beneath the extrusive volcanism is not known. The dashed square indicates the position of Figure 11. **A)** Map of Denmark with locations of Fur, Ølst and Store Bælt indicated **B)** Topographic map of the island of Fur (22 km²). The high topography in the north of the island is a partially overturned anticline of Fur Formation and upper Stolleklint Clay strata. Map courtesy of Egon Nørmark.

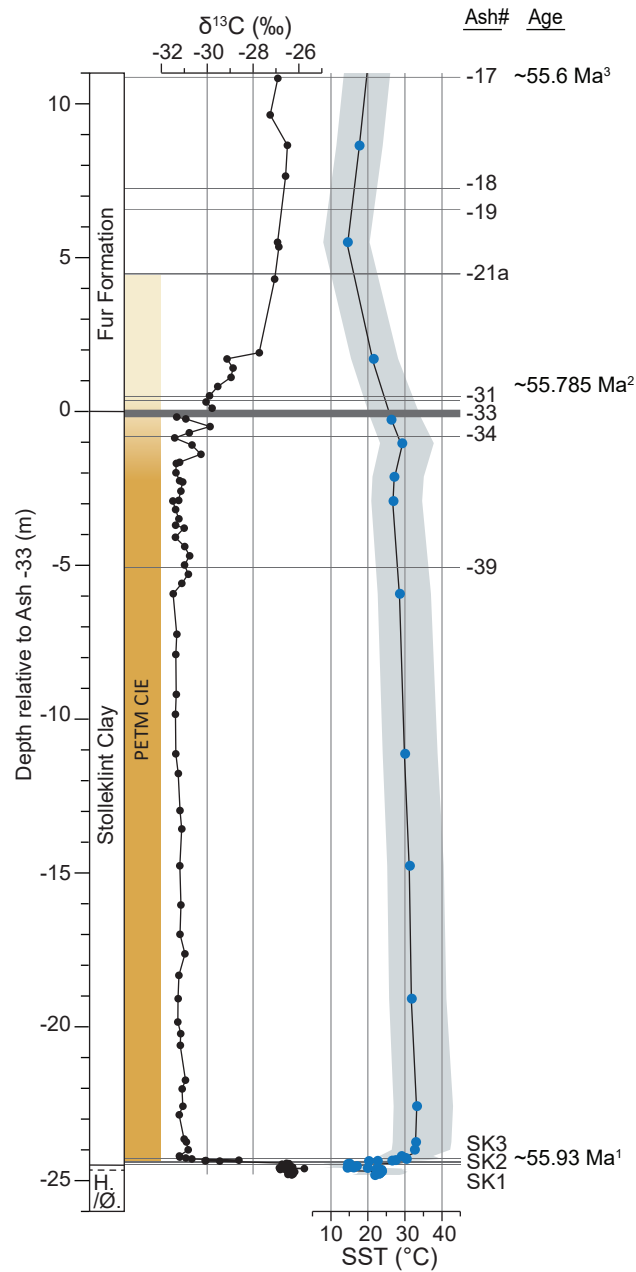


Figure 2: Data from the Stolleklint beach and a nearby quarry (Fig. 3), with lithological units indicated to the left. The depth scale is measured upwards and downwards from the main marker bed Ash -33. The yellow column indicates the interpreted duration of the PETM CIE, based on the $\delta^{13}\text{C}$ curve from Jones et al. (2019). The base of the column marks the CIE onset, and the gradually lighter colours toward the top marks the CIE recovery. Sea surface temperature (SST) variations are given as BAYSPAR calibrated TEX86 SSTs with 1σ error bars indicated by the light blue area (Stokke et al., 2020a). Ages are indicated based on ¹Westerhold et al., 2018; ²Charles et al. (2011), assuming the timings of the Svalbard and Fur CIEs are coeval; ³Age of Ash -17 from Storey et al. (2007a) recalibrated by Jones et al. (2019).

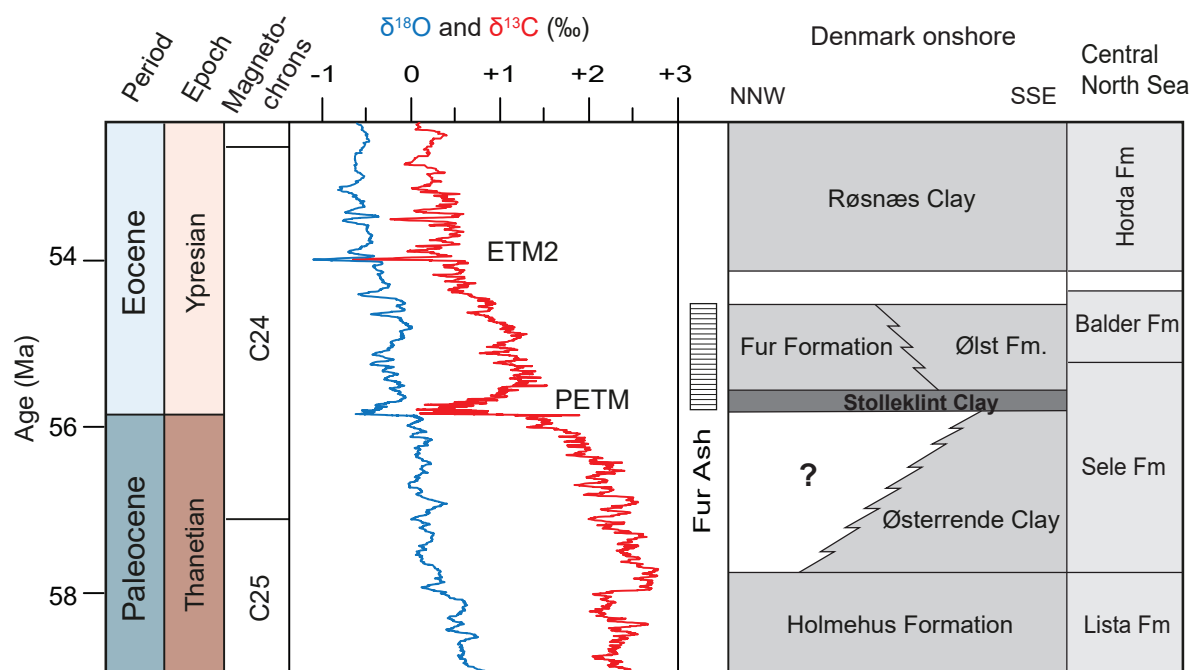


Figure 3: Composite figure of the late Paleocene and early Eocene interval, indicating both the Danish stratigraphy and the correlative offshore North Sea stratigraphy. Stratigraphy from King (2016) and Schiøler et al. (2007). The $\delta^{13}\text{C}$ and $\delta^{18}\text{O}$ curves indicate the stratigraphic position of two periods of carbon perturbation; the Paleocene-Eocene Thermal Maximum (PETM) and the Eocene Thermal Maximum 2 (ETM2). Carbon and oxygen isotope data from Cramer et al. (2009) and Littler et al. (2014) and plotted on the GTS2012 timescale (Ogg, 2012).

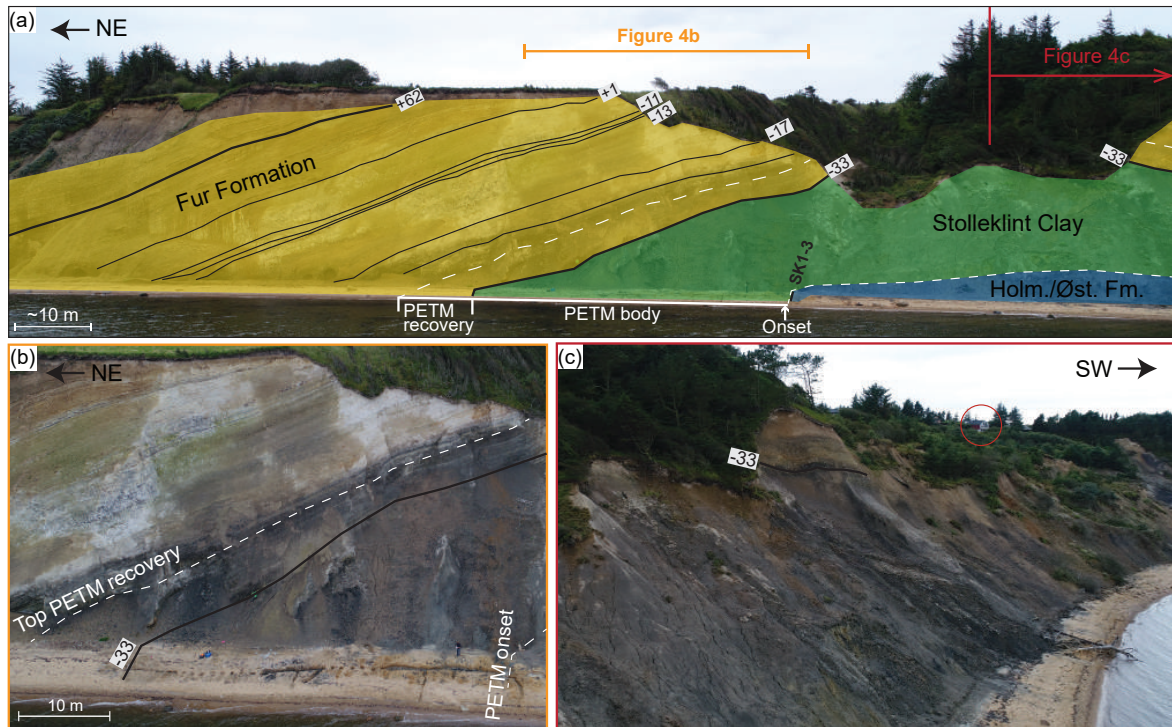


Figure 4: **A)** Picture of the coastal cliff at the Stolleklint beach with the main stratigraphic units shown in yellow (Fur Formation), green (Stolleklint Clay), and blue (Holmehus/Østerrende Formation). The black lines indicate certain key ash layers, and white dashed lines indicate the upper and lower bounds of the PETM CIE. **B)** Close up of the central part of the cliff face showing the colour difference between the dark PETM clays and the light post-PETM diatomites. Ash -33 and the PETM CIE are indicated. Note the 43 m long ditch on the beach where most of the samples were collected. **C)** Picture of the continuation of the cliff side towards the west, showing the extensive coastal erosion. Approximate location of Ash -33 is indicated. House for scale in red circle.

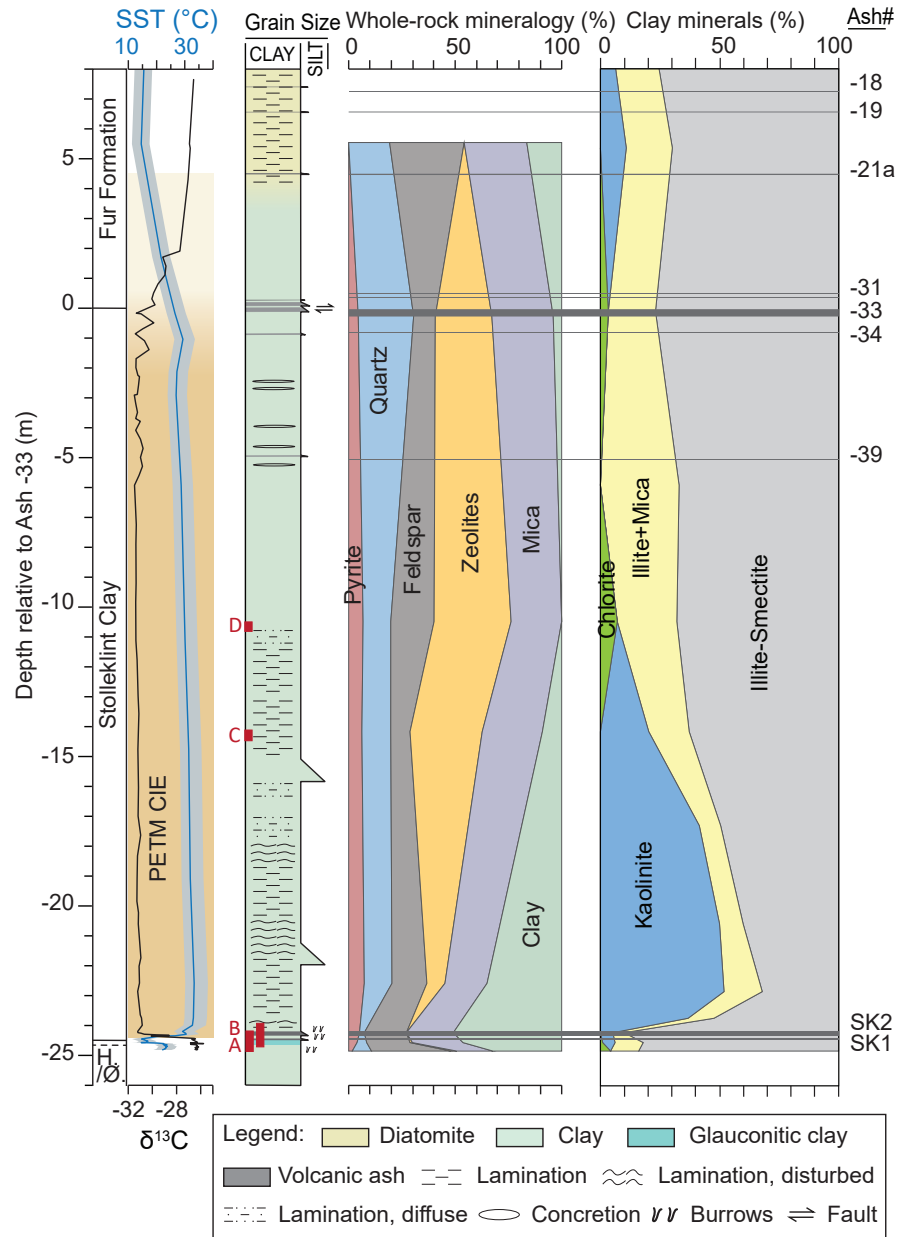


Figure 5: Sedimentological log from Stolleklint with legend below. Red squares labelled A-D indicate the position of the XRF box-core scans in Figure 6. Bulk-rock and clay mineralogy is presented as percentage. $\delta^{13}\text{C}$ data from Jones et al. (2019), TEX86 data from Stokke et al. (2020a).

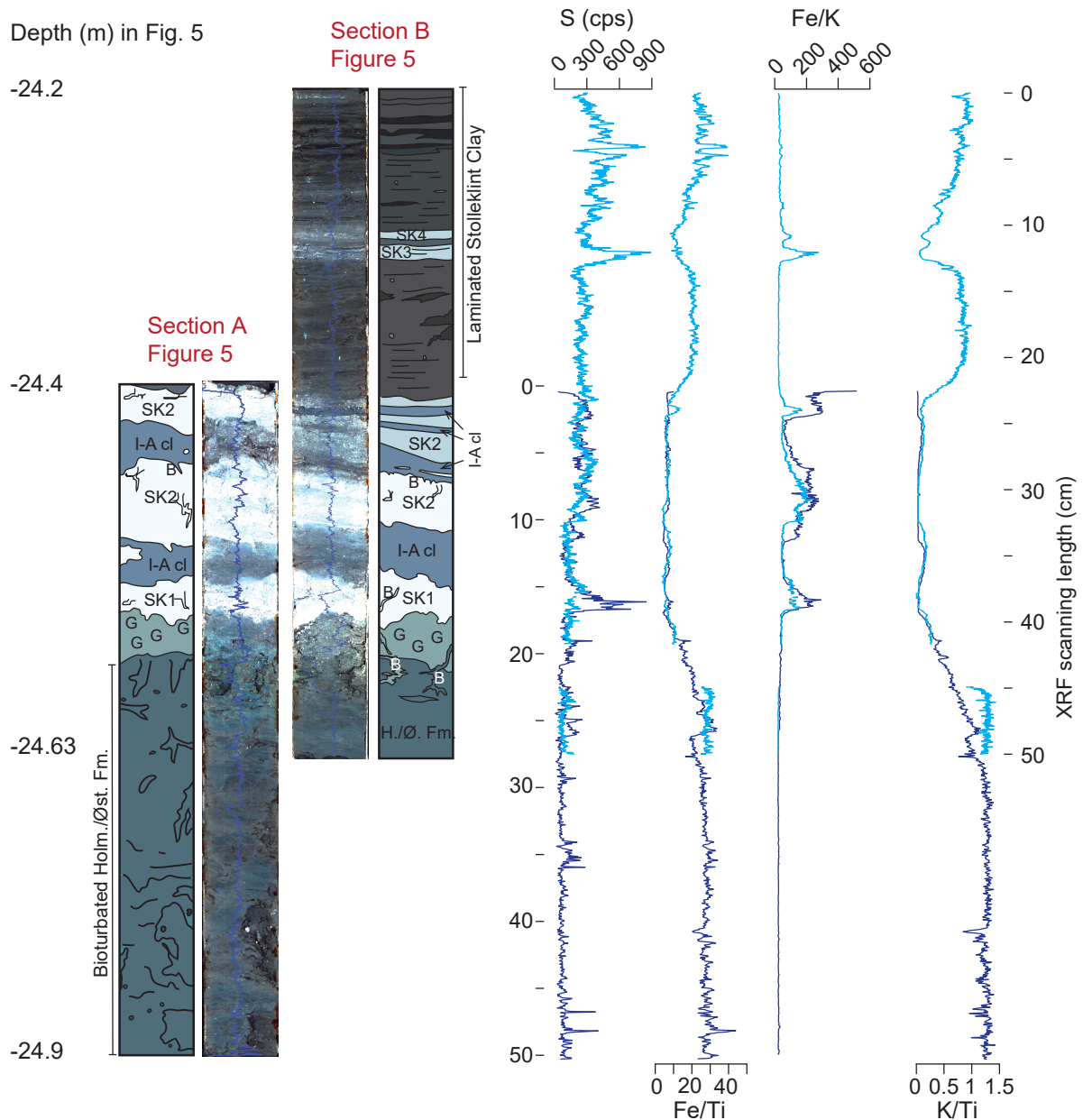


Figure 6: XRF element core scans and radiographic images of two box-cores crossing the PETM onset from the Stolleklint beach. Interpretive logs next to the images indicate the lithological changes. G=Glaucanite; B=Burrow; I-A cl=Inter-ash clay. The corrected stratigraphic depth relative to Ash -33 of each section is indicated to the left and in Figure 6. XRF scanning length indicate actual core length. XRF data given as counts per second (cps) or as dimensionless ratios.

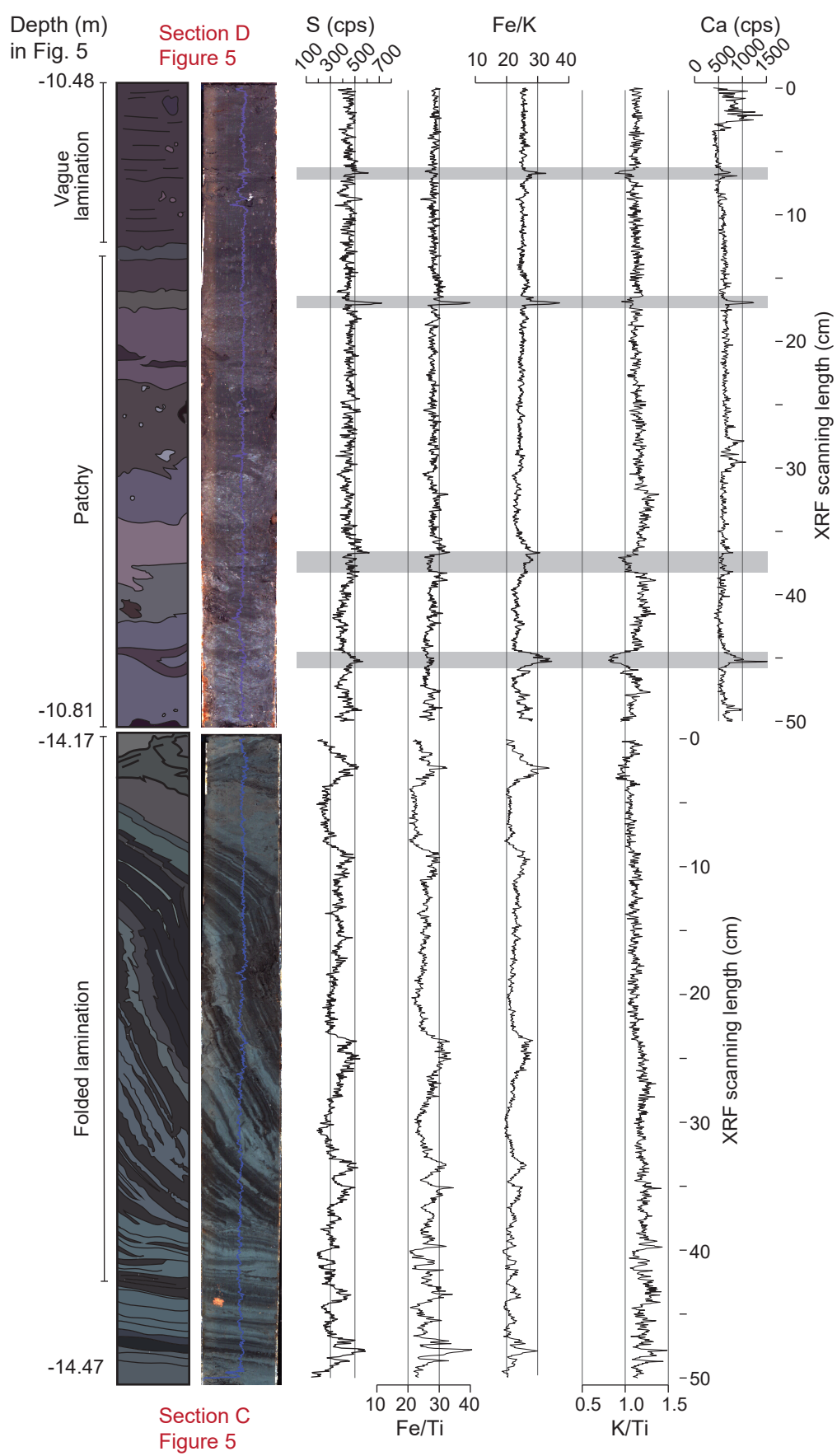


Figure 7: XRF element core scans and radiographic images of two box-cores within the PETM body from the Stolleklint beach. Interpretive logs next to the images indicate the lithological changes. The corrected stratigraphic depth relative to Ash -33 for each section is indicated to the left and in Figure 6. XRF scanning length to the right indicate actual core length. Grey bands in section D indicate potentially tephra-rich horizons. XRF data given as counts per second (cps) or as dimensionless ratios.

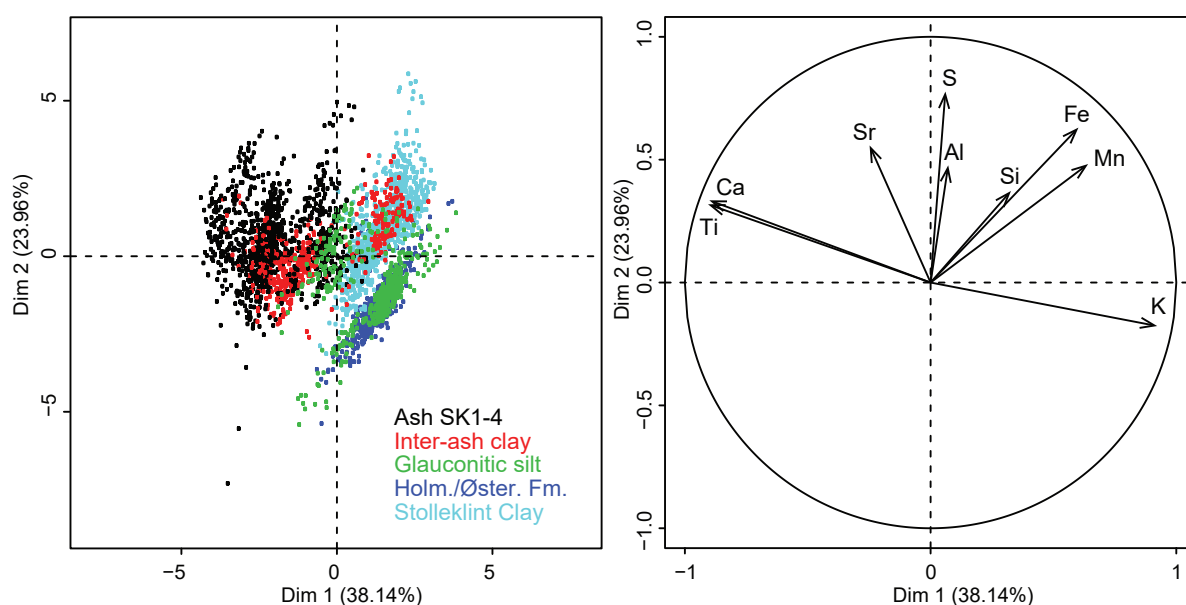


Figure 8: Biplot and correlation circle with Dimensions 1 and 2 (denoted as Dim 1 and Dim 2) of the principal component analysis applied to XRF core scanning data from box cores 1 and 2 across the PETM onset. Dimensions 1 and 2 represent 62 % of the total variability. The inter-ash clay in the Biplot refers to the clay between ashes SK1 and SK2 as indicated in Figure 7.

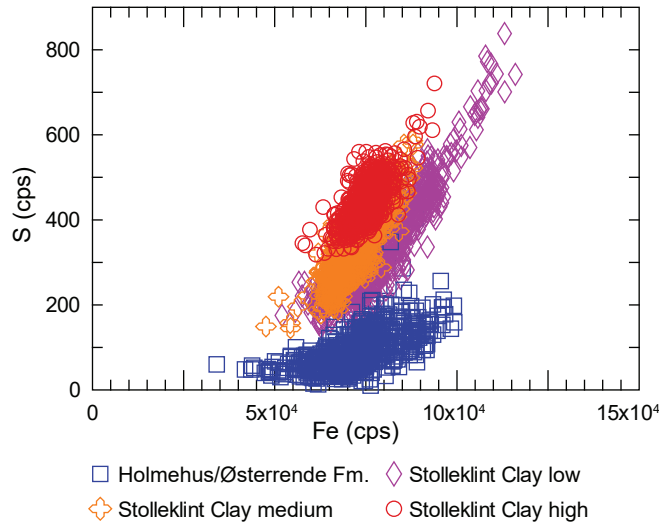


Figure 9: Biplot of Fe and S. Data from XRF element core scans of all four box-cores. CPS = Counts Per Second.

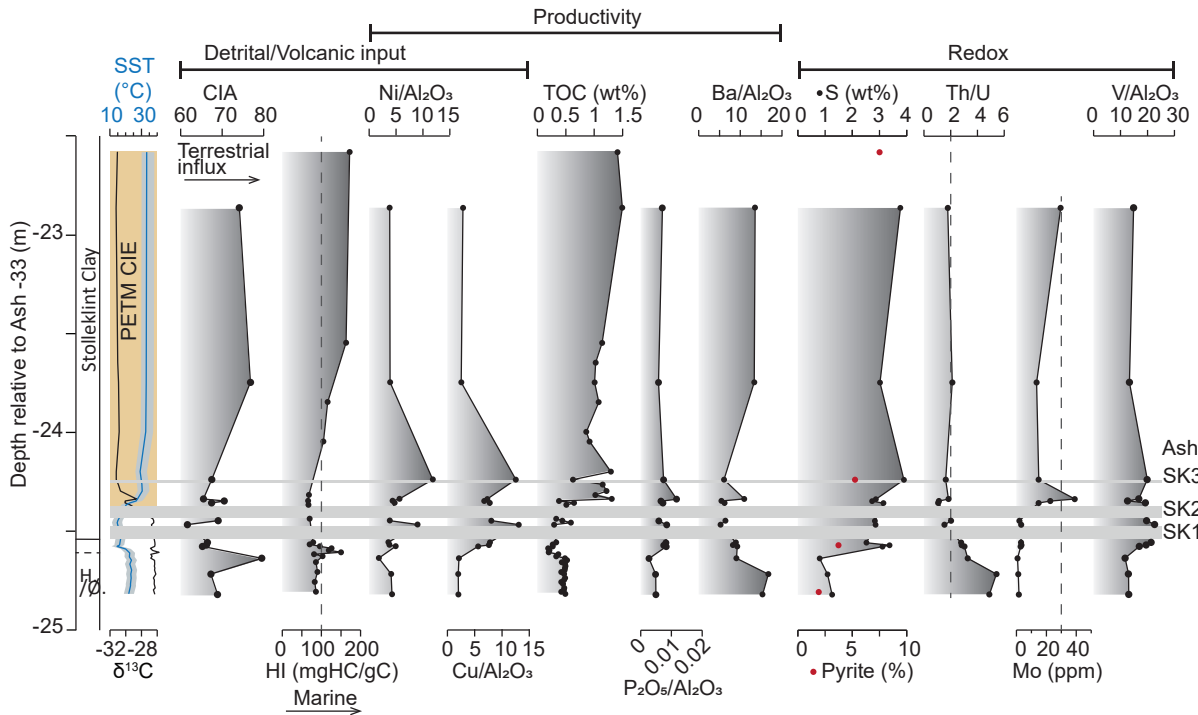


Figure 10: The lowermost 2.5 m of the Stolleklint beach section showing a close-up of the CIE onset. Graphs show: TEX86 data from Stokke et al. (2020a); $\delta^{13}\text{C}$ and Total Organic Carbon (TOC) data from Jones et al. (2019); Chemical Index of Alteration (CIA); Hydrogen Index (HI) where vertical line divide between dominantly terrigenous (<100) and marine (>100) organic material; productivity proxies Ni, Cu, P2O5, and Ba normalised to Al2O3; fraction of pyrite from bulk XRD analyses; S concentrations in wt%; Th/U ratio where vertical line divide anoxic (<2) from oxic (2-7) sediments; molybdenum concentrations in ppm where vertical line divide between anoxic (<30 ppm) and euxinic (>30 ppm); V normalised to Al2O3.

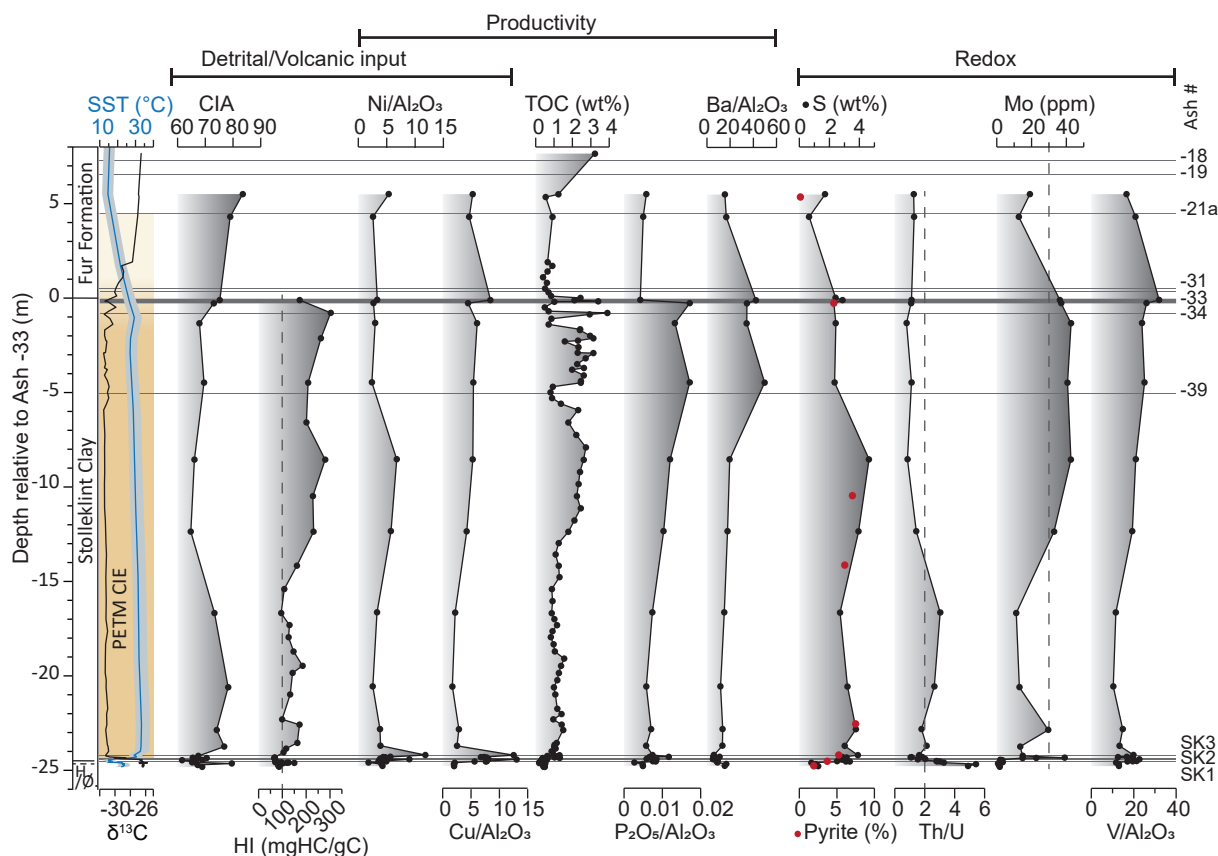


Figure 11: The section covering the whole Stolleklint PETM, with some additional samples from the nearby quarry FQ16 (Figure 2) between -5.6 and 2 m depth. See Figure 10 for details on each graph.

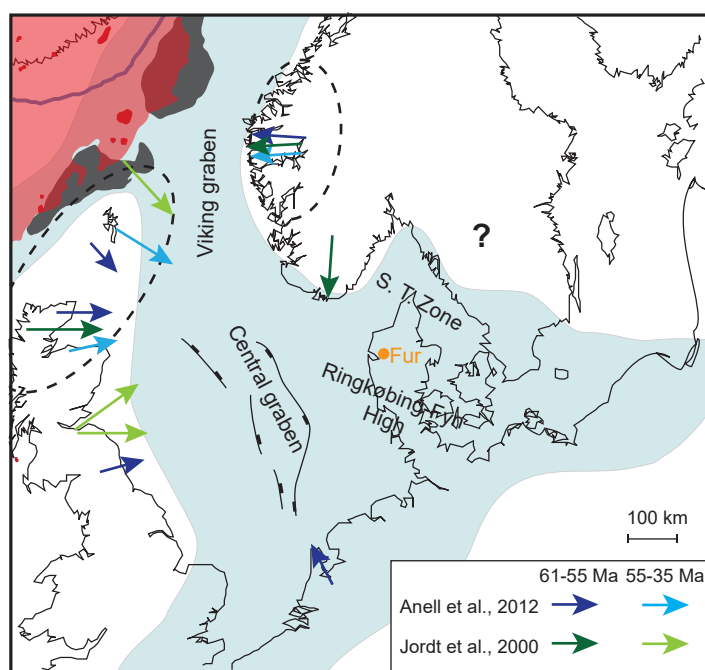


Figure 12: Close up of Figure 1 with modifications based on Schiøler et al. (2007). Dashed circles indicate main sedimentary source areas for the North Sea during the Paleocene and Eocene from Anell et al. (2012). Arrows indicate the main sediment transport directions

Supplementary Information

Rapid and sustained environmental response to global warming: The Paleocene-Eocene Thermal Maximum in Denmark

Ella W. Stokke^{1*}, Morgan T. Jones¹, Lars Riber², Haflidi Haflidason^{3,4}, Ivar Midtkandal², Bo Pagh Schultz⁵, and Henrik H. Svensen¹

¹CEED, University of Oslo, PO Box 1028, 0315 Oslo, Norway (*Correspondence: e.w.stokke@geo.uio.no)

²Department of Geosciences, University of Oslo, P.O. Box 1047, Blindern, NO 0316 Oslo, Norway

³Department of Earth Science, University of Bergen, Allégt. 41, N-5007 Bergen, Norway

⁴Bjerknes Centre for Climate Research, Jahnebakken 5, 5007 Bergen, Norway

⁵Museum Salling, Fur Museum, Nederby 28, 7884 Fur, Denmark

Included supplementary tables

Table 1: XRD bulk-rock data

Table 2: XRD clay fraction data

Table 3: Rock-Eval pyrolysis data

Table 4: ICP-MS major and trace elements, and Element Analyser sulfur data

The XRF element core scanner data is too big to include, but available at request.

Supplementary Table 1: Bulk-rock mineralogical data plotted in Figure 5.

Sample Name	Depth relative to Ash -33 (m)	Bulk mineralogy (%)					
		Quartz	Feldspar	Mica	Clay	Zeolites	Pyrite
SK17 -0.25 to -0.26	-24.81	9.07	37.36	17.11	32.3	2.34	1.91
SK17B-HC1-31-32	-24.57	5.02	20.01	23.7	46.43	1.09	3.723
SK17 0.310-0.315	-24.24	2.215	19.69	22.27	50.59	0	5.253
SK17B-3.5	-22.58	12.89	16.31	19.95	35.02	8.34	7.5
SK17B-16	-14.17	12.54	7.91	26.31	8.36	31.65	6.06
SK17B-22	-10.48	12.63	20.52	23.67	0	36.1	7.08
SK17B-37.5	-0.28	26.06	9.8	28.7	4.25	26.61	4.59
Fur15-5.35	5.35	19	35.23	29	16.64	0	0.11

Supplementary Table 2: Clay mineralogical data plotted in Figure 5. The percentage of smectite in illite-smectite is indicated to the right.

Sample Name	Depth relative to Ash -33 (m)	Clay mineralogy (%)				
		Illite-smectite	Mica+illite	Kaolinite	Chlorite	Smec% in I-S
SK17-0.25 to -0.26	-24.81	84	12	0	4	69
SK17-001to-0.02	-24.57	82	12	5	1	80
SK170.310-0.315	-24.24	90	5	5	0	99
SK17-0.8-0.81	-23.75	53	11	37	0	
SK17B-3.0	-22.86	32	16	52	0	72
SK17B-6.5	-20.6	40	10	50	0	
SK17B-11	-17.31	50	9	42	0	
SK17B-16	-14.17	63	17	20	0	76
SK17B-22	-10.48	68	25	0	7	70
SK17B-29	-5.93	67	33	0	0	
Sk17B-38	-0.11	77	20	0	3	84
FUR15-5.35	5.35	70	19	11	0	80

Supplementary Table 3: The data from Rock-Eval pyrolysis. The Hydrogen Index (HI) values are plotted in Figures 10 and 11. OI = Oxygen Index.

Sample	Depth relative to Ash -33	Tmax (°C)	HI mgHC/gC	OI mgHC/gC
SK17 -0.25 to -0.26	-24.81	345	86	38
SK17 -0.20 to -0.21	-24.76	413	83	33
SK17 -0.15 to -0.16	-24.71	403	90	36
SK17 -0.10 to -0.11	-24.66	403	86	37
SK17 -0.07 to -0.08	-24.63	382	103	30
SK17 -0.06 to -0.07	-24.62	330	81	26
SK17 -0.05 to -0.06	-24.61	422	150	25
SK17 -0.04 to -0.05	-24.60	335	119	33
SK17 -0.03 to -0.04	-24.59	335	126	37
SK17 -0.02 to -0.03	-24.58	343	96	78
SK17 -0.01 to -0.02	-24.57	368	70	89
SK17 0 to -0.01	-24.56	358	79	82
SK17 0.11 to 0.12	-24.44	375	70	94
SK17 0.18 to 0.19	-24.37	380	67	69
SK17 0.20 to 0.21	-24.35	395	66	71
SK17 0.23 to 0.24	-24.32	411	68	51
SK17 0.50 to 0.51	-24.05	413	105	26
SK17 0.70 to 0.71	-23.85	412	116	28
SK17 0.100 to 0.101	-23.55	414	163	27
SK17B 3.5	-22.58	410	172	32
SK17B 4	-22.30	411	99	42
SK17B 6	-20.98	412	133	29
SK17B 7.5	-19.84	411	143	33
SK17B 8	-19.46	413	185	34
SK17B 9	-18.71	415	147	29
SK17B 10	-17.95	413	126	26
SK17B 11	-17.31	412	130	34
SK17B 12	-16.68	411	95	38
SK17B 14	-15.40	410	108	34
SK17B 16	-14.17	412	161	30
SK17B 19	-12.37	410	231	33
SK17B 22	-10.48	408	228	34
SK17B 25	-8.56	409	280	30
SK17B 28	-6.58	406	201	31
SK17B 31	-4.48	405	208	36
SK17B 34	-2.12	410	262	32
SK17B 36	-0.78	408	303	30
SK17B 38	-0.11	399	173	29
SK17B 38.5	0.01	404	258	28

Supplementary Table 4: Major and trace elements from ICP-MS analyses. Sulfur concentrations from Elemental Analysis. Data plotted in Figures 10 and 11.

Sample Name	Depth relative to Ash -33	Fe2O3 wt%	Al2O3 wt%	MgO wt%	CaO wt%	Na2O wt%	K2O wt%	TiO2 wt%	P2O5 wt%	S wt%	V ppm	Ni ppm	Cu ppm	Mo ppm	Ba ppm	Th ppm	U ppm
Detection Limit ICP-MS		0.016	0.076	0.022	0.005	0.040	0.457	0.013	0.007	3.035	0.212	0.035	0.532	2.736	0.199	0.071	
SK17_-0.26 to -0.27	-24.82	7.20	17.24	2.61	0.32	2.08	3.50	0.91	0.09	1.26	224.92	73.28	34.76	1.68	264.53	11.10	2.27
SK17_-0.16 to -0.17	-24.72	6.65	15.90	2.60	0.28	2.05	3.55	0.81	0.08	1.09	205.93	65.05	31.57	1.21	266.40	11.11	2.05
SK17-0.08 to -0.09	-24.64	4.66	19.31	1.80	0.20	1.35	2.20	0.61	0.05	0.80	226.17	34.83	40.86	0.75	175.10	7.83	2.39
SK17_-0.02 to -0.03	-24.58	9.31	18.60	2.30	2.05	2.66	1.66	1.96	0.15	3.11	316.49	91.80	104.85	2.85	172.20	8.01	2.64
SK17B_HCl_31-32cm	-24.57	9.37	20.44	2.12	2.11	2.84	1.78	2.35	0.15	3.37	399.01	77.09	155.43	3.42	168.11	7.49	2.65
SK17B_0.01	-24.56	7.60	20.02	2.31	2.05	2.76	1.70	2.39	0.16	2.52	427.69	71.51	155.89	3.06	178.50	7.99	2.88
SK17_0.08-0.09	-24.47	9.76	30.68	2.67	5.35	4.94	1.15	5.16	0.26	2.86	696.13	276.44	400.84	3.16	160.80	3.83	2.50
SK17_0.10-0.11	-24.45	7.66	23.24	2.27	2.15	2.92	1.57	2.67	0.14	2.83	458.54	89.12	187.33	2.01	149.42	5.74	2.83
SK17_0.19-0.20	-24.36	7.22	23.88	1.92	3.05	2.76	1.31	3.04	0.17	3.15	459.24	113.26	185.57	14.84	147.95	5.41	5.11
SK17_0.20-0.21	-24.35	6.50	28.51	1.86	3.44	2.74	1.09	2.90	0.19	2.73	359.61	124.44	192.52	22.66	156.23	5.78	5.15
SK17_0.21-0.22	-24.34	7.32	18.41	1.92	2.30	1.99	2.07	2.11	0.22	2.87	308.84	104.24	134.71	39.00	201.84	8.38	4.56
SK17_0.310-0.315	-24.24	8.46	16.39	2.29	2.02	2.04	0.80	2.33	0.12	3.90	326.13	193.67	205.36	14.89	99.49	3.71	2.28
SK17_0.8-0.81	-23.75	7.15	18.21	2.10	0.29	1.10	2.93	0.87	0.11	3.02	242.23	71.17	46.14	13.46	243.37	12.31	5.80
SK17B_3.0	-22.86	7.92	18.62	1.84	0.36	1.27	3.47	0.86	0.13	3.77	276.49	71.05	53.26	29.59	252.08	11.59	6.50
SK17B_6.5	-20.60	7.36	22.57	1.98	0.40	1.29	3.16	0.94	0.13	3.21	234.39	57.35	38.52	13.03	263.03	12.53	4.74
SK17B_12	-16.68	6.50	18.18	2.17	0.36	1.47	3.28	0.82	0.13	2.71	210.75	60.01	39.95	11.18	271.66	12.48	4.12
SK17B_19	-12.37	7.31	13.11	1.70	0.52	1.88	2.85	0.78	0.14	3.94	253.47	75.35	55.68	32.93	233.10	10.16	7.10
SKB_25	-8.56	7.38	13.20	1.71	0.51	1.63	2.92	0.76	0.16	4.64	276.71	89.47	70.06	42.60	258.63	9.67	11.42
SK17B_31	-4.48	5.28	12.58	1.49	0.36	1.23	2.61	0.80	0.22	2.35	315.39	30.11	68.18	40.63	626.20	10.26	9.20
SK17B_35	-1.34	6.20	11.55	1.39	0.23	1.24	2.77	0.65	0.15	2.43	276.08	34.26	70.16	42.71	396.53	8.76	11.13
SK17B_37.5	-0.28	6.67	11.30	1.47	0.70	0.43	2.02	0.65	0.19	2.30	294.31	30.05	50.67	37.01	389.98	6.26	5.77
SK17B_38	-0.11	6.26	11.95	2.05	0.44	0.61	1.96	0.78	0.05	2.88	381.98	39.85	100.74	36.27	505.46	7.71	6.91
Fur15_4.30	4.30	4.03	10.76	1.60	0.38	0.44	1.33	1.00	0.05	0.65	224.46	27.74	50.33	12.65	179.43	4.14	3.21
Fur15_5.50	5.50	4.47	9.47	1.40	0.12	0.26	1.13	0.79	0.05	1.71	157.13	50.77	50.13	19.05	146.84	5.38	4.26